A hybrid finite-volume finite-difference rotational Boussinesq-type model of surf-zone hydrodynamics

Benjamin Tatlock

Thesis submitted to the University of Nottingham
for the degree of Doctor of Philosophy

December 2015

Abstract

An investigation into the numerical and physical behaviour of a hybrid finite-volume finite-difference Boussinesq-type model, using a rotational surface roller approach in the surf-zone is presented. The relevant theory for the required development of a numerical model implementing this technique is outlined. The proposed method looks to achieve a more physically realistic description of the hydrodynamics by considering the rotational nature of the highly turbulent flow found during wave breaking. This involves a semi-analytical solution to the vorticity transport equation and provides a mechanism by which energy is dissipated. Resolving vorticity within the flow also allows vertical profiles of the horizontal velocity to be constructed, offering valuable detail that is otherwise unavailable when using equivalent irrotational Boussinesq-type models. By obtaining additional information about the structure of the flow, other quantities can be determined, such as the undertow, which has a key role in morphodynamic processes occurring in this region. These benefits are combined with a finite-volume finite-difference scheme, which yields improvements in stability and possesses inherent shock-capturing capabilities.

The ability of the model to replicate laboratory observations is verified, and identified shortcomings are explained in the context of the numerical procedure and the assumptions made during the derivation of the governing equations. Although the weak nonlinearity of the Boussinesq-type equations means the shoaling characteristics of the model do not accurately reflect those found experimentally, the adopted formulation of the finite-volume scheme is shown to prevent the inclusion of the necessary higher-order derivatives which exist in a fully-nonlinear formulation. In order to establish a realistic dissipation mechanism, it is vital that the extent of any misleading numerical artefacts are recognised and their effects alleviated. This study explores a range of physical attributes predicted by the present model and discusses the numerical features of the scheme, evaluating how these influence the results.

Acknowledgements

I wish to take this opportunity to acknowledge those who have helped me to reach this point. I greatly appreciate the time they have generously given, and the knowledge and expertise that they have shared. In particular, I wish to thank my supervisor, Dr Riccardo Briganti, for providing this opportunity and offering his help and guidance at every stage. I would also like to thank Professor Nicholas Dodd for encouraging me to undertake this project. I value the ongoing advice I have received from Dr Rosaria Musumeci, and enjoyed the time I spent at The University of Catania, Italy. Additionally, I am thankful for the helpful discussions with Professor Maurizio Brocchini. I am also grateful for the financial support provided by the Engineering and Physical Sciences Research Council. Finally, I wish to thank my parents for their continual help and support.

Contents

List of Figures

List of Tables

Acronyms

BTE	Boussinesq-type equation
BTM	Boussinesq-type model
DIRANS	Depth integrated Reynolds averaged Navier-Stokes
EVBM	Eddy viscosity breaking model
FD	Finite-difference
FNB	Fully-nonlinear BTE
FOCMT	Fourth-order compact MUSCL-TVD
FV	Finite-volume
FVFD	Finite-volume finite-difference
HBM	HFA breaking model
HFA	Hydrostatic front approximation
LDV	Laser Doppler velocimeter
LES	Large eddy simulation
MUSCL	Monotone upstream-centred scheme for conservation laws
NBM	No breaking model
NSE	Navier-Stokes equation
NSWE	Nonlinear shallow water equation
RANS	Reynolds averaged Navier-Stokes
RBM	Rotational breaking model
SRM	Surface roller method
TVD	Total variation diminishing
VTE	Vorticity transport equation
WNB	Weakly-nonlinear BTE

Nomenclature

Symbol	Description	Dimensions
A_o	Amplitude length scale	L
A_g	Generation wave amplitude	L
a	Tridiagonal coefficient	
B	Dispersive parameter	
b	Tridiagonal coefficient	
$\boldsymbol{b}_+$	Vector for boundary conditions	
$\boldsymbol{b}_-$	Vector for boundary conditions	
C	Solitary wave celerity	$\mathrm{L\,T^{-1}}$
c	Phase celerity	$\mathrm{L\,T^{-1}}$
D	Hybrid flux for momentum equation	$\mathrm{L^2\,T^{-1}}$
D_h	Continuity equation breaking term for EVBM	$\mathrm{L\,T^{-1}}$
D_s	Viscous shear stress	$\mathrm{L^2\,T^{-2}}$
$\widehat{D_\mathrm{s}}$	Nondimensional viscous shear stress	
D_u	Momentum equation breaking term for EVBM	$\mathrm{L^2\,T^{-2}}$
d	Total water depth	L
$\hat{d}$	Nondimensional total water depth	
d_c	Total water depth at roller crest	L
d_d	Total downstream water depth	L
d_L	Total water depth left of cell boundary	L
d_R	Total water depth right of cell boundary	L
d_*	Estimated solution of depth for HLL Riemann solver	L
d_t	Total water depth at roller toe	L

Symbol	Description	Dimensions
d_u	Total upstream water depth	L
E	Temporal wave surface profile variance	L^2
$\boldsymbol{E}$	Hybrid flux vector	$\mathrm{L\,T^{-1}}$; $\mathrm{L^2\,T^{-2}}$
E_b	Temporal wave surface profile variance at breaking point	L^2
F	Coefficient for Fourier series	T^{-2}
$\boldsymbol{F}$	Flux vector	$\mathrm{L^2\,T^{-1}}$; $\mathrm{L^3\,T^{-2}}$
$F_{xx}^{\pm}$	Force acting in x-direction on positive/negative face normal to x-axis	$\mathrm{M\,L\,T^{-2}}$
$F_{xy}^{\pm}$	Force acting in y-direction on positive/negative face normal to x-axis	$\mathrm{M\,L\,T^{-2}}$
$F_{xz}^{\pm}$	Force acting in z-direction on positive/negative face normal to x-axis	$\mathrm{M\,L\,T^{-2}}$
$F_{yx}^{\pm}$	Force acting in x-direction on positive/negative face normal to y-axis	$\mathrm{M\,L\,T^{-2}}$
$F_{yy}^{\pm}$	Force acting in y-direction on positive/negative face normal to y-axis	$\mathrm{M\,L\,T^{-2}}$
$F_{yz}^{\pm}$	Force acting in z-direction on positive/negative face normal to y-axis	$\mathrm{M\,L\,T^{-2}}$
$F_{zx}^{\pm}$	Force acting in x-direction on positive/negative face normal to z-axis	$\mathrm{M\,L\,T^{-2}}$
$F_{zy}^{\pm}$	Force acting in y-direction on positive/negative face normal to z-axis	$\mathrm{M\,L\,T^{-2}}$
$F_{zz}^{\pm}$	Force acting in z-direction on positive/negative face normal to z-axis	$\mathrm{M\,L\,T^{-2}}$
$\boldsymbol{F}_\mathrm{H}$	Flux vector between left and right shocks of HLL Riemann solver	$\mathrm{L^2\,T^{-1}}$; $\mathrm{L^3\,T^{-2}}$
$\boldsymbol{F}_\mathrm{L}$	Flux vector left of cell boundary	$\mathrm{L^2\,T^{-1}}$; $\mathrm{L^3\,T^{-2}}$
$\boldsymbol{F}_\mathrm{R}$	Flux vector right of cell boundary	$\mathrm{L^2\,T^{-1}}$; $\mathrm{L^3\,T^{-2}}$
f	Arbitrary variable	
f_w	Wave frequency	T^{-1}
G	Coefficient for Fourier series	T^{-1}
$\boldsymbol{G}$	Numerical hybrid flux vector	L; $\mathrm{L^2\,T^{-1}}$
g	Acceleration due to gravity in z-direction	$\mathrm{L\,T^{-2}}$
$\boldsymbol{g}$	Three-dimensional vector of acceleration due to gravity	$\mathrm{L\,T^{-2}}$
H	Wave height	L

Symbol	Description	Dimensions
$\boldsymbol{H}$	Vector of free surface elevation and volumetric flow rate per unit length	L; $\mathrm{L}^2\,\mathrm{T}^{-1}$
H_o	Offshore wave height	L
H_b	Wave height at breaking point	L
H_g	Group wave height	L
H_m	Wave height envelope	L
h	Still water depth	L
$\hat{h}$	Nondimensional still water depth	
$\boldsymbol{h}$	Diagonal matrix of still water depth	L
h_o	Still water depth at offshore boundary	L
I	Tridiagonal coefficient	
i	Spatial numerical grid index	
J	Tridiagonal coefficient	
j	Temporal numerical grid index	
K	Tridiagonal coefficient	
k	Wavenumber	L^{-1}
k_o	Typical wavenumber	L^{-1}
L	Number of vertical elements	
l	Summation or product index	
l_r	Roller length	L
l_s	Still water slope length	L
l_t	Turbulence length scale	L
M	Upper limit of summation	
$\boldsymbol{M}$	Matrix of convective momentum terms	$\mathrm{L}^4\,\mathrm{T}^{-2}$
M_t	Largest integer less than the number of timesteps in four wave periods	
m	Fluid mass	M
N	Number of cells in computational domain	
n	Summation, product or series index	
n_b	Number of data points inside bottom boundary layer	
O	Dispersive operator	

Symbol	Description	Dimensions
P	Auxiliary term for tridiagonal solution	
$\boldsymbol{P}$	Matrix of rate of change of pressures induced by vertical acceleration due to flow rotation	$\mathrm{L}^4\,\mathrm{T}^{-2}$
p	Reynolds averaged pressure	$\mathrm{M}\,\mathrm{L}^{-1}\,\mathrm{T}^{-2}$
$\check{p}$	Pressure	$\mathrm{M}\,\mathrm{L}^{-1}\,\mathrm{T}^{-2}$
Q	Auxiliary term for tridiagonal solution	
q	Volumetric flow rate per unit length	$\mathrm{L}^2\,\mathrm{T}^{-1}$
$\hat{q}$	Nondimensional volumetric flow rate per unit length	
q_{L}	Volumetric flow rate per unit length left of cell boundary	$\mathrm{L}^2\,\mathrm{T}^{-1}$
q_{R}	Volumetric flow rate per unit length right of cell boundary	$\mathrm{L}^2\,\mathrm{T}^{-1}$
q_{u}	Upstream volumetric flow rate per unit length	$\mathrm{L}^2\,\mathrm{T}^{-1}$
R	Vertical discretisation of rotational velocity	$\mathrm{L}\,\mathrm{T}^{-1}$
$\boldsymbol{R}$	Matrix of rotational velocities	$\mathrm{L}\,\mathrm{T}^{-1}$
R_{e}	Reynolds number	
r	Summation index	
$\boldsymbol{r}$	Location of fluid particle in three-dimensional space	L
S	Auxiliary term for tridiagonal solution	
$\boldsymbol{S}$	Source vector	$\mathrm{L}\,\mathrm{T}^{-1}$; $\mathrm{L}^2\,\mathrm{T}^{-2}$
S_{L}	Wave speed left of cell boundary	$\mathrm{L}\,\mathrm{T}^{-1}$
S_{m}	Maximum wave speed throughout domain	$\mathrm{L}\,\mathrm{T}^{-1}$
S_{R}	Wave speed right of cell boundary	$\mathrm{L}\,\mathrm{T}^{-1}$
s	Discretised σ-coordinates	
T	Wave period	T
t	Time	T
$\hat{t}$	Nondimensional time	
t^*	Roller development timescale	T
t_{B}	Breaker age	T
U	Conserved variable for tridiagonal solution	$\mathrm{L}^2\,\mathrm{T}^{-1}$
$\boldsymbol{U}$	Vector of total water depth and volumetric flow rate per unit length	L; $\mathrm{L}^2\,\mathrm{T}^{-1}$

Symbol	Description	Dimensions
$\boldsymbol{U}_{\mathrm{H}}$	Data state between left and right shocks of HLL Riemann solver	L; $\mathrm{L}^2\,\mathrm{T}^{-1}$
$\boldsymbol{U}_{\mathrm{L}}$	Vector of total water depth and volumetric flow rate per unit length left of cell boundary	L; $\mathrm{L}^2\,\mathrm{T}^{-1}$
$\boldsymbol{U}_{\mathrm{R}}$	Vector of total water depth and volumetric flow rate per unit length right of cell boundary	L; $\mathrm{L}^2\,\mathrm{T}^{-1}$
u	Horizontal Reynolds averaged velocity	$\mathrm{L}\,\mathrm{T}^{-1}$
$\bar{u}$	Depth averaged horizontal velocity	$\mathrm{L}\,\mathrm{T}^{-1}$
$\check{u}$	Horizontal velocity	$\mathrm{L}\,\mathrm{T}^{-1}$
$\hat{u}$	Nondimensional horizontal Reynolds averaged velocity	
$\hat{\bar{u}}$	Nondimensional depth averaged horizontal velocity	
$\boldsymbol{u}$	Velocity	$\mathrm{L}\,\mathrm{T}^{-1}$
$\hat{u}_{\mathrm{p}}$	Nondimensional potential velocity	
$\hat{\bar{u}}_{\mathrm{p}}$	Nondimensional depth averaged potential velocity	
u_{r}	Rotational velocity	$\mathrm{L}\,\mathrm{T}^{-1}$
$\bar{u}_{\mathrm{r}}$	Depth averaged rotational velocity	$\mathrm{L}\,\mathrm{T}^{-1}$
$\hat{u}_{\mathrm{r}}$	Nondimensional rotational velocity	
$\hat{\bar{u}}_{\mathrm{r}}$	Nondimensional depth averaged rotational velocity	
u_{u}	Undertow	$\mathrm{L}\,\mathrm{T}^{-1}$
V	Arbitrary variable	
v	Horizontal Reynolds averaged velocity	$\mathrm{L}\,\mathrm{T}^{-1}$
$\check{v}$	Horizontal velocity	$\mathrm{L}\,\mathrm{T}^{-1}$
W	Arbitrary variable	
$\boldsymbol{W}$	Conserved vector	L; $\mathrm{L}^2\,\mathrm{T}^{-1}$
w	Vertical Reynolds averaged velocity	$\mathrm{L}\,\mathrm{T}^{-1}$
$\check{w}$	Vertical velocity	$\mathrm{L}\,\mathrm{T}^{-1}$
$\hat{w}$	Nondimensional vertical Reynolds averaged velocity	
X	Arbitrary variable	
$\boldsymbol{X}$	Arbitrary matrix	
x	Horizontal abscissa	L
$\hat{x}$	Nondimensional horizontal abscissa	

Symbol	Description	Dimensions
x_{C}	Location of interpolated roller crest	L
x_{c}	Location of roller crest	L
x_{g}	Centre of wave generation region	L
x_{o}	Location of offshore boundary	L
x_{s}	Length of sponge layer	L
x_{T}	Location of interpolated roller toe	L
x_{t}	Location of roller toe	L
Y	Arbitrary variable	
$\boldsymbol{Y}$	Arbitrary matrix	
y	Horizontal applicate	L
Z	Arbitrary variable	
$\boldsymbol{Z}$	Arbitrary matrix	
z	Vertical ordinate	L
$\hat{z}$	Nondimensional vertical ordinate	
z_{b}	Bathymetric elevation	L
ΔE	Temporal wave surface profile variance relative to that at breaking point	L^2
$\Delta \boldsymbol{H}$	Vector of intercell jumps	L; $\mathrm{L}^2\,\mathrm{T}^{-1}$
$\Delta^* \boldsymbol{H}$	Vector of limited fourth-order cell slopes	L; $\mathrm{L}^2\,\mathrm{T}^{-1}$
$\Delta \grave{\boldsymbol{H}}$	Vector of limited third-order cell slopes	L; $\mathrm{L}^2\,\mathrm{T}^{-1}$
ΔM	Convective momentum term	$\mathrm{L}^3\,\mathrm{T}^{-2}$
$\widehat{\Delta M}$	Nondimensional convective momentum term	
ΔP	Pressure induced by vertical acceleration due to flow rotation	$\mathrm{L}^4\,\mathrm{T}^{-1}$
$\widehat{\Delta P}$	Nondimensional pressure induced by vertical acceleration due to flow rotation	
Δt	Temporal grid resolution	T
ΔX	Polynomial interpolation interval	
Δx	Spatial grid resolution	L
α	Wave generation dispersion parameter	
α_{r}	Function for distribution of injected vorticity	

Symbol	Description	Dimensions
α_{v}	Coefficient for distribution of injected vorticity	
β	Wave generation region width coefficient	
Γ	Numerical width of solitary wave	L
γ	Maximum representable real number	
Δ	Change in quantity	
δ	Nonlinearity	
$\delta_{i,j}$	Kronecker delta function	
ϵ_1	Quadratic error across one dimension	
ϵ_2	Quadratic error across two dimensions	
ζ	Free surface elevation relative to still water level	L
$\hat{\zeta}$	Nondimensional free surface elevation relative to still water level	
$\boldsymbol{\zeta}$	Vector of free surface elevation throughout computational domain	L
ζ_{e}	Free surface elevation of single-phase fluid	L
$\hat{\zeta}_{\mathrm{e}}$	Nondimensional free surface elevation of single-phase fluid	
ζ_{m}	Mean free surface elevation	L
ζ_{r}	Relative mean free surface elevation	L
ζ_{s}	Free surface elevation relative to set-up	L
ζ_{t}	Trough of free surface elevation	L
$\boldsymbol{\eta}$	Vector of free surface elevation of single-phase fluid throughout computational domain	L
Θ	Horizontal abscissa for roller coordinate system	
θ	Angle of free surface to horizontal at roller toe	
θ_{o}	Breaking termination angle	
θ_{B}	Breaking initiation angle	
ι	Hybrid flux for continuity equation	L
κ	Weighting parameter for FOCMT reconstruction	
Λ	Temporal component of wave generation source function	
λ	Wavelength	L
μ	Dispersivity	

Symbol	Description	Dimensions
ν	Kinematic viscosity	$\mathrm{L}^2\,\mathrm{T}^{-1}$
ν_h	Diffusivity function for EVBM	$\mathrm{L}^2\,\mathrm{T}^{-1}$
ν_t	Eddy viscosity	$\mathrm{L}^2\,\mathrm{T}^{-1}$
$\hat{\nu}_\mathrm{t}$	Nondimensional eddy viscosity	
ξ_o	Offshore Iribarren number	
ξ_b	Iribarren number at breaking point	
$\boldsymbol{\Pi}$	Weighted ratios of the diameter of a circle to its circumference	
π	Ratio of the circumference of a circle to its diameter	
ρ	Fluid density	$\mathrm{M}\,\mathrm{L}^{-3}$
σ	Transformed z-coordinate	
$\boldsymbol{\sigma}$	Three-dimensional vector of fluid stresses	$\mathrm{M}\,\mathrm{L}^{-1}\,\mathrm{T}^{-2}$
σ_{xx}	Normal stress acting in x-direction	$\mathrm{M}\,\mathrm{L}^{-1}\,\mathrm{T}^{-2}$
σ_{yy}	Normal stress acting in y-direction	$\mathrm{M}\,\mathrm{L}^{-1}\,\mathrm{T}^{-2}$
σ_{zz}	Normal stress acting in z-direction	$\mathrm{M}\,\mathrm{L}^{-1}\,\mathrm{T}^{-2}$
τ	Stress	$\mathrm{M}\,\mathrm{L}^{-1}\,\mathrm{T}^{-2}$
$\breve{\tau}$	Reynolds stress	$\mathrm{M}\,\mathrm{L}^{-1}\,\mathrm{T}^{-2}$
τ^v	Viscous stress	$\mathrm{M}\,\mathrm{L}^{-1}\,\mathrm{T}^{-2}$
τ_{xx}	Modelled stress acting in x-direction on face normal to x-axis	$\mathrm{M}\,\mathrm{L}^{-1}\,\mathrm{T}^{-2}$
τ_{xy}	Modelled stress acting in y-direction on face normal to x-axis	$\mathrm{M}\,\mathrm{L}^{-1}\,\mathrm{T}^{-2}$
$\breve{\tau}_{xy}$	Stress acting in y-direction on face normal to x-axis	$\mathrm{M}\,\mathrm{L}^{-1}\,\mathrm{T}^{-2}$
τ_{xz}	Modelled stress acting in z-direction on face normal to x-axis	$\mathrm{M}\,\mathrm{L}^{-1}\,\mathrm{T}^{-2}$
$\breve{\tau}_{xz}$	Stress acting in z-direction on face normal to x-axis	$\mathrm{M}\,\mathrm{L}^{-1}\,\mathrm{T}^{-2}$
τ_{yx}	Modelled stress acting in x-direction on face normal to y-axis	$\mathrm{M}\,\mathrm{L}^{-1}\,\mathrm{T}^{-2}$
$\breve{\tau}_{yx}$	Stress acting in x-direction on face normal to y-axis	$\mathrm{M}\,\mathrm{L}^{-1}\,\mathrm{T}^{-2}$
τ_{yy}	Modelled stress acting in y-direction on face normal to y-axis	$\mathrm{M}\,\mathrm{L}^{-1}\,\mathrm{T}^{-2}$
τ_{yz}	Modelled stress acting in z-direction on face normal to y-axis	$\mathrm{M}\,\mathrm{L}^{-1}\,\mathrm{T}^{-2}$

Symbol	Description	Dimensions
$\check{\tau}_{yz}$	Stress acting in z-direction on face normal to y-axis	$\mathrm{M\,L^{-1}\,T^{-2}}$
τ_{zx}	Modelled stress acting in x-direction on face normal to z-axis	$\mathrm{M\,L^{-1}\,T^{-2}}$
$\check{\tau}_{zx}$	Stress acting in x-direction on face normal to z-axis	$\mathrm{M\,L^{-1}\,T^{-2}}$
τ_{zy}	Modelled stress acting in y-direction on face normal to z-axis	$\mathrm{M\,L^{-1}\,T^{-2}}$
$\check{\tau}_{zy}$	Stress acting in y-direction on face normal to z-axis	$\mathrm{M\,L^{-1}\,T^{-2}}$
τ_{zz}	Modelled stress acting in z-direction on face normal to z-axis	$\mathrm{M\,L^{-1}\,T^{-2}}$
Υ	Sponge layer strength parameter	$\mathrm{T^{-1}}$
υ	Distribution of injected vorticity	
$\boldsymbol{\Phi}$	Spatial component of wave generation source function	$\mathrm{L\,T^{-1}}$
ϕ_3	Symmetric third-order slope limiter	
ϕ_4	Fourth-order slope limiter	
ϕ_{M}	Fourth-order minmod limiter	
ϕ_{m}	Third-order minmod limiter	
ϕ_{v}	Van-Leer limiter	
χ	Sum of breaking terms	$\mathrm{L^2\,T^{-2}}$
Ψ	Absorbing boundary source term	$\mathrm{L^2\,T^{-2}}$
ψ	Lagrangian stream function	$\mathrm{L^2T^{-1}}$
$\hat{\psi}$	Nondimensional Lagrangian stream function	
$\hat{\Omega}$	Nondimensional function for homogonised vorticity	
$\boldsymbol{\Omega}$	Matrix of vertically scaled vorticities at lower edge of roller	$\mathrm{T^{-1}}$
ω	Vorticity	$\mathrm{T^{-1}}$
$\hat{\omega}$	Nondimensional vorticity	
$\boldsymbol{\omega}$	Matrix of vorticities	$\mathrm{T^{-1}}$
ω_{m}	Coefficient for maximum vorticity injection at lower edge of roller	
ω_{s}	Vorticity at lower edge of roller	$\mathrm{T^{-1}}$
$\hat{\omega}_{\mathrm{s}}$	Nondimensional vorticity at lower edge of roller	
$\boldsymbol{\nabla}$	Vector differential operator	

Symbol	Description	Dimensions
$\mathbb{N}_0$	Set of natural numbers corresponding to the non-negative integers	
$\mathbb{N}_1$	Set of natural numbers corresponding to the positive integers	
$\mathcal{C}$	Courant number	
$\mathcal{C}_n$	Courant number coefficient	
$\mathcal{G}$	Wave groupiness	
$\mathcal{L}$	Lagrange form interpolation polynomial	
ℓ	Cardinal polynomial	
$\mathcal{N}$	Degree of polynomial interpolation	
$\mathcal{S}$	Horizontal slosh	$\mathrm{L\,T^{-1}}$
$\mathcal{V}$	Numerical control volume	
$\mathfrak{C}$	Coefficient for matrix multiplication	
$\mathfrak{C}$	Matrix of coefficients for multiplication	
$\mathfrak{d}$	Vector of reciprocal of total water depth	L
$\mathfrak{G}$	Matrix of Fourier series coefficients throughout computational domain	$\mathrm{T^{-1}}$
$\mathfrak{p}$	Weighted ratios of the cube of the diameter of a circle to its circumference	
$\mathfrak{R}$	Coefficient for matrix multiplication	
$\mathfrak{R}$	Matrix of coefficients for multiplication	
$\mathfrak{r}$	Vector of rotational velocities at bed throughout computational domain	$\mathrm{L\,T^{-1}}$
$\mathfrak{U}$	Matrix of spatial gradients of horizontal velocity	$\mathrm{T^{-1}}$
$\mathfrak{u}$	Matrix of horizontal velocities	$\mathrm{L\,T^{-1}}$
$\bar{\mathfrak{u}}$	Matrix of depth averaged horizontal velocities	$\mathrm{L\,T^{-1}}$
$\mathfrak{V}$	Coefficient for matrix multiplication	
$\mathfrak{V}$	Matrix of coefficients for multiplication	
$\mathfrak{v}$	Vector of vorticities at lower edge of roller throughout computational domain	$\mathrm{T^{-1}}$

Chapter 1

Introduction

1.1 Background

Throughout much of human history, the coastal environment has held significant engineering importance due to the growth of communities in regions near the shore. Protecting populations inhabiting land in close proximity to the sea has remained a key concern for many developing civilisations, and therefore become a focus of scientific research. By improving technical understanding of oceanographic processes and their impact within the environment, planning and design activities can be better informed. Continued construction in marine environments extends the engineering relevance of the physics governing flows in this region.

Expanding computational capabilities have allowed greater amounts of engineering design to be informed by numerical simulations. This has led to the development of a field of science known as computational fluid dynamics, where the ability of computers to perform large numbers of simple calculations is exploited. This has required mathematical problems to be formulated in a way that suits such an approach, and spawned new investigations into ways of increasing the efficiency with which problems can be posed in a form that is appropriate for numerical solution.

The generation of ocean waves begins with disturbing forces perturbing the water surface, after which a second force restores equilibrium. The characteristic dominant driving forces for a range of wave periods can be seen in Figure 1.1 (Lin, 2008). The chief consideration here will be waves primarily created by wind and gravitational forces. As wind generated shear forces at the sea surface are exerted over a fetch, they continuously add energy to the waves which, over large spaces such as the ocean, becomes significant. The work presented here regards existing waves as they enter the nearshore region, and looks to study the transformations that subsequently take place.

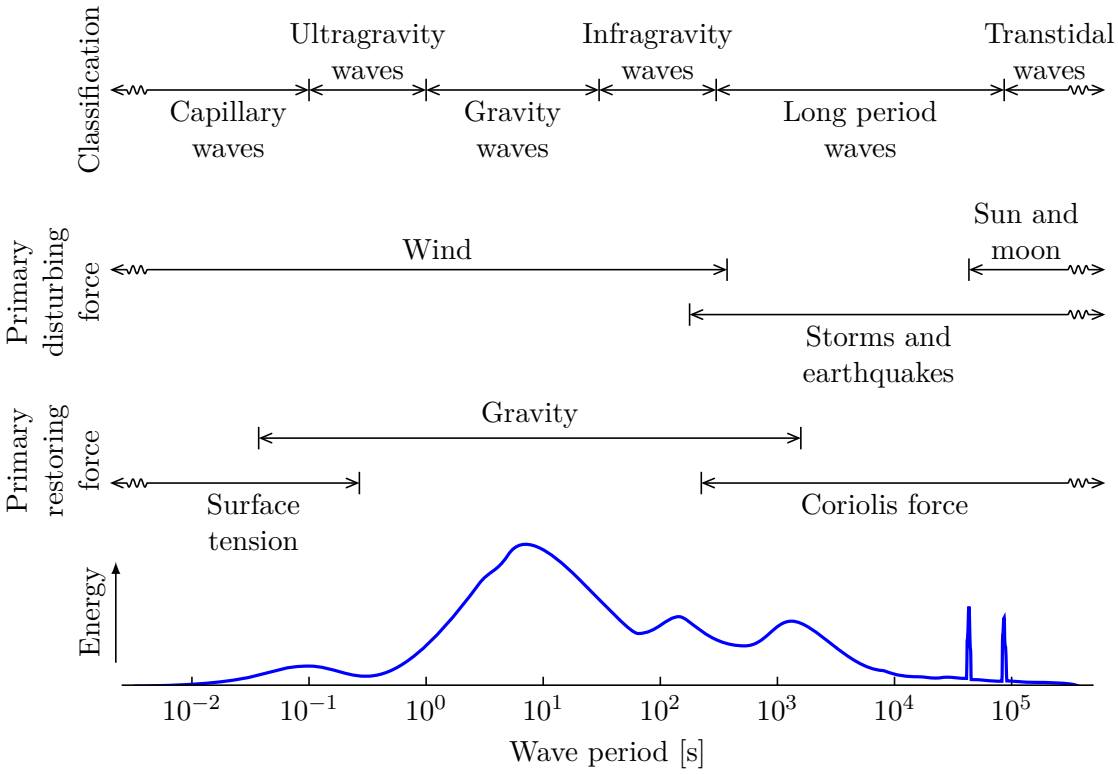

Figure 1.1: Illustrative classification of ocean waves, dominant forces and representative embodied energy (Munk, 1950; Kinsman, 1984).

1.2 Governing equations

There has been much interest in the study of coastal processes amongst the research community. The nonlinear shallow water equations (NSWEs) have long been used to simulate wave propagation, but are only applicable when the ratio between the wave height and wavelength is sufficiently small (Svendsen, 2006). Recent decades have seen many advances in the use of Boussinesq-type equations (BTEs), which allow numerous physical phenomena to be replicated while maintaining a reasonable level of mathematical simplicity (Boussinesq, 1872; Peregrine, 1967). As such, BTEs remain computationally efficient when implemented in numerical models, allowing wave propagation to be simulated numerically using a single approach over a wide region of interest (Madsen et al., 1991). Accordingly, BTEs can accurately reproduce hydrodynamics in deeper water than is possible with the NSWEs, allowing a more comprehensive and complete approach to be taken when modelling wave propagation from further offshore.

With the derivation of BTEs often involving the assumption of potential flow, any rotation within the fluid is neglected. This hypothesis becomes invalid during wave breaking due to the high levels of turbulence that are encountered. As the turbulent forces become significant, a major limitation of the BTEs is revealed. To facilitate the use of BTEs for practical predictions, it is necessary to add a method to simulate the

breaking process. Introducing accurate representations of wave breaking into Boussinesq-type models (BTMs) has thus been crucial in allowing their application to nearshore simulations.

1.3 Research objectives

This work aims to develop an effective means of simulating the flow in the surf-zone in a computationally efficient manner. In order to ensure the physical appropriateness of the method adopted here, a consideration of the hydrodynamic processes occurring in this region forms the basis of the description used. The present study achieves this through the adoption of a rotational roller approach, which retains a physically realistic foundation for replicating the energy dissipation observed during wave breaking events. A new method is suggested, whereby an approach considering rotation within the flow is implemented in a hybrid finite-volume finite-difference (FVFD) BTM. The feasibility of this procedure is subsequently assessed, and the attributes and capabilities of such an approach considered.

The research outlined in this thesis provides an insight into the methodology of the aforementioned technique and the benefits it provides, but also looks to consider any limitations that exist, both within the proposed scheme and other existing models adopting similar methods. In order to thoroughly evaluate finer aspects of the scheme, a number of detailed tests are undertaken which collectively trial several qualities. These allow the effectiveness and accuracy of the model to be measured, and provide a means by which the performance can be assessed by considering its ability to replicate a range of hydrodynamic features.

It is important that any numerical effects of an adopted scheme are recognised, and their impact during simulations minimised. Consequently, a major focus of this investigation is the identification and attribution of any artefacts present in model predictions. The proposed approach looks to provide a suitable balance between computational efficiency, numerical stability, and the physical grounding of the observed model behaviour, reducing the overall compromise in these characteristics when compared with existing alternatives. Previous approaches have encountered problems whereby artificial properties of the model mask the true nature of the hydrodynamics. Reducing the prevalence of such deficiencies allows a better description of wave propagation through the surf-zone.

1.4 Thesis outline

In order to develop a numerical model capable of simulating the complex features present in the region of interest, it is important that the context of the processes studied here is understood. Properly separating numerical and physical effects requires a good

understanding of the governing physics and the intricacies of the mathematical approach used to solve the relevant equations. A brief description of the nearshore region is therefore given in Chapter 2. The role of turbulence during breaking is then discussed, and a selection of modelling techniques used to represent this process outlined.

Chapters 3 and 4 detail the mathematical formulation of the equations solved by the model, thereby providing the expressions used in the present study to describe the hydrodynamics in the nearshore region. An overview of numerical techniques used by similar models is provided in Chapter 5, along with a detailed description of the approach exploited in this work and the method used to generate waves within the domain.

The performance of the model is then assessed in Chapter 6, where existing experimental observations are used to validate the results and identify any limitations. A more detailed investigation of the numerical properties of the model is then conducted in Chapter 7. Chapter 8 contains further discussion of the findings and highlights the successes of the study. Finally, the appendices provide further details of subject matter considered elsewhere, and are referenced in the text where additional information may be required.

Chapter 2

The surf-zone

2.1 Nearshore hydrodynamics

The hydrodynamics near the shore are of fundamental importance in most aspects of coastal engineering. The influence of wave breaking on surf-zone hydrodynamics reinforces the need to improve the current understanding of the physics involved due to the subsequent impact on many coastal processes, including interactions with structures, morphodynamics and the health and distribution of local organisms (Losada et al., 2005).

As ocean waves propagate over a beach slope, a number of processes prompt their transformation. Within the nearshore region, the depth of water becomes sufficiently small for the bed to influence the surface of the waves. The effect of this varies as the wave travels shoreward, and the nearshore region is categorised into the distinct areas based on the dominant processes occurring at each stage, as shown in Figure 2.1.

At greater depths, the interaction with the bathymetry causes the height of the wave to increase. This process is known as shoaling, from which the shoaling region is designated. The shoaling also accentuates the difference in velocity between the fluid travelling at the crest and the trough. With greater speeds present higher in the water column, the wave shape begins to deform. This phenomenon continues as the water depth diminishes further, until the resulting steepness of the wave is such that the stability of free surface can no longer be maintained. At this point, the wave begins to break, marking the start of the surf-zone. This is the main region of interest for the study presented here.

Although not all of the factors influencing the transformation of a wave approaching breaking are fully understood, it is apparent that the surface tension and initial distribution of energy both play key roles (Duncan, 2001). The breaking process leads to the dissipation of energy from a wave, causing a reduction in wave height. In turn, the wave regains stability and therefore ceases breaking.

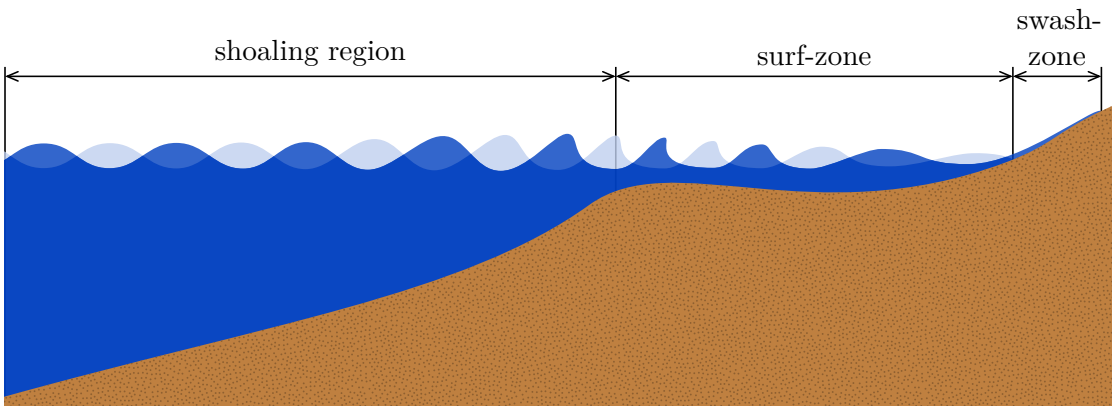

Figure 2.1: Surf-zone hydrodynamics in the nearshore region.

The shoreline is located where the bed level exceeds that of the free surface. Any remaining momentum carries the fluid up the beach slope, creating a region which is periodically wetted in sequence with the incoming waves. The region in which the bed goes through a cycle of wet and dry states because of this action is known as the swash-zone.

As a wave propagates shoreward, the resulting combination of water pressure and particle velocities introduce a momentum flux. The radiation stress quantifies the wave induced effects averaged over time (Longuet-Higgins and Stewart, 1964). Spatial and temporal variations in height due to the shoaling and breaking of a wave lead to variations in this stress. The shoreward increase in mean water level that balances the gradient of the radiation stress is referred to as the set-up (Fredsøe and Deigaard, 1992; Goda, 2010).

The importance of surf-zone hydrodynamics is further stressed by the interplay between the processes occurring in this region and others. In particular, the turbulence generated during breaking can persist onwards into the swash-zone, where the ensuing currents modify the morphodynamic impact of the flow (Puleo et al., 2000). Improving the description of surf-zone hydrodynamics means that the flow beyond this region can be better understood and more accurately modelled.

2.2 Breaker types

The bathymetric gradient and wave height together influence the type of breaker that forms in the surf-zone. The Iribarren number gives a measure of the bed slope relative to the wave height, thereby providing a means by which breaker types can be classified (Lin, 2008). A value can be established offshore with (Galvin, 1968)

$$\xi_0 = \frac{\partial h}{\partial x}\sqrt{\frac{2\pi}{kH_0}}, \tag{2.1}$$

Table 2.1: Breaker types according to Iribarren number (Battjes, 1974).

Breaker type	Iribarren number	
	Offshore	Breaking point
Spilling	$\xi_0 < 0.5$	$\xi_\mathrm{b} < 0.4$
Plunging	$0.5 < \xi_0 < 3.3$	$0.4 < \xi_\mathrm{b} < 2.0$
Surging or collapsing	$\xi_0 > 3.3$	$\xi_\mathrm{b} > 2.0$

or at the point of breaking, with

$$\xi_\mathrm{b} = \frac{\partial h}{\partial x}\sqrt{\frac{2\pi}{kH_\mathrm{b}}}. \tag{2.2}$$

Here, h is the still water level, k is the wavenumber, x is the horizontal abscissa and $\pi \approx 3.14159$. The wave heights offshore and at the breaking point are denoted by H_o and H_b, respectively.

Figure 2.2 illustrates the different breaker types, while Table 2.1 gives the corresponding ranges for the Iribarren number both offshore and at the breaking point. Although discrete categories are used to catalogue breakers, the intricate differences between each type can be subtle, and in reality, a gradual transition between each case exists.

Spilling breakers are typically characterised by a foamy surface on the shoreward face of the breaker, created as instabilities cause a cascading of the crest, with the resulting turbulent mixing causing the entrainment of air into the fluid. Such waves exhibit a relatively small change in fluid motion at the onset of breaking. As gentle bathymetries and steep waves are readily available in nature, spilling breakers are found to occur most often.

Plunging breakers are identified by a crest that curls over the front face and collides with the water below, resulting in a large amount of splash. This overturning motion generates the largest amount of turbulence of any breaker, and the intensity of the vortical motions created by the falling jet can sometimes be significant enough to propagate as far as the bed, resulting in bed scour. The impingement of the crest onto the trough of the wave produces the most striking breaking case, with the resulting tube leading to high levels of aeration.

Both surging and collapsing breakers possess an unbroken crest, with the surf-zone narrow or absent in the former. Surging breakers possess minor levels of breaking and see the front face of the wave wash up the beach slope. Collapsing breakers are largely viewed as a combination of plunging and surging, with an irregular distribution of turbulence found at the surface following the steepening and subsequent descent of the shoreward front (Dean and Dalrymple, 1991; Dabiri and Gharib, 1997; Smith, 2003).

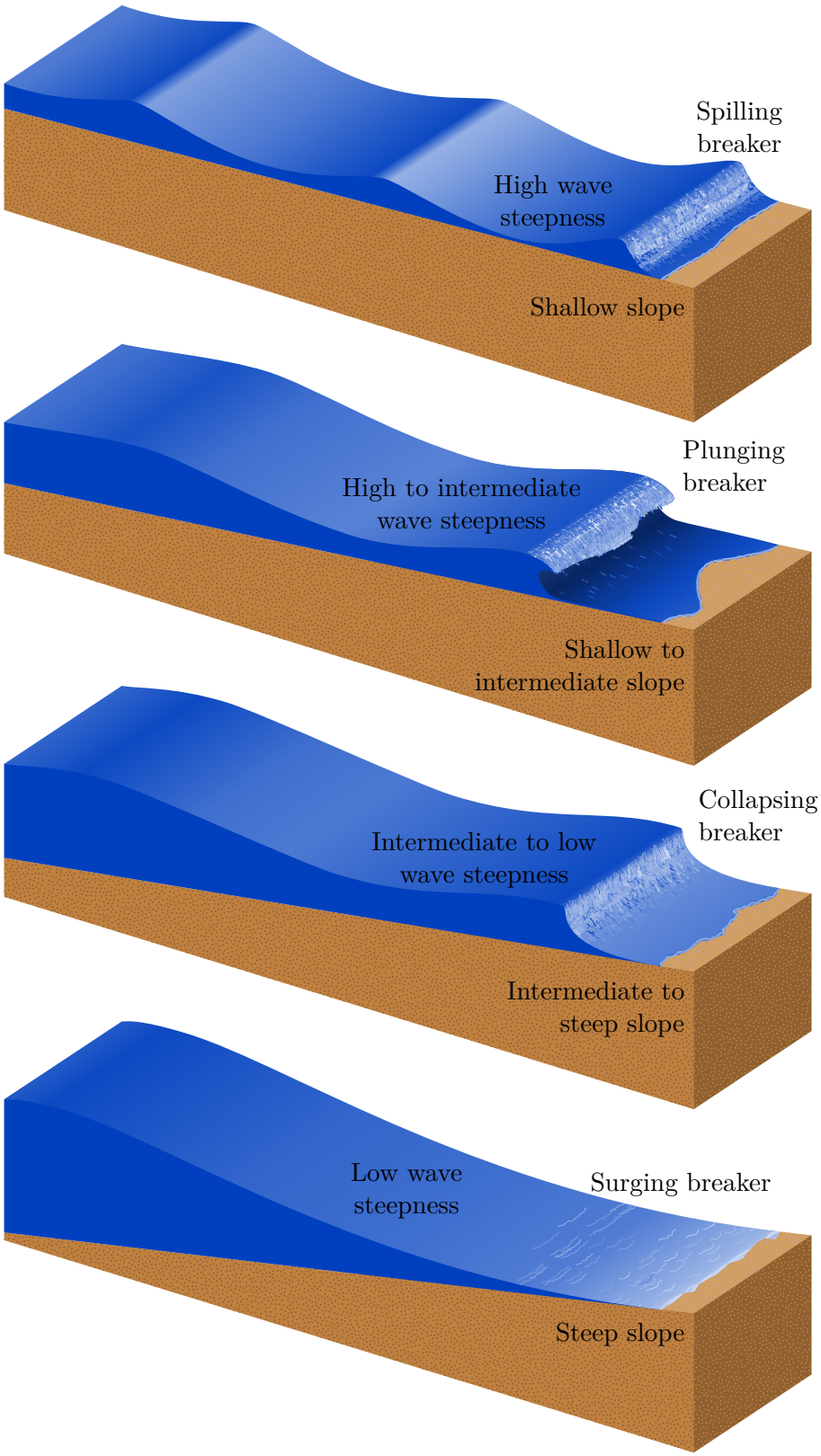

Figure 2.2: Breaker types according to relative wave and slope steepness (Davis, 1994; Holthuijsen, 2007).

2.3 Turbulence during breaking

A key attribute of breaking is the transformation of the potential and kinetic energy propagating with the wave into other, locally confined forms. This is manifested in many complex processes, in particular through the formation of eddies (Duncan, 2001). As a phenomenon affecting many aspects of physics, turbulence has been studied in numerous different contexts, each with commonalities that allow mathematical descriptions to be shared. Broadly speaking, turbulence describes an irregular motion within a fluid, although this definition can bring some ambiguity. For the purposes of this study, ocean turbulence is taken to describe the small scale processes occurring near the surface when a wave breaks. The dynamics found in such turbulent flow sees cascading eddies fragmented into ever smaller components (Foiaş et al., 2001; Thorpe, 2007).

As direct simulation of turbulent processes drastically enlarges the numerical complexity of the problem, it is convenient to devise an approach that is able to represent the physics that exist within the flow without solving every intricate detail comprehensively. By considering the formation of a surface roller, a simplified method of energy dissipation during breaking can be developed (Svendsen, 1984a; Karambas and Koutitas, 1992). Surface roller methods (SRMs) employ a variety of techniques to implement this approach in numerical simulations of wave breaking. A primary consideration in the selection of a particular SRM is the appropriate turbulence model, the most common of which use large eddy simulation (LES) and Reynolds averaged Navier-Stokes (RANS) methods (Dimakopoulos and Dimas, 2011).

An LES approach considers the range of scales at which turbulent processes occur and applies a filtering technique to remove the smaller processes described by an exact solution of the Navier-Stokes equations (NSEs). This brings computational gains to simulations, but requires further treatment to mimic the effects of the small scale turbulence that is no longer resolved, most commonly with the addition of an appropriate numerical method (Sagaut, 2006). Amongst others, Christensen and Deigaard (2001) and Lubin et al. (2006), demonstrated the use of an LES model to simulate the turbulent flow field produced during wave breaking. Although this can provide a detailed three-dimensional view of the flow under breaking, the resolution required to simulate eddy currents in this complex region still bears relatively large computational costs.

Conversely, using a RANS approach allows larger numerical grids to be adopted and offers improved computational performance. While the coarser resolutions are generally considered less suited to the more erratic flow fields resulting from plunging breakers, steadier cases usually lend themselves to more extensive filtering techniques which allow the governing equations to be simplified.

The formulation of the RANS equations is detailed in Appendix A.3, where turbulent fluctuations are separated from the time-averaged component of the flow. As shown in Appendix A.4, the depth integrated Reynolds averaged Navier-Stokes (DIRANS) equations are then obtained by averaging over the vertical water column, thereby further simplifying

the problem. As a result, the rotational component of the flow is no longer resolved, and it is necessary to reintroduce this aspect of the hydrodynamics by other means. While the assumption of irrotationality can be retained in areas with negligible levels of vorticity, the breaking region requires special treatment. The main focus of the present study is the provision of this using the SRM.

2.4 The surface roller

Unsteady breaking events located in deep water are typically found to be spilling or plunging. Steady breakers can be divided into two and three-dimensional cases, with the latter normally classed within the spilling to plunging range. All two-dimensional steady breakers can be described as spilling breakers, and have been more widely studied as their less chaotic and more stable nature makes them easier to observe. In particular, the similarities found between the flow fields of spilling breakers and weak hydraulic jumps allow measurements made in a more controlled environment to be used to better understand the dynamics of such cases (Longo et al., 2002). This overcomes some of the difficulties encountered when attempting to observe wave breaking, and provides the basis for the roller approach used in the model outlined by the present work.

In the absence of breaking, waves can be described as the transport of energy through a medium that results in the movement of individual fluid particles. This is generally along a closed elliptical path and therefore results in a localised oscillatory motion. In contrast to this, the breaking mechanism in the surf-zone creates a shoreward transport of mass as the wave carries the fluid inside the roller region. The undertow current is located towards the bottom of the water column, and returns fluid carried onshore back in the seaward direction. Because the strength of this current and its proximity to the bed introduce a significant shear stress, it is of particular interest when studying morphodynamics in the surf-zone (Fredsøe and Deigaard, 1992; Davis and Fitzgerald, 2009).

2.4.1 Modelling approaches

When modelling using the SRM, the flow is no longer considered to be entirely single-phase. Instead, a roller region is defined in which two-phase flow exists (Svendsen, 1984b). As fluid in the surface roller experiences little vertical acceleration, the pressure is assumed to be hydrostatic. This leads to the introduction of a shear stress at the interface at the lower edge of the roller (Deigaard and Fredsøe, 1989). For the present work, the approach proposed by Svendsen et al. (1996) is adopted, whereby vorticity is injected into the fluid along this lower edge, although many other variants of the SRM have been suggested to represent the turbulent flow in the roller region.

Examples of SRMs that do not interpret the vorticity in the flow include Deigaard and Fredsøe (1989), who suggested that the energy dissipation caused by breaking can

be attributed to an increase in pressure due to the mass of the fluid within the roller. The eddy viscosity approach is another alternative method adopted by Zelt (1991) and Kennedy et al. (2000), whereby wave height decay during breaking is simulated by considering an energy deficit in the momentum equation. Cienfuegos et al. (2010) later extended this technique by contemplating a similar imbalance in the continuity equation.

Modelling the vorticity within the flow with an SRM means the physics of the breaking process are more closely reproduced without adding significant computational demand over conventional depth averaged BTMs. This technique requires the vorticity transport equation (VTE) to be solved alongside the BTEs, and has been employed previously in other models, including those outlined by Veeramony and Svendsen (2000), Briganti et al. (2004) and Musumeci et al. (2005). As the class of models using this method consider the rotationality within the flow in order to replicate the breaking process, they shall henceforth be referred to as rotational breaking models (RBMs). In addition to the dissipative terms needed to represent the breaking process, other important quantities can also be estimated by considering the recirculation of the flow within the roller region. The RBMs considered here use the SRM to inject vorticity into the flow, and then calculate the transport of this quantity through the fluid.

The construction of velocity profiles allows a more detailed picture of the flow in the surf-zone to be established, while predictions of the undertow are valuable when considering sediment transport occurring in the nearshore region. Lynett (2006) presents a model capable of calculating the velocity and undertow under breaking waves with existing depth integrated BTMs, but this is done in isolation and therefore lacks the physical rigour of an RBM. By coupling BTEs with the VTE, the acquired breaking terms are more firmly connected to the velocity and undertow predictions, thereby allowing the physical influence of the RBM to be more realistically validated against laboratory data of free surface and velocity profiles. This also provides an effective means to quantify morphodynamic processes caused by turbulent flow under breaking waves. By understanding these systems, sediment transport mechanisms can be better simulated, allowing important coastal processes such as bar migration to be predicted.

Chapter 3

Boussinesq equations

3.1 Motivations

Fluid flows can be described with great accuracy using the NSEs derived in Appendix A.2, but the resulting detail with which processes are replicated means the computational cost is often unfeasibly high. By instead formulating problems in terms of BTEs, a numerical economy is gained and a mathematical well-posedness obtained. This ensures a reasonable level of computational simplicity is achieved. The growing use of contemporary BTMs amongst the oceanographic community is a reflection of their effectiveness and functionality for the practical modelling of complex phenomena for coastal engineering purposes (Brocchini, 2013).

The derivation performed here follows a similar approach to that of Veeramony and Svendsen (2000), but with the alternative steps needed to construct a solution in the form required by the FVFD scheme. The relations obtained also include the fully-nonlinear BTEs (FNBs) and the additional breaking term introduced by Musumeci et al. (2005), but instead provide a system of equations in terms of the flow rate and total water depth, rather than the depth averaged velocity and free surface elevation. In order to ensure the formulation is consistent with that used in the present work, the composition of the equations provided differs from that utilised in the literature discussed. The details of the derivation provided here also illustrate the way in which physical aspects of the flow are described within the model.

3.2 Formulation

Appendix A details the derivation of the BTEs, thereby outlining the assumptions and simplifications that are assigned in order to obtain the equations used in the present work. An overview of the key requirements of this procedure is provided here in order to summarise the steps taken.

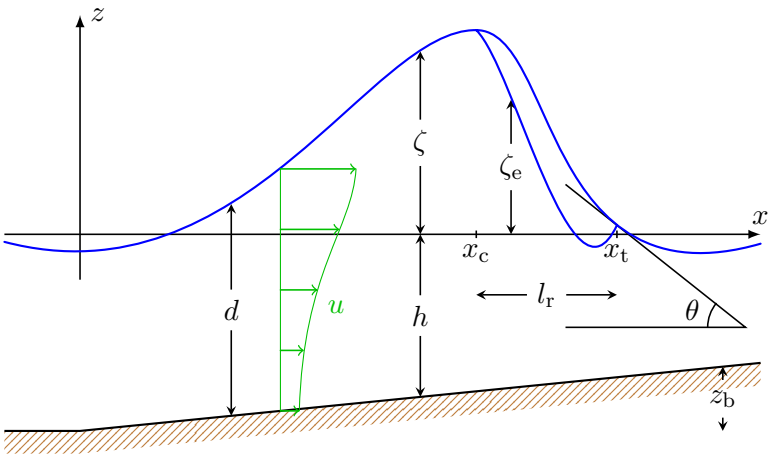

Figure 3.1: Description of equation variables and surface roller geometry.

3.2.1 Reynolds averaged Navier-Stokes equations

The first stage in formulating the BTEs from the NSEs involves the separation of small scale processes in order to simplify the governing equations. This is outlined in greater depth in Appendix A.3. The present work does not include the effects of longshore processes as the formulation only considers two-dimensions. This further simplifies the governing equations and reduces the computational requirements of models implementing such an approach. With this procedure, the RANS equations are obtained in two dimensions:

$$\frac{\partial u}{\partial t} + \frac{\partial u^2}{\partial x} + \frac{\partial}{\partial z}(uw) = \frac{1}{\rho}\left(\frac{\partial \tau_{xx}}{\partial x} + \frac{\partial \tau_{xz}}{\partial z}\right) - \frac{1}{\rho}\frac{\partial p}{\partial x} \tag{3.1}$$

$$\frac{\partial w}{\partial t} + \frac{\partial}{\partial x}(uw) + \frac{\partial w^2}{\partial z} = \frac{1}{\rho}\left(\frac{\partial \tau_{xz}}{\partial x} + \frac{\partial \tau_{zz}}{\partial z}\right) - \frac{1}{\rho}\frac{\partial p}{\partial z} - g \tag{3.2}$$

Here, u and w denote the horizontal and vertical fluid velocities respectively, while ρ is the density, p the pressure, t the time, z the vertical ordinate and $g = 9.81\,\mathrm{m\,s^{-2}}$ the acceleration due to gravity. The terms τ_{xx} and τ_{zz} give the normal stresses acting on the fluid, and τ_{xz} the tangential stresses. Figure 3.1 provides an overview of a selection of the equation variables.

3.2.2 Depth integrated Reynolds averaged Navier-Stokes equations

The model presented in this work utilises the RANS equations defined in Equations (3.1) and (3.2) as the basis for both the BTEs and the derivation of the breaking terms constructed from the semi-analytical solution to the VTE obtained in Chapter 4. As such, the RBM looks to mitigate the impact of any further approximations made when deriving the BTEs from the RANS equations. It is therefore considered reasonable to simplify the general description of the flow with the knowledge that any physical processes that are subsequently unresolved can be reintroduced by alternative terms where necessary, namely where the flow is considered turbulent (Brocchini, 2013).

Having established a suitable strategy for simplifying the governing equations, a further reduction is achieved by averaging the RANS equations over the depth of the water column in order to provide a one-dimensional model. The depth averaged value of a given variable, f, is taken as

$$\bar{f} = \frac{1}{\zeta + h} \int_{-h}^{\zeta} f \, \mathrm{d}z, \tag{3.3}$$

where ζ denotes the free surface elevation relative to the still water level. Additionally, the bed is assumed to be fixed, such that

$$\frac{\partial h}{\partial t} = 0, \tag{3.4}$$

and the gauge pressure at the surface is taken to be zero:

$$p|_{z=\zeta} = 0 \tag{3.5}$$

The full derivation of the DIRANS equations is outlined in Appendix A.4, and provides the following continuity and momentum equations:

$$\frac{\partial d}{\partial t} + \frac{\partial q}{\partial x} = 0 \tag{3.6}$$

$$\begin{aligned}
&\frac{\partial q}{\partial t} + \frac{\partial}{\partial x}\int_{-h}^{\zeta} u^2 - \frac{\tau_{xx}}{\rho} \, \mathrm{d}z + gd\frac{\partial \zeta}{\partial x} - \int_{-h}^{\zeta} \frac{\partial^2}{\partial x \partial t} \int_{z}^{\zeta} \frac{\partial}{\partial x} \int_{-h}^{z'} u \, \mathrm{d}z'' \, \mathrm{d}z' \, \mathrm{d}z \\
&- \int_{-h}^{\zeta} \frac{\partial^2}{\partial x^2} \left(\int_{z}^{\zeta} u \frac{\partial}{\partial x} \int_{-h}^{z'} u \, \mathrm{d}z'' + \frac{\tau_{xz}}{\rho} \, \mathrm{d}z' \right) \mathrm{d}z \\
&+ \int_{-h}^{\zeta} \frac{\partial}{\partial x} \left[\frac{\tau_{zz}}{\rho} - \left(\frac{\partial}{\partial x} \int_{-h}^{z} u \, \mathrm{d}z' \right)^2 \right] \mathrm{d}z - d\frac{\partial}{\partial x} \left[\left(\frac{\tau_{zz}}{\rho} - \frac{\tau_{xz}}{\rho} \frac{\partial \zeta}{\partial x} \right) \Big|_{z=\zeta} \right] \\
&- \left(\frac{\tau_{xz}}{\rho} - \frac{\tau_{xx}}{\rho} \frac{\partial \zeta}{\partial x} \right) \Big|_{z=\zeta} + \left(\frac{\tau_{xz}}{\rho} + \frac{\tau_{xx}}{\rho} \frac{\partial h}{\partial x} \right) \Big|_{z=-h} = 0
\end{aligned} \tag{3.7}$$

Here, the total water depth is given as

$$d = h + \zeta, \tag{3.8}$$

while the flow rate is calculated as

$$q = d\bar{u} = \int_{-h}^{\zeta} u \, \mathrm{d}z. \tag{3.9}$$

It should be noted that although the present work uses the DIRANS equations to obtain a one-dimensional model, an alternative derivation performed by Nwogu (1993) is also widely employed elsewhere, using a velocity at a reference depth rather than an average value for the water column.

Equations (3.6) and (3.7) include several terms describing the shear stresses acting within the flow and at fluid boundaries. It is convenient to disregard these variables when their influence is suitably small relative to the remaining terms. The influence of

the wind at the surface in the surf-zone has relatively little impact on the hydrodynamics of the flow and can therefore also be reasonably neglected (Veeramony and Svendsen, 2000). As such, the horizontal shear forces at the surface are ignored, such that

$$\tau_{xx}|_{z=\zeta} = \tau_{xz}|_{z=\zeta} = 0. \tag{3.10}$$

Similarly, with turbulence generated by the breaking process at least an order of magnitude larger than that produced by bed friction, it is reasonable to neglect the effects of the bottom boundary layer (Musumeci et al., 2005). As such, a free slip boundary condition is applied, which assumes horizontal stresses at the bottom to be zero, giving

$$\tau_{xx}|_{z=-h} = \tau_{xz}|_{z=-h} = 0. \tag{3.11}$$

As the pressure is the dominant force acting vertically and horizontally, the remaining normal stresses acing along these axes are also assumed to be negligible, such that

$$\tau_{xx} = \tau_{zz} = 0. \tag{3.12}$$

The remaining stress is considered to be significant and is therefore retained. The definition of this term is acquired from the eddy viscosity model described in Appendix A.3.1, which takes

$$\tau_{xz} = \rho\nu_\mathrm{t}\left(\frac{\partial u}{\partial z} + \frac{\partial w}{\partial x}\right) \tag{3.13}$$

to denote the horizontal shear stress. Here, ν_t defines the eddy viscosity.

With Equations (3.7) and (3.10) to (3.13), the combined momentum equation then reduces to

$$\begin{aligned}
&\frac{\partial q}{\partial t} + \frac{\partial}{\partial x}\int_{-h}^{\zeta} u^2 \,\mathrm{d}z + gd\frac{\partial \zeta}{\partial x} - \int_{-h}^{\zeta}\frac{\partial^2}{\partial x \partial t}\int_{z}^{\zeta}\frac{\partial}{\partial x}\int_{-h}^{z'} u \,\mathrm{d}z''\,\mathrm{d}z'\,\mathrm{d}z \\
&\quad - \int_{-h}^{\zeta}\frac{\partial^2}{\partial x^2}\left[\int_{z}^{\zeta} u\frac{\partial}{\partial x}\int_{-h}^{z'} u \,\mathrm{d}z'' + \nu_\mathrm{t}\left(\frac{\partial u}{\partial z} + \frac{\partial w}{\partial x}\right)\,\mathrm{d}z'\right]\,\mathrm{d}z \\
&\quad - \int_{-h}^{\zeta}\frac{\partial}{\partial x}\left[\left(\frac{\partial}{\partial x}\int_{-h}^{z} u \,\mathrm{d}z'\right)^2\right]\,\mathrm{d}z = 0,
\end{aligned} \tag{3.14}$$

giving the final form of the DIRANS equations utilised here.

3.2.3 The stream function and nondimensionalisation

The formulation used in this chapter also requires the definition of the stream function, ψ, which is given here according to the description in Appendix A.6 where, for two-dimensional incompressible flow, the horizontal and vertical velocities can be expressed as (Graebel, 2007)

$$u = \frac{\partial \psi}{\partial z} \tag{3.15}$$

and

$$w = -\frac{\partial \psi}{\partial x}. \tag{3.16}$$

In order to quantify the nonlinearity,

$$\delta = \frac{A_o}{h_o}, \tag{3.17}$$

and dispersivity,

$$\mu = k_o h_o, \tag{3.18}$$

of the terms in Equations (3.6) and (3.7), the DIRANS equations can be written in nondimensional form, with the dimensionless form of a given variable, f, denoted by $\hat{f}$. Here, A_o, h_o and k_o denote the amplitude length scale, offshore still water depth, and typical wavenumber, respectively.

The nondimensionalisation is performed by first defining a number of variables according to appropriate scaling operations based on typical values of each quantity. The stream function is nondimensionalised according to

$$\hat{\psi} = \frac{\psi}{A_o\sqrt{gh_o}} = \frac{\psi}{\delta\sqrt{gh_o^3}}. \tag{3.19}$$

The horizontal abscissa and vertical ordinate are scaled by a typical wavenumber and characteristic water depth respectively:

$$\hat{x} = k_o x = \mu\frac{x}{h_o} \tag{3.20}$$

$$\hat{z} = \frac{z}{h_o} \tag{3.21}$$

The nondimensional still water depth and free-surface elevation are obtained using the offshore water depth and the amplitude length scale:

$$\hat{h} = \frac{h}{h_o} \tag{3.22}$$

$$\hat{\zeta} = \frac{\zeta}{A_o} = \frac{\zeta}{\delta h_o} \tag{3.23}$$

Finally, the time is scaled according to

$$\hat{t} = k_o\sqrt{gh_o}t = \mu\sqrt{\frac{g}{h_o}}t, \tag{3.24}$$

and the eddy viscosity using

$$\hat{\nu}_t = \frac{\nu_t}{\mu\sqrt{gh_o^3}}. \tag{3.25}$$

Using Equations (3.8), (3.9), (3.15), (3.16) and (3.19) to (3.23), several other nondimensional quantities are also defined:

$$\hat{u} = \frac{\partial\hat{\psi}}{\partial\hat{z}} = \frac{h_o}{\delta\sqrt{gh_o^3}}\frac{\partial\psi}{\partial z} = \frac{u}{\delta\sqrt{gh_o}} \tag{3.26}$$

$$\hat{w} = -\frac{\partial \hat{\psi}}{\partial \hat{x}} = -\frac{h_\mathrm{o}}{\delta\mu\sqrt{gh_\mathrm{o}^3}}\frac{\partial \psi}{\partial x} = \frac{w}{\delta\mu\sqrt{gh_\mathrm{o}}} \tag{3.27}$$

$$\hat{d} = \frac{d}{h_\mathrm{o}} = \hat{h} + \delta\hat{\zeta} \tag{3.28}$$

$$\hat{q} = \int_{-\hat{h}}^{\delta\hat{\zeta}} \hat{u}\ \mathrm{d}\hat{z} = \frac{1}{\delta\sqrt{gh_\mathrm{o}^3}}\int_{-h}^{\zeta} u\ \mathrm{d}z = \frac{q}{\delta\sqrt{gh_\mathrm{o}^3}} \tag{3.29}$$

By neglecting the horizontal stresses at the boundaries according to Equations (3.10) and (3.11) and nondimensionalising variables according to Equations (3.20) to (3.28), Equation (3.14) can be rewritten as follows:

$$\begin{aligned}
&\frac{\partial \hat{q}}{\partial \hat{t}} + \delta\frac{\partial}{\partial \hat{x}}\int_{-\hat{h}}^{\delta\hat{\zeta}} \hat{u}^2\ \mathrm{d}\hat{z} + \hat{d}\frac{\partial \hat{\zeta}}{\partial \hat{x}} - \mu^2\int_{-\hat{h}}^{\delta\hat{\zeta}} \frac{\partial^2}{\partial \hat{x}\partial \hat{t}}\int_{\hat{z}}^{\delta\hat{\zeta}} \frac{\partial}{\partial \hat{x}}\int_{-\hat{h}}^{\hat{z}'} \hat{u}\ \mathrm{d}\hat{z}''\ \mathrm{d}\hat{z}'\ \mathrm{d}\hat{z} \\
&- \mu^2\int_{-\hat{h}}^{\delta\hat{\zeta}} \frac{\partial^2}{\partial \hat{x}^2}\int_{\hat{z}}^{\delta\hat{\zeta}} \hat{\nu}_\mathrm{t}\frac{\partial \hat{u}}{\partial \hat{z}}\ \mathrm{d}\hat{z}'\ \mathrm{d}\hat{z} - \delta\mu^2\int_{-\hat{h}}^{\delta\hat{\zeta}} \frac{\partial^2}{\partial \hat{x}^2}\int_{\hat{z}}^{\delta\hat{\zeta}} \hat{u}\frac{\partial}{\partial \hat{x}}\int_{-\hat{h}}^{\hat{z}'} \hat{u}\ \mathrm{d}\hat{z}''\ \mathrm{d}\hat{z}'\ \mathrm{d}\hat{z} \\
&- \delta\mu^2\int_{-\hat{h}}^{\delta\hat{\zeta}} \frac{\partial}{\partial \hat{x}}\left[\left(\frac{\partial}{\partial \hat{x}}\int_{-\hat{h}}^{\hat{z}} \hat{u}\ \mathrm{d}\hat{z}'\right)^2\right]\ \mathrm{d}\hat{z} - \mu^4\int_{-\hat{h}}^{\delta\hat{\zeta}} \frac{\partial^2}{\partial \hat{x}^2}\int_{\hat{z}}^{\delta\hat{\zeta}} \hat{\nu}_\mathrm{t}\frac{\partial \hat{w}}{\partial \hat{x}}\ \mathrm{d}\hat{z}'\ \mathrm{d}\hat{z} = 0
\end{aligned} \tag{3.30}$$

3.2.4 Rotational components

Equation (3.30) requires the evaluation of complicated functions of the velocity involving integrals and derivatives, which are not well suited to efficient numerical calculations. In order to express Equation (3.30) in a more convenient form, a formulation in terms of vorticity is established. This allows the rotational dynamics of the flow to be retained, which is necessary when modelling the turbulent flow in the surf-zone.

Calculations can be simplified by describing the flow at a reference depth and using additional terms to represent the vortical motion. In order to simplify the resulting expressions, it is acceptable to truncate the equations by neglecting terms $\mathcal{O}(\mu^4)$, which are relatively small in magnitude (Svendsen, 2006). Some of the implications of removing these terms form part of later discussions. To find an expression for the velocity involving the rotationality of the flow, Equations (3.15) and (3.16) are used to consider the vorticity in terms of the stream function:

$$\omega = \frac{\partial u}{\partial z} - \frac{\partial w}{\partial x} = \frac{\partial^2 \psi}{\partial z^2} + \frac{\partial^2 \psi}{\partial x^2} \tag{3.31}$$

The assumption of an impermeable bed requires that

$$\psi|_{z=-h} = 0. \tag{3.32}$$

Additionally, with no vorticity present at the bed,

$$\omega|_{z=-h} = 0. \tag{3.33}$$

Integrating Equation (3.31) twice from the bed to an arbitrary depth gives

$$\int_{-h}^{z}\int_{-h}^{z'}\omega \,\mathrm{d}z''\,\mathrm{d}z' = \psi - \psi|_{z=-h} - \left.\frac{\partial\psi}{\partial z}\right|_{z=-h}(z+h) + \int_{-h}^{z}\int_{-h}^{z'}\frac{\partial^2\psi}{\partial x^2}\,\mathrm{d}z''\,\mathrm{d}z', \quad (3.34)$$

which, with Equations (3.15) and (3.32), provides

$$\psi = \int_{-h}^{z}\int_{-h}^{z'}\omega \,\mathrm{d}z''\,\mathrm{d}z' + u|_{z=-h}(z+h) - \int_{-h}^{z}\int_{-h}^{z'}\frac{\partial^2\psi}{\partial x^2}\,\mathrm{d}z''\,\mathrm{d}z'. \quad (3.35)$$

The nondimensional vorticity can be found from Equations (3.19) to (3.21) and (3.31):

$$\hat{\omega} = \sqrt{\frac{h_\mathrm{o}}{g}}\frac{\omega}{\delta} = \frac{\partial^2\hat{\psi}}{\partial z^2} + \mu^2\frac{\partial^2\hat{\psi}}{\partial x^2} \quad (3.36)$$

With Equations (3.19), (3.21), (3.22), (3.26) and (3.36), the nondimensional form of the stream function stated in Equation (3.35) can be expressed as

$$\hat{\psi} = \int_{-\hat{h}}^{\hat{z}}\int_{-\hat{h}}^{\hat{z}'}\hat{\omega}\,\mathrm{d}\hat{z}''\,\mathrm{d}\hat{z}' + \hat{u}|_{\hat{z}=-\hat{h}}\left(\hat{z}+\hat{h}\right) - \mu^2\int_{-\hat{h}}^{\hat{z}}\int_{-\hat{h}}^{\hat{z}'}\frac{\partial^2\hat{\psi}}{\partial\hat{x}^2}\,\mathrm{d}\hat{z}''\,\mathrm{d}\hat{z}'. \quad (3.37)$$

Equation (3.37) can then be differentiated twice with respect to $\hat{x}$, retaining terms $\mathcal{O}\left(\mu^2\right)$, to give

$$\begin{aligned}\frac{\partial^2\hat{\psi}}{\partial\hat{x}^2} = {} & \frac{\partial^2}{\partial\hat{x}^2}\int_{-\hat{h}}^{\hat{z}}\int_{-\hat{h}}^{\hat{z}'}\hat{\omega}\,\mathrm{d}\hat{z}''\,\mathrm{d}\hat{z}' + 2\frac{\partial\hat{h}}{\partial\hat{x}}\frac{\partial}{\partial\hat{x}}\left(\hat{u}|_{\hat{z}=-\hat{h}}\right) \\ & + \left(\hat{z}+\hat{h}\right)\frac{\partial^2}{\partial\hat{x}^2}\left(\hat{u}|_{\hat{z}=-\hat{h}}\right) + \hat{u}|_{\hat{z}=-\hat{h}}\frac{\partial^2\hat{h}}{\partial\hat{x}^2} + \mathcal{O}\left(\mu^2\right).\end{aligned} \quad (3.38)$$

In order to move the x derivative in Equation (3.38) outside the integral, the Leibniz rule is used:

$$\frac{\mathrm{d}}{\mathrm{d}X}\left[\int_{V(X)}^{W(X)} f(X,Y)\ \mathrm{d}Y\right] = \int_{V}^{W}\frac{\partial f}{\partial X}\,\mathrm{d}Y + f|_{Y=W}\frac{\mathrm{d}W}{\mathrm{d}X} - f|_{Y=V}\frac{\mathrm{d}V}{\mathrm{d}X} \quad (3.39)$$

Appendix C.1 provides a derivation of this relation. With Equation (3.36), a nondimensional form of the boundary condition stated in Equation (3.33) can be applied to Equation (3.38), which with Equation (3.39) gives

$$\begin{aligned}\frac{\partial^2\hat{\psi}}{\partial\hat{x}^2} = {} & \int_{-\hat{h}}^{\hat{z}}\int_{-\hat{h}}^{\hat{z}'}\frac{\partial^2\hat{\omega}}{\partial\hat{x}^2}\,\mathrm{d}\hat{z}''\,\mathrm{d}\hat{z}' + 2\frac{\partial\hat{h}}{\partial\hat{x}}\frac{\partial}{\partial\hat{x}}\left(\hat{u}|_{\hat{z}=-\hat{h}}\right) \\ & + \left(\hat{z}+\hat{h}\right)\frac{\partial^2}{\partial\hat{x}^2}\left(\hat{u}|_{\hat{z}=-\hat{h}}\right) + \hat{u}|_{\hat{z}=-\hat{h}}\frac{\partial^2\hat{h}}{\partial\hat{x}^2} + \mathcal{O}\left(\mu^2\right).\end{aligned} \quad (3.40)$$

By substituting Equation (3.40) into Equation (3.37), the following relation is then

obtained:

$$\begin{aligned}\hat{\psi} &= \int_{-\hat{h}}^{\hat{z}}\int_{-\hat{h}}^{\hat{z}'}\hat{\omega}\,\mathrm{d}\hat{z}''\,\mathrm{d}\hat{z}' + \hat{u}|_{\hat{z}=-\hat{h}}\left(\hat{z}+\hat{h}\right) - \mu^2\int_{-\hat{h}}^{\hat{z}}\int_{-\hat{h}}^{\hat{z}'}\left[\int_{-\hat{h}}^{\hat{z}''}\int_{-\hat{h}}^{\hat{z}'''}\frac{\partial^2\hat{\omega}}{\partial\hat{x}^2}\,\mathrm{d}\hat{z}''''\,\mathrm{d}\hat{z}'''\right.\\ &\quad\left. + 2\frac{\partial\hat{h}}{\partial\hat{x}}\frac{\partial}{\partial\hat{x}}\left(\hat{u}|_{\hat{z}=-\hat{h}}\right) + \left(\hat{z}''+\hat{h}\right)\frac{\partial^2}{\partial\hat{x}^2}\left(\hat{u}|_{\hat{z}=-\hat{h}}\right) + \hat{u}|_{\hat{z}=-\hat{h}}\frac{\partial^2\hat{h}}{\partial\hat{x}^2}\right]\,\mathrm{d}\hat{z}''\,\mathrm{d}\hat{z}' + \mathcal{O}\left(\mu^4\right)\\ &= \int_{-\hat{h}}^{\hat{z}}\int_{-\hat{h}}^{\hat{z}'}\hat{\omega}\,\mathrm{d}\hat{z}''\,\mathrm{d}\hat{z}' + \hat{u}|_{\hat{z}=-\hat{h}}\left(\hat{z}+\hat{h}\right) - \mu^2\int_{-\hat{h}}^{\hat{z}}\int_{-\hat{h}}^{\hat{z}'}\int_{-\hat{h}}^{\hat{z}''}\int_{-\hat{h}}^{\hat{z}'''}\frac{\partial^2\hat{\omega}}{\partial\hat{x}^2}\,\mathrm{d}\hat{z}''''\,\mathrm{d}\hat{z}'''\,\mathrm{d}\hat{z}''\,\mathrm{d}\hat{z}'\\ &\quad - \frac{\mu^2}{2}\left(\hat{z}+\hat{h}\right)^2\left[2\frac{\partial\hat{h}}{\partial\hat{x}}\frac{\partial}{\partial\hat{x}}\left(\hat{u}|_{\hat{z}=-\hat{h}}\right) + \hat{u}|_{\hat{z}=-\hat{h}}\frac{\partial^2\hat{h}}{\partial\hat{x}^2}\right]\\ &\quad - \frac{\mu^2}{6}\left(\hat{z}+\hat{h}\right)^3\frac{\partial^2}{\partial\hat{x}^2}\left(\hat{u}|_{\hat{z}=-\hat{h}}\right) + \mathcal{O}\left(\mu^4\right)\end{aligned} \tag{3.41}$$

Equation (3.41) can then be substituted into Equation (3.26) to give the nondimensional horizontal velocity as

$$\hat{u} = \hat{u}_\mathrm{p} + \hat{u}_\mathrm{r}, \tag{3.42}$$

where

$$\begin{aligned}\hat{u}_\mathrm{p} &= \hat{u}|_{\hat{z}=-\hat{h}} - \mu^2\left(\hat{z}+\hat{h}\right)\left[2\frac{\partial\hat{h}}{\partial\hat{x}}\frac{\partial}{\partial\hat{x}}\left(\hat{u}|_{\hat{z}=-\hat{h}}\right) + \hat{u}|_{\hat{z}=-\hat{h}}\frac{\partial^2\hat{h}}{\partial\hat{x}^2} + \frac{\hat{z}+\hat{h}}{2}\frac{\partial^2}{\partial\hat{x}^2}\left(\hat{u}|_{\hat{z}=-\hat{h}}\right)\right]\\ &\quad + \mathcal{O}\left(\mu^4\right)\end{aligned} \tag{3.43}$$

denotes the nondimensional potential velocity, and

$$\hat{u}_\mathrm{r} = \int_{-\hat{h}}^{\hat{z}}\hat{\omega}\,\mathrm{d}\hat{z}' - \mu^2\int_{-\hat{h}}^{\hat{z}}\int_{-\hat{h}}^{\hat{z}'}\int_{-\hat{h}}^{\hat{z}''}\frac{\partial^2\hat{\omega}}{\partial\hat{x}^2}\,\mathrm{d}\hat{z}'''\,\mathrm{d}\hat{z}''\,\mathrm{d}\hat{z}' + \mathcal{O}\left(\mu^4\right) \tag{3.44}$$

denotes the nondimensional rotational velocity. Here, the contribution of the vorticity to the velocity is represented in $\hat{u}_\mathrm{r}$, while the contribution from $\hat{u}_\mathrm{p}$ relies on the velocity at a reference depth.

By expressing Equation (3.30) in terms of the potential and rotational velocities, it is possible to obtain a more simple form of the equation that is better suited to a depth averaged model. The weakly-nonlinear BTEs (WNBs) are acquired when terms $\mathcal{O}\left(\delta\mu^2,\mu^4\right)$ are neglected. The gradient of the bed is assumed to be small, such that terms $\mathcal{O}\left[\mu^2\left(\frac{\partial\hat{h}}{\partial\hat{x}}\right)^2,\mu^2\frac{\partial^2\hat{h}}{\partial\hat{x}^2}\right]$ can also be removed, along with rotational terms $\mathcal{O}\left(\mu^2\frac{\partial\hat{h}}{\partial\hat{x}}\right)$. This assumption is authenticated in Section 6.4, where the dispersivity is compared to the bathymetric gradient for each test case performed in the present study. Following the procedure detailed in Appendix A.5, this allows Equation (3.30) to be written as

$$\begin{aligned}&\frac{\partial\hat{q}}{\partial\hat{t}} + \frac{1}{\delta}\left[\frac{\partial}{\partial\hat{x}}\left(\frac{\hat{d}^2}{2}\right) - \hat{d}\frac{\partial\hat{h}}{\partial\hat{x}}\right] + \delta\left[\frac{\partial}{\partial\hat{x}}\left(\frac{\hat{q}^2}{\hat{d}}\right) + \frac{\partial}{\partial\hat{x}}\left(\widehat{\Delta M}\right)\right]\\ &\quad - \mu^2\left[\frac{\hat{h}}{3}\frac{\partial}{\partial\hat{t}}\left(\hat{h}\frac{\partial^2\hat{q}}{\partial\hat{x}^2} + \frac{\partial\hat{h}}{\partial\hat{x}}\frac{\partial\hat{q}}{\partial\hat{x}}\right) - \frac{\partial^3}{\partial\hat{x}^2\partial\hat{t}}\left(\widehat{\Delta P}\right) + \widehat{D}_\mathrm{s}\right] = \mathcal{O}\left(\delta\mu^2,\mu^2\frac{\partial\hat{h}}{\partial\hat{x}},\mu^4\right).\end{aligned} \tag{3.45}$$

Here,

$$\widehat{\Delta M} = \int_{-\hat{h}}^{\delta\hat{\zeta}} \hat{u}_{\mathrm{r}}^2 - \hat{\bar{u}}_{\mathrm{r}}^2 \, \mathrm{d}\hat{z}, \tag{3.46}$$

$$\widehat{\Delta P} = -\int_{-\hat{h}}^{\delta\hat{\zeta}} \int_{\hat{z}}^{\delta\hat{\zeta}} \int_{-\hat{h}}^{\hat{z}'} \hat{u}_{\mathrm{r}} - \hat{\bar{u}}_{\mathrm{r}} \, \mathrm{d}\hat{z}'' \, \mathrm{d}\hat{z}' \, \mathrm{d}\hat{z} \tag{3.47}$$

and

$$\widehat{D_{\mathrm{s}}} = \int_{-\hat{h}}^{\delta\hat{\zeta}} \frac{\partial^2}{\partial \hat{x}^2} \int_{\hat{z}}^{\delta\hat{\zeta}} \hat{\nu}_{\mathrm{t}} \frac{\partial \hat{u}}{\partial \hat{z}} \, \mathrm{d}\hat{z}' \, \mathrm{d}\hat{z} \tag{3.48}$$

are the nondimensional breaking terms which represent the rotation within the flow. The numerical solution of Equation (3.45) is more straightforward than that of Equation (3.30), and the isolation of rotational terms allows the more complex numerical integrations to be performed independently.

3.2.5 Dispersive enhancement

For the WNBs, the Boussinesq approximation assumes weak nonlinearity and dispersivity, such that $\delta < 1$ and $\mu^2 < 1$, and balanced nonlinear and dispersive effects, such that $\delta = \mathcal{O}(\mu^2)$. These restrictions can be reduced by retaining higher-order terms, giving the FNBs, although this results in a system of equations with greater complexity, as illustrated in the derivation provided in Appendix A.5. While the simplifications for the WNBs introduce some limitations, they are assumed to be outweighed by the inconveniences of the more elaborate and extensive FNBs. It is worth noting that the procedure for deriving the equations presented here would remain unchanged if higher-order terms were to be retained.

A range of methods have been proposed to enhance the dispersive characteristics of BTEs and thereby allow their application to be extended to greater depths. Madsen et al. (1991) derived the dispersion relation for a range of forms of BTEs and allowed the phase celerity,

$$c = \frac{\lambda}{T}, \tag{3.49}$$

to be determined from

$$\frac{c^2}{gh} = \frac{1 + B\mu^2}{1 + \left(B + \frac{1}{3}\right)\mu^2}. \tag{3.50}$$

Here,

$$T = \frac{1}{f_{\mathrm{w}}} \tag{3.51}$$

is the wave period, λ is the wavelength, f_{w} denotes the wave frequency, and B is the dispersive parameter, which allows various forms of the BTEs to be recovered. Commonly assumed values include $B = \frac{1}{6}$, $B = -\frac{1}{3}$ (Mei, 1989) and $B = \frac{1}{15}$ (Madsen et al., 1997), while $B = 0$ recovers the standard BTEs. In the present study, the approach taken by Veeramony and Svendsen (2000) is adopted, whereby the dispersive characteristics are

improved in deeper water by applying the following linear operator (Madsen and Schäffer, 1998):

$$O = 1 + B\mu^2\hat{h}^2\frac{\partial^2}{\partial\hat{x}^2} \tag{3.52}$$

Using a value of $B = \frac{1}{15}$ has been found to closely replicate linear dispersion and is therefore used here.

It should first be noted from Equation (3.28) that

$$\begin{aligned}\frac{1}{\delta}\frac{\partial^2}{\partial\hat{x}^2}\left[\frac{\partial}{\partial\hat{x}}\left(\frac{\hat{d}^2}{2}\right) - \hat{d}\frac{\partial\hat{h}}{\partial\hat{x}}\right] &= \frac{1}{\delta}\frac{\partial^2}{\partial\hat{x}^2}\left[\hat{d}\frac{\partial}{\partial\hat{x}}\left(\hat{d}-\hat{h}\right)\right] = \frac{\partial^2}{\partial\hat{x}^2}\left[\left(\delta\hat{\zeta}+\hat{h}\right)\frac{\partial\hat{\zeta}}{\partial\hat{x}}\right] \\ &= \left(\delta\frac{\partial^2\hat{\zeta}}{\partial\hat{x}^2} + \frac{\partial^2\hat{h}}{\partial\hat{x}^2}\right)\frac{\partial\hat{\zeta}}{\partial\hat{x}} + 2\left(\delta\frac{\partial\hat{\zeta}}{\partial\hat{x}} + \frac{\partial\hat{h}}{\partial\hat{x}}\right)\frac{\partial^2\hat{\zeta}}{\partial\hat{x}^2} + \left(\delta\hat{\zeta}+\hat{h}\right)\frac{\partial^3\hat{\zeta}}{\partial\hat{x}^3} \\ &= \left(2\frac{\partial\hat{h}}{\partial\hat{x}}\frac{\partial^2\hat{\zeta}}{\partial\hat{x}^2} + \hat{h}\frac{\partial^3\hat{\zeta}}{\partial\hat{x}^3}\right) + \mathcal{O}\left(\delta, \frac{\partial^2\hat{h}}{\partial\hat{x}^2}\right)\end{aligned} \tag{3.53}$$

Multiplying Equation (3.45) by Equation (3.52) and substituting Equations (3.28) and (3.53) provides

$$\begin{aligned}&\frac{\partial\hat{q}}{\partial\hat{t}} + \frac{1}{\delta}\left[\frac{\partial}{\partial\hat{x}}\left(\frac{\hat{d}^2}{2}\right) - \hat{d}\frac{\partial\hat{h}}{\partial\hat{x}}\right] + \delta\left[\frac{\partial}{\partial\hat{x}}\left(\frac{\hat{q}^2}{\hat{d}}\right) + \frac{\partial}{\partial\hat{x}}\left(\widehat{\Delta M}\right)\right] \\ &\quad - \mu^2\left[\frac{\hat{h}}{3}\frac{\partial}{\partial\hat{t}}\left(\hat{h}\frac{\partial^2\hat{q}}{\partial\hat{x}^2} + \frac{\partial\hat{h}}{\partial\hat{x}}\frac{\partial\hat{q}}{\partial\hat{x}}\right) - \frac{\partial^3}{\partial\hat{x}^2\partial\hat{t}}\left(\widehat{\Delta P}\right) + \widehat{D_\mathrm{s}}\right. \\ &\quad \left. - B\hat{h}^2\left(\frac{\partial^3\hat{q}}{\partial\hat{x}^2\partial\hat{t}} + 2\frac{\partial\hat{h}}{\partial\hat{x}}\frac{\partial^2\hat{\zeta}}{\partial\hat{x}^2} + \hat{h}\frac{\partial^3\hat{\zeta}}{\partial\hat{x}^3}\right)\right] = \mathcal{O}\left(\delta\mu^2, \mu^2\frac{\partial\hat{h}}{\partial\hat{x}}, \mu^4\right).\end{aligned} \tag{3.54}$$

3.2.6 Dimensional form

With Equations (3.20), (3.22) to (3.24), (3.28) and (3.29), the dimensional form of Equation (3.54) is then given as

$$\begin{aligned}&\frac{\partial q}{\partial t} + g\left[\frac{\partial}{\partial x}\left(\frac{d^2}{2}\right) - d\frac{\partial h}{\partial x}\right] + \frac{\partial}{\partial x}\left(\frac{q^2}{d}\right) - \frac{h}{3}\frac{\partial}{\partial t}\left(h\frac{\partial^2 q}{\partial x^2} + \frac{\partial h}{\partial x}\frac{\partial q}{\partial x}\right) \\ &\quad + Bh^2\left(\frac{\partial^3 q}{\partial x^2\partial t} + 2g\frac{\partial h}{\partial x}\frac{\partial^2\zeta}{\partial x^2} + gh\frac{\partial^3\zeta}{\partial x^3}\right) + \chi = 0,\end{aligned} \tag{3.55}$$

where terms $\mathcal{O}\left(\delta^2\mu^3, \delta\mu^3\frac{\partial\hat{h}}{\partial\hat{x}}, \delta\mu^5\right)$ have been neglected and

$$\chi = \frac{\partial\left(\Delta M\right)}{\partial x} + \frac{\partial^3\left(\Delta P\right)}{\partial x^2\partial t} - D_\mathrm{s} \tag{3.56}$$

represents the breaking terms. From Equations (3.3), (3.20) to (3.23), (3.25), (3.26), (3.42) and (3.46) to (3.48), the dimensional forms of the breaking terms are given as

$$\Delta M = \delta^2 g h_0^2\widehat{\Delta M} = \int_{-h}^{\zeta} u_\mathrm{r}^2 - \bar{u}_\mathrm{r}^2\,\mathrm{d}z, \tag{3.57}$$

$$\Delta P = \delta g h_{\mathrm{o}}^3 \sqrt{\frac{h_{\mathrm{o}}}{g}} \widehat{\Delta P} = -\int_{-h}^{\zeta} \int_{z}^{\zeta} \int_{-h}^{z'} u_{\mathrm{r}} - \bar{u}_{\mathrm{r}} \, \mathrm{d}z'' \, \mathrm{d}z' \, \mathrm{d}z \tag{3.58}$$

and

$$D_{\mathrm{s}} = \delta \mu^3 g h_{\mathrm{o}} \widehat{D_{\mathrm{s}}} = \int_{-h}^{\zeta} \frac{\partial^2}{\partial x^2} \int_{z}^{\zeta} \nu_{\mathrm{t}} \frac{\partial u}{\partial z} \, \mathrm{d}z' \, \mathrm{d}z. \tag{3.59}$$

Here, the rotational component of the velocity is given by u_{r}.

3.2.7 Conservative form

In order to express the conservation and momentum equations in a form suited to the finite-volume (FV) method, Equations (3.6) and (3.55) are rearranged and written as

$$\frac{\partial \boldsymbol{W}}{\partial t} + \frac{\partial \boldsymbol{F}}{\partial x} = \boldsymbol{S}, \tag{3.60}$$

where

$$\boldsymbol{W} = \begin{bmatrix} d \\ q - \dfrac{h}{3} \dfrac{\partial h}{\partial x} \dfrac{\partial q}{\partial x} + \left(B - \dfrac{1}{3} \right) h^2 \dfrac{\partial^2 q}{\partial x^2} \end{bmatrix}, \tag{3.61}$$

$$\boldsymbol{F} = \begin{bmatrix} q \\ \dfrac{q^2}{d} + \dfrac{g d^2}{2} \end{bmatrix} \tag{3.62}$$

and

$$\boldsymbol{S} = \begin{bmatrix} 0 \\ g d \dfrac{\partial h}{\partial x} - B g h^2 \left(2 \dfrac{\partial h}{\partial x} \dfrac{\partial^2 \zeta}{\partial x^2} + h \dfrac{\partial^3 \zeta}{\partial x^3} \right) - \chi \end{bmatrix}. \tag{3.63}$$

By using an FV scheme to solve these equations, a stable model with good shock-capturing capabilities can be created. Such qualities are well suited to modelling wave propagation through the surf-zone.

3.3 Nonlinear shallow water equations

It is worth noting that the NSWEs are reached by neglecting the higher-order dispersive terms and dissipative breaking terms from the BTEs. As such, Equations (3.60) to (3.63) reduce to

$$\frac{\partial}{\partial t} \begin{bmatrix} d \\ q \end{bmatrix} + \frac{\partial}{\partial x} \begin{bmatrix} q \\ \dfrac{q^2}{d} + \dfrac{g d^2}{2} \end{bmatrix} = \begin{bmatrix} 0 \\ g d \dfrac{\partial h}{\partial x} \end{bmatrix}. \tag{3.64}$$

By using the NSWEs an assumption of hydrostatic pressure is introduced, as the non-hydrostatic components contained within the BTEs are no longer represented. It should

therefore be emphasised that practical use of Equation (3.64) is restricted to regions where $\delta = \mathcal{O}(1)$ and the long wave approximation holds true, such that $\mu \ll 1$ (Svendsen, 2006).

Chapter 4

Vorticity transport equation

4.1 Flow rotation

In response to the negation of rotational components of the flow encountered when deriving the BTEs from the RANS equations, the RBM endeavours to calculate the vorticity within the flow and represent this aspect of the hydrodynamics by determining additional terms to be introduced into the governing equations. Further offshore, where a larger water depth is found, the assumption of irrotationality embedded in the previously derived BTEs is reasonable and provides an adequate description of the hydrodynamics. When modelling breaking waves, the resulting levels of rotation within the flow mean that this approximation is no longer suitable, and requires further considerations to be made (Svendsen, 2006).

4.2 Formulation of equation

The shortcomings resulting from the irrotational assumptions discussed previously are addressed with the introduction of ω to describe the vortical motion of the fluid. This term brings an additional equation which must be solved concurrently. This relation describes the spatial and temporal evolution of the vorticity, and is derived from the RANS equations obtained in Chapter 3. Differentiating Equation (3.2) with respect to x and subtracting from Equation (3.1) differentiated with respect to z gives

$$\frac{\partial}{\partial t}\left(\frac{\partial w}{\partial x}-\frac{\partial u}{\partial z}\right)+w\frac{\partial}{\partial x}\left(\frac{\partial u}{\partial x}+\frac{\partial w}{\partial z}\right)+2\left(\frac{\partial u}{\partial x}+\frac{\partial w}{\partial z}\right)\left(\frac{\partial w}{\partial x}-\frac{\partial u}{\partial z}\right)+u\frac{\partial}{\partial x}\left(\frac{\partial w}{\partial x}-\frac{\partial u}{\partial z}\right)$$
$$+w\frac{\partial}{\partial z}\left(\frac{\partial w}{\partial x}-\frac{\partial u}{\partial z}\right)-u\frac{\partial}{\partial z}\left(\frac{\partial u}{\partial x}+\frac{\partial w}{\partial z}\right)=\frac{1}{\rho}\left(\frac{\partial^2\tau_{xz}}{\partial x^2}+\frac{\partial^2\tau_{zz}}{\partial x\partial z}-\frac{\partial^2\tau_{xx}}{\partial x\partial z}-\frac{\partial^2\tau_{xz}}{\partial z^2}\right). \tag{4.1}$$

The horizontal and vertical normal stresses are described by the eddy viscosity model outlined in Appendix A.3.1, which gives

$$\tau_{xx} = 2\rho\nu_{\mathrm{t}}\frac{\partial u}{\partial x} \tag{4.2}$$

and

$$\tau_{zz} = 2\rho\nu_{\mathrm{t}}\frac{\partial w}{\partial z}. \tag{4.3}$$

By substituting Equations (3.6), (3.13), (3.31), (4.2) and (4.3) into Equation (4.1), the required form of the VTE is obtained:

$$\frac{\partial\omega}{\partial t} + u\frac{\partial\omega}{\partial x} + w\frac{\partial\omega}{\partial z} = \nu_{\mathrm{t}}\left(\frac{\partial^3 w}{\partial x^3} + \frac{\partial^3 w}{\partial x\partial z^2} - \frac{\partial^3 u}{\partial x^2\partial z} - \frac{\partial^3 u}{\partial z^3}\right) = \nu_{\mathrm{t}}\left(\frac{\partial^2\omega}{\partial x^2} + \frac{\partial^2\omega}{\partial z^2}\right) \tag{4.4}$$

4.3 Closure mechanism

As Madsen and Svendsen (1983) remarked, the closure mechanism should attempt to replicate any significant characteristics exhibited in turbulent regions. In particular, the downstream convection and moderate dissipation of vorticity in the wake of the roller region should be captured. When building an image of the vorticity with a depth averaged model, the turbulence must be equated to the mean flow by considering the vertical variation of the horizontal velocity (Svendsen and Madsen, 1984).

In the present work, the problem is closed using the semi-analytical solution presented by Veeramony and Svendsen (2000). The boundary conditions state that there is no vorticity at the bed or the free surface and assume an initially irrotational state, such that

$$\omega|_{z=\zeta} = 0, \tag{4.5}$$

$$\omega|_{z=-h} = 0 \tag{4.6}$$

and

$$\omega|_{t=0} = 0. \tag{4.7}$$

The vorticity is introduced along the lower edge of the roller, located at ζ_{e}, by defining an injected quantity, ω_{s}, along this boundary:

$$\omega|_{z=\zeta_{\mathrm{e}}} = \omega_{\mathrm{s}} \tag{4.8}$$

With Equations (3.20), (3.21), (3.24) to (3.27) and (3.36), the dimensionless form of Equation (4.4) is found to be

$$\frac{\partial\hat{\omega}}{\partial\hat{t}} + \delta\hat{u}\frac{\partial\hat{\omega}}{\partial\hat{x}} + \delta\hat{w}\frac{\partial\hat{\omega}}{\partial\hat{z}} = \hat{\nu}_{\mathrm{t}}\left(\mu^2\frac{\partial^2\hat{\omega}}{\partial\hat{x}^2} + \frac{\partial^2\hat{\omega}}{\partial\hat{z}^2}\right). \tag{4.9}$$

In order to solve the VTE using a semi-analytical method, the z-coordinates are transformed onto a new coordinate system defined by

$$\sigma = \frac{h+z}{h+\zeta_{\mathrm{e}}} = \frac{\hat{h}+\hat{z}}{\hat{h}+\delta\hat{\zeta}_{\mathrm{e}}}. \tag{4.10}$$

As such, σ is zero at the bed and one at the lower edge of the roller. Since the rotational components of Equation (3.54) are $\mathcal{O}\left(\delta, \mu^2\right)$, terms of the VTE are only needed to $\mathcal{O}\left(\mu^2\right)$ for the overall solution to remain accurate to $\mathcal{O}\left(\delta\mu^2, \mu^4\right)$. With Equation (4.10), Equation (4.9) can be written in terms of the σ coordinate system as follows:

$$\begin{aligned}
&\frac{\partial \hat{\omega}}{\partial \hat{t}} + \frac{\partial \sigma}{\partial \hat{t}}\frac{\partial \hat{\omega}}{\partial \sigma} + \delta\hat{u}\left(\frac{\partial \hat{\omega}}{\partial \hat{x}} + \frac{\partial \sigma}{\partial \hat{x}}\frac{\partial \hat{\omega}}{\partial \sigma}\right) + \delta\hat{w}\frac{\partial \sigma}{\partial \hat{z}}\frac{\partial \hat{\omega}}{\partial \sigma} \\
&= \frac{\partial \hat{\omega}}{\partial \hat{t}} - \frac{\delta\sigma}{\hat{h}+\delta\hat{\zeta}_\mathrm{e}}\frac{\partial \hat{\zeta}_\mathrm{e}}{\partial \hat{t}}\frac{\partial \hat{\omega}}{\partial \sigma} + \delta\hat{u}\left[\frac{\partial \hat{\omega}}{\partial \hat{x}} - \frac{\sigma}{\hat{h}+\delta\hat{\zeta}_\mathrm{e}}\frac{\partial}{\partial \hat{x}}\left(\hat{h}+\delta\hat{\zeta}_\mathrm{e}\right)\frac{\partial \hat{\omega}}{\partial \sigma}\right] + \frac{\delta\hat{w}}{\hat{h}+\delta\hat{\zeta}_\mathrm{e}}\frac{\partial \hat{\omega}}{\partial \sigma} \\
&= \hat{\nu}_\mathrm{t}\left(\frac{\partial \sigma}{\partial \hat{z}}\right)^2\frac{\partial^2 \hat{\omega}}{\partial \sigma^2} + \mathcal{O}\left(\mu^2\right) = \frac{\hat{\nu}_\mathrm{t}}{\left(\hat{h}+\delta\hat{\zeta}_\mathrm{e}\right)^2}\frac{\partial^2 \hat{\omega}}{\partial \sigma^2} + \mathcal{O}\left(\mu^2\right)
\end{aligned} \tag{4.11}$$

The vorticity and velocity inside the roller during breaking have not yet been adequately quantified experimentally, but Equations (4.5) and (4.8) provide boundary conditions along the upper and lower edges of this region. The approach adopted here assumes a linear vorticity distribution, as in Musumeci et al. (2005). It is important to note that the vorticity calculated inside the roller region does not influence the RBM. In order to further simplify the boundary conditions, the function describing the vorticity outside the roller is homogenised (Veeramony and Svendsen, 2000). This provides the following expression for the vorticity within the flow:

$$\hat{\omega} = \begin{cases} \hat{\Omega} + \sigma\hat{\omega}_\mathrm{s} & \hat{z} \leq \hat{\zeta}_\mathrm{e} \\ \dfrac{\hat{\zeta}-\hat{z}}{\hat{\zeta}-\hat{\zeta}_\mathrm{e}}\hat{\omega}_\mathrm{s} & \hat{\zeta}_\mathrm{e} < \hat{z} \leq \hat{\zeta} \end{cases} \tag{4.12}$$

For the gentle bathymetry assumed in the present derivation,

$$\frac{\partial \hat{h}}{\partial \hat{x}} = \mathcal{O}\left(\mu^2\right). \tag{4.13}$$

To ensure this statement is valid, the gradient of the bed is later verified for the tests performed in the present study. Accordingly, bed slope terms are then also separated. With Equations (4.10) and (4.12), Equation (4.11) is then written as

$$\begin{aligned}
&\frac{\partial \hat{\Omega}}{\partial \hat{t}} + \sigma\frac{\partial \hat{\omega}_\mathrm{s}}{\partial \hat{t}} - \frac{\delta\sigma\hat{\omega}_\mathrm{s}}{\hat{h}+\delta\hat{\zeta}_\mathrm{e}}\frac{\partial \hat{\zeta}_\mathrm{e}}{\partial \hat{t}} + \frac{\delta}{\hat{h}+\delta\hat{\zeta}_\mathrm{e}}\left(\hat{w} - \delta\sigma\hat{u}\frac{\partial \hat{\zeta}_\mathrm{e}}{\partial \hat{x}} - \sigma\frac{\partial \hat{\zeta}_\mathrm{e}}{\partial \hat{t}}\right)\left(\frac{\partial \hat{\Omega}}{\partial \sigma} + \hat{\omega}_\mathrm{s}\right) \\
&+ \delta\hat{u}\frac{\partial \hat{\Omega}}{\partial \hat{x}} + \delta\hat{u}\sigma\frac{\partial \hat{\omega}_\mathrm{s}}{\partial \hat{x}} = \frac{\hat{\nu}_\mathrm{t}}{\left(\hat{h}+\delta\hat{\zeta}_\mathrm{e}\right)^2}\frac{\partial^2 \hat{\Omega}}{\partial \sigma^2} + \mathcal{O}\left(\mu^2, \delta\frac{\partial \hat{h}}{\partial \hat{x}}\right).
\end{aligned} \tag{4.14}$$

With Equations (4.10) and (4.12), the boundary conditions given by Equations (4.6) to (4.8) can be written as

$$\hat{\Omega}\Big|_{\sigma=1} = 0, \tag{4.15}$$

$$\hat{\Omega}\Big|_{\sigma=0} = 0 \tag{4.16}$$

and

$$\hat{\Omega}\Big|_{t=0} = 0. \tag{4.17}$$

4.4 Perturbation analysis

Next, it is assumed that $\hat{\Omega}$ can be expanded using a perturbation approach as follows (Mei, 1997):

$$\hat{\Omega} = \hat{\omega}^{(1)} + \delta\hat{\omega}^{(2)} + \mathcal{O}\left(\delta^2\right) \tag{4.18}$$

The first part of the final term in Equation (4.14) can be rewritten using a Taylor series expansion about zero (see Appendix C.3):

$$\frac{\hat{\nu}_\mathrm{t}}{\left(\hat{h}+\delta\hat{\zeta}_\mathrm{e}\right)^2} = \frac{\hat{\nu}_\mathrm{t}}{\hat{h}^2}\sum_{n=0}^{\infty}(n+1)\left(-\delta\frac{\hat{\zeta}_\mathrm{e}}{\hat{h}}\right)^n = \frac{\hat{\nu}_\mathrm{t}}{\hat{h}^2}\left(1-2\delta\frac{\hat{\zeta}_\mathrm{e}}{\hat{h}}+6\delta^2\frac{\hat{\zeta}_\mathrm{e}^2}{\hat{h}^2}\right)+\mathcal{O}\left(\delta^3\right) \tag{4.19}$$

By substituting Equations (4.18) and (4.19) into Equation (4.14), a new form of the VTE is reached:

$$\begin{aligned}
&\frac{\partial\hat{\omega}^{(1)}}{\partial\hat{t}}+\delta\frac{\partial\hat{\omega}^{(2)}}{\partial\hat{t}}+\delta^2\frac{\partial\hat{\omega}^{(3)}}{\partial\hat{t}}+\sigma\frac{\partial\hat{\omega}_\mathrm{s}}{\partial\hat{t}}-\frac{\delta\sigma\hat{\omega}_\mathrm{s}}{\hat{h}+\delta\hat{\zeta}_\mathrm{e}}\frac{\partial\hat{\zeta}_\mathrm{e}}{\partial\hat{t}}\\
&+\frac{\delta}{\hat{h}+\delta\hat{\zeta}_\mathrm{e}}\left(\hat{w}-\delta\sigma\hat{u}\frac{\partial\hat{\zeta}_\mathrm{e}}{\partial\hat{x}}-\sigma\frac{\partial\hat{\zeta}_\mathrm{e}}{\partial\hat{t}}\right)\left(\frac{\partial\hat{\omega}^{(1)}}{\partial\sigma}+\delta\frac{\partial\hat{\omega}^{(2)}}{\partial\sigma}+\hat{\omega}_\mathrm{s}\right)+\delta\hat{u}\frac{\partial\hat{\omega}^{(1)}}{\partial\hat{x}}+\delta^2\hat{u}\frac{\partial\hat{\omega}^{(2)}}{\partial\hat{x}}\\
&+\delta\hat{u}\sigma\frac{\partial\hat{\omega}_\mathrm{s}}{\partial\hat{x}}=\frac{\hat{\nu}_\mathrm{t}}{\hat{h}^2}\left(1-2\delta\frac{\hat{\zeta}_\mathrm{e}}{\hat{h}}+6\delta^2\frac{\hat{\zeta}_\mathrm{e}^2}{\hat{h}^2}\right)\frac{\partial^2}{\partial\sigma^2}\left(\hat{\omega}^{(1)}+\delta\hat{\omega}^{(2)}\right)+\mathcal{O}\left(\mu^2,\delta^2,\delta\frac{\partial\hat{h}}{\partial\hat{x}}\right)
\end{aligned} \tag{4.20}$$

Here, the solution is obtained from an infinite series of linear problems with diminishing orders of magnitude.

4.4.1 First-order solution

The first system is constructed from the terms $\mathcal{O}(1)$ in Equation (4.20), which with Equations (3.20), (3.22) to (3.25), (3.36), (4.12) and (4.18), can be written in dimensional form as

$$\frac{\partial\omega^{(1)}}{\partial t}+\sigma\frac{\partial\omega_\mathrm{s}}{\partial t}=\frac{\nu_\mathrm{t}}{h^2}\frac{\partial^2\omega^{(1)}}{\partial\sigma^2}. \tag{4.21}$$

Using the method described in Appendix C.4, the terms in Equation (4.21) can be expanded using a trigonometric Fourier series of the form

$$-\sigma\frac{\partial\omega_\mathrm{s}}{\partial t}=\sum_{n=1}^{\infty}F_n^{(1)}\sin\left(n\pi\sigma\right), \tag{4.22}$$

where

$$F_n^{(1)} = -2\frac{\partial\omega_\mathrm{s}}{\partial t}\int_0^1\sigma\sin\left(n\pi\sigma\right)\,\mathrm{d}\sigma = 2\frac{(-1)^n}{n\pi}\frac{\partial\omega_\mathrm{s}}{\partial t}\quad n\in\mathbb{N}_1. \tag{4.23}$$

Assuming the solution takes the form

$$\omega^{(1)} = \sum_{n=1}^{\infty} G_n^{(1)} \sin(n\pi\sigma), \tag{4.24}$$

where G_n is independent of σ, Equation (4.21) then becomes

$$\sum_{n=1}^{\infty} \frac{\partial G_n^{(1)}}{\partial t} \sin(n\pi\sigma) - \sum_{n=1}^{\infty} F_n^{(1)} \sin(n\pi\sigma) = -\frac{\nu_t}{h^2} \sum_{n=1}^{\infty} n^2\pi^2 G_n^{(1)} \sin(n\pi\sigma), \tag{4.25}$$

which can be rearranged to give

$$\sum_{n=1}^{\infty} \left(\frac{\partial G_n^{(1)}}{\partial t} + \frac{\nu_t}{h^2} n^2\pi^2 G_n^{(1)} - F_n^{(1)} \right) \sin(n\pi\sigma) = 0. \tag{4.26}$$

For this to hold for all values of σ, the following statement must also be true:

$$\frac{\partial G_n^{(1)}}{\partial t} + \frac{\nu_t}{h^2} n^2\pi^2 G_n^{(1)} - F_n^{(1)} = 0 \quad n \in \mathbb{N}_1 \tag{4.27}$$

As a first-order nonhomogeneous linear equation, Equation (4.27) can be solved using the variation of parameters method (Powers, 2006). The following expression is then obtained:

$$G_n^{(1)} = \exp\left(-\frac{\nu_t}{h^2} n^2\pi^2 t\right) \left[\int_0^t \exp\left(\frac{\nu_t}{h^2} n^2\pi^2 t'\right) F_n^{(1)} \, \mathrm{d}t' - G_n^{(1)}\Big|_{t=0} \right] \quad n \in \mathbb{N}_1. \tag{4.28}$$

Equations (4.7) and (4.24) provide the relation

$$\sum_{n=1}^{\infty} G_n^{(1)}\Big|_{t=0} \sin(n\pi\sigma) = 0, \tag{4.29}$$

which, in order to be satisfied for all values of σ, requires the initial condition

$$G_n^{(1)}\Big|_{t=0} = 0 \quad n \in \mathbb{N}_1 \tag{4.30}$$

to be true. Equation (4.28) then becomes

$$G_n^{(1)} = \int_0^t \exp\left[\frac{\nu_t}{h^2} n^2\pi^2 (t' - t)\right] F_n^{(1)} \, \mathrm{d}t' \quad n \in \mathbb{N}_1. \tag{4.31}$$

4.4.2 Second-order solution

For subsequent higher-order solutions, the following Taylor series expansion about zero must be applied to Equation (4.20) in order to obtain the second-order solution (see Appendix C.3):

$$\frac{1}{\hat{h} + \delta\hat{\zeta}_e} = \frac{1}{\hat{h}} \sum_{n=0}^{\infty} \left(-\frac{\delta\hat{\zeta}_e}{\hat{h}} \right)^n = \frac{1}{\hat{h}} + \mathcal{O}(\delta) \tag{4.32}$$

By neglecting the effects of the roller thickness, Equations (3.6), (3.8) and (3.9) can be used to approximate the rate of change of ζ_e as

$$\frac{\partial \zeta_e}{\partial t} \simeq -\frac{\partial q}{\partial x} = -\left(\frac{\partial h}{\partial x} + \frac{\partial \zeta}{\partial x} \right) \bar{u} - (h + \zeta) \frac{\partial \bar{u}}{\partial x}. \tag{4.33}$$

With Equations (3.20), (3.22) to (3.24) and (3.26), and noting that

$$\hat{\bar{u}} = \hat{\bar{u}}^{(0+1)} + \delta\hat{\bar{u}}^{(2)}, \tag{4.34}$$

the following nondimensional approximation of Equation (4.33) is provided:

$$\frac{\partial\hat{\zeta}_{\mathrm{e}}}{\partial\hat{t}} = -\left(\frac{\partial\hat{h}}{\partial\hat{x}} + \delta\frac{\partial\hat{\zeta}}{\partial\hat{x}}\right)\hat{\bar{u}} - \left(\hat{h} + \delta\hat{\zeta}\right)\frac{\partial\hat{\bar{u}}}{\partial\hat{x}} = -\hat{h}\frac{\partial\hat{\bar{u}}^{(0+1)}}{\partial\hat{x}} + \mathcal{O}\left(\delta, \frac{\partial\hat{h}}{\partial\hat{x}}\right) \tag{4.35}$$

The same procedure as before is then followed to find a solution of the form

$$\omega^{(2)} = \sum_{n=1}^{\infty} G_n^{(2)} \sin\left(n\pi\sigma\right) \tag{4.36}$$

from the terms $\mathcal{O}\left(\delta\right)$ in Equation (4.20) which, with Equations (3.20), (3.22) to (3.27), (3.36), (4.12), (4.18), (4.32), (4.34) and (4.35), provides the dimensional equation

$$\frac{\partial\omega^{(2)}}{\partial t} - \frac{\nu_{\mathrm{t}}}{h^2}\frac{\partial^2\omega^{(2)}}{\partial\sigma^2} = F^{(2)}, \tag{4.37}$$

where

$$\begin{aligned} F^{(2)} = &-\sigma\frac{\partial\hat{u}}{\partial x}\left(2\omega_{\mathrm{s}} + \frac{\partial\omega^{(1)}}{\partial\sigma}\right) - \frac{w^{(0+1)}}{h}\left(\frac{\partial\omega^{(1)}}{\partial\sigma} + \omega_{\mathrm{s}}\right) \\ &- u^{(0+1)}\frac{\partial}{\partial x}\left(\omega^{(1)} + \sigma\omega_{\mathrm{s}}\right) - 2\frac{\nu_{\mathrm{t}}}{h^2}\frac{\zeta_{\mathrm{e}}}{h}\frac{\partial^2\omega^{(1)}}{\partial\sigma^2}. \end{aligned} \tag{4.38}$$

The use of the Equation (4.35) has additional advantages in that the substitution simplifies the calculation of $F^{(2)}$. Consequently, there is an improvement in the computational performance, and potentially a reduction in numerical noise that may otherwise be introduced into the system by the presence of a greater number of spatial derivatives.

A second sinusoidal Fourier series expansion is used to give the following relations:

$$F^{(2)} = \sum_{n=1}^{\infty} F_n^{(2)} \sin\left(n\pi\sigma\right) \tag{4.39}$$

$$F_n^{(2)} = 2\int_0^1 F^{(2)} \sin\left(n\pi\sigma\right)\ \mathrm{d}\sigma \quad n \in \mathbb{N}_1 \tag{4.40}$$

Substituting Equations (4.36) and (4.39) into Equation (4.37) and again noting that the combined summation must hold for all values of σ, another first-order nonhomogeneous linear equation is obtained:

$$\frac{\partial G_n^{(2)}}{\partial t} + \frac{\nu_{\mathrm{t}}}{h^2}n^2\pi^2 G_n^{(2)} - F_n^{(2)} = 0 \tag{4.41}$$

Equation (4.36) is solved with the variation of parameters method used previously and the initial condition provided by Equations (4.7) and (4.36), giving

$$G_n^{(2)} = \int_0^t \exp\left[\frac{\nu_{\mathrm{t}}}{h^2}n^2\pi^2\left(t' - t\right)\right]F_n^{(2)}\ \mathrm{d}t' \quad n \in \mathbb{N}_1. \tag{4.42}$$

4.4.3 Vorticity profile

Substituting Equations (3.36), (4.18), (4.24) and (4.36) into Equation (4.12) allows the vorticity to be expressed in dimensional form as

$$\omega = \begin{cases} \sigma\omega_{\mathrm{s}} + \sum_{n=1}^{\infty}\left(G_n^{(1)} + G_n^{(2)}\right)\sin\left(n\pi\sigma\right) & z \leq \zeta_{\mathrm{e}} \\ \dfrac{\zeta - z}{\zeta - \zeta_{\mathrm{e}}}\omega_{\mathrm{s}} & \zeta_{\mathrm{e}} < z \leq \zeta. \end{cases} \tag{4.43}$$

To simplify the numerical description of ω, another sinusoidal Fourier series expansion is applied to the first term in Equation (4.43), such that

$$\sigma\omega_{\mathrm{s}} = \sum_{n=1}^{\infty} G_n^{(0)} \sin\left(n\pi\sigma\right) \tag{4.44}$$

and

$$G_n^{(0)} = 2\int_0^1 \sigma\omega_{\mathrm{s}} \sin\left(n\pi\sigma\right)\ \mathrm{d}\sigma = -2\omega_{\mathrm{s}}\frac{(-1)^n}{n\pi} \quad n \in \mathbb{N}_1. \tag{4.45}$$

With Equation (4.44), Equation (4.43) can be written as

$$\omega = \begin{cases} \sum_{n=1}^{\infty} G_n \sin\left(n\pi\sigma\right) & z \leq \zeta_{\mathrm{e}} \\ \dfrac{\zeta - z}{\zeta - \zeta_{\mathrm{e}}}\omega_{\mathrm{s}} & \zeta_{\mathrm{e}} < z \leq \zeta, \end{cases} \tag{4.46}$$

where

$$G_n = G_n^{(0)} + G_n^{(1)} + G_n^{(2)} \quad n \in \mathbb{N}_1. \tag{4.47}$$

4.5 Rotational velocity

In order to establish breaking terms from the solution to the VTE, it is necessary to determine the rotational velocity from the calculated value of the vorticity. First, Equations (3.21), (3.22), (3.26) and (3.36) are used to express Equation (3.44) in dimensional form up to $\mathcal{O}\left(\mu^2\right)$, and the integration divided at $z = \zeta_{\mathrm{e}}$:

$$u_{\mathrm{r}} = \int_{-h}^{z} \omega\ \mathrm{d}z' = \begin{cases} \int_{-h}^{z} \omega\ \mathrm{d}z' & z \leq \zeta_{\mathrm{e}} \\ u_{\mathrm{r}}|_{z=\zeta_{\mathrm{e}}} + \int_{\zeta_{\mathrm{e}}}^{z} \omega\ \mathrm{d}z' & \zeta_{\mathrm{e}} < z \leq \zeta \end{cases} \tag{4.48}$$

With Equations (4.10) and (4.46), the vorticity can then be integrated in σ-coordinates from the bed to an arbitrary depth outside the roller:

$$\begin{aligned} \int_{-h}^{z} \omega\ \mathrm{d}z' &= (h + \zeta_{\mathrm{e}}) \int_0^{\sigma} \sum_{n=1}^{\infty} G_n \sin\left(n\pi\sigma\right)\ \mathrm{d}\sigma' \quad z \leq \zeta_{\mathrm{e}} \\ &= (h + \zeta_{\mathrm{e}}) \sum_{n=1}^{\infty} \frac{G_n}{n\pi}\left[1 - \cos\left(n\pi\sigma\right)\right] \quad z \leq \zeta_{\mathrm{e}} \end{aligned} \tag{4.49}$$

Integrating Equation (4.46) over an arbitrary distance within the roller region gives

$$\begin{aligned}\int_{\zeta_\mathrm{e}}^{z} \omega \, \mathrm{d}z' &= \frac{\omega_\mathrm{s}}{\zeta - \zeta_\mathrm{e}} \int_{\zeta_\mathrm{e}}^{z} \zeta - z' \, \mathrm{d}z' \quad z \leq \zeta \\ &= \frac{\omega_\mathrm{s}}{\zeta - \zeta_\mathrm{e}} \left[\zeta \left(z - \zeta_\mathrm{e} \right) - \frac{z^2 - \zeta_\mathrm{e}^2}{2} \right] \quad z \leq \zeta. \end{aligned} \tag{4.50}$$

Equations (4.49) and (4.50) can be substituted into Equation (4.48) to give

$$u_\mathrm{r} = \begin{cases} \left(h + \zeta_\mathrm{e} \right) \sum_{n=1}^{\infty} \frac{G_n}{n\pi} \left[1 - \cos\left(n\pi\sigma \right) \right] & z \leq \zeta_\mathrm{e} \\ u_\mathrm{r}|_{z=\zeta_\mathrm{e}} + \frac{\omega_\mathrm{s}}{\zeta - \zeta_\mathrm{e}} \left[\zeta \left(z - \zeta_\mathrm{e} \right) - \frac{z^2 - \zeta_\mathrm{e}^2}{2} \right] & \zeta_\mathrm{e} < z \leq \zeta. \end{cases} \tag{4.51}$$

4.6 Horizontal velocity

Having obtained an expression for the rotational velocity, the calculation of the horizontal velocity follows naturally. Equations (3.3) and (4.51), allow the depth averaged rotational velocity to be calculated as

$$\bar{u}_\mathrm{r} = \begin{cases} \left(h + \zeta_\mathrm{e} \right) \sum_{n=1}^{\infty} \frac{G_n}{n\pi} & z \leq \zeta_\mathrm{e} \\ \frac{\zeta - \zeta_\mathrm{e}}{d} \, u_\mathrm{r}|_{z=\zeta_\mathrm{e}} - \frac{\omega_\mathrm{s}}{3d} \left(\zeta - \zeta_\mathrm{e} \right)^2 & \zeta_\mathrm{e} < z \leq \zeta. \end{cases} \tag{4.52}$$

As shown in Appendix A.5, the horizontal velocity can approximated as

$$u = \bar{u} + u_\mathrm{r} - \bar{u}_\mathrm{r}. \tag{4.53}$$

The procedure outlined in Appendix A.4.2 uses the continuity equation and bottom boundary condition to obtain the following relation:

$$w = -\frac{\partial}{\partial x} \int_{-h}^{z} u \, \mathrm{d}z' \tag{4.54}$$

An approximation for the vertical velocity is then obtained in σ-coordinates from Equations (4.10), (4.32), (4.53) and (4.54), giving

$$w^{(0+1)} = -h \frac{\partial}{\partial x} \int_{0}^{\sigma} u^{(0+1)} \, \mathrm{d}\sigma'. \tag{4.55}$$

Equations (4.51) and (4.52) can then be substituted into Equation (4.53) to give

$$u = \begin{cases} \bar{u} - \left(h + \zeta_\mathrm{e} \right) \sum_{n=1}^{\infty} \frac{G_n}{n\pi} \cos\left(n\pi\sigma \right) & z \leq \zeta_\mathrm{e} \\ \bar{u} - \left(\frac{\zeta - \zeta_\mathrm{e}}{d} - 1 \right) u_\mathrm{r}|_{z=\zeta_\mathrm{e}} - \omega_\mathrm{s} \left[\frac{z^2 - \zeta_\mathrm{e}^2}{2\left(\zeta - \zeta_\mathrm{e} \right)} - \zeta \frac{z - \zeta_\mathrm{e}}{\zeta - \zeta_\mathrm{e}} - \frac{\left(\zeta - \zeta_\mathrm{e} \right)^2}{3d} \right] & \zeta_\mathrm{e} < z \leq \zeta. \end{cases} \tag{4.56}$$

As such, by combining the depth averaged horizontal velocity obtained from the BTEs with the rotational velocity calculated using the VTE, vertical profiles of the horizontal velocity can be constructed.

4.7 Calculation of breaking terms

The breaking terms given in Chapter 3 involve the integration of a number of terms across the depth of the fluid. With a few additional steps, it is possible to manipulate the equations used in determining the breaking terms in order to provide a form better suited to numerical solution. With Equation (3.3), Equation (3.57) can be written as

$$\begin{aligned}\Delta M &= \int_{-h}^{\zeta} u_{\mathrm{r}}^2 - \left(\frac{1}{h+\zeta}\int_{-h}^{\zeta} u_{\mathrm{r}}\,\mathrm{d}z'\right)^2\,\mathrm{d}z \\ &= \int_{-h}^{\zeta_{\mathrm{e}}} u_{\mathrm{r}}^2\,\mathrm{d}z + \int_{\zeta_{\mathrm{e}}}^{\zeta} u_{\mathrm{r}}^2\,\mathrm{d}z - \frac{1}{h+\zeta}\left(\int_{-h}^{\zeta_{\mathrm{e}}} u_{\mathrm{r}}\,\mathrm{d}z + \int_{\zeta_{\mathrm{e}}}^{\zeta} u_{\mathrm{r}}\,\mathrm{d}z\right)^2. \end{aligned} \tag{4.57}$$

Substituting Equation (4.51) into Equation (4.57) and using Equation (4.10) to express integrals outside the roller region in σ-coordinates then provides the following:

$$\begin{aligned}\Delta M = (h+\zeta_{\mathrm{e}})\int_0^1 &\left\{(h+\zeta_{\mathrm{e}})\sum_{n=1}^{\infty}\frac{G_n}{n\pi}\left[1-\cos\left(n\pi\sigma\right)\right]\right\}^2\,\mathrm{d}\sigma \\ &+ \int_{\zeta_{\mathrm{e}}}^{\zeta}\left\{u_{\mathrm{r}}|_{z=\zeta_{\mathrm{e}}} + \frac{\omega_{\mathrm{s}}}{\zeta-\zeta_{\mathrm{e}}}\left[\zeta\left(z-\zeta_{\mathrm{e}}\right) - \frac{z^2-\zeta_{\mathrm{e}}^2}{2}\right]\right\}^2\,\mathrm{d}z \\ &- \frac{1}{h+\zeta}\left\{(h+\zeta_{\mathrm{e}})\int_0^1 (h+\zeta_{\mathrm{e}})\sum_{n=1}^{\infty}\frac{G_n}{n\pi}\left[1-\cos\left(n\pi\sigma\right)\right]\,\mathrm{d}\sigma\right. \\ &\left. + \int_{\zeta_{\mathrm{e}}}^{\zeta} u_{\mathrm{r}}|_{z=\zeta_{\mathrm{e}}} + \frac{\omega_{\mathrm{s}}}{\zeta-\zeta_{\mathrm{e}}}\left[\zeta\left(z-\zeta_{\mathrm{e}}\right) - \frac{z^2-\zeta_{\mathrm{e}}^2}{2}\right]\,\mathrm{d}z\right\}^2 \end{aligned} \tag{4.58}$$

Noting that

$$\left(\sum_{n=1}^{\infty} f_n\right)^2 = \sum_{n=1}^{\infty} f_n^2 + \sum_{n=1}^{\infty}\sum_{\substack{l=1\\ l\neq n}}^{\infty} f_n f_l, \tag{4.59}$$

and

$$\int_0^1 \cos\left(n\pi\sigma\right)\,\mathrm{d}\sigma = 0 \quad n\in\mathbb{N}_1, \tag{4.60}$$

Equation (4.58) becomes

$$\begin{aligned}\Delta M = (h+\zeta_{\mathrm{e}})^3 &\left(\sum_{n=1}^{\infty}\frac{G_n^2}{n^2\pi^2} + \frac{1}{2}\sum_{n=1}^{\infty}\frac{G_n^2}{n^2\pi^2} + \sum_{n=1}^{\infty}\sum_{\substack{l=1\\ l\neq n}}^{\infty}\frac{G_n G_l}{nl\pi^2}\right) \\ &+ (\zeta-\zeta_{\mathrm{e}})\left(u_{\mathrm{r}}|_{z=\zeta_{\mathrm{e}}}\right)^2 + \frac{2}{3}\,u_{\mathrm{r}}|_{z=\zeta_{\mathrm{e}}}\,\omega_{\mathrm{s}}\left(\zeta-\zeta_{\mathrm{e}}\right)^2 + \frac{2}{15}\omega_{\mathrm{s}}\left(\zeta-\zeta_{\mathrm{e}}\right)^3 \\ &- \frac{1}{h+\zeta}\left[(h+\zeta_{\mathrm{e}})^2\sum_{n=1}^{\infty}\frac{G_n}{n\pi} + (\zeta-\zeta_{\mathrm{e}})\,u_{\mathrm{r}}|_{z=\zeta_{\mathrm{e}}} + \frac{\omega_{\mathrm{s}}}{3}\left(\zeta-\zeta_{\mathrm{e}}\right)^2\right]^2. \end{aligned} \tag{4.61}$$

Equation (4.59) then allows Equation (4.61) to be written as

$$\Delta M = (h+\zeta_\mathrm{e})^3 \left[\left(\sum_{n=1}^{\infty} \frac{G_n}{n\pi} \right)^2 + \frac{1}{2} \sum_{n=1}^{\infty} \left(\frac{G_n}{n\pi} \right)^2 \right] + (\zeta - \zeta_\mathrm{e}) \left(u_\mathrm{r}|_{z=\zeta_\mathrm{e}} \right)^2 + \frac{2}{3}\, u_\mathrm{r}|_{z=\zeta_\mathrm{e}}\, \omega_\mathrm{s}\, (\zeta - \zeta_\mathrm{e})^2 + \frac{2}{15} \omega_\mathrm{s} (\zeta - \zeta_\mathrm{e})^3 - \frac{1}{h+\zeta} \left[(h+\zeta_\mathrm{e})^2 \sum_{n=1}^{\infty} \frac{G_n}{n\pi} + (\zeta - \zeta_\mathrm{e})\, u_\mathrm{r}|_{z=\zeta_\mathrm{e}} + \frac{\omega_\mathrm{s}}{3} (\zeta - \zeta_\mathrm{e})^2 \right]^2 . \tag{4.62}$$

Similarly, Equations (3.3) and (3.58) provide

$$\Delta P = - \int_{-h}^{\zeta} \int_{z}^{\zeta} \int_{-h}^{z'} u_\mathrm{r} - \frac{1}{h+\zeta} \int_{-h}^{\zeta} u_\mathrm{r}\, \mathrm{d}z'''\, \mathrm{d}z''\, \mathrm{d}z'\, \mathrm{d}z. \tag{4.63}$$

When calculating ΔP, the influence of the rotational velocity within the roller is assumed to be sufficiently small that it may be reasonably neglected (Veeramony and Svendsen, 2000). On this basis, $\zeta \simeq \zeta_\mathrm{e}$ is assumed for the limits of integration for rotational terms. With Equations (4.10) and (4.51), Equation (4.63) then becomes

$$\Delta P \simeq - (h+\zeta_\mathrm{e})^3 \int_0^1 \int_\sigma^1 \int_0^{\sigma'} \left\{ (h+\zeta_\mathrm{e}) \sum_{n=1}^{\infty} \frac{G_n}{n\pi} \left[1 - \cos\left(n\pi\sigma'' \right) \right] - \int_0^1 (h+\zeta_\mathrm{e}) \sum_{n=1}^{\infty} \frac{G_n}{n\pi} \left[1 - \cos\left(n\pi\sigma''' \right) \right] \mathrm{d}\sigma''' \right\} \mathrm{d}\sigma''\, \mathrm{d}\sigma'\, \mathrm{d}\sigma. \tag{4.64}$$

With Equation (4.60), the approximation in Equation (4.64) can be simplified to give

$$\Delta P = - (h+\zeta_\mathrm{e})^4 \sum_{n=1}^{\infty} \frac{(-1)^n}{n^3\pi^3} G_n. \tag{4.65}$$

Equation (4.65) can then be differentiated in time, which with Equations (3.20), (3.23), (3.24), (3.26) and (4.35), provides the following relation:

$$\frac{\partial}{\partial t} (\Delta P) = (h+\zeta_\mathrm{e})^3 \sum_{n=1}^{\infty} \frac{(-1)^n}{n^3\pi^3} \left[4h \frac{\partial \bar{u}}{\partial x} G_n - (h+\zeta_\mathrm{e}) \frac{\partial G_n}{\partial t} \right] \tag{4.66}$$

4.8 Spectral solution

A numerical approach must be established in order to perform the temporal integration present in the expressions for $G_n^{(1)}$. The terms in Equation (4.47) up to $\mathcal{O}(\delta)$,

$$G_n^{(0+1)} = G_n^{(0)} + G_n^{(1)}, \tag{4.67}$$

are evaluated at a time t', which with Equations (4.23), (4.31) and (4.45) gives

$$G_n^{(0+1)}\Big|_{t=t'} = -2\, \omega_\mathrm{s}|_{t=t'} \frac{(-1)^n}{n\pi} + 2 \frac{(-1)^n}{n\pi} \int_0^{t'} \exp\left[\frac{\nu_\mathrm{t}}{h^2} n^2\pi^2 \left(t'' - t' \right) \right] \frac{\partial \omega_\mathrm{s}}{\partial t}\, \mathrm{d}t'' \quad n \in \mathbb{N}_1. \tag{4.68}$$

The following integral expression is obtained with the procedure given in Appendix C.2:

$$\int V(X)\,\frac{\partial W}{\partial X}\,\mathrm{d}X = VW - \int W\frac{\partial V}{\partial X}\,\mathrm{d}X \tag{4.69}$$

With Equation (4.69), Equation (4.68) can also be evaluated after a constant timestep, Δt, to give

$$\begin{aligned} G_n^{(0+1)}\Big|_{t=t'+\Delta t} = {} & -2\,\omega_\mathrm{s}|_{t=t'+\Delta t}\,\frac{(-1)^n}{n\pi} \\ & + 2\frac{(-1)^n}{n\pi}\exp\left(-\frac{\nu_\mathrm{t}}{h^2}n^2\pi^2\Delta t\right)\left\{\int_0^{t'}\exp\left[\frac{\nu_\mathrm{t}}{h^2}n^2\pi^2\left(t''-t'\right)\right]\frac{\partial\omega_\mathrm{s}}{\partial t}\,\mathrm{d}t''\right. \\ & \qquad + \frac{h^2}{\nu_\mathrm{t}n^2\pi^2}\left[\exp\left(\frac{\nu_\mathrm{t}}{h^2}n^2\pi^2\Delta t\right)-1\right]\frac{\partial\omega_\mathrm{s}}{\partial t} \\ & \qquad \left. - \int_{t'}^{t'+\Delta t}\exp\left[\frac{\nu_\mathrm{t}}{h^2}n^2\pi^2\left(t''-t'\right)\right]\frac{\partial^2\omega_\mathrm{s}}{\partial t^2}\,\mathrm{d}t''\right\} \quad n\in\mathbb{N}_1. \end{aligned} \tag{4.70}$$

In order to simplify the integration of the temporal gradient of vorticity along the lower edge of the roller, the change in $\frac{\partial\omega_\mathrm{s}}{\partial t}$ is assumed negligible over a single timestep, such that, for numerical purposes,

$$\frac{\partial^2\omega_\mathrm{s}}{\partial t^2} = 0. \tag{4.71}$$

Substituting Equations (4.68) and (4.71) into Equation (4.70) then gives

$$\begin{aligned} G_n^{(0+1)}\Big|_{t=t'+\Delta t} = {} & \exp\left(-\frac{\nu_\mathrm{t}}{h^2}n^2\pi^2\Delta t\right)G_n^{(0+1)}\Big|_{t=t'} + 2\frac{(-1)^n}{n\pi}\left\{\exp\left(-\frac{\nu_\mathrm{t}}{h^2}n^2\pi^2\Delta t\right)\omega_\mathrm{s}|_{t=t'}\right. \\ & \left. - \omega_\mathrm{s}|_{t=t'+\Delta t} + \frac{h^2}{\nu_\mathrm{t}n^2\pi^2}\left[1-\exp\left(-\frac{\nu_\mathrm{t}}{h^2}n^2\pi^2\Delta t\right)\right]\frac{\partial\omega_\mathrm{s}}{\partial t}\right\} \quad n\in\mathbb{N}_1. \end{aligned} \tag{4.72}$$

Equations (4.47), (4.67) and (4.72) then provide an expression to update the value of G_n based on that obtained at the previous timestep. In order to calculate higher-order terms, $F_n^{(2)}$ is needed, which in turn requires an expression to update $G_n^{(1)}$ at each timestep. A procedure similar to that used previously can be followed to determine $G_n^{(1)}$, and subsequently, $G_n^{(2)}$. Evaluating Equations (4.31) and (4.42) at time $t'+\Delta t$ and substituting the result back into the same equation evaluated at time t' gives

$$\begin{aligned} G_n^{(1)}\Big|_{t=t'+\Delta t} = {} & \exp\left(-\frac{\nu_\mathrm{t}}{h^2}n^2\pi^2\Delta t\right)\left\{G_n^{(1)}\Big|_{t=t'}\right. \\ & \left. + \int_{t'}^{t'+\Delta t}\exp\left[\frac{\nu_\mathrm{t}}{h^2}n^2\pi^2\left(t''-t'\right)\right]F_n^{(1)}\,\mathrm{d}t''\right\} \quad n\in\mathbb{N}_1 \end{aligned} \tag{4.73}$$

and

$$G_n^{(2)}\Big|_{t=t'+\Delta t} = \exp\left(-\frac{\nu_\mathrm{t}}{h^2}n^2\pi^2\Delta t\right)\left\{G_n^{(2)}\Big|_{t=t'} + \int_{t'}^{t'+\Delta t}\exp\left[\frac{\nu_\mathrm{t}}{h^2}n^2\pi^2\left(t''-t'\right)\right]F_n^{(2)}\ \mathrm{d}t''\right\} \quad n\in\mathbb{N}_1. \tag{4.74}$$

With Equations (4.23), (4.69), (4.71) and (4.73), it follows that

$$G_n^{(1)}\Big|_{t=t'+\Delta t} = \exp\left(-\frac{\nu_\mathrm{t}}{h^2}n^2\pi^2\Delta t\right)G_n^{(1)}\Big|_{t=t'} + \frac{2\left(-1\right)^n h^2}{\nu_\mathrm{t}n^3\pi^3}\left[1-\exp\left(-\frac{\nu_\mathrm{t}}{h^2}n^2\pi^2\Delta t\right)\right]\frac{\partial\omega_\mathrm{s}}{\partial t} \quad n\in\mathbb{N}_1. \tag{4.75}$$

For the calculation of $F_n^{(2)}$, the influence of the rotational velocity within the roller region is again neglected. With Equations (4.10), (4.32), (4.43) and (4.48), the approximation for the rotational horizontal velocity up to $\mathcal{O}\left(1\right)$ is calculated as

$$u_\mathrm{r}^{(0+1)} = h\int_0^\sigma \sigma\omega_\mathrm{s} + \sum_{n=1}^{\infty}G_n^{(1)}\sin\left(n\pi\sigma\right)\ \mathrm{d}\sigma' = h\left\{\frac{\sigma^2}{2}\omega_\mathrm{s} - \sum_{n=1}^{\infty}\frac{G_n^{(1)}}{n\pi}\left[\cos\left(n\pi\sigma\right)-1\right]\right\}. \tag{4.76}$$

Equations (3.3), (4.10), (4.53) and (4.60) together provide the following approximation for the horizontal velocity:

$$\begin{aligned} u^{(0+1)} &= \bar{u}^{(0+1)} \\ &\quad + h\left\{\frac{\sigma^2}{2}\omega_\mathrm{s} - \sum_{n=1}^{\infty}\frac{G_n^{(1)}}{n\pi}\left[\cos\left(n\pi\sigma\right)-1\right] - \int_0^1 \frac{\sigma^2}{2}\omega_\mathrm{s} - \sum_{n=1}^{\infty}\frac{G_n^{(1)}}{n\pi}\left[\cos\left(n\pi\sigma\right)-1\right]\ \mathrm{d}\sigma'\right\} \\ &= \bar{u}^{(0+1)} + h\left[\left(\frac{\sigma^2}{2}-\frac{1}{6}\right)\omega_\mathrm{s} - \sum_{n=1}^{\infty}\frac{G_n^{(1)}}{n\pi}\cos\left(n\pi\sigma\right)\right] \end{aligned} \tag{4.77}$$

Equation (4.77) can then be substituted into Equation (4.55) to give

$$w^{(0+1)} = -h\frac{\partial}{\partial x}\left\{\sigma\bar{u}^{(0+1)} + h\left[\frac{\sigma}{6}\left(\sigma^2-1\right)\omega_\mathrm{s} - \sum_{n=1}^{\infty}G_n^{(1)}\frac{\sin\left(n\pi\sigma\right)}{n^2\pi^2}\right]\right\}. \tag{4.78}$$

Substituting Equations (4.10), (4.24), (4.77) and (4.78) into Equation (4.38) then gives

$$\begin{aligned} F^{(2)} &= -\sigma\frac{\partial\bar{u}^{(0+1)}}{\partial x}\left[2\omega_\mathrm{s} + \sum_{n=1}^{\infty}G_n^{(1)}n\pi\cos\left(n\pi\sigma\right)\right] + \left\{\sigma\frac{\partial\bar{u}^{(0+1)}}{\partial x}\right. \\ &\quad \left. + h\left[\frac{\sigma}{6}\left(\sigma^2-1\right)\frac{\partial\omega_\mathrm{s}}{\partial x} - \sum_{n=1}^{\infty}\frac{\partial G_n^{(1)}}{\partial x}\frac{\sin\left(n\pi\sigma\right)}{n^2\pi^2}\right]\right\}\left[\omega_\mathrm{s} + \sum_{n=1}^{\infty}G_n^{(1)}n\pi\cos\left(n\pi\sigma\right)\right] \\ &\quad - \left\{\bar{u}^{(0+1)} + h\left[\left(\frac{\sigma^2}{2}-\frac{1}{6}\right)\omega_\mathrm{s} - \sum_{n=1}^{\infty}\frac{G_n^{(1)}}{n\pi}\cos\left(n\pi\sigma\right)\right]\right\}\left[\sigma\frac{\partial\omega_\mathrm{s}}{\partial x} + \sum_{n=1}^{\infty}\frac{\partial G_n^{(1)}}{\partial x}\sin\left(n\pi\sigma\right)\right] \\ &\quad + 2\frac{\nu_\mathrm{t}}{h^2}\frac{\zeta_\mathrm{e}}{h}\sum_{n=1}^{\infty}G_n^{(1)}n^2\pi^2\sin\left(n\pi\sigma\right) + \mathcal{O}\left(\frac{\partial h}{\partial x}\right). \end{aligned} \tag{4.79}$$

With Equations (4.60) and (4.69) and the expressions given in Appendix C.5, several additional identities are provided in order to rewrite Equation (4.40) as part of the treatment of $F_n^{(2)}$ that follows:

$$\int_0^1 \sigma \sin(n\pi\sigma)\ \mathrm{d}\sigma = -\frac{(-1)^n}{n\pi} \quad n \in \mathbb{N}_1 \tag{4.80}$$

$$\int_0^1 \sigma^3 \sin(n\pi\sigma)\ \mathrm{d}\sigma = \frac{(-1)^n}{n\pi}\left(\frac{6}{n^2\pi^2} - 1\right) \quad n \in \mathbb{N}_1 \tag{4.81}$$

$$\begin{aligned}\int_0^1 \sin(n\pi\sigma)\sin(l\pi\sigma)\ \mathrm{d}\sigma &= \frac{1}{2}\int_0^1 \cos[(n-l)\pi\sigma] - \cos[(n+l)\pi\sigma]\ \mathrm{d}\sigma \\ &= \begin{cases} \frac{1}{2} - \frac{\sin(2n\pi)}{2n\pi} & n = l \\ \frac{\sin[(n-l)\pi]}{2(n-l)\pi} - \frac{\sin[(n+l)\pi]}{2(n+l)\pi} & n \neq l \end{cases} \\ &= \begin{cases} \frac{1}{2} & n = l \\ 0 & n \neq l \end{cases} \quad n, l \in \mathbb{N}_1\end{aligned} \tag{4.82}$$

$$\begin{aligned}&\int_0^1 \left(\sigma^2 - \frac{1}{3}\right)\sin(n\pi\sigma)\sin(l\pi\sigma)\ \mathrm{d}\sigma \\ &= \frac{1}{2}\int_0^1 \sigma^2\cos[(n-l)\pi\sigma] - \sigma^2\cos[(n+l)\pi\sigma] - \frac{1}{3}\cos[(n-l)\pi\sigma] + \frac{1}{3}\cos[(n+l)\pi\sigma]\ \mathrm{d}\sigma \\ &= \begin{cases} \frac{1}{2}\int_0^1 \sigma^2 - \sigma^2\cos(2\pi n\sigma) - \frac{1}{3}\ \mathrm{d}\sigma & n = l \\ \frac{1}{2}\int_0^1 \sigma^2\cos[(n-l)\pi\sigma] - \sigma^2\cos[(n+l)\pi\sigma]\ \mathrm{d}\sigma & n \neq l \end{cases} \\ &= \begin{cases} -\frac{1}{4n^2\pi^2} & n = l \\ \frac{4nl(-1)^{n+l}}{(n^2-l^2)^2\pi^2} & n \neq l \end{cases} \quad n, l, r \in \mathbb{N}_1\end{aligned} \tag{4.83}$$

$$\begin{aligned}\int_0^1 \sin(n\pi\sigma)\cos(l\pi\sigma)\sin(r\pi\sigma)\ \mathrm{d}\sigma &= \frac{1}{2}\int_0^1 \sin[(n-l)\pi\sigma]\sin(r\pi\sigma) \\ &\quad + \sin[(n+l)\pi\sigma]\sin(r\pi\sigma)\ \mathrm{d}\sigma \\ &= \begin{cases} \frac{1}{4} & n-l = r,\ n+l = r \\ 0 & n-l \neq r \neq n+l \end{cases} \quad n, l, r \in \mathbb{N}_1\end{aligned} \tag{4.84}$$

$$\begin{aligned}
\int_0^1 \sigma \sin\left(n\pi\sigma\right)\cos\left(l\pi\sigma\right)\ \mathrm{d}\sigma &= \frac{1}{2}\int_0^1 \sigma \sin\left[\left(n-l\right)\pi\sigma\right] + \sigma\sin\left[\left(n+l\right)\pi\sigma\right]\ \mathrm{d}\sigma \\
&= \begin{cases} -\dfrac{\cos\left(2n\pi\right)}{4n\pi} & n = l \\ -\dfrac{\left(-1\right)^{n-l}}{2\left(n-l\right)\pi} - \dfrac{\left(-1\right)^{n+l}}{2\left(n+l\right)\pi} & n \neq l \end{cases} \\
&= \begin{cases} -\dfrac{1}{4n\pi} & n = l \\ -\dfrac{n\left(-1\right)^{n+l}}{\left(n^2-l^2\right)\pi} & n \neq l \end{cases} \qquad n, l \in \mathbb{N}_1
\end{aligned} \tag{4.85}$$

$$\begin{aligned}
&\int_0^1 \sigma^3 \sin\left(n\pi\sigma\right)\cos\left(l\pi\sigma\right)\ \mathrm{d}\sigma \\
&= \frac{1}{2}\int_0^1 \sigma^3 \sin\left[\left(n-l\right)\pi\sigma\right] + \sigma^3\sin\left[\left(n+l\right)\pi\sigma\right]\ \mathrm{d}\sigma \\
&= \begin{cases} -\dfrac{\cos\left(2n\pi\right)}{4n\pi} + \dfrac{3\cos\left(2n\pi\right)}{8n^3\pi^3} & n = l \\ \dfrac{\left(-1\right)^{n-l}}{2\left(n-l\right)\pi}\left[\dfrac{6}{\left(n-l\right)^2\pi^2} - 1\right] + \dfrac{\left(-1\right)^{n+l}}{2\left(n+l\right)\pi}\left[\dfrac{6}{\left(n+l\right)^2\pi^2} - 1\right] & n \neq l \end{cases} \\
&= \begin{cases} \dfrac{1}{4n\pi}\left(\dfrac{3}{2n^2\pi^2} - 1\right) & n = l \\ \dfrac{n\left(-1\right)^{n+l}}{\left(n^2-l^2\right)\pi}\left[\dfrac{6n^2+18l^2}{\left(n^2-l^2\right)^2\pi^2} - 1\right] & n \neq l \end{cases} \qquad n, l \in \mathbb{N}_1
\end{aligned} \tag{4.86}$$

With Equations (4.79) to (4.86) and bed terms neglected, Equation (4.40) can be written as follows:

$$\begin{aligned}
F_n^{(2)} = {} & 2\frac{\left(-1\right)^n}{n\pi}\left[\bar{u}^{(0+1)}\frac{\partial\omega_\mathrm{s}}{\partial x} + \omega_\mathrm{s}\frac{\partial\bar{u}^{(0+1)}}{\partial x} - \left(\frac{2}{n^2\pi^2} - \frac{1}{3}\right)h\omega_\mathrm{s}\frac{\partial\omega_\mathrm{s}}{\partial x}\right] \\
& - \frac{3h}{4n^2\pi^2}\left(\frac{\partial G_n^{(1)}}{\partial x}\omega_\mathrm{s} + \frac{G_n^{(1)}}{2}\frac{\partial\omega_\mathrm{s}}{\partial x}\right) - \bar{u}^{(0+1)}\frac{\partial G_n^{(1)}}{\partial x} + 2\frac{\nu_\mathrm{t}\zeta_\mathrm{e}}{h^3}n^2\pi^2 G_n^{(1)} \\
& + \frac{h}{2}\sum_{\substack{l=1\\ n-l=r}}^{\infty}\sum_{r=1}^{\infty}\left(1 - \frac{l^2}{r^2}\right)\frac{G_l^{(1)}}{l\pi}\frac{\partial G_r^{(1)}}{\partial x} + \frac{h}{2}\sum_{\substack{l=1\\ n+l=r}}^{\infty}\sum_{r=1}^{\infty}\left(1 - \frac{l^2}{r^2}\right)\frac{G_l^{(1)}}{l\pi}\frac{\partial G_r^{(1)}}{\partial x} \\
& + 2h\frac{\partial\omega_\mathrm{s}}{\partial x}\sum_{\substack{l=1\\ l\neq n}}^{\infty}\frac{nl\left(-1\right)^{n+l}}{n^2-l^2}\left[\frac{n^2+3l^2}{\left(n^2-l^2\right)^2\pi^2} - \frac{1}{l^2\pi^2} - \frac{1}{3}\right]G_l^{(1)} \\
& - 4h\omega_\mathrm{s}\sum_{\substack{l=1\\ l\neq n}}^{\infty}\frac{nl\left(-1\right)^{n+l}}{\left(n^2-l^2\right)^2\pi^2}\frac{\partial G_l^{(1)}}{\partial x} \qquad n \in \mathbb{N}_1
\end{aligned} \tag{4.87}$$

By taking the value of $\bar{u}^{(0+1)}$ in terms $\mathcal{O}(\delta)$, the variable can be more simply taken as $\bar{u}$ throughout.

4.8.1 Evaluation of series summations

Although it is not possible to calculate an infinite series for the summations used here, the magnitude of successive terms diminishes, meaning a convergent solution is obtained. As such, the upper limit for the summation, M, can be chosen such that a sufficiently accurate value is obtained.

It is worth noting the computational efficiency earned by employing matrix algebra in the calculation of the summations is exploited to numerically evaluate the integrals used to ascertain the vorticity, rotational velocity and breaking terms. This is well suited to a numerical implementation and improves the speed with which the solution is computed. A new algebraic formulation is therefore proposed to yield the benefits of an algorithm implemented using matrices. This technique is demonstrated by first postulating the calculation of Z for the N cells in the domain according to

$$Z_{i,V} = \sum_{n=1}^{M} X_{i,n} Y_{n,V} \quad i \in \{1, 2, \ldots, N\}, \; V \in \{1, 2, \ldots, L\}. \tag{4.88}$$

Here i indicates the cell in the domain, while L defines the number of points in the vertical discretisation of σ used for the numerical solution. Equation (4.88) can be solved according to

$$\boldsymbol{Z}_{N,L} = \boldsymbol{X}_{N,M} \boldsymbol{Y}_{M,L}, \tag{4.89}$$

where

$$\boldsymbol{Z}_{N,L} = \begin{bmatrix} Z_{1,1} & Z_{1,2} & \ldots & Z_{1,O} \\ Z_{2,1} & Z_{2,2} & \ldots & Z_{2,O} \\ \vdots & \vdots & \ddots & \vdots \\ Z_{N,1} & Z_{N,2} & \ldots & Z_{N,O} \end{bmatrix}, \tag{4.90}$$

$$\boldsymbol{X}_{N,M} = \begin{bmatrix} X_{1,1} & X_{1,2} & \ldots & X_{1,M} \\ X_{2,1} & X_{2,2} & \ldots & X_{2,M} \\ \vdots & \vdots & \ddots & \vdots \\ X_{N,1} & X_{N,2} & \ldots & X_{N,M} \end{bmatrix} \tag{4.91}$$

and

$$\boldsymbol{Y}_{M,L} = \begin{bmatrix} Y_{1,1} & Y_{1,2} & \ldots & Y_{1,O} \\ Y_{2,1} & Y_{2,2} & \ldots & Y_{2,O} \\ \vdots & \vdots & \ddots & \vdots \\ Y_{M,1} & Y_{M,2} & \ldots & Y_{M,O} \end{bmatrix}. \tag{4.92}$$

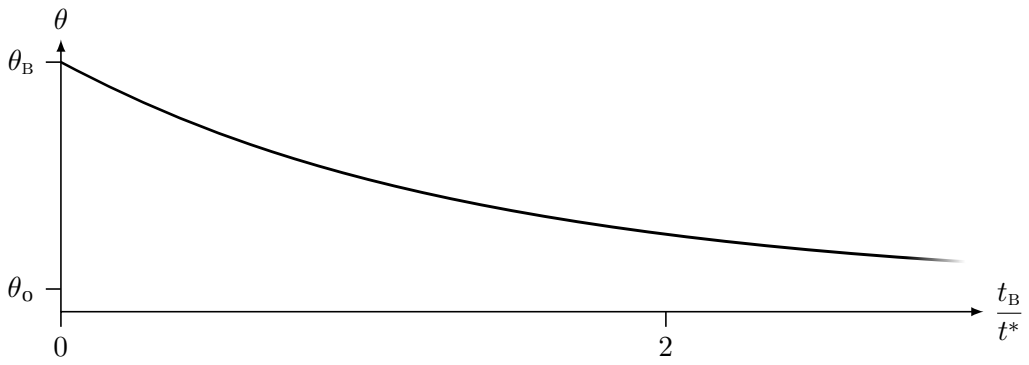

Figure 4.1: Evolution of breaking angle with ageing roller.

In addition to the inherent numerical efficiency gained by utilising matrix multiplication, this form is also convenient for the equations solved here as it allows variables corresponding to $\boldsymbol{Y}$ to be precomputed before the simulation advances in time, thereby removing the need to recalculate the coefficients within the summation. The application of this procedure is given in more detail in Appendix B.

4.9 Roller method

The approach described by Schäffer et al. (1993) is used to establish breaking initiation and termination criteria and locate the roller crest and toe. This method uses the maximum local wave slope to indicate the breaking state of a wave.

4.9.1 Geometric definition

As shown in Figure 3.1, the crest is identified by x_c, which is located at the local maximum free surface elevation of the wave. The location of the toe, x_t, is defined as the point at which the angle of the free surface slope to the horizontal is

$$\theta = \arctan\left[\tan\theta_\mathrm{o} + (\tan\theta_\mathrm{B} - \tan\theta_\mathrm{o})\exp\left(-\frac{t_\mathrm{B}}{t^*}\ln 2\right)\right]. \tag{4.93}$$

Here, θ_B and θ_o denote the angles at which breaking starts and ends, respectively, while t_B is the age of the breaker and t^* is the timescale over which the roller develops. Figure 4.1 illustrates the development of θ described by Equation (4.93) as the roller progresses.

Zero-upcrossing points are used to identify individual waves by defining the boundary between successive waves at the point where $\zeta_i < 0$ and $\zeta_{i+1} > 0$. The existence of a roller is then considered for each wave. As the age and current breaking status of waves need to be retained between consecutive timesteps, the location of each crest is tracked. This allows the progression of each roller to be monitored and the formation and cessation of rollers to be managed appropriately.

In order to inject vorticity into the system, it is first necessary to define geometric aspects of the roller region (Svendsen et al., 2000). This is done by estimating the

thickness of the roller according to the following empirical formula established from observations of hydraulic jumps:

$$\zeta_{\mathrm{e}} = \zeta - 0.78 d_{\mathrm{c}} \sqrt{\frac{d_{\mathrm{c}}}{d_{\mathrm{t}}}} \Theta \left(1 - \Theta\right) \exp\left(-\Theta\right) \tag{4.94}$$

Here,

$$\Theta = \begin{cases} \dfrac{x_{\mathrm{T}} - x}{l_{\mathrm{r}}} & x_{\mathrm{C}} < x < x_{\mathrm{T}} \\ 0 & \text{otherwise,} \end{cases} \tag{4.95}$$

where the length of the roller is given by

$$l_{\mathrm{r}} = x_{\mathrm{T}} - x_{\mathrm{C}}. \tag{4.96}$$

The positions of x_{C} and x_{T} are determined during the numerical refinement of the crest and toe locations respectively, which is discussed in detail in Section 5.8.

4.9.2 Vorticity injection

Having established the required geometry, the vorticity injected along the lower edge of the roller is calculated as

$$\omega_{\mathrm{s}} = \omega_{\mathrm{m}} \sqrt{\frac{g d_{\mathrm{t}}}{2 d_{\mathrm{c}}^3} \left(d_{\mathrm{t}} + d_{\mathrm{c}}\right)} \upsilon, \tag{4.97}$$

where ω_{m} is used to influence the strength of the vorticity injected into the fluid (Veeramony and Svendsen, 2000). This provides the upper boundary condition required when solving the VTE outlined here. The term denoted by υ describes the spatial distribution of the injected vorticity in the roller region. This is derived from the function fitted to experimental data of hydraulic jump observations by Svendsen et al. (2000), given as $1 - \Theta$. As the discontinuity introduced by this function at the roller toe can result in numerical instabilities, it is modified to be

$$\upsilon = \alpha_{\mathrm{r}} \left[1 - \exp\left(-\alpha_{\mathrm{v}} \Theta\right)\right] \left(1 - \Theta\right). \tag{4.98}$$

This function provides two additional parameters to allow the profile to be controlled as necessary. Increasing the value of α_{v} results in a steeper slope at the toe, bringing the curve closer to the function fitted to the empirical observations. Changes in α_{r} represent a more artificial representation of ω_{s} which concentrates a greater amount of the injected vorticity towards the toe of the roller. This adjustment is illustrated in Figure 4.2, which shows υ to concentrate the injected vorticity towards the toe of the roller.

It is important to note that, within the roller region, the area under the different functions used to describe α_{r} remains the same throughout this study. The area under the curve defined by υ is obtained by integrating Equation (4.98) from the crest to the toe, and indicates the total quantity of vorticity injected along the lower edge of the roller. Table 4.1 provides the areas calculated for the combinations of α_{v} and α_{r} used in the present work. Larger values indicate higher levels of vorticity injection across the entire roller region.

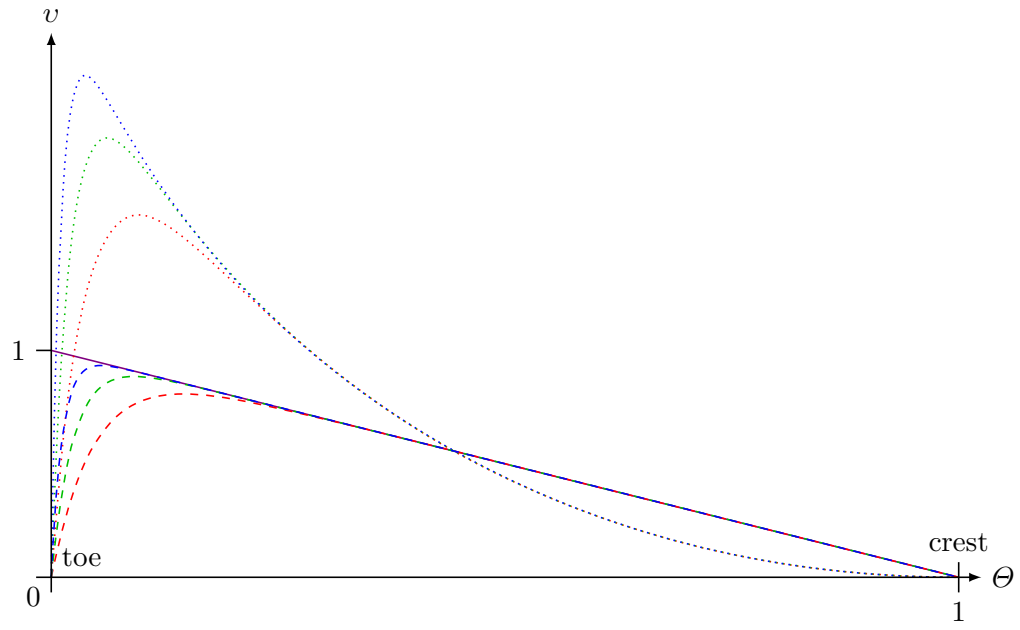

Figure 4.2: Distribution of injected vorticity across roller region adopted from experimental observations of hydraulic jumps (——) and for numerical model with exponent coefficients $\alpha_v = 20$ (•), $\alpha_v = 40$ (•) and $\alpha_v = 80$ (•), and distribution functions $\alpha_r = 1$ (- - - -) and $\alpha_r = 3\left(1 - \sqrt{\Theta}\right)$ (·····).

Table 4.1: Integral of injected vorticity distribution, υ, across roller region with different combinations of α_v and α_r.

Function for distribution of injected vorticity, α_r	Coefficient for distribution of injected vorticity, α_v		
	20	40	80
1	0.452	0.476	0.488
$3\left(1 - \sqrt{\Theta}\right)$	0.585	0.637	0.667

Chapter 5

Numerical solution

5.1 Historical approaches

Previous RBMs have used finite-difference (FD) schemes to solve the BTEs and, as a result, have encountered several limitations. A particularly noteworthy problem highlighted by Briganti et al. (2004) is the need to intensively filter the numerical solution, which results in artificial dissipation. This masks the physical behaviour of the breaking terms, and yet still fails to eliminate many of the issues of stability resulting from the high-order nature of the BTEs. In response to the problems faced by FD models, there has been an increase in the use of FV schemes for solving these equations. Such approaches have benefited from improved stability, and the inherent capability of FV schemes to capture shocks makes them well suited to modelling wave breaking and bore-like propagation.

Unfortunately, the benefits of FV schemes are somewhat outweighed by the complexities of expressing higher-order terms present in BTEs in a straightforward manner. As this task can be achieved relatively easily with an FD scheme, it is logical to combine the two methods in order to exploit the stability and flexibility offered by each technique. Consequently, there has been a trend in the use of this approach which has been especially apparent in BTMs, giving rise to a number of hybrid FVFD schemes solving BTEs, such as that of Tonelli and Petti (2009).

Existing FVFD BTMs adopt a more basic approach to wave breaking than that seen in previous FD RBMs. Neglecting the higher-order terms in the BTEs sees the NSWEs recovered, which conveniently possess the ability to represent the dissipation of energy seen across a bore. This intrinsic property simplifies the simulation of breaking and is adopted with the rationale that, relative to the nonlinear terms, the dispersive terms for a wave approaching breaking become progressively unimportant. This hydrostatic front approximation (HFA) has been used to replicate the effects of wave breaking in a number of BTMs, including that of Shi et al. (2012), as well as with other models, such as the RANS solver of Shirkavand and Badiei (2014). The use of an HFA breaking model

(HBM) requires that a criterion is established to determine a breaking location. It is at this point that a switch from BTEs to NSWEs is performed. By adopting the NSWEs, the propagation speed of the waves simulated by the model becomes directly proportional to the square of the total water depth. This means the velocity is greatest at the peak and smallest at the trough, causing the wave to steepen and eventually break (Svendsen, 2006).

A number of different breaking criteria have been used with HBMs. Tonelli and Petti (2010) locate the transition in governing equations according to the ratio of wave height to water depth, while Orszaghova et al. (2012) and Tissier et al. (2012) use the local free surface gradient to signify the onset of breaking. Other breaking initiation criteria include those based on the local momentum gradient (Roeber and Cheung, 2012) and the rate of change of free surface elevation (McCabe et al., 2013; Smit et al., 2013).

Like alternative, non-hydrostatic NSWE-type approaches such as the widely used model of Zijlema et al. (2011), HBMs fail to include many of the physical phenomena present during the breaking process. These schemes instead neglect dispersive terms and continue to disregard the rotationality of the flow. While the use of the NSWEs leads to the expected reduction in wave height, the bore that forms provides a less accurate prediction of the wave shape. This limits the accuracy of such models in cases involving wave reforming, where breaking terminates and reinitiates. Here, it is difficult to fully recover the dispersive effects of the BTEs once the wave is considered to have broken.

These problems can be addressed by retaining Boussinesq terms throughout the breaking process and introducing additional terms to account for the vorticity in the surface roller region. In an attempt to provide a more accurate measure of the true physics exhibited by breaking waves, the use of an RBM allows a model to encompass a more realistic depiction of the hydrodynamics. Several parameters are introduced by the new terms, offering a means to calibrate the model based on tangible quantities related to the fluid and the nature of the breaking event. This provides an opportunity for numerical models to be tuned to a range of cases according to the physical characteristics of representative waves.

By predicting the vorticity in the flow, RBM BTMs also benefit from additional information about the flow, allowing velocity data to be obtained. This allows realistic depth velocity profiles to be determined without adding significant computational demand to the original potential flow formulation. The model presented in the current study implements an RBM in an FVFD BTM, as in Tatlock et al. (2014).

Other recent attempts to include a description of rotationality within a BTM include that of Son and Lynett (2014), where additional stress terms were used to portray the turbulence within the fluid. Alternative formulations and numerical techniques, such as that used by Panda et al. (2014), also provide models that consider rotational components of the flow. Another method developed by Zhang et al. (2013) instead used a polynomial expansion without irrotational assumptions in order to achieve vertical variation in the

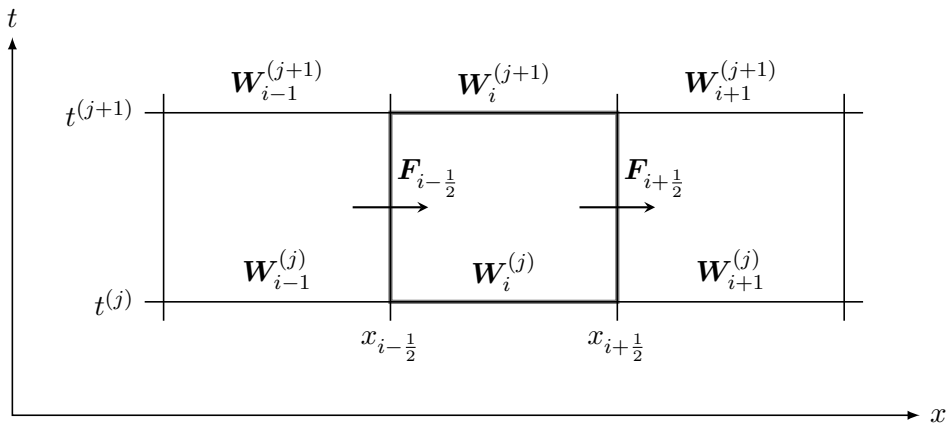

Figure 5.1: Control volume for numerical discretisation and associated variables used for the FV scheme.

horizontal velocity profile. This was later tested against surf-zone applications by Zhang et al. (2014), however the use of a more complete turbulence model was recommended.

5.2 Reformulation of governing equations

In order to construct a hybrid FVFD scheme, the governing equations must be modified. An FV numerical solver is derived by first expressing the differential form of the conservation law provided by Equation (3.60) in the integral form

$$\oint_{\mathcal{V}_i} (\boldsymbol{W}\,\mathrm{d}x + \boldsymbol{F}\,\mathrm{d}t) = \oint_{\mathcal{V}_i} \boldsymbol{S}\,\mathrm{d}x\,\mathrm{d}t, \tag{5.1}$$

where $\mathcal{V}_i$ is a control volume. The numerical grid used by the present model is established by defining the rectangular control volume illustrated in Figure 5.1, which is bounded by $x_{i-\frac{1}{2}} \leq x \leq x_{i+\frac{1}{2}}$ and $t^{(j)} \leq t \leq t^{(j+1)}$. Here, i and j are used to denote the spatial and temporal grid indices respectively. It then follows that the grid interval sizes are given by

$$\Delta x = x_{i+\frac{1}{2}} - x_{i-\frac{1}{2}} \tag{5.2}$$

and

$$\Delta t = t^{(j+1)} - t^{(j)}. \tag{5.3}$$

This allows Equation (5.1) to be written as

$$\begin{aligned}&\int_{x_{i-\frac{1}{2}}}^{x_{i+\frac{1}{2}}} \boldsymbol{W}|_{t=t^{(j+1)}} - \boldsymbol{W}|_{t=t^{(j)}}\ \mathrm{d}x + \int_{t^{(j)}}^{t^{(j+1)}} \boldsymbol{F}|_{x=x_{i+\frac{1}{2}}} - \boldsymbol{F}|_{x=x_{i-\frac{1}{2}}}\ \mathrm{d}t \\ &= \int_{t^{(j)}}^{t^{(j+1)}} \int_{x_{i-\frac{1}{2}}}^{x_{i+\frac{1}{2}}} \boldsymbol{S}\,\mathrm{d}x\,\mathrm{d}t.\end{aligned} \tag{5.4}$$

The spatial cell averages along $t^{(j)}$ and $t^{(j+1)}$ can then be expressed as

$$\boldsymbol{W}_i^{(j)} \equiv \frac{1}{\Delta x} \int_{x_{i-\frac{1}{2}}}^{x_{i+\frac{1}{2}}} \boldsymbol{W}|_{t=t^{(j)}}\ \mathrm{d}x \tag{5.5}$$

and

$$\boldsymbol{W}_i^{(j+1)} \equiv \frac{1}{\Delta x} \int_{x_{i-\frac{1}{2}}}^{x_{i+\frac{1}{2}}} \boldsymbol{W}|_{t=t^{(j+1)}} \, \mathrm{d}x, \tag{5.6}$$

respectively (LeVeque, 2002). Similarly, the cell average of the source term is given by

$$\boldsymbol{S}_i \equiv \frac{1}{\Delta x} \int_{x_{i-\frac{1}{2}}}^{x_{i+\frac{1}{2}}} \boldsymbol{S} \, \mathrm{d}x. \tag{5.7}$$

Substituting Equations (5.5) to (5.7) into Equation (5.4) and dividing by Δx then gives

$$\boldsymbol{W}_i^{(j+1)} - \boldsymbol{W}_i^{(j)} = \int_{t^{(j)}}^{t^{(j+1)}} \boldsymbol{E}_i \, \mathrm{d}t', \tag{5.8}$$

where

$$\boldsymbol{E}_i = \boldsymbol{S}_i - \frac{\boldsymbol{F}_i}{\Delta x} \tag{5.9}$$

and

$$\boldsymbol{F}_i = \boldsymbol{F}|_{x=x_{i+\frac{1}{2}}} - \boldsymbol{F}|_{x=x_{i-\frac{1}{2}}} . \tag{5.10}$$

5.3 Linear multistep method

The integral in Equation (5.8) can be evaluated by constructing a polynomial interpolation from previous values of $\boldsymbol{E}_i$. The quadratic interpolation detailed in Appendix C.6 allows the integration to be performed on a fixed grid using the values from the previous three timesteps:

$$\begin{aligned} \int_t^{t+\Delta t} \boldsymbol{E} \, \mathrm{d}t' = \int_t^{t+\Delta t} \Bigg[& \frac{t'^2 - (t - \Delta t + t - 2\Delta t)\, t' + (t - \Delta t)\,(t - 2\Delta t)}{2\Delta t^2} \boldsymbol{E}^{(j)} \\ & - \frac{t'^2 - (t + t - 2\Delta t)\, t' + t\,(t - 2\Delta t)}{\Delta t^2} \boldsymbol{E}^{(j-1)} \\ & + \frac{t'^2 - (t + t - \Delta t)\, t' + t\,(t - \Delta t)}{2\Delta t^2} \boldsymbol{E}^{(j-2)} \Bigg] \, \mathrm{d}t' \\ = \frac{\Delta t}{12} & \left(23\boldsymbol{E}^{(j)} - 16\boldsymbol{E}^{(j-1)} + 5\boldsymbol{E}^{(j-2)} \right) \end{aligned} \tag{5.11}$$

Equation (5.11) is known as the Adams-Bashforth method (Bashforth and Adams, 1883; Butcher, 2008). With an estimate for $\boldsymbol{W}$ at the next timestep, a more precise interpolation can be performed using the newly obtained predicted value and the fixed

grid cubic interpolation given in Appendix C.6:

$$\begin{aligned}\int_t^{t+\Delta t} \boldsymbol{E}\ \mathrm{d}t' = \frac{1}{6\Delta t^3}\int_t^{t+\Delta t} \Big(\Big\{ t'^3 - 3\left(t-\Delta t\right)t'^2 + \left[t\left(t-\Delta t\right) + \left(2t-\Delta t\right)\left(t-2\Delta t\right)\right]t' \\ - t\left(t-\Delta t\right)\left(t-2\Delta t\right)\Big\}\boldsymbol{E}^{(j+1)} - 3\Big\{t'^3 - \left(3t-2\Delta t\right)t'^2 \\ + \left[\left(t+\Delta t\right)\left(t-\Delta t\right) + 2t\left(t-2\Delta t\right)\right]t' - \left(t+\Delta t\right)\left(t-\Delta t\right)\left(t-2\Delta t\right)\Big\}\boldsymbol{E}^{(j)} \\ + 3\Big\{t'^3 - \left(3t-\Delta t\right)t'^2 + \left[\left(t+\Delta t\right)t + \left(2t+\Delta t\right)\left(t-2\Delta t\right)\right]t' \\ - \left(t+\Delta t\right)t\left(t-2\Delta t\right)\Big\}\boldsymbol{E}^{(j-1)} - \Big\{t'^3 - 3tt'^2 \\ + \left[\left(t+\Delta t\right)t + \left(2t+\Delta t\right)\left(t-\Delta t\right)\right]t' - \left(t+\Delta t\right)t\left(t-\Delta t\right)\Big\}\boldsymbol{E}^{(j-2)}\Big)\ \mathrm{d}t' \\ = \frac{\Delta t}{24}\left(9\boldsymbol{E}^{(j+1)} + 19\boldsymbol{E}^{(j)} - 5\boldsymbol{E}^{(j-1)} + \boldsymbol{E}^{(j-2)}\right)\end{aligned} \tag{5.12}$$

Equation (5.12) is known as the Adams-Moulton method, and together with Equation (5.11), forms the Adams-Bashforth-Moulton method used to advance the solution in time.

5.4 Predictor-corrector scheme

With Equations (5.8), (5.11) and (5.12), a time marching model is reached, whereby the solution is periodically updated according to

$$\boldsymbol{W}_i^{(j+1)} = \boldsymbol{W}_i^{(j)} + \boldsymbol{G}_i^{(j)}, \tag{5.13}$$

with

$$\boldsymbol{G}_i^{(j)} = \begin{bmatrix} \iota_i^{(j)} \\ D_i^{(j)} \end{bmatrix} = \frac{\Delta t}{12}\left(23\boldsymbol{E}^{(j)} - 16\boldsymbol{E}^{(j-1)} + 5\boldsymbol{E}^{(j-2)}\right) \tag{5.14}$$

at the predictor stage, and

$$\boldsymbol{G}_i^{(j)} = \begin{bmatrix} \iota_i^{(j)} \\ D_i^{(j)} \end{bmatrix} = \frac{\Delta t}{24}\left(9\boldsymbol{E}^{(j+1)} + 19\boldsymbol{E}^{(j)} - 5\boldsymbol{E}^{(j-1)} + \boldsymbol{E}^{(j-2)}\right) \tag{5.15}$$

at the corrector stage (Cheney and Kincaid, 2008).

At each timestep, the predictor stage is performed first, followed by the corrector stage. The corrector stage is then repeated until successive values of

$$\boldsymbol{U}_i = \begin{bmatrix} d_i \\ q_i \end{bmatrix} \tag{5.16}$$

are considered sufficiently similar, such that

$$\frac{\sum_{i=1}^{N}\left|\boldsymbol{U}_i^{(j+1)}-\acute{\boldsymbol{U}}_i^{(j+1)}\right|}{\sum_{i=1}^{N}\left|\boldsymbol{U}_i^{(j+1)}\right|}<10^{-3}, \tag{5.17}$$

where $\acute{\boldsymbol{U}}_i^{(j+1)}$ is the value of $\boldsymbol{U}_i^{(j+1)}$ obtained from the previous iteration of the corrector stage.

5.5 Tridiagonal algorithm

At each timestep, d can be incrementally updated using Equation (5.13), but further treatment is required for the solution of q. In order to solve Equation (3.61) numerically, the second term in the vector $\boldsymbol{W}$ can be expressed in terms of the conserved variable, q, providing a new term,

$$U_i=q_i-\frac{h_i}{3}\left(\frac{\partial h}{\partial x}\right)_i\left(\frac{\partial q}{\partial x}\right)_i+\left(B-\frac{1}{3}\right)h_i^2\left(\frac{\partial^2 q}{\partial x^2}\right)_i. \tag{5.18}$$

Several numerical derivatives are treated using the FD approach described in Appendix C.7, which provides estimates of first and second order differentials according to

$$\left(\frac{\partial f}{\partial X}\right)_1=\frac{f_2-f_0}{2\Delta X} \tag{5.19}$$

and

$$\left(\frac{\partial^2 f}{\partial X^2}\right)_1=\frac{f_2-2f_1+f_0}{\Delta X^2}, \tag{5.20}$$

respectively. With Equations (5.19) and (5.20), the numerical approximations of the derivatives of the flow rate in Equation (5.18) can be expressed as

$$\left(\frac{\partial q}{\partial x}\right)_i=\frac{q_{i+1}-q_{i-1}}{2\Delta x} \tag{5.21}$$

and

$$\left(\frac{\partial^2 q}{\partial x^2}\right)_i=\frac{q_{i-1}-2q_i+q_{i+1}}{\Delta x^2}. \tag{5.22}$$

Equations (5.18), (5.21) and (5.22) then give

$$U_i^{(j)}=I_iq_{i-1}^{(j)}+J_iq_i^{(j)}+K_iq_{i+1}^{(j)}, \tag{5.23}$$

where

$$I_i=a_i+b_i, \tag{5.24}$$

$$J_i=1-2b_i, \tag{5.25}$$

$$K_i = b_i - a_i, \tag{5.26}$$

$$a_i = \frac{h_i}{6\Delta x}\left(\frac{\partial h}{\partial x}\right)_i \tag{5.27}$$

and

$$b_i = \left(B - \frac{1}{3}\right)\left(\frac{h_i}{\Delta x}\right)^2. \tag{5.28}$$

With Equations (5.13) to (5.15) and (5.23), the following relation is obtained:

$$I_i q_{i-1}^{(j+1)} + J_i q_i^{(j+1)} + K_i q_{i+1}^{(j+1)} = I_i q_{i-1}^{(j)} + J_i q_i^{(j)} + K_i q_{i+1}^{(j)} + D_i^{(j)} \tag{5.29}$$

It is then possible to update the value of q at each timestep using a tridiagonal algorithm (Press et al., 1992). In order to improve computational efficiency, Equations (5.24) to (5.28) can be used to precompute the following terms once at the start of the simulation:

$$P_i = \frac{K_i}{S_i} \tag{5.30}$$

$$S_i = \begin{cases} J_1 & i = 1 \\ J_i - I_i P_{i-1} & i = 2, \ldots, N \end{cases} \tag{5.31}$$

The flow rate is then updated using the following system of equations:

$$q_i^{(j+1)} = \begin{cases} Q_i^{(j)} - P_i q_{i+1}^{(j+1)} & i = 1, \ldots, N-1 \\ Q_i^{(j)} & i = N \end{cases} \tag{5.32}$$

$$Q_i^{(j)} = \frac{1}{S_i}\begin{cases} D_1^{(j)} & i = 1 \\ D_i^{(j)} - I_i q_{i-1}^{(j)} & i = 2, \ldots, N \end{cases} \tag{5.33}$$

It is worth mentioning the limitations imposed by the tridiagonal algorithm, which is unable to the solve the FNBs in the form used for the present study. Equation (5.23) requires the time derivative in the momentum equation to be expressed using coefficients of q at three consecutive cells. As q is the only time dependent term in the momentum part of Equation (3.61), a solution to the WNBs can be obtained in this fashion. As shown in Appendix A.5, time derivatives involving d can be separated into their constituent parts to provide a portion involving h, which is independent of time, and a higher-order component involving ζ, which can be disregarded. When retaining fully-nonlinear terms, the second part of this division can no longer be neglected. Consequently, it is not possible to extend the model to use the FNBs unless significant changes to the numerical scheme are made. This limitation also applies to other similar formulations for FVFD schemes, such as those used by Roeber et al. (2010), Tonelli and Petti (2010) and Kazolea and Delis (2013). In response to this, Donahue et al. (2015) considered a formulation in terms of the pressure in order to represent higher-order dispersive terms, thereby overcoming the complexities otherwise introduced with the inclusion of both spatial and temporal derivatives.

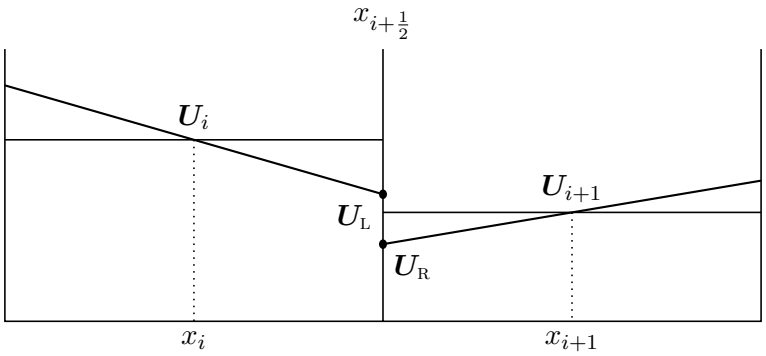

Figure 5.2: Local linear MUSCL reconstruction at $x_{i+\frac{1}{2}}$.

5.6 Finite-volume scheme

The present model employs the HLL Riemann solver proposed by Harten et al. (1983) to determine the intercell fluxes required by Equation (5.10). The free surface profile and flow rate are defined by

$$\boldsymbol{H}_i = \begin{bmatrix} \zeta_i \\ q_i \end{bmatrix} \tag{5.34}$$

at each cell in the domain. The slope between consecutive values of this quantity is then used to determine the flux between adjacent cells.

5.6.1 Riemann problem construction

The reconstruction of $\boldsymbol{U}$ is performed using a monotone upstream-centred scheme for conservation laws (MUSCL) (Leer, 1977; 1984) at each cell boundary according to

$$\boldsymbol{U}_{i\pm\frac{1}{2}} = \boldsymbol{U}_i + \frac{x_{i\pm\frac{1}{2}} - x_i}{\Delta x} \Delta \grave{\boldsymbol{H}}_i, \tag{5.35}$$

where $\Delta \grave{\boldsymbol{H}}$ denotes the cell slope. This allows boundary extrapolated values to be obtained for each cell, as shown in Figure 5.2. Equation (5.35) gives the local reconstruction values of $\boldsymbol{U}$ to the left and right of the cell boundary at $x_{i+\frac{1}{2}}$ as

$$\boldsymbol{U}_{\mathrm{L}} = \begin{bmatrix} d_{\mathrm{L}} \\ q_{\mathrm{L}} \end{bmatrix} = \boldsymbol{U}_i + \frac{1}{2} \Delta \grave{\boldsymbol{H}}_i \tag{5.36}$$

and

$$\boldsymbol{U}_{\mathrm{R}} = \begin{bmatrix} d_{\mathrm{R}} \\ q_{\mathrm{R}} \end{bmatrix} = \boldsymbol{U}_{i+1} - \frac{1}{2} \Delta \grave{\boldsymbol{H}}_{i+1}, \tag{5.37}$$

respectively. The slopes at each cell, $\Delta \grave{\boldsymbol{H}}$, allow the construction of boundary values, from which a Riemann problem is formed at each cell interface.

The high-order nature of this scheme can introduce unwanted numerical oscillations into the system. As a reduction in total entropy is expected with time, a total variation diminishing (TVD) scheme can be employed by applying the following restriction to the solution (Harten et al., 1983):

$$\sum_{i=2}^{N} \left| \boldsymbol{H}_i^{(j+1)} - \boldsymbol{H}_{i-1}^{(j+1)} \right| \leqq \sum_{i=2}^{N} \left| \boldsymbol{H}_i^{(j)} - \boldsymbol{H}_{i-1}^{(j)} \right| \tag{5.38}$$

To ensure TVD conditions are met, a third-order slope limiter, ϕ_3, can be applied. A TVD central-difference scheme can then be considered with

$$\Delta \grave{\boldsymbol{H}}_i = \phi_3 \left(\Delta^* \boldsymbol{H}_{i+\frac{1}{2}}, \Delta^* \boldsymbol{H}_{i-\frac{1}{2}} \right). \tag{5.39}$$

Here, $\Delta^* \boldsymbol{H}$ denotes the slope at each cell interface. The corresponding upwind-difference scheme is given by

$$\Delta \grave{\boldsymbol{H}}_i = \phi_3 \left(\Delta^* \boldsymbol{H}_{i-\frac{1}{2}}, \Delta^* \boldsymbol{H}_{i+\frac{1}{2}} \right). \tag{5.40}$$

In the present model, the slope at each cell is determined with the fourth-order compact MUSCL-TVD (FOCMT) scheme of Yamamoto and Daiguji (1993), where a linear combination of Equations (5.39) and (5.40) can be expressed as

$$\Delta \grave{\boldsymbol{H}}_i = \frac{1-\kappa}{2} \phi_3 \left(\Delta^* \boldsymbol{H}_{i-\frac{1}{2}}, \Delta^* \boldsymbol{H}_{i+\frac{1}{2}} \right) + \frac{1+\kappa}{2} \phi_3 \left(\Delta^* \boldsymbol{H}_{i+\frac{1}{2}}, \Delta^* \boldsymbol{H}_{i-\frac{1}{2}} \right), \tag{5.41}$$

which, with $\kappa = \frac{1}{3}$, is equivalent to the scheme used by Yamamoto et al. (1998). Equation (5.41) reduces to the central-difference scheme when $\kappa = 1$ and the upwind-difference scheme when $\kappa = -1$. By restricting the choice of ϕ_3 to only symmetric limiters, such that

$$\phi_3 (X, Y) \equiv \phi_3 (Y, X), \tag{5.42}$$

Equation (5.41) can be written more simply as

$$\Delta \grave{\boldsymbol{H}}_i = \phi_3 \left(\Delta^* \boldsymbol{H}_{i-\frac{1}{2}}, \Delta^* \boldsymbol{H}_{i+\frac{1}{2}} \right). \tag{5.43}$$

Erduran et al. (2005) suggest the use of the van-Leer limiter, $\phi_3 = \phi_\mathrm{v}$, with the FOCMT scheme to satisfy TVD requirements:

$$\phi_\mathrm{v} (X, Y) = \begin{cases} \dfrac{2XY}{X+Y} & XY > 0 \\ 0 & XY \leq 0 \end{cases} \tag{5.44}$$

Figure 5.3 shows the van-Leer limiter along with the region within which a function must be confined in order to meet the TVD requirements.

Alternatively, the third-order minmod limiter illustrated in Figure 5.4 can be implemented with

$$\phi_\mathrm{m} (X, Y) = \operatorname{sgn}(X) \max \{0, \min [|X|, Y \operatorname{sgn}(X)]\}. \tag{5.45}$$

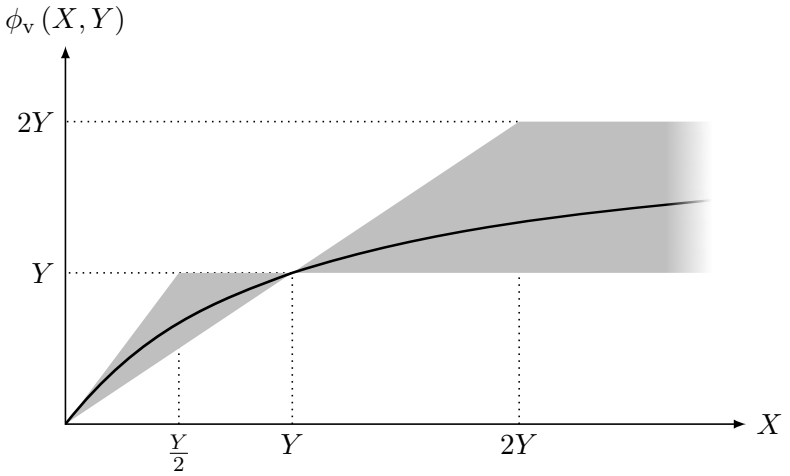

Figure 5.3: Van-Leer limiter described by Equation (5.44) (——) within TVD region (●).

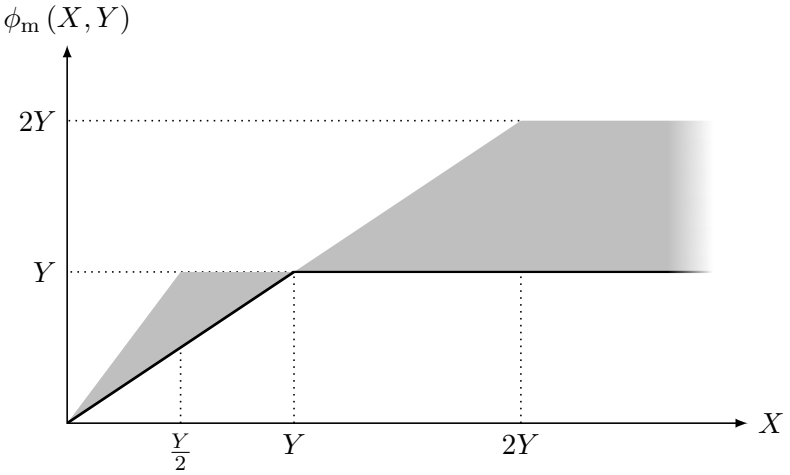

Figure 5.4: Third-order minmod limiter described by Equation (5.44) (——) within TVD region (●).

The Taylor series expansions at x_i and x_{i+1} about $x_{i+\frac{1}{2}}$ provide the following relations:

$$\begin{aligned}\boldsymbol{H}_i = \boldsymbol{H}_{i+\frac{1}{2}} &- \frac{\Delta x}{2}\left(\frac{\partial \boldsymbol{H}}{\partial x}\right)_{i+\frac{1}{2}} + \frac{\Delta x^2}{8}\left(\frac{\partial^2 \boldsymbol{H}}{\partial x^2}\right)_{i+\frac{1}{2}} \\ &- \frac{\Delta x^3}{48}\left(\frac{\partial^3 \boldsymbol{H}}{\partial x^3}\right)_{i+\frac{1}{2}} + \frac{\Delta x^4}{384}\left(\frac{\partial^4 \boldsymbol{H}}{\partial x^4}\right)_{i+\frac{1}{2}} + \mathcal{O}\left(\Delta x^5\right)\end{aligned} \tag{5.46}$$

$$\begin{aligned}\boldsymbol{H}_{i+1} = \boldsymbol{H}_{i+\frac{1}{2}} &+ \frac{\Delta x}{2}\left(\frac{\partial \boldsymbol{H}}{\partial x}\right)_{i+\frac{1}{2}} + \frac{\Delta x^2}{8}\left(\frac{\partial^2 \boldsymbol{H}}{\partial x^2}\right)_{i+\frac{1}{2}} \\ &+ \frac{\Delta x^3}{48}\left(\frac{\partial^3 \boldsymbol{H}}{\partial x^3}\right)_{i+\frac{1}{2}} + \frac{\Delta x^4}{384}\left(\frac{\partial^4 \boldsymbol{H}}{\partial x^4}\right)_{i+\frac{1}{2}} + \mathcal{O}\left(\Delta x^5\right)\end{aligned} \tag{5.47}$$

Subtracting Equation (5.46) from Equation (5.47) and rearranging gives

$$\left(\frac{\partial \boldsymbol{H}}{\partial x}\right)_{i+\frac{1}{2}} = \frac{\boldsymbol{H}_{i+1} - \boldsymbol{H}_i}{\Delta x} - \frac{\Delta x^2}{24}\left(\frac{\partial^3 \boldsymbol{H}}{\partial x^3}\right)_{i+\frac{1}{2}} + \mathcal{O}\left(\Delta x^4\right). \tag{5.48}$$

With Equation (5.20), the third spatial derivative of $\boldsymbol{H}$ at the cell interface can be approximated as

$$\left(\frac{\partial^3 \boldsymbol{H}}{\partial x^3}\right)_{i+\frac{1}{2}} = \frac{4}{\Delta x^2}\left[\left(\frac{\partial \boldsymbol{H}}{\partial x}\right)_{i-\frac{1}{2}} - 2\left(\frac{\partial \boldsymbol{H}}{\partial x}\right)_{i+\frac{1}{2}} + \left(\frac{\partial \boldsymbol{H}}{\partial x}\right)_{i+\frac{3}{2}}\right]. \tag{5.49}$$

The intercell jump,

$$\Delta \boldsymbol{H}_{i+\frac{1}{2}} \equiv \boldsymbol{H}_{i+1} - \boldsymbol{H}_i, \tag{5.50}$$

represents the first-order part of Equation (5.48), allowing Equation (5.49) to be written in the form

$$\left(\frac{\partial^3 \boldsymbol{H}}{\partial x^3}\right)_{i+\frac{1}{2}} = \frac{4\Delta \boldsymbol{H}_{i-\frac{1}{2}} - 8\Delta \boldsymbol{H}_{i+\frac{1}{2}} + 4\Delta \boldsymbol{H}_{i+\frac{3}{2}}}{\Delta x^3}. \tag{5.51}$$

A fourth-order limiter, ϕ_4, is employed for the numerical solution of Equation (5.51), which with Equations (5.48) and (5.50), then provides an expression for the slopes at each cell boundary:

$$\begin{aligned}\Delta^* \boldsymbol{H}_{i+\frac{1}{2}} = \Delta \boldsymbol{H}_{i+\frac{1}{2}} &- \frac{1}{6}\Big[\phi_4\left(\Delta \boldsymbol{H}_{i-\frac{1}{2}}, \Delta \boldsymbol{H}_{i+\frac{1}{2}}, \Delta \boldsymbol{H}_{i+\frac{3}{2}}\right) \\ &- 2\phi_4\left(\Delta \boldsymbol{H}_{i+\frac{1}{2}}, \Delta \boldsymbol{H}_{i+\frac{3}{2}}, \Delta \boldsymbol{H}_{i-\frac{1}{2}}\right) + \phi_4\left(\Delta \boldsymbol{H}_{i+\frac{3}{2}}, \Delta \boldsymbol{H}_{i-\frac{1}{2}}, \Delta \boldsymbol{H}_{i+\frac{1}{2}}\right)\Big]\end{aligned} \tag{5.52}$$

The following minmod limiter is used for the fourth-order limiter, $\phi_4 = \phi_{\mathrm{M}}$, and is selected for all cases presented here:

$$\phi_{\mathrm{M}}(X, Y, Z) = \operatorname{sgn}(X) \max\left\{0, \min\left[|X|, Y \operatorname{sgn}(X), Z \operatorname{sgn}(X)\right]\right\} \tag{5.53}$$

A visual representation of Equation (5.53) is presented in Figure 5.5.

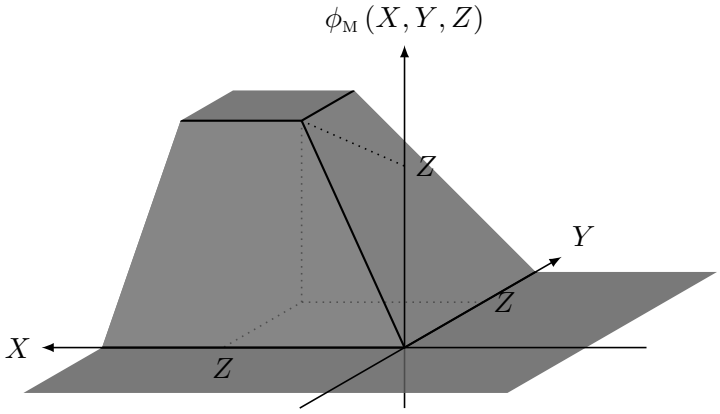

Figure 5.5: Fourth-order minmod limiter described by Equation (5.53).

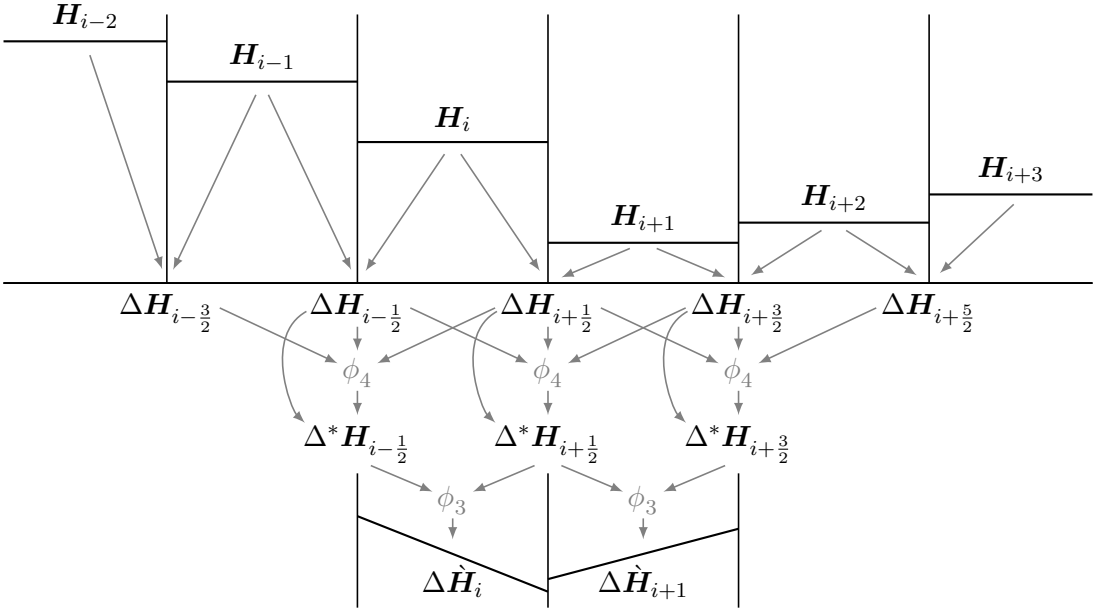

Figure 5.6: Construction of FOCMT slopes at cells i and $i+1$.

Equations (5·36), (5·37), (5·43), (5·44), (5·52) and (5·53) together provide the FOCMT scheme used by the present model. By exploiting the symmetric nature of the van-Leer limiter, the form of Equation (5·43) is more straightforward than that used by Erduran et al. (2005), but mathematically identical. Figure 5.6 provides a schematic summary of the construction of each cell slope based on the values of $\boldsymbol{U}$ at the surrounding cells.

It is worth noting that a third-order scheme can be recovered by using

$$\phi_4 = 0. \tag{5·54}$$

A further reduction to a second-order scheme is possible through appropriate selection of the third-order limiter in conjunction with Equation (5·54). With

$$\phi_3 (X, Y) = Y, \tag{5·55}$$

the influence of both limiters is removed and the scheme becomes equivalent to the Beam-Warming method. Similarly,

$$\phi_3 (X, Y) = X, \tag{5·56}$$

equates to the Lax-Wendroff method. Finally, a Fromm scheme is recovered with

$$\phi_3 (X, Y) = \frac{X + Y}{2}. \tag{5·57}$$

5.6.2 Riemann solution

As they are responsible for a large proportion of computational effort when solving a system of equations, the demand of the iterative procedure adopted by exact Riemann solvers becomes significant. In many cases, the resulting gains in accuracy do not justify the additional execution time. Approximate Riemann solvers look to strike a balance between precision and computational cost and provide a process whereby a solution to the Riemann problem is obtained without iterations. The HLL Riemann solver used here provides one such approach, and maintains a robust numerical scheme that is able to adapt to a range of scenarios that may be encountered.

The Riemann problem constructed by the FOCMT scheme considers the two initial value problems observed in Figures 5.7a and 5.8a. The resulting characteristics seen in Figures 5.7b and 5.8b define paths along which the solution is constant, and then provide the compressive case shown in Figure 5.7c or the expansive case in Figure 5.8c (LeVeque, 2002; Toro, 2009). As illustrated in Figure 5.9, one of three solutions is then considered based on the relative values on either side of the cell boundary. The solution provides left and right wave speeds, S_{L} and S_{R}, which are considered for a number of possible permutations shown in Figures 5.10 and 5.11. By assessing wet and dry cases, the solver is inherently able to handle treatment of a shoreline.

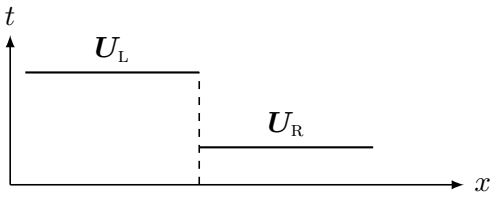

(a) Discontinuous initial data.

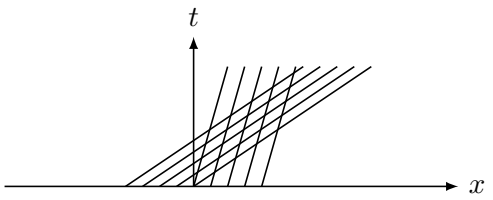

(b) Characteristics.

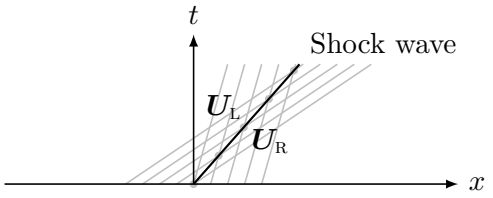

(c) x-t plane solution.

Figure 5.7: Compressive Riemann problem (Toro, 2009).

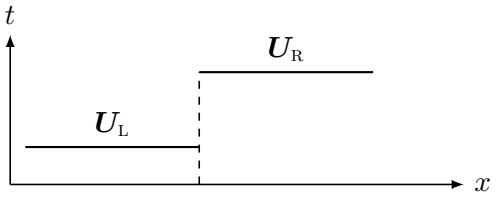

(a) Discontinuous initial data.

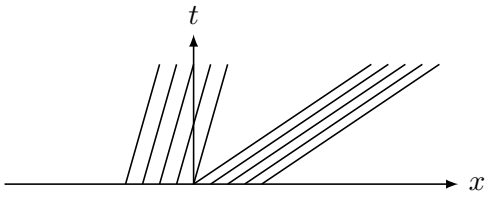

(b) Characteristics.

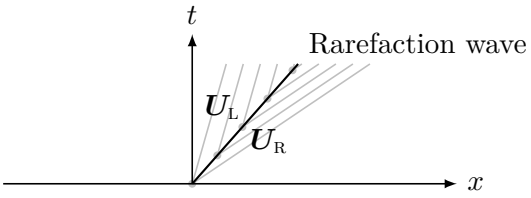

(c) x-t plane solution.

Figure 5.8: Expansive Riemann problem (Toro, 2009).

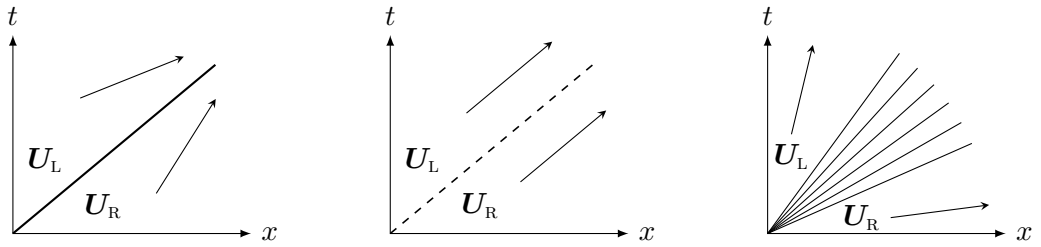

(a) Shock wave. **(b)** Contact wave. **(c)** Rarefaction wave.

Figure 5.9: Wave solutions of the Riemann problem.

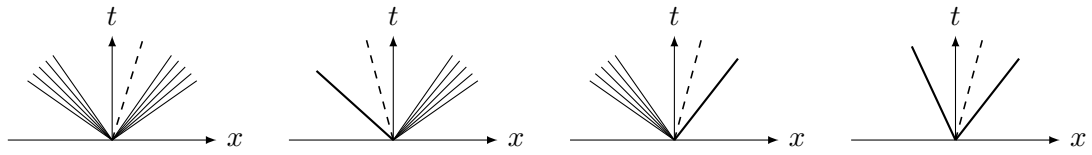

(a) Rarefaction-rarefaction. **(b)** Shock-rarefaction. **(c)** Rarefaction-shock. **(d)** Shock-shock.

Figure 5.10: Riemann solutions for wet bed cases: possible combinations of rarefaction (——), contact(- - - -) and shock (——) discontinuities (Toro, 2009).

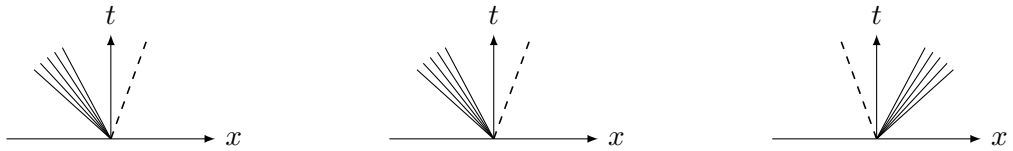

(a) Dry bed on right. **(b)** Dry bed in centre. **(c)** Dry bed on left.

Figure 5.11: Riemann solutions for dry bed cases: possible combinations of rarefaction (——) and contact (- - - -) discontinuities (Toro, 2001; 2009).

The flux in each cell is calculated from Equation (3.62), giving the following expressions:

$$\boldsymbol{F}_{\mathrm{L}} = \begin{bmatrix} q_{\mathrm{L}} \\ \dfrac{q_{\mathrm{L}}^2}{d_{\mathrm{L}}} + \dfrac{g d_{\mathrm{L}}^2}{2} \end{bmatrix} \tag{5.58}$$

$$\boldsymbol{F}_{\mathrm{R}} = \begin{bmatrix} q_{\mathrm{R}} \\ \dfrac{q_{\mathrm{R}}^2}{d_{\mathrm{R}}} + \dfrac{g d_{\mathrm{R}}^2}{2} \end{bmatrix} \tag{5.59}$$

The HLL Riemann solver considers a third state, $\boldsymbol{U}_{\mathrm{H}}$, situated between left and right shocks. The corresponding flux in this region is denoted by $\boldsymbol{F}_{\mathrm{H}}$. Applying the Rankine-Hugoniot conditions from this region and the left and right shocks gives

$$\boldsymbol{F}_{\mathrm{H}} - \boldsymbol{F}_{\mathrm{L}} = S_{\mathrm{L}} \left(\boldsymbol{U}_{\mathrm{H}} - \boldsymbol{U}_{\mathrm{L}} \right) \tag{5.60}$$

and

$$\boldsymbol{F}_{\mathrm{H}} - \boldsymbol{F}_{\mathrm{R}} = S_{\mathrm{R}} \left(\boldsymbol{U}_{\mathrm{H}} - \boldsymbol{U}_{\mathrm{R}} \right), \tag{5.61}$$

respectively. Equations (5.60) and (5.61) together provide the following:

$$\boldsymbol{F}_{\mathrm{H}} = \frac{S_{\mathrm{R}} \boldsymbol{F}_{\mathrm{L}} - S_{\mathrm{L}} \boldsymbol{F}_{\mathrm{R}} + S_{\mathrm{L}} S_{\mathrm{R}} \left(\boldsymbol{U}_{\mathrm{R}} - \boldsymbol{U}_{\mathrm{L}} \right)}{S_{\mathrm{R}} - S_{\mathrm{L}}} \tag{5.62}$$

The intercell flux for the HLL Riemann solver is therefore calculated as

$$\boldsymbol{F}|_{x=x_{i+\frac{1}{2}}} = \begin{cases} \boldsymbol{F}_{\mathrm{L}} & 0 \leq S_{\mathrm{L}} \\ \dfrac{S_{\mathrm{R}} \boldsymbol{F}_{\mathrm{L}} - S_{\mathrm{L}} \boldsymbol{F}_{\mathrm{R}} + S_{\mathrm{L}} S_{\mathrm{R}} \left(\boldsymbol{U}_{\mathrm{R}} - \boldsymbol{U}_{\mathrm{L}} \right)}{S_{\mathrm{R}} - S_{\mathrm{L}}} & S_{\mathrm{L}} < 0 < S_{\mathrm{R}} \\ \boldsymbol{F}_{\mathrm{R}} & 0 \geq S_{\mathrm{R}}. \end{cases} \tag{5.63}$$

Toro (2001) states that experience suggests an accurate and robust scheme is achieved using the following estimate of the left and right wave speeds:

$$S_{\mathrm{L}} = \begin{cases} \dfrac{q_{\mathrm{L}}}{d_{\mathrm{L}}} - \sqrt{\dfrac{\left(d_* + d_{\mathrm{L}} \right) g d_*}{2 d_{\mathrm{L}}}} & d_* > d_{\mathrm{L}} \\ \dfrac{q_{\mathrm{L}}}{d_{\mathrm{L}}} - \sqrt{g d_{\mathrm{L}}} & d_* \leq d_{\mathrm{L}} \end{cases} \tag{5.64}$$

$$S_{\mathrm{R}} = \begin{cases} \dfrac{q_{\mathrm{L}}}{d_{\mathrm{L}}} + \sqrt{\dfrac{\left(d_* + d_{\mathrm{R}} \right) g d_*}{2 d_{\mathrm{R}}}} & d_* > d_{\mathrm{R}} \\ \dfrac{q_{\mathrm{R}}}{d_{\mathrm{R}}} + \sqrt{g d_{\mathrm{R}}} & d_* \leq d_{\mathrm{R}} \end{cases} \tag{5.65}$$

$$d_* = \frac{1}{4g} \left(\sqrt{g d_{\mathrm{L}}} + \sqrt{g d_{\mathrm{R}}} + \frac{q_{\mathrm{L}}}{2 d_{\mathrm{L}}} - \frac{q_{\mathrm{R}}}{2 d_{\mathrm{R}}} \right)^2 \tag{5.66}$$

5.7 Courant number

For numerical stability to be maintained, it is important to consider the wave speed in each cell. The Courant number, as discussed by Courant et al. (1928), defines the ratio of the maximum wave propagation speed to the grid speed, with the purpose of selecting an appropriate resolution for spatial and temporal discretisation. Under the assumption of a constant solution along the intercell boundary, the distance travelled by a wave in a given time, Δt, can be calculated. The maximum wave speed, S_m, is then used to calculate the Courant number for a given timestep according to the following relation:

$$\mathcal{C} = S_\mathrm{m} \frac{\Delta t}{\Delta x} \tag{5.67}$$

In order to prevent the path of any wave extending beyond the bounds of a cell, it must be ensured that

$$0 \leq \mathcal{C} \leq 1. \tag{5.68}$$

Although more sophisticated schemes can be developed to accurately determine S_m, the simple and effective approach adopted here uses the maximum velocity calculated at the previous timestep as a representative value of the wave speed for the succeeding timestep. In reality, variations in the solution along the intercell boundary must be accounted for, and an increase in the maximum velocity within the domain allowed for. A maximum permissible value of the Courant number must therefore be defined such that the value remains below one, and numerical stability is maintained (LeVeque, 2002; Toro, 2009).

While the maximum Courant number must be limited, it is also important that immoderately small values are also avoided, as they can introduce oscillations where derivatives in time exist. Additionally, the computation time is enlarged as the Courant number is reduced. The value of Δt chosen for numerical simulations must therefore be carefully considered and should be selected to complement the chosen spatial resolution. In some cases, this choice can be automated and adapt dynamically by updating Δt at each timestep based on a chosen Courant number coefficient.

5.8 Roller crest and toe interpolation

Since the scheme locates the crest and toe at the nearest cell centre, oscillations in the numerical length of the roller can emerge from propagating waves. In turn, this can cause undesirable disturbances in the injected vorticity, and therefore needs to be addressed by locating the bounds of the roller more precisely. Improvements in the calculation of ω_s and ζ_e are achieved by using the quadratic Lagrange polynomial interpolation described in Appendix C.6, which produces a smoother temporal evolution in the length of the roller. First, the following expression for the derivative of a function, f, with respect to x is obtained from the cubic interpolation formula:

$$\frac{\partial f}{\partial x} = \frac{2x - x_1 - x_2}{2\Delta x^2} f|_{x=x_0} - \frac{2x - x_0 - x_2}{\Delta x^2} f|_{x=x_1} + \frac{2x - x_0 - x_1}{2\Delta x^2} f|_{x=x_2} \tag{5.69}$$

Equation (5.69) can then be rearranged and written as

$$x = \frac{2\Delta x^2 \frac{\partial f}{\partial x} + f|_{x=x_0}(x_1 + x_2) - 2\, f|_{x=x_1}(x_0 + x_2) + f|_{x=x_2}(x_0 + x_1)}{2\, f|_{x=x_0} - 4\, f|_{x=x_1} + 2\, f|_{x=x_2}}, \quad (5.70)$$

which, since $x_1 = x_0 + \Delta x = x_2 - \Delta x$, becomes

$$x = x_1 + \Delta x \frac{2\Delta x \frac{\partial f}{\partial x} + f|_{x=x_0} - f|_{x=x_2}}{2\, f|_{x=x_0} - 4\, f|_{x=x_1} + 2\, f|_{x=x_2}}. \quad (5.71)$$

Since the crest and toe are located where $\frac{\partial \zeta}{\partial x} = 0$ and $\frac{\partial \zeta}{\partial x} = \tan\theta$, the corresponding interpolated locations are then found to be at

$$x_{\mathrm{C}} = x_{\mathrm{c}} + \Delta x \frac{\zeta|_{x=x_{\mathrm{c}}-\Delta x} - \zeta|_{x=x_{\mathrm{c}}+\Delta x}}{2\,\zeta|_{x=x_{\mathrm{c}}-\Delta x} - 4\,\zeta|_{x=x_{\mathrm{c}}} + 2\,\zeta|_{x=x_{\mathrm{c}}+\Delta x}} \quad (5.72)$$

and

$$x_{\mathrm{T}} = x_{\mathrm{t}} + \Delta x \frac{2\Delta x \tan\theta + \zeta|_{x=x_{\mathrm{t}}-\Delta x} - \zeta|_{x=x_{\mathrm{t}}+\Delta x}}{2\,\zeta|_{x=x_{\mathrm{t}}-\Delta x} - 4\,\zeta|_{x=x_{\mathrm{t}}} + 2\,\zeta|_{x=x_{\mathrm{t}}+\Delta x}}, \quad (5.73)$$

respectively.

The location of the roller toe can be particularly sensitive and therefore susceptible to relatively large changes between successive timesteps. As an additional safeguard against unwanted oscillations that may subsequently arise, the necessary adjustment to the toe location is anticipated to be no greater than one cell. Accordingly, the magnitude of the component added to the toe location to obtain an interpolated value is limited to $\frac{\Delta x}{2}$.

5.9 Internal wave generation

Having assembled a scheme capable of simulating wave propagation, it is necessary to introduce a generation method in order to create waves within the domain. The present study adopts the approach used by Schäffer and Sørensen (2006), whereby an internal source function, $\Lambda\Phi$, is added to the continuity equation for the BTEs derived by Madsen and Sørensen (1992). This allows the one-dimensional form of the generation method described by Wei et al. (1999) to be used. Since all the tests presented here have a known wave period, an analytical solution is reached, providing a simple sinusoidal function. The oscillating component of the source function is then provided by

$$\Lambda = \cos\left(\frac{2\pi}{T}t\right). \quad (5.74)$$

The peak amplitude and spatial distribution of the source function can be calculated once at the start of the simulation according to

$$\Phi = \frac{A_{\mathrm{g}}}{T}\sqrt{\frac{20}{\pi}}\frac{4\pi^2 - \left(\alpha + \frac{1}{3}\right) gT^2k^4h^3}{\beta\pi^2\left[1 - \alpha\,(kh)^2\right]} \exp\left\{\frac{(\beta\pi)^2}{80} - 20\left[\frac{k\,(x - x_{\mathrm{g}})}{\beta\pi}\right]^2\right\}, \quad (5.75)$$

where β is used to control the width of the source region and A_g denotes the generation amplitude. The tests presented here adopt a value of $\alpha = -0.39$. An approximate solution to the dispersion relation,

$$\left(\frac{2\pi}{T}\right)^2 = gk\tanh\left(kh\right), \tag{5.76}$$

is used to obtain an estimate of the wavenumber, k, for the specified wave parameters (Dean and Dalrymple, 1991). Since this relationship is linear, the WNBs used here are not satisfied, but a stable solution is reached as the wave propagates onshore. For this reason, the tests presented here allow the waves to travel over a level stretch before reaching the region of interest. In the present work, this technique is only used for simulations of monochromatic waves and wave groups.

5.10 Moving shoreline

As discussed previously, the Riemann solver is inherently able to handle wet-dry interfaces. While this is sufficient for schemes simulating breaking by exploiting the similarity with bore propagation, the higher-order terms present in BTMs mean complications arise as waves propagate into shallower water (Briganti and Dodd, 2009). The Riemann solver prescribes a minimum water depth, below which cells are considered to be dry. At smaller depths cells can still be considered dry, but experience significant oscillations due to the Boussinesq terms. This can introduce irregularities into the scheme that compromise the stability of the model and produce spurious results.

As the influence of the Boussinesq terms is relatively small at shallower depths, their subsequent growth can be attributed to entirely numerical effects. Since this phenomenon is entirely non-physical, is is reasonable to neglect the higher-order Boussinesq terms near the shoreline (Bellotti and Brocchini, 2002; Lo Re et al., 2012). A second threshold water depth is therefore included in addition to the minimum water depth considered by the Riemann solver, beyond which the Boussinesq terms and breaking terms are neglected. As such, the model uses the intrinsic properties of the Riemann solver to manage the shoreline by switching to the NSWEs. This approach provides a single model that is able to simulate the physics governing the flow from deep water to the swash-zone.

5.11 Boundary conditions

The tests presented here utilise a range of boundary conditions in order to describe the flow at the limits of the domain. These conditions are introduced by considering two additional cells outside of the domain being modelled. The behaviour dictating the state of the fluid in these cells determines the conditions created at the boundaries of the numerical domain. As the wave propagation tests presented in this work include a shoreline, the right boundary conditions have no effect on the results, while the left boundary corresponds to the offshore conditions.

5.11.1 Transmissive conditions

Transmissive conditions aim to replicate fluid freely leaving or entering the domain based on the conditions in the cells by the boundary.

Left boundary

At the left boundary, transmissive conditions are defined by

$$\boldsymbol{U}_0 = \boldsymbol{b}_+ \boldsymbol{U}_1 \tag{5.77}$$

and

$$\boldsymbol{U}_{-1} = \boldsymbol{b}_- \boldsymbol{U}_2, \tag{5.78}$$

where

$$\boldsymbol{b}_+ \equiv \begin{bmatrix} 1 & 0 \\ 0 & 1 \end{bmatrix} \tag{5.79}$$

and

$$\boldsymbol{b}_- \equiv \begin{bmatrix} 1 & 0 \\ 0 & -1 \end{bmatrix}. \tag{5.80}$$

Right boundary

Transmissive conditions at the right boundary are given by

$$\boldsymbol{U}_{N+1} = \boldsymbol{b}_+ \boldsymbol{U}_N \tag{5.81}$$

and

$$\boldsymbol{U}_{N+2} = \boldsymbol{b}_+ \boldsymbol{U}_{N-1}. \tag{5.82}$$

5.11.2 Reflective conditions

Reflective boundary conditions return any outgoing signal back into the domain by matching the state of the cells outside the domain with that of the two cells nearest the boundary inside the domain.

Left boundary

At the left boundary, reflective conditions are defined according to

$$\boldsymbol{U}_0 = \boldsymbol{b}_- \boldsymbol{U}_1 \tag{5.83}$$

and

$$\boldsymbol{U}_{-1} = \boldsymbol{b}_- \boldsymbol{U}_2. \tag{5.78}$$

Right boundary

The right boundary condition is reflective when

$$\boldsymbol{U}_{N+1} = \boldsymbol{b}_{-}\boldsymbol{U}_{N} \tag{5.84}$$

and

$$\boldsymbol{U}_{N+2} = \boldsymbol{b}_{-}\boldsymbol{U}_{N-1}. \tag{5.85}$$

5.11.3 Prescribed discharge and depth

For tests requiring an imposed surface elevation or flow rate at the boundary, it is necessary to define boundary conditions capable of producing a fixed depth or constant discharge at the boundaries. In these cases, the transmissive conditions are modified, with the left and right boundaries corresponding to upstream and downstream locations, respectively. The flow rate at the left boundary is regulated using

$$\boldsymbol{U}_{0} = \begin{bmatrix} d_{\mathrm{l}} \\ q_{\mathrm{u}} \end{bmatrix} \tag{5.86}$$

and

$$\boldsymbol{U}_{-1} = \boldsymbol{b}_{-}\boldsymbol{U}_{2}, \tag{5.78}$$

while a constant depth at the right boundary is achieved with the following conditions:

$$\boldsymbol{U}_{N+1} = \begin{bmatrix} d_{\mathrm{d}} \\ q_{N} \end{bmatrix} \tag{5.87}$$

$$\boldsymbol{U}_{N+2} = \boldsymbol{b}_{+}\boldsymbol{U}_{N-1} \tag{5.82}$$

5.11.4 Absorbing boundary condition

The reflective boundary conditions described in Section 5.11.2 can be used to ensure that the total mass within the domain is conserved. A sponge layer is then required to prevent interference from reflected waves. This defines a region close to the boundary which artificially dissipates energy from the flow, thereby removing the majority of the energy before the wave reaches the boundary and preventing disturbances which would otherwise be created by the reflections. This is achieved by introducing

$$\Psi = \begin{cases} \dfrac{\Upsilon q}{\exp(1) - 1} \left\{ \exp\left[\left(\dfrac{x - x_{\mathrm{o}}}{x_{\mathrm{s}}} \right)^{2} \right] - 1 \right\} & x \leq x_{\mathrm{s}} \\ 0 & x > x_{\mathrm{s}} \end{cases} \tag{5.88}$$

into the source term, such that Equation (3.63) becomes

$$\boldsymbol{S} = \begin{bmatrix} 0 \\ gd\dfrac{\partial h}{\partial x} - Bgh^{2}\left(2\dfrac{\partial h}{\partial x}\dfrac{\partial^{2}\zeta}{\partial x^{2}} + h\dfrac{\partial^{3}\zeta}{\partial x^{3}} \right) - \chi - \Psi \end{bmatrix}. \tag{5.89}$$

Here, the length of the sponge layer is given by x_s, and the offshore boundary of the domain is located at x_o. The parameter determining the strength of the sponge layer adopts the same value of $\Upsilon = 10\,\mathrm{s}^{-1}$ for all of the tests performed in the present study. The function given by Equation (5.88) ensures that the dissipative term is introduced smoothly and removes an increasing proportion of any remaining momentum from the flow as outgoing waves get closer to the boundary. Since the sponge layer is only used here for tests including a shoreline, it is only implemented at the offshore boundary in cases involving wave generation.

5.12 Shapiro filter

The use of a numerical filter is desirable in order to address the unwanted oscillations that may arise from the high-order nature of the FD breaking terms. By smoothing out the intermediate variables, the introduction of the breaking terms into the model results in fewer instabilities. The present model uses a simple first-order Shapiro filter, which calculates the filtered value, $\dot{f}$, for a given variable, f, as follows (Shapiro, 1970):

$$\dot{f}_i = \frac{f_{i-1} + 2f_i + f_{i+1}}{4} \tag{5.90}$$

This treatment is used for the calculation of $\frac{\partial(\Delta M)}{\partial x}$, $\frac{\partial^3(\Delta P)}{\partial x^2 \partial t}$ and D_s, along with several intermediate numerical variables used in their calculation. The Shapiro filter is not used by the model in any tests that do not utilise an external breaking mechanism.

Chapter 6

Model validation

6.1 Numerical tests

In order to validate the performance of the model proposed in the present work, it is necessary to perform a range of tests and evaluate the results in each case. The predictions obtained using the numerical model described in previous chapters are compared with analytical and experimental results to provide a measure of their accuracy.

With the exception of the solitary wave case in Section 6.2.3, the velocity at the start of all tests performed here is taken as zero, thereby simplifying the initial conditions issued to the model. As a consequence of this, a longer simulation time is often required in order to allow the model to reach a stable state.

6.2 Non-breaking cases

The FV component of the model is first considered by using a number of classical tests to verify that the solver functions as expected. The model is therefore assessed without the presence of any additional dissipative terms by conducting a series of tests in which breaking is expected to be absent. As such, simulations are performed with $\chi = 0\,\mathrm{m^2\,s^{-2}}$. Exact free surface and velocity profiles for the non-breaking tests can be calculated from analytical solutions, and are presented alongside the numerical results in order to assess the performance of the model. These tests assess the ability of the model to accurately solve the NSWEs, and therefore initially only consider Equation (3.64).

For tests which do not require a regular temporal resolution, Δt can be updated at each timestep. A coefficient, $\mathcal{C}_\mathrm{n} < 1$, is used to ensure the Courant number remains sufficiently small. From Equation (5.67), the new value is then determined as

$$\Delta t = \mathcal{C}_\mathrm{n} \frac{\Delta x}{S_\mathrm{m}}, \tag{6.1}$$

where the shock speed is estimated as

$$S_{\mathrm{m}} = \max_{i\in\{1,2,\ldots,N\}} \left(|u_i| + \sqrt{g d_i} \right). \tag{6.2}$$

In order to prevent unreasonably large values of S_{m}, Equation (6.2) ignores cells with less than the minimum water depth.

6.2.1 Dam break test

The first case defines two initial depths of fluid, d_{u} and d_{d}, separated by a gate located at $x = x_0$. At $t = 0$ s, the test considers the instantaneous removal of this gate. The resulting discontinuity provides an effective means to assess the shock-capturing capabilities of the numerical scheme and ensure the model is able to replicate sharp changes in the free-surface and velocity.

Analytical solutions for the depth and velocity when $d_{\mathrm{u}} > d_{\mathrm{d}}$ are provided by (Delestre et al., 2012)

$$d = \begin{cases} d_{\mathrm{u}} & x \leq x_1 \\ \dfrac{4}{9g}\left(\sqrt{g d_{\mathrm{u}}} - \dfrac{x - x_0}{2t}\right)^2 & x_1 < x \leq x_2 \\ d_1 & x_2 < x \leq x_3 \\ d_{\mathrm{d}} & x_3 < x \end{cases} \tag{6.3}$$

and

$$u = \begin{cases} 0 & x \leq x_1 \\ \dfrac{2}{3}\left(\dfrac{x - x_0}{t} + \sqrt{g d_{\mathrm{u}}}\right) & x_1 < x \leq x_2 \\ 2\left(\sqrt{g d_{\mathrm{u}}} - \sqrt{g d_1}\right) & x_2 < x \leq x_3 \\ 0 & x_3 < x, \end{cases} \tag{6.4}$$

respectively, where

$$x_1 = x_0 - t\sqrt{g d_{\mathrm{u}}}, \tag{6.5}$$

$$x_2 = x_0 + t\left(2\sqrt{g d_{\mathrm{u}}} - 3\sqrt{g d_1}\right), \tag{6.6}$$

$$x_3 = x_0 + \frac{2 t d_1 \left(\sqrt{g d_{\mathrm{u}}} - \sqrt{g d_1}\right)}{d_1 - d_{\mathrm{d}}}, \tag{6.7}$$

and d_1 is obtained from the solution to the following cubic equation (Hervouet, 2007):

$$d_1^3 - d_1 d_{\mathrm{d}}\left(8 d_{\mathrm{u}} - 16\sqrt{d_{\mathrm{u}} d_1} + 9 d_1 + d_{\mathrm{d}}\right) + d_{\mathrm{d}}^3 = 0 \tag{6.8}$$

Simulations are performed with reflective boundary conditions at each end of the domain. The model remains stable throughout the simulation with $\mathcal{C}_{\mathrm{n}} = 0.9$. Figure 6.1

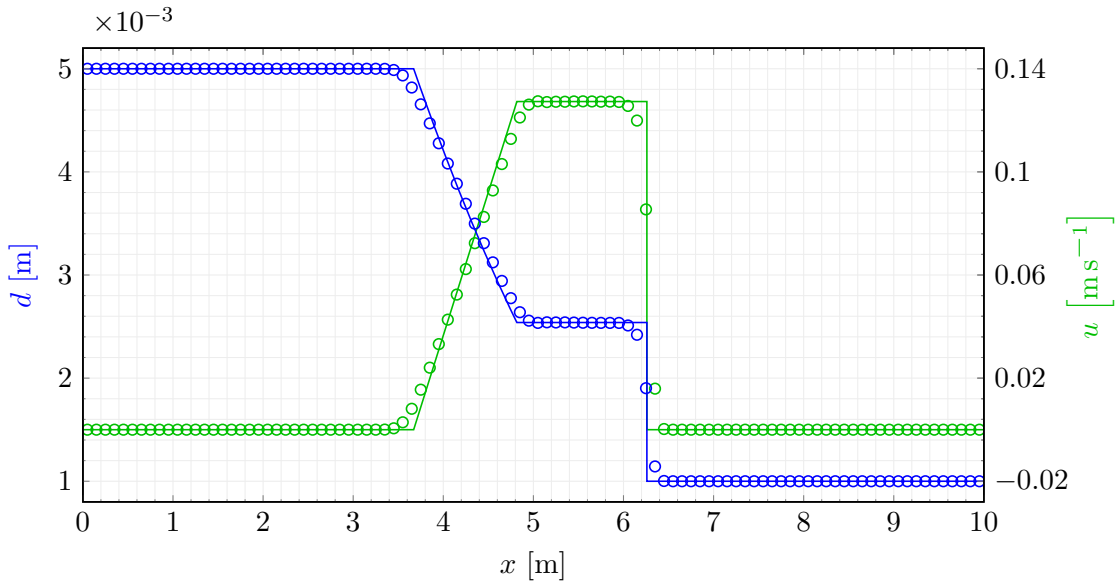

Figure 6.1: Analytical (——) and numerical (○) free surface elevation (●) and horizontal velocity (●) for dam break test.

Table 6.1: Boundary conditions for steady flow tests.

Test	d_u [m]	q_u $\left[\mathrm{m\,s^{-2}}\right]$
Subcritical flow	2	4.42
Transcritical flow without shock	0.66	1.53
Transcritical flow with shock	0.33	0.18

shows the numerical results obtained from the model along with the analytical solution at $t = 6\,\mathrm{s}$. It can be seen that the speed of the shock is accurately captured by the scheme, although some discrepancies are found where there is an abrupt change in gradient in the solution. This can be attributed to the dissipative nature of the scheme, which is known to result in a smoothing of the solution where second-order derivatives are non-zero. Despite this feature, the shock is captured well, and the dissipation shown to be acceptably small, with any appreciable effect seen over only three to four cells.

6.2.2 Steady flow tests

In order to further inspect the capabilities of the scheme, several steady flow tests are performed using the boundary conditions given in Table 6.1 and the bathymetric profile described by the following equation (Vázquez-Cendón, 1999; Zhou et al., 2001; Xing and Shu, 2005):

$$z_\mathrm{b} = \begin{cases} \dfrac{4 - (x-10)^2}{20} & 8 < x < 12 \\ 0 & \text{otherwise} \end{cases} \tag{6.9}$$

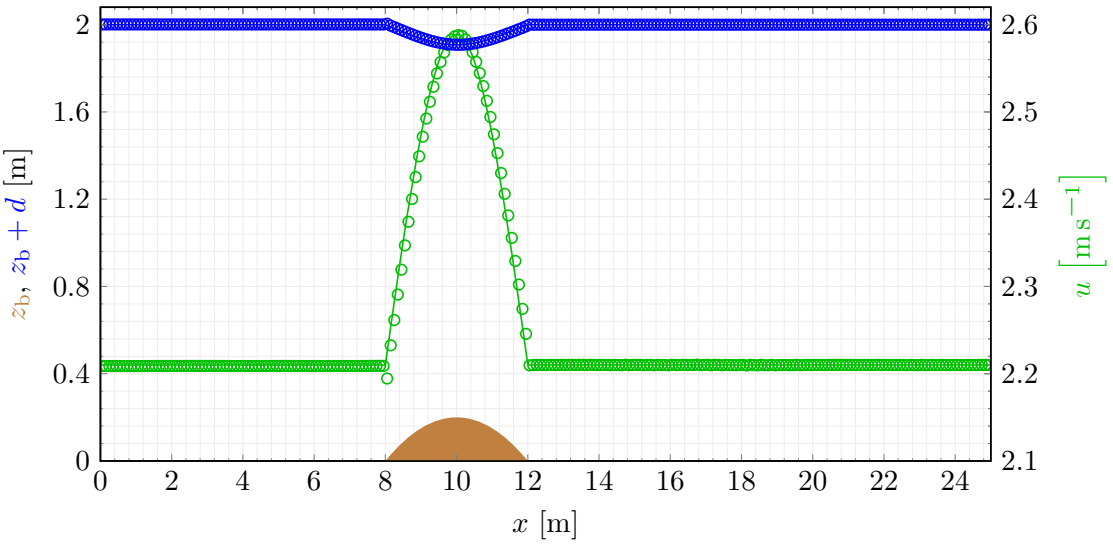

Figure 6.2: Analytical (——) and numerical (○) free surface elevation (●) and horizontal velocity (●) for subcritical flow over bathymetric perturbation (●).

Here, z_b represents the bathymetric elevation relative to that at the offshore boundary.

For all three tests, the initial free surface profile matches that imposed at the right boundary. A Courant number coefficient of $\mathcal{C}_n = 0.75$ is employed in all cases. Results are presented after an adequately long period has passed in order to ensure that the system has reached a stable state. Analytical solutions for the depth are obtained using the relations described below. By assuming the flow rate to be constant, the depth averaged velocity can then be calculated with Equation (3.9).

Subcritical flow

An analytical solution for the first steady flow test is obtained from the following equation:

$$d^3 + \left(z_b - \frac{q_u^2}{2g d_u^2} - d_u \right) d^2 + \frac{q_u^2}{2g} = 0 \tag{6.10}$$

Figure 6.2 provides a comparison between analytical and numerical solutions and shows the model to be capable of accurately predicting the free surface profile and velocity.

Transcritical flow without shock

Figure 6.3 compares the predictions obtained by the model with the analytical solution obtained from the solution to

$$d^3 + \left(z_b - \frac{q_u^2}{2g d_1^2} - d_1 - \frac{1}{5} \right) d^2 + \frac{q_u^2}{2g} = 0, \tag{6.11}$$

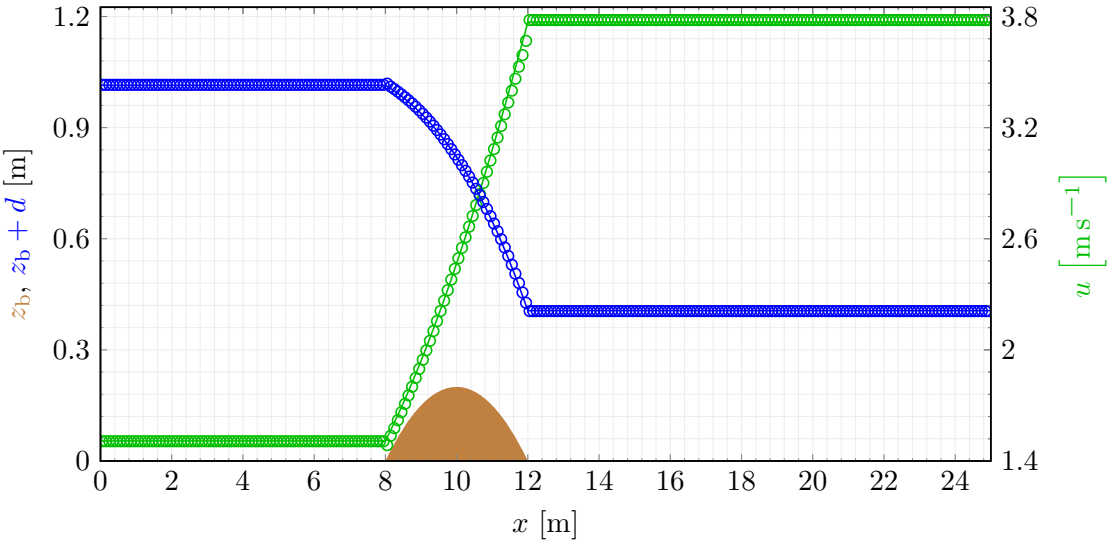

Figure 6.3: Analytical (——) and numerical (○) free surface elevation (●) and horizontal velocity (●) for transcritical flow without shock over bathymetric perturbation (●).

where d_1 denotes the depth where the bed elevation is highest. Since the flow at this point is critical, this depth can be determined as

$$d_1 = \sqrt[3]{\frac{q_u^2}{g}}. \tag{6.12}$$

The results again confirm the model to be correctly simulating the hydrodynamics, although a very small discrepancy is seen where the bathymetric gradient transitions from zero.

Transcritical flow with shock

The final steady flow case also examines the ability of the model to reproduce transcritical flow, but additionally tests the shock-capturing capabilities. For the analytical solution, the jump is located according to the Rankine-Hugoniot relation given by

$$q_u^2 \left(\frac{1}{d_2} - \frac{1}{d_3} \right) + \frac{g}{2} \left(d_2^2 - d_3^2 \right) = 0, \tag{6.13}$$

where the depths downstream and upstream of the shock, d_2 and d_3, are obtained from Equations (6.11) and (6.12) and Equation (6.10) respectively. Figure 6.4 compares the numerical results with the analytical solution, again illustrating that the model behaves well and is able to correctly locate a hydraulic jump across which the Rankine-Hugoniot conditions are satisfied. It is therefore evident that the model is able to accurately capture the complex hydrodynamic processes that are present in the steady flow tests.

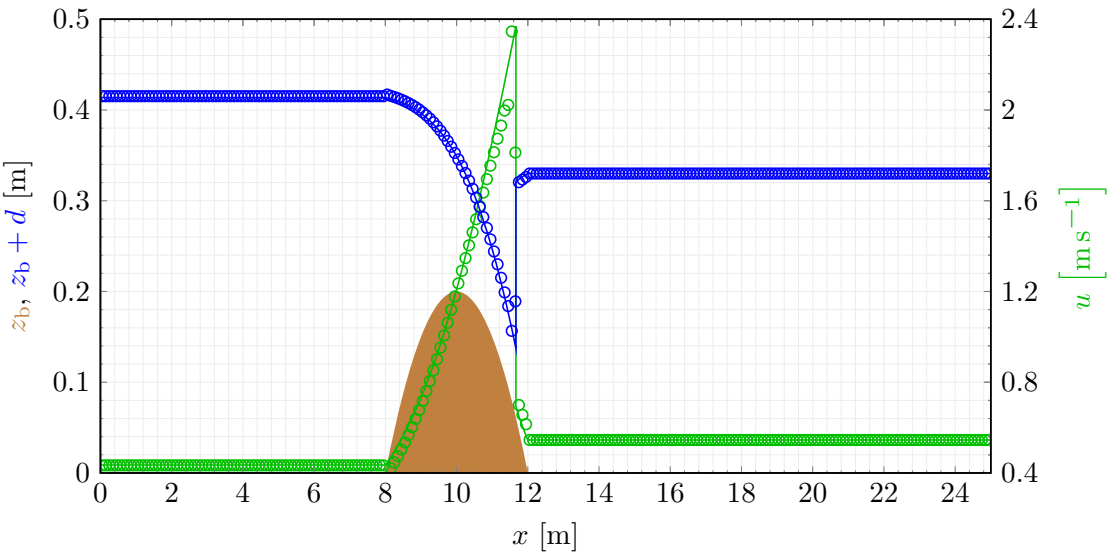

Figure 6.4: Analytical (——) and numerical (○) free surface elevation (●) and horizontal velocity (●) for transcritical flow with shock over bathymetric perturbation (●).

6.2.3 Solitary wave tests

The higher-order Boussinesq terms are assessed by repeating the solitary wave tests performed by Tonelli and Petti (2009), thereby evaluating the capabilities of the model when solving the WNBs. The free surface elevation and horizontal velocity are given as

$$\zeta = A_g \operatorname{sech}^2 \left[\sqrt{\frac{3A_g}{4h^3}} (x - x_g) \right] \tag{6.14}$$

and

$$u = \frac{C\zeta}{h}, \tag{6.15}$$

respectively, with the celerity given by

$$C = \sqrt{gh} \tag{6.16}$$

and the centre of the wave specified by x_g (Pagliara and Chiavaccini, 2005; Tonelli and Petti, 2009). With Equations (3.8), (3.9) and (6.15), the depth averaged velocity is calculated as

$$\bar{u} = \frac{C\zeta}{h} \left(1 - \frac{\zeta}{h} \right) \left[1 + \frac{\zeta}{2h^2} \left(A_g - \frac{3\zeta}{2} \right) \right], \tag{6.17}$$

which can be used together with Equation (6.14) to define the initial conditions in order to generate the wave within the model.

Although this definition produces a solitary wave with infinite length, the elevation and velocities eventually become negligible and have no practical significance. As very small values can produce numerical problems, the width is limited to

$$\Gamma = \sqrt{\frac{16h^3}{3A_g}} \cosh^{-1} \sqrt{\gamma} \tag{6.18}$$

in order to prevent arithmetic overflow. Here, γ is the largest number that can be represented by the numerical solver. To confirm that this approximation is appropriate, the proportion of the theoretical wave represented within this length can be calculated as

$$\frac{\int_{-\frac{\Gamma}{2}}^{\frac{\Gamma}{2}} \zeta \, \mathrm{d}x}{\int_{-\infty}^{\infty} \zeta \, \mathrm{d}x} = \frac{2A_\mathrm{g} \tanh\left(\sqrt{\frac{3A_\mathrm{g}}{4h^3}}\frac{\Gamma}{2}\right)}{\sqrt{\frac{3A_\mathrm{g}}{4h^3}}} \frac{\sqrt{\frac{3A_\mathrm{g}}{4h^3}}}{2A_\mathrm{g}} = \sqrt{1-\frac{1}{\gamma}}. \tag{6.19}$$

All of the tests presented here are performed using double-precision floating-point arithmetic, for which

$$\gamma = 2^{1023}\left(2-2^{-52}\right) \approx 1.8 \times 10^{308}. \tag{6.20}$$

This ensures any truncation of the volume of the wave is negligible, and hugely beyond the accuracy that can be expected from the model (Muller et al., 2010; Chivers and Sleightholme, 2012).

For this set of tests, transmissive boundary conditions are adopted to allow fluid to freely enter and leave the domain. Figure 6.5 provides views of the free surface elevation at periodic intervals for a number of different amplitudes, allowing the temporal evolution of the propagating wave to be visualised. As in Tonelli and Petti (2009), a small amount of numerical dissipation is detected, causing the wave amplitude to gradually decrease over time. With larger initial amplitudes, the greater nonlinearity increases the demands placed on the model and causes the dissipative effects to become more significant. Nevertheless, the scheme is shown to provide an acceptably small level of dissipation, retaining an accurate wave shape and satisfactory amplitude over extended distances.

6.3 Common model parameters for breaking tests

Having verified the non-breaking performance of the model against analytical solutions, more complicated tests can be undertaken. These are validated against a number of experimental results, each of which is selected to analyse the ability of the model to replicate the physical processes that occur during breaking events.

In order to simplify the comparison between the various methods and cases discussed here, an effort is made to reduce the variation in the value of these parameters between each test. As the experimental scale of the simulations is of the same order throughout, a number of common parameters are established for all of the breaking cases. This limits the complexity added by the RBM and allows the calibration process to remain relatively simple.

As the wavelength is of the order of one metre for the tests performed here, the length of the sponge layer is defined as $x_\mathrm{s} = 5\,\mathrm{m}$ in all cases. Reflective boundary conditions are imposed at the offshore end of the domain. An appropriate length is included from the point of generation to the start of the slope in order to allow the created waves to

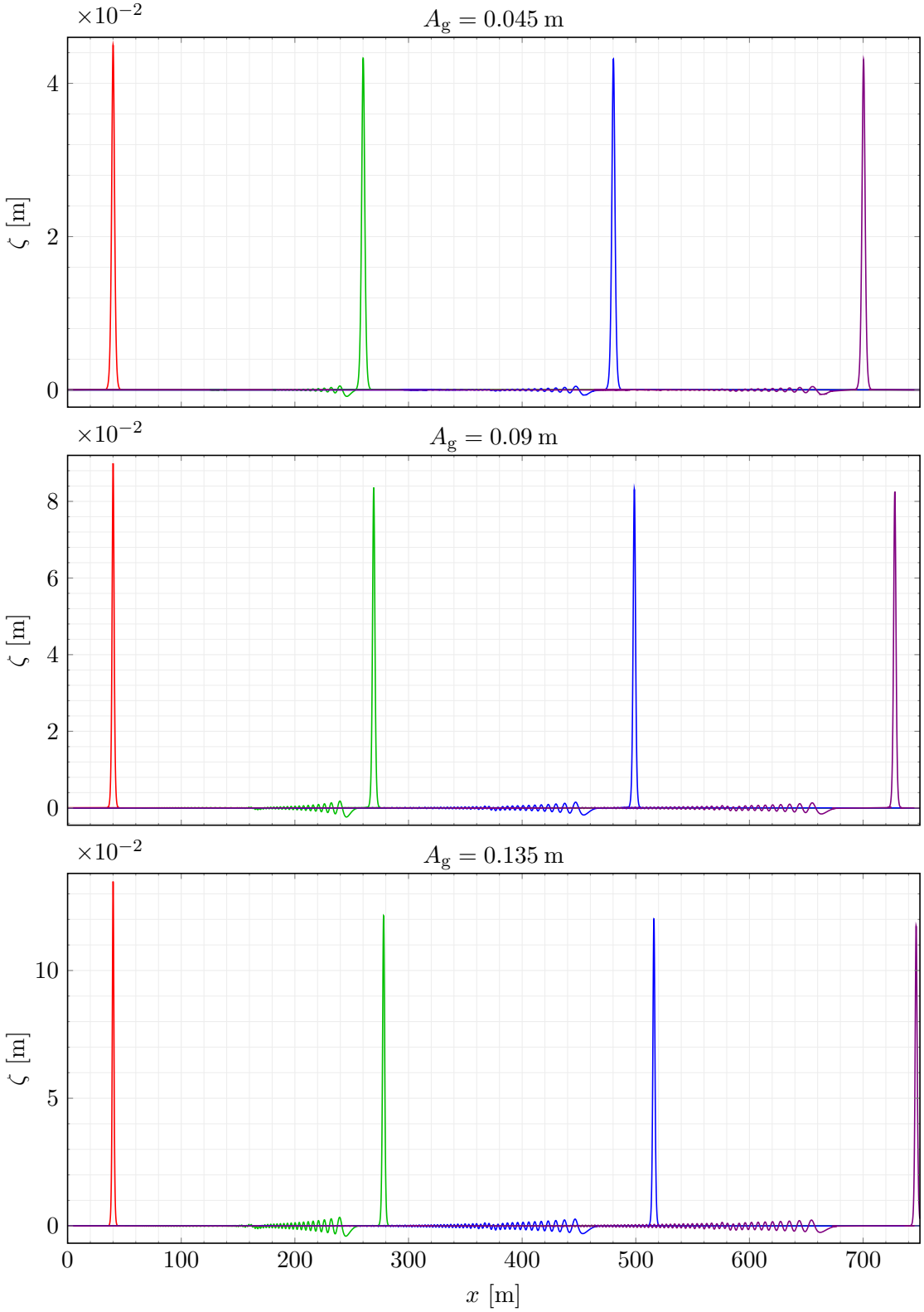

Figure 6.5: Solitary wave tests at $t = 0$ s (——), $t = 100$ s (——), $t = 200$ s (——) and $t = 300$ s (——) for a range of initial amplitudes.

reach a stable state. The source region centre, x_g, is therefore located 10 m from the offshore boundary and 20 m from the toe of the slope. For all results presented here, the toe of the slope is located at $x = 0$ m.

The RBM incorporates a number of parameters to describe the physical characteristics of the breaking process, and therefore increases the potential for calibration of the model. The parameters controlling the RBM allow the dissipation of energy from the system to be finely tuned. To allow a more direct comparison between tests, the majority of these values are kept constant in each case. The location and time at which breaking initiates and terminates is determined from the threshold angles given by $\theta_B = 20°$ and $\theta_o = 10°$, respectively. A scale factor, $t^* = 0.4$ s, is adopted to control the rate at which the termination angle evolves in accordance with Equation (4.93). The maximum vorticity injected along the lower edge of the roller is taken to be $\omega_m = 4$. For all of the tests performed in this chapter, the profile for the injected vorticity is decided with $\alpha_r = 1$ and the coefficient for the exponent, $\alpha_v = 40$, suggested by Veeramony and Svendsen (2000). The eddy viscosity parameter controls the damping of vorticity as it is transported from the point of injection. This is particularly influential in how the vorticity is advected in the wake of the roller, and is therefore tailored to each individual case in order to ensure sensible breaking terms are established throughout. A reasonable evolution in vorticity was found with $0.01\,\mathrm{m^2\,s^{-1}} \leq \nu_t \leq 0.04\,\mathrm{m^2\,s^{-1}}$.

The RBM can be sensitive to changes in the spatial and temporal resolution, which should therefore be considered in detail. Coarser resolutions may be insufficient as they can sometimes fail to adequately establish the free surface angle, leading to an absence of breaking initiation. As FV schemes can remain stable when using grid sizes smaller than those typically selected for equivalent FD BTMs, a reduction in numerical dissipation is achieved. The inclusion of FD Boussinesq and breaking terms means instabilities can be introduced which may become problematic at higher resolutions. While careful filtering can reduce the adverse effects resulting from higher resolutions, the difference in grid size favoured by FD and FV schemes means it is necessary to reach a balance. The FD RBM of Musumeci et al. (2005) adopted grid sizes as large as $\Delta x = 0.08$ m, while the FVFD scheme of Tonelli and Petti (2010) employs values as small as $\Delta x = 0.02$ m. In the present work, the appropriate resolution for the equivalent cases was found to lie between these two grid sizes, with $0.04\,\mathrm{m} \leq \Delta x \leq 0.05\,\mathrm{m}$ selected for the tests that follow in this chapter.

In order to correctly show the propagation of waves, the time at which the numerical data is presented remains consistent between plots for all of the results presented here. It should be noted that, in some cases, the timing of experimental data has been adjusted in order to ensure the observations can be directly compared with the results provided by the model, particularly with the occurrence of certain features of interest.

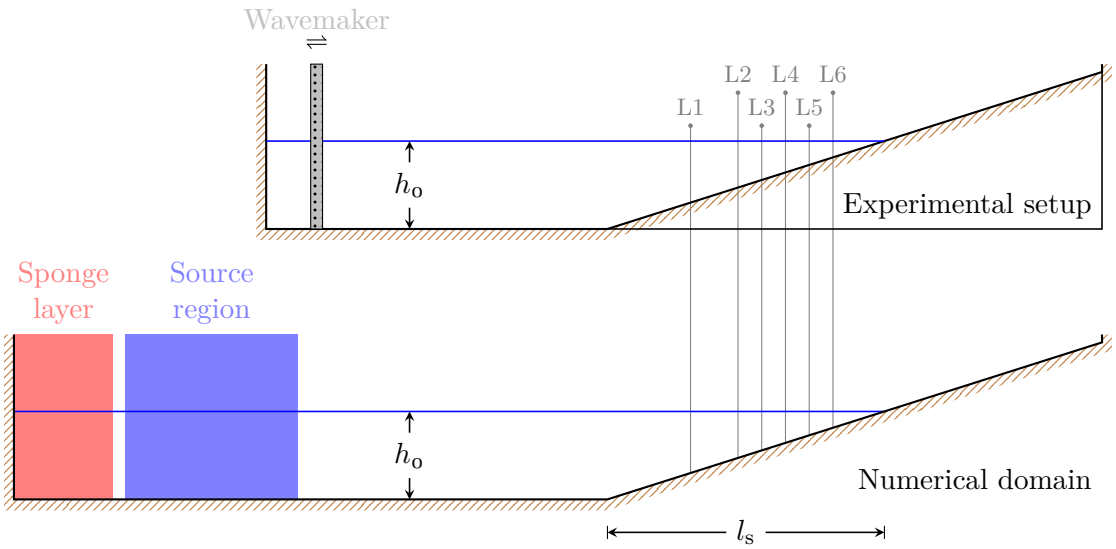

Figure 6.6: Experimental setup and corresponding numerical domain, with gauge locations for experiments of Cox et al. (1995).

6.4 Monochromatic wave cases

The first cases inherit the configurations used by Hansen and Svendsen (1979) and Cox et al. (1995), which involve wave propagation over a simple slope, as illustrated in Figure 6.6. The bathymetric slope steepness is dictated by the distance, l_s, between the initial shoreline position and the toe of the slope. Validations are made using the experimental observations of free surface elevation. The tests performed by Cox et al. (1995) also include measurements of the horizontal velocity, which allow the vorticity resolved by the model to be assessed indirectly.

With Equations (3.18), (3.51) and (5.76), the dispersivity can be calculated for a range of bed gradients, water depths and wave frequencies. Table 6.2 confirms that $\frac{\partial \hat{h}}{\partial \hat{x}} = \frac{1}{\mu}\frac{\partial h}{\partial x} < \mu^2$ for each of the tests involving higher-order Boussinesq terms undertaken within the present study. This demonstrates the appropriateness of the assumptions made about the bed steepness and dispersivity in Equation (4.13).

It should be noted that a net increase in mass was found over a single wave period when using the variable timestep described in Section 5.7 with the wave generation technique outlined in Section 5.9. Since the temporal discretisation of the source function is influenced by the varying maximum water depth and velocity, the source function at each timestep does not sum to zero over a single wave period. Although the resulting error is small, the cumulative effect over long simulations can be significant, as the sign of the total discrepancy is consistent over successive wave periods. Furthermore, although rapid changes in the Courant number are not to be expected, the derivation of the breaking terms assumes the rate of change of Δt to be negligible. Accordingly, for tests involving internal wave generation or the inclusion of breaking terms, a fixed

Table 6.2: Values of maximum bed gradient and dispersivity squared for range of slope lengths, still water depths and wave frequencies studied here..

l_s [m]	h_0 [m]	f_w $\left[s^{-1}\right]$	$\frac{1}{\mu}\frac{\partial h}{\partial x}$	μ^2
12.3336	0.36	0.6	0.0369	0.626
12.3336	0.36	0.55	0.0409	0.51
12.3336	0.36	0.5	0.0456	0.41
12.3336	0.36	0.45	0.0512	0.324
12.3336	0.36	0.4	0.0583	0.251
12.3336	0.36	0.35	0.0672	0.188
12.3336	0.36	0.3	0.0791	0.136
14	0.4	0.6667	0.0297	0.923
14	0.4	0.625	0.0322	0.785
14	0.4	0.4545	0.0468	0.373
14	0.4	0.4	0.0539	0.281

Table 6.3: Wave parameters for Hansen and Svendsen (1979) tests and Iribarren numbers calculated from recorded values of wave height and wavenumber.

Test	f_w $\left[s^{-1}\right]$	H [m]	ξ_0	Breaker type
O	0.5	0.0375	0.38	Spilling
Q	0.4	0.0399	0.44	Spilling
R	0.3	0.0433	0.52	Plunging

timestep is used to ensure the mean water level remains constant and the breaking terms are correct.

6.4.1 Hansen and Svendsen (1979) tests

In order to examine the ability of the model to simulate wave breaking, a series of tests are performed using monochromatic cnoidal waves. By testing the model with different values for the wave amplitude and frequency, a range of breaking conditions are generated. Table 6.3 lists the parameters used for the cases reproduced in this section, which correspond to a selection of the experimental observations of Hansen and Svendsen (1979). The configurations of these tests are described in detail by Hansen (1980).

The experimental observations also provide a view of the free surface profile at a number of gauge locations. Although none of these gauges provide measurements at positions after the initiation of breaking, valuable comparisons can still be made using the available data. The numerical model is occasionally found to experience the effects of the breaking terms before the point at which they are introduced, in particular where instabilities may appear and subsequently propagate offshore. Assessing the free surface

profile at the available gauge locations therefore allows the stability of the scheme to be monitored, while also verifying the capabilities of the non-breaking components of the model. This also provides a means to authenticate the internal wave generation mechanism and ensure that, before any change in the bathymetry occurs, the incoming waves simulated by the model match those measured experimentally.

For the first three cases, the model is executed using both an RBM and an HBM in order to compare the behaviour observed with each approach, with the latter providing a model similar to that of Tonelli and Petti (2010). Each simulation starts from a state of quiescence, and continues for fifty wave periods in order to negate the effects of any instabilities arising during initialisation of the test.

The still water depth and length of initially submerged slope are $h_o = 0.36\,\mathrm{m}$ and $l_s = 12.3336\,\mathrm{m}$, respectively. The tests performed here adopt a spatial grid size of $\Delta x = 0.04\,\mathrm{m}$, while the temporal resolution is given by $\Delta t = 0.012\,\mathrm{s}$. The resulting Courant number is then close to that used in the equivalent set of tests performed by Tonelli and Petti (2010).

The behaviour of the model is assessed from the predictions of free surface elevation. As such, the amplitude used for the internal generation of waves is calibrated to ensure the wave height at the toe of the slope matches that seen in the experimental data. The dissipation of energy present in each case is quantified by the maximum wave height, H_m, measured over the final four wave periods of the simulation. This is calculated as the difference between the maximum and minimum free surface elevations observed over the monitored interval. The mean free surface elevation is also recorded over this time in order to appraise the set-up in each case.

Test O

The eddy viscosity used for the first monochromatic wave test is given by $\nu_t = 0.01\,\mathrm{m^2\,s^{-1}}$. In the present work, the breaking model is tuned by selecting an appropriate value for this parameter. The results obtained with the RBM can be seen in Figure 6.7, where the free-surface elevation is presented over the final wave period of the simulation. Here, a number of expected physical phenomena are visible, such as the deformation of the surface profile experienced by the propagating waves. The decrease in wavelength and celerity is also evident as the waves travel in the onshore direction. The influence of the bathymetry is clearly illustrated, and the steepening of the surface profile can be seen as the waves shoal.

As the free surface angle reaches the threshold value declared for breaking initiation, the subsequent reduction in wave height anticipated in such cases is observed. The breaking terms are sufficiently smooth, and do not introduce any significant oscillations in the wake of the breaker. The interpolated crest and toe of the roller are shown to be located correctly, while the evolution of the breaking angle and wave height means the roller length reduces in time, as expected.

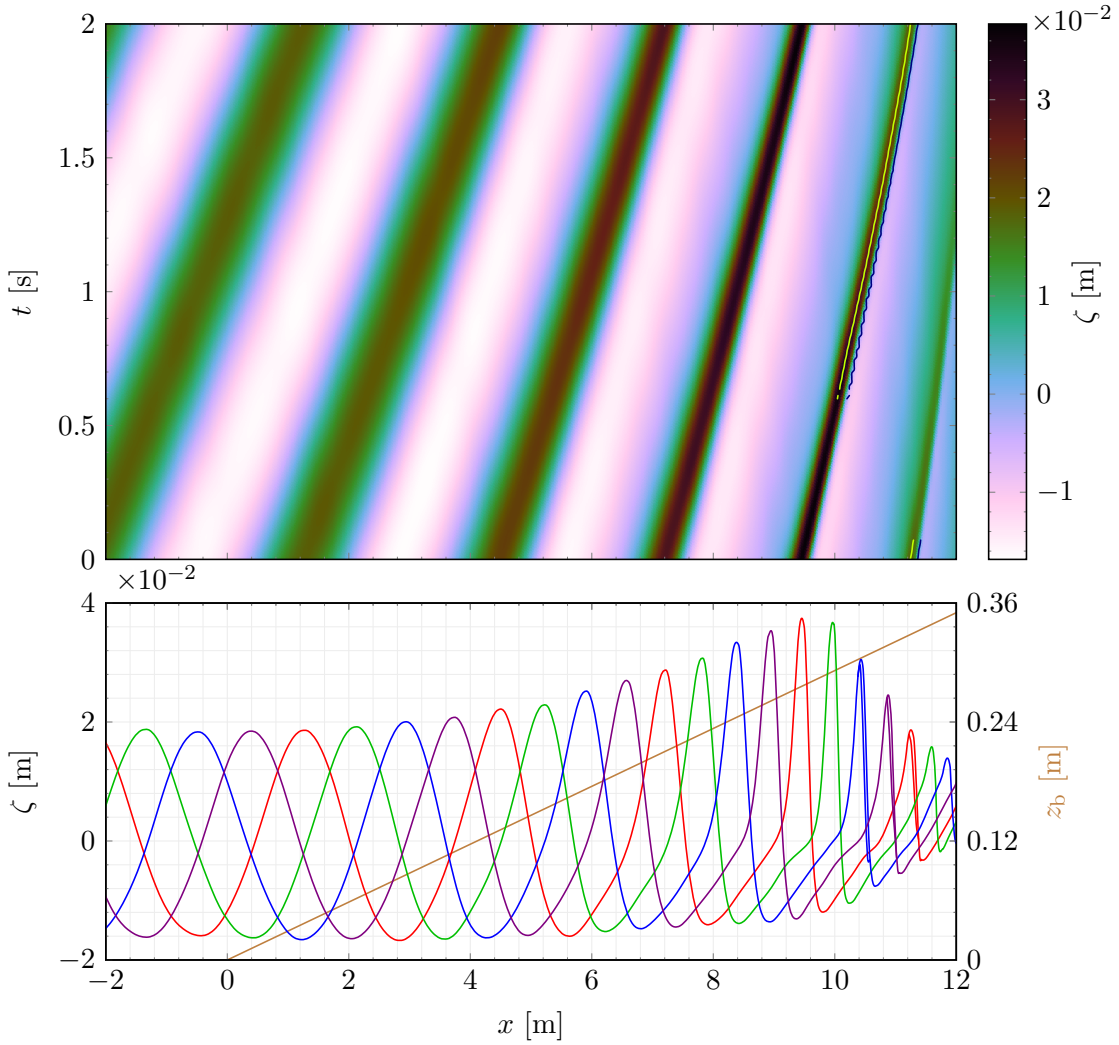

Figure 6.7: Free surface elevation and interpolated crest (——) and toe (——) locations over one wave period (top) and at $t = 0\,\mathrm{s}$ (——), $t = 0.504\,\mathrm{s}$ (——), $t = 0.996\,\mathrm{s}$ (——) and $t = 1.5\,\mathrm{s}$ (——), and lower edge of rollers and bathymetric elevation (——) (bottom) for Test O using the RBM.

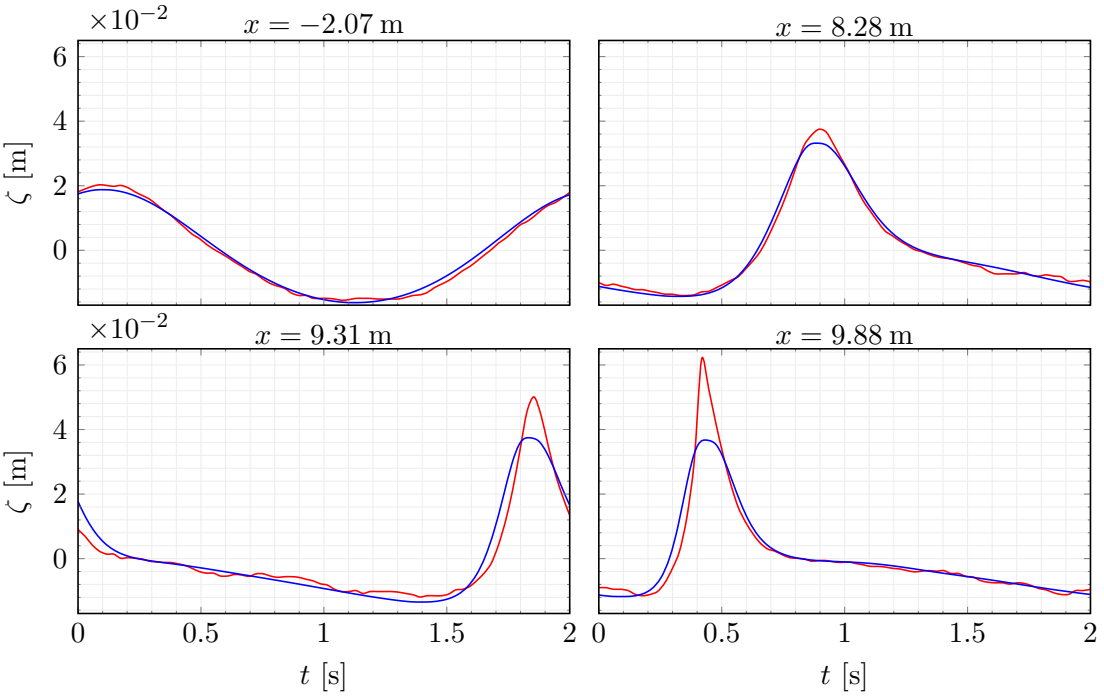

Figure 6.8: Experimental (——) and numerical (——) free surface profiles for Test O.

Although a slightly premature initiation of breaking is seen as the roller briefly appears prior to the main breaking event, this does not have any noticeable effect on the dissipation from the flow. This behaviour can be attributed to the sensitivities that may arise as the angle of the free surface is estimated from discrete depth values, which are particularly changeable in the vicinity of high gradients. Despite this, the remainder of the breaking event is seen to be stable and consistent. The small levels of variability are also indicated by the oscillating location of the interpolated toe, although this is not found to cause any problems, and decreases as the free surface of the wave becomes less steep.

In order to provide a better quantitative assessment of the wave shape predicted before breaking, Figure 6.8 compares the numerical and experimental results at four gauge locations. As the model presented here adopts WNBs, the shoaling seen in the experimental observations is not fully replicated and the peak wave heights do not match. Musumeci et al. (2005) showed the increase in wave height to more closely resemble that seen in the experimental data of Hansen and Svendsen (1979) when the WNBs are extended to provide an RBM using FNBs. It is therefore reasonable to expect such an extension would provide the same benefits when applied to the present study. The wave shape predicted by the model is otherwise similar to that observed experimentally.

A comparison of the experimental and numerical wave height envelope for Test O is presented in Figure 6.9, using both HBM and RBM methods. A reasonably similar reduction in wave height is seen with each approach, and although slightly greater levels of dissipation are obtained with the HBM, fewer oscillations are introduced at the onset

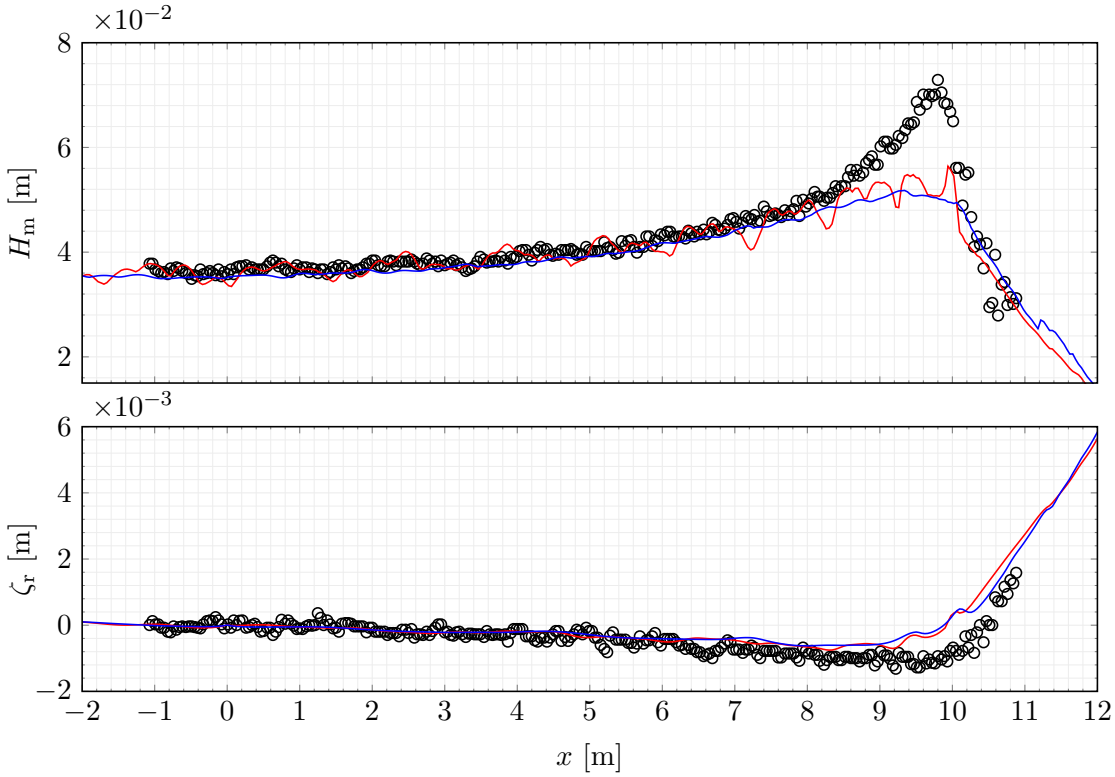

Figure 6.9: Wave height (top) and mean water level (bottom) for Test O with an HBM (——) and an RBM (——) compared to experimental results of Hansen and Svendsen (1979) (○).

of breaking with the RBM, meaning a more stable outcome is achieved.

The mean of the free surface elevation, ζ_m, is analysed according to

$$\zeta_\mathrm{r} = \zeta_\mathrm{m}|_{x=0}\,. \tag{6.21}$$

Both breaking models predict a very similar set-up which exhibits the expected behaviour as the wave propagates into shallower water.

Test Q

For this test, the wave frequency is reduced and the incoming amplitude increased, and the RBM is adjusted to $\nu_\mathrm{t} = 0.013\,\mathrm{m^2\,s^{-1}}$. Figures 6.10 to 6.12 provide the equivalent collection of results for the second spilling breaker test. In this case, the speed at which the waves propagate relative to the wave period is less than that found with the previous test. This means the comparative time between breaking initiation and termination is larger, resulting in a proportionally longer breaking duration and dissipative terms that act over a greater proportion of a wave period.

The conclusions that can be drawn from Test Q are similar to those discussed with regards to Test O. The observations therefore support the findings outlined previously, demonstrating consistent behaviour for the spilling breaker cases.

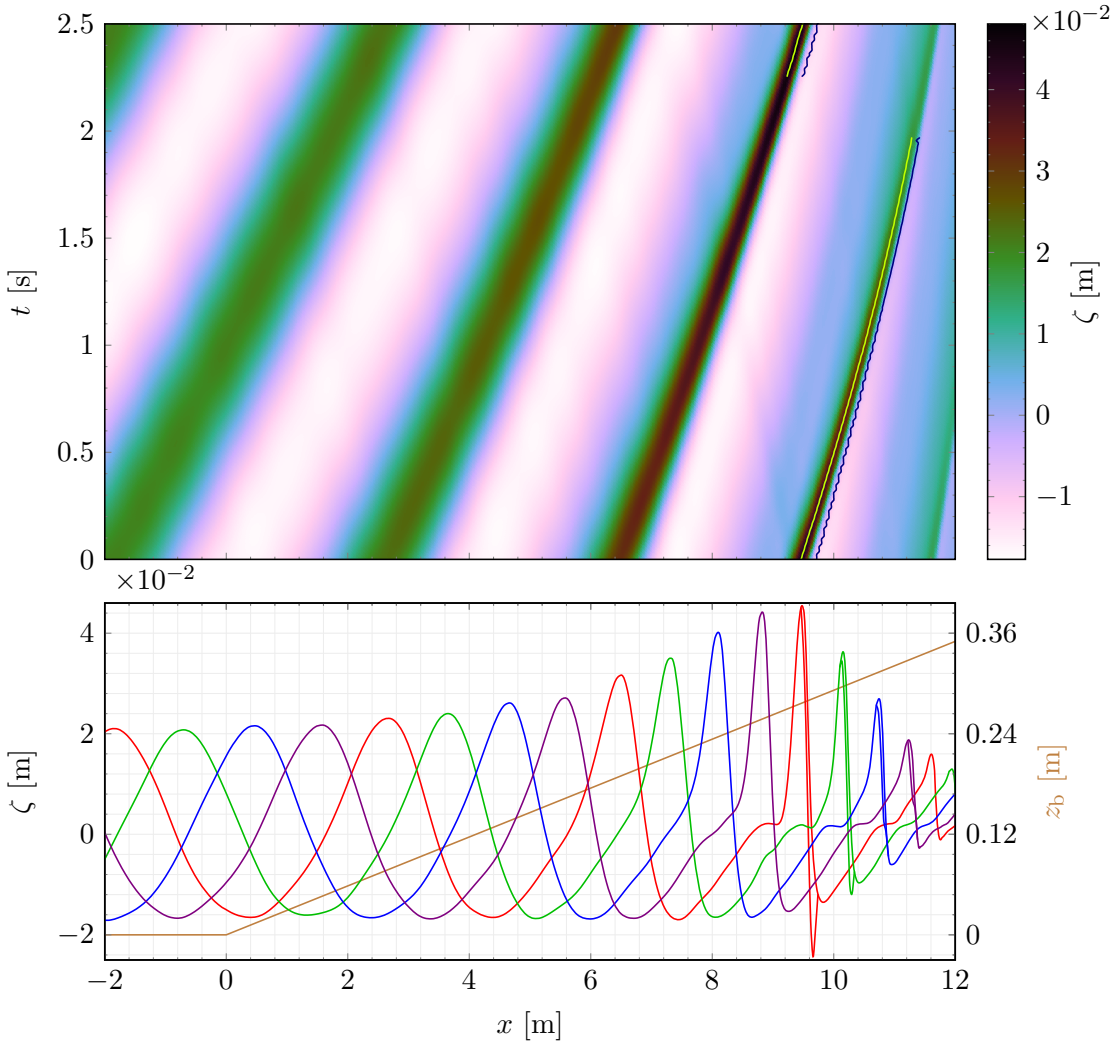

Figure 6.10: Free surface elevation and interpolated crest (——) and toe (——) locations over one wave period (top) and at $t = 0$ s (——), $t = 0.624$ s (——), $t = 1.248$ s (——) and $t = 1.872$ s (——), and lower edge of rollers and bathymetric elevation (——) (bottom) for Test Q using the RBM.

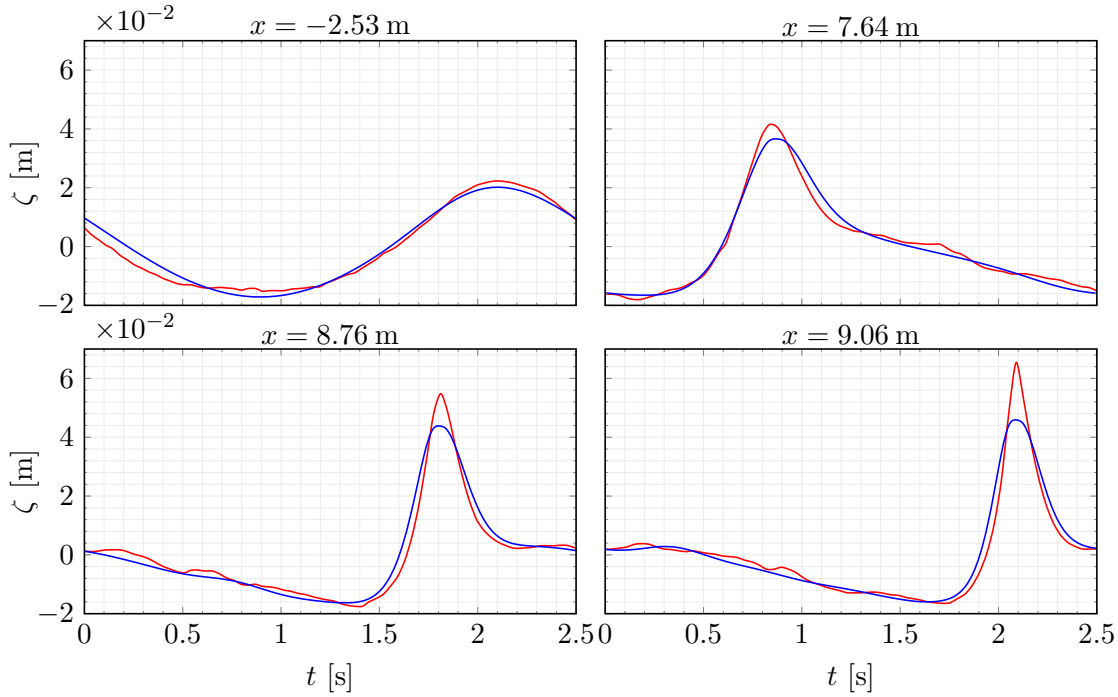

Figure 6.11: Experimental (——) and numerical (——) free surface profiles for Test Q.

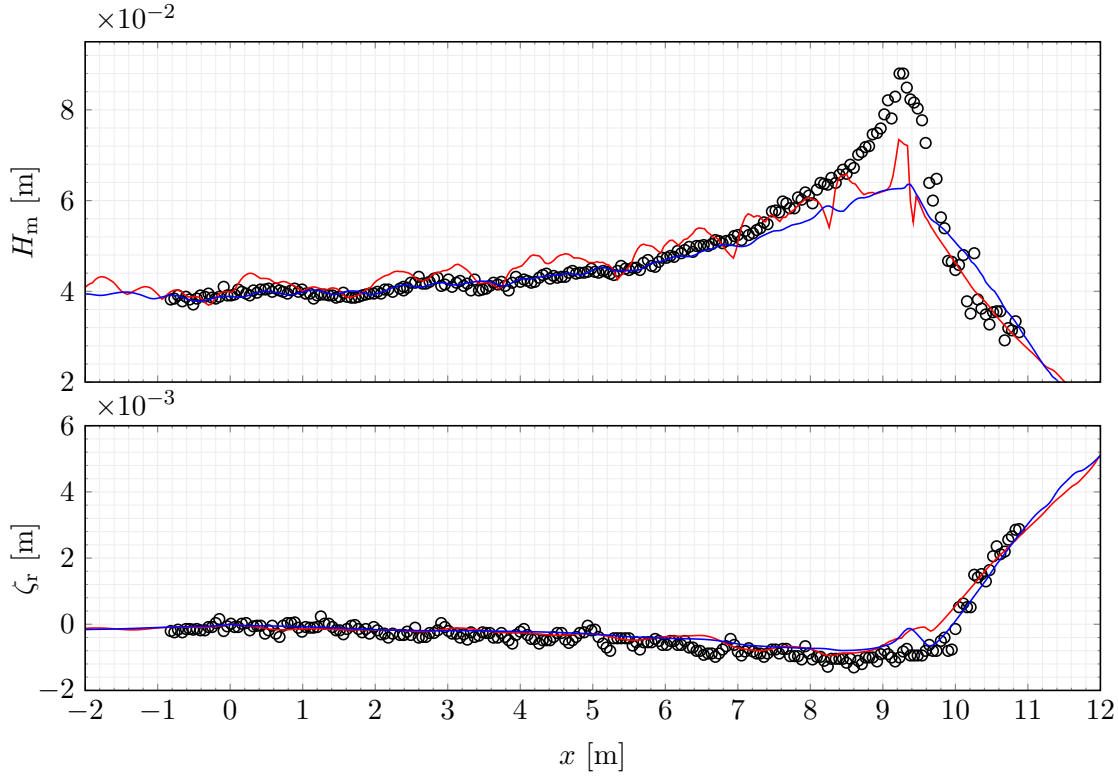

Figure 6.12: Wave height (top) and mean water level (bottom) for Test Q with an HBM (——) and an RBM (——) compared to experimental results of Hansen and Svendsen (1979) (○).

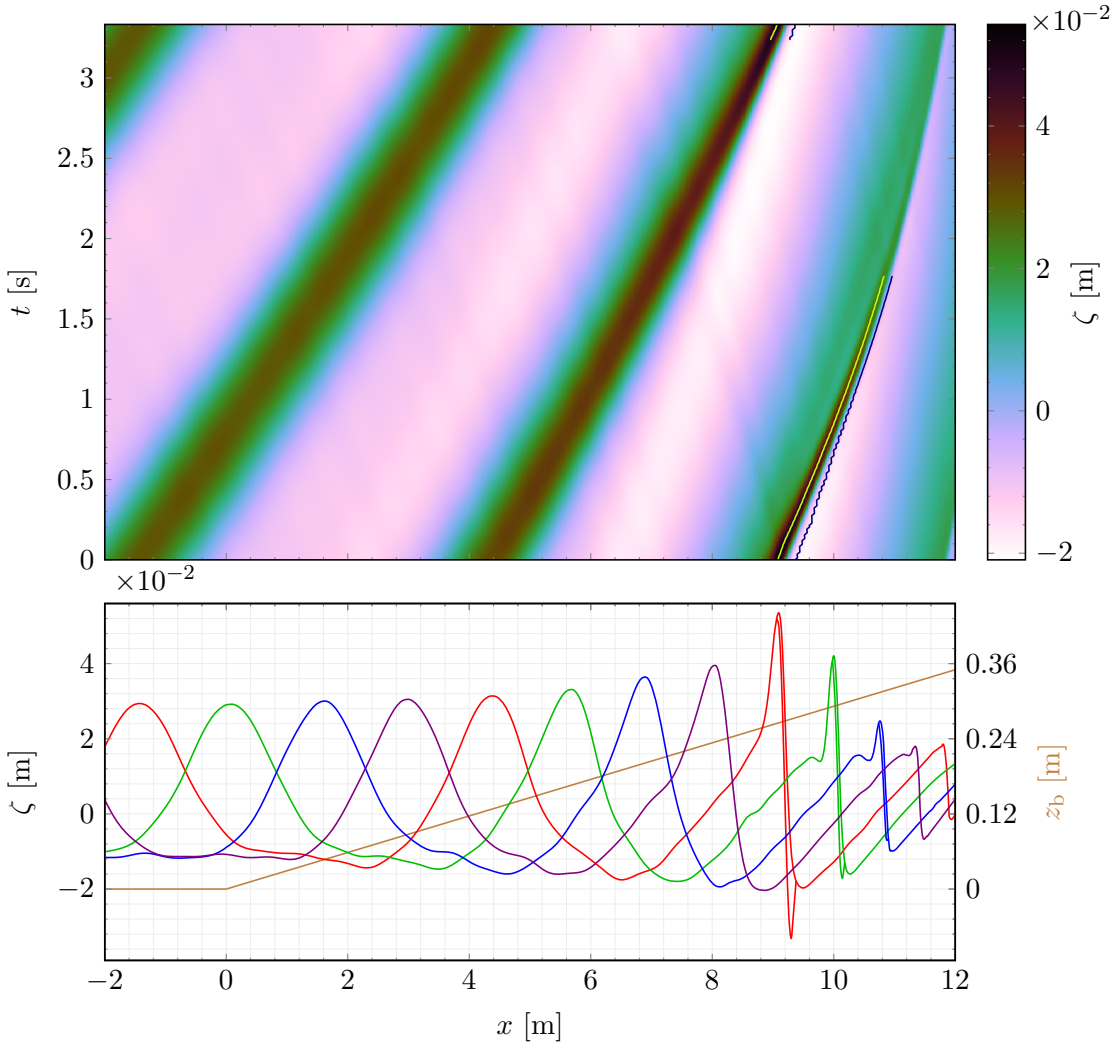

Figure 6.13: Free surface elevation and interpolated crest (——) and toe (——) locations over one wave period (top) and at $t = 0\,\mathrm{s}$ (——), $t = 0.828\,\mathrm{s}$ (——), $t = 1.668\,\mathrm{s}$ (——) and $t = 2.496\,\mathrm{s}$ (——), and lower edge of rollers and bathymetric elevation (——) (bottom) for Test R using the RBM.

Test R

The results of the final test case replicating the experiments of Hansen and Svendsen (1979) allow the examination of the model performance for a plunging breaker. It is important to note that the more complex processes present in this case fall beyond the scope of RBMs. The overturning motion of the fluid results in multiple free surfaces at some x-locations, nullifying the depth averaging approach adopted for the derivation of the governing BTEs. Although this means the water column can no longer be described as a continuous single phase fluid, the RBM still provides a mechanism by which energy can be dissipated during breaking events, and allows calibration based on physical properties. For the results presented here, $\nu_\mathrm{t} = 0.016\,\mathrm{m^2\,s^{-1}}$ is used.

The characteristics displayed in Figure 6.13 are similar to those found in Test O and

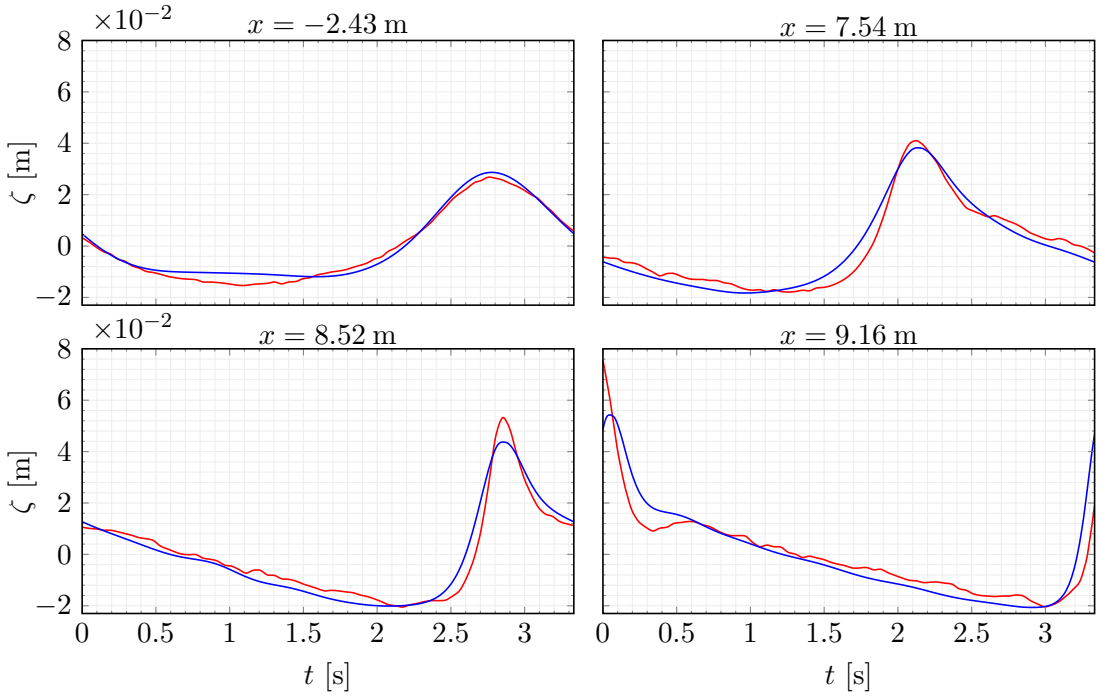

Figure 6.14: Experimental (——) and numerical (——) free surface profiles for Test R.

Test Q, although the relative change in celerity becomes more pronounced for cases with a greater wave height and smaller wave frequency. Here, the evolution of the breaking process is comparatively quick, and more strongly influenced by the rapid change in bathymetry due to the faster propagation speed. The resulting pace of the dissipation mechanism places more demands on the model. Consequently, some oscillations in the free surface profile are visible in the wake of the roller, although these are relatively small and do not compromise the stability of the model. These are primarily introduced where the distribution of the breaking terms is not correctly aligned with the shape of the wave.

Figure 6.14 again shows the wave shape to be accurately reproduced, albeit with some discrepancies in the height due to the shoaling limitations discussed previously. The results presented in Figure 6.15 show similar average wave heights with both the RBM and the HBM, although the results obtained with the former method are generally less favourable than for Test O and Test Q, where the simulations are more in line with the experimental observations. Even though Test R exceeds the intended application of the RBM, the model is shown to perform well and dissipate a reasonable amount of energy from the system.

6.4.2 Cox et al. (1995) test

The next experiment allows the velocity predictions of the model to be evaluated against laboratory data for the tests detailed by Cox et al. (1996). The monochromatic waves in this test have a period of $T = 2.2\,\mathrm{s}$, the offshore depth is $h_o = 0.4\,\mathrm{m}$, and the initial

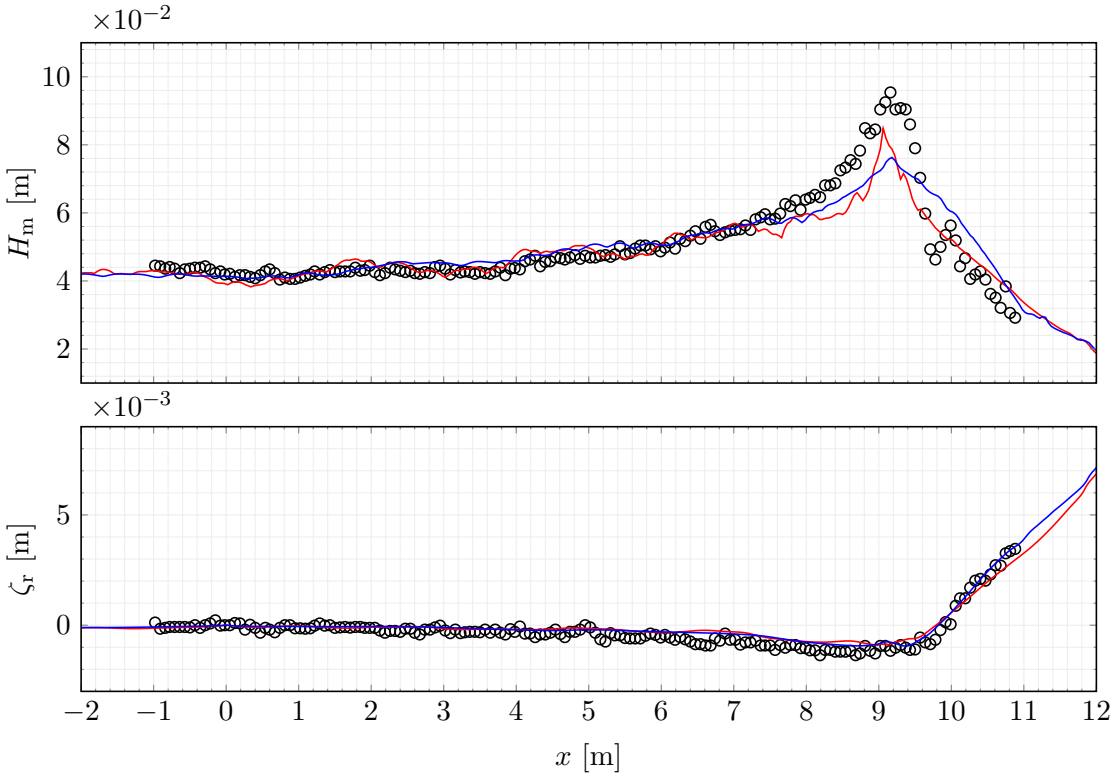

Figure 6.15: Wave height (top) and mean water level (bottom) for Test R with an HBM (——) and an RBM (——) compared to experimental results of Hansen and Svendsen (1979) (○).

shoreline is $l_s = 14$ m from the start of the slope. The temporal and spatial resolutions used for the numerical tests are $\Delta t = 0.015$ s and $\Delta x = 0.05$ m, respectively.

The gauge locations used for this test are identified in Figure 6.6. Those within the shoaling region are labelled L1, L2 and L3, corresponding to the points in the domain that lie $x = 4.2$ m, $x = 6.6$ m and $x = 7.8$ m after the toe of the slope. The remaining locations marked by L4, L5 and L6 are inside the surf-zone, positioned at $x = 9$ m, $x = 10.2$ m and $x = 11.4$ m, respectively.

Horizontal velocity and free surface profiles

Figure 6.16 provides the numerical estimates for the horizontal velocity, which can be compared with the experimental laser Doppler velocimeter (LDV) measurements made by Cox et al. (1995), visualised at the same scale in Figure 6.17. A direct comparison of numerical and experimental horizontal velocities is provided in Figure 6.18, where the results are presented at discrete periodic intervals. Before the roller has formed, the horizontal velocity consists exclusively of the potential component. Differences from the standard Boussinesq model materialise as rotationality is introduced, at which point vertical variations in the velocity profile can be perceived.

Although the RBM does not aim to simulate the flow within the roller region, estimates

are made to give a more complete impression of the overall hydrodynamic behaviour predicted by the model. In reality, the highly turbulent flow expected in this area is likely to be more chaotic and include much smaller scale processes than are depicted here. The limitations of the linear vorticity distribution assumed across the roller are evidenced by the small disparity in horizontal velocity found at the lower edge of this region.

While the experimental results provide only a partial view of the velocity profile, the model predictions can be seen to resemble the physical observations in the regions where data is available. The peak horizontal velocities are found towards the crest of the wave and near the lower edge of the roller region.

In order to quantify the variation between the experimental and numerical results, the quadratic error is determined. This first requires the computed values to be mapped onto the same grid as the measured data, which is done here using a cubic interpolation. The error along one dimension for a given quantity, f, can then be calculated as

$$\epsilon_1(f) = \frac{\sum_{n=n_\mathrm{b}}^{M} \left[(f_\mathrm{c})_n - (f_\mathrm{m})_n\right]^2}{\sum_{n=n_\mathrm{b}}^{M} \left[(f_\mathrm{m})_n\right]^2}, \tag{6.22}$$

where measured and interpolated computed values are represented by f_m and f_c respectively, and M denotes the number of samples along the water column. The choice of n_b allows the data in the bottom boundary layer to be ignored, since the present model does not attempt to simulate the effects found in this region. When f is a matrix with dimensions $M_1 \times M_2$, a single value for the quadratic error can be obtained with the following relation:

$$\epsilon_2(f) = \frac{\sum_{n=n_\mathrm{b}}^{M_1} \sum_{l=1}^{M_2} \left[(f_\mathrm{c})_{n,l} - (f_\mathrm{m})_{n,l}\right]^2}{\sum_{n=n_\mathrm{b}}^{M_1} \sum_{l=1}^{M_2} \left[(f_\mathrm{m})_{n,l}\right]^2} \tag{6.23}$$

In this case, the number of samples along the water column is given by M_1, while M_2 indicates the number of samples in a given wave period.

The results presented here assume the boundary layer thickness to be five percent of the still water depth. By presenting the data in this form, the results generated using an FVFD scheme can be subjected to the equivalent analysis performed by Briganti et al. (2004) using an FD scheme. The small sample interval, $\Delta t = 0.01$ s, of the experimental data makes the resulting error susceptible to peaks where anomalies exist. This is particularly true where f_m is particularly small and f_c relatively large. In order to reduce the prominence of these misleading features, a median filter with a window size of five is applied to the quadratic error, which is then presented in Figure 6.19.

The most considerable quadratic error is observed at gauge L4, where a particularly large difference between the experimental and numerical results is evident. This is seen

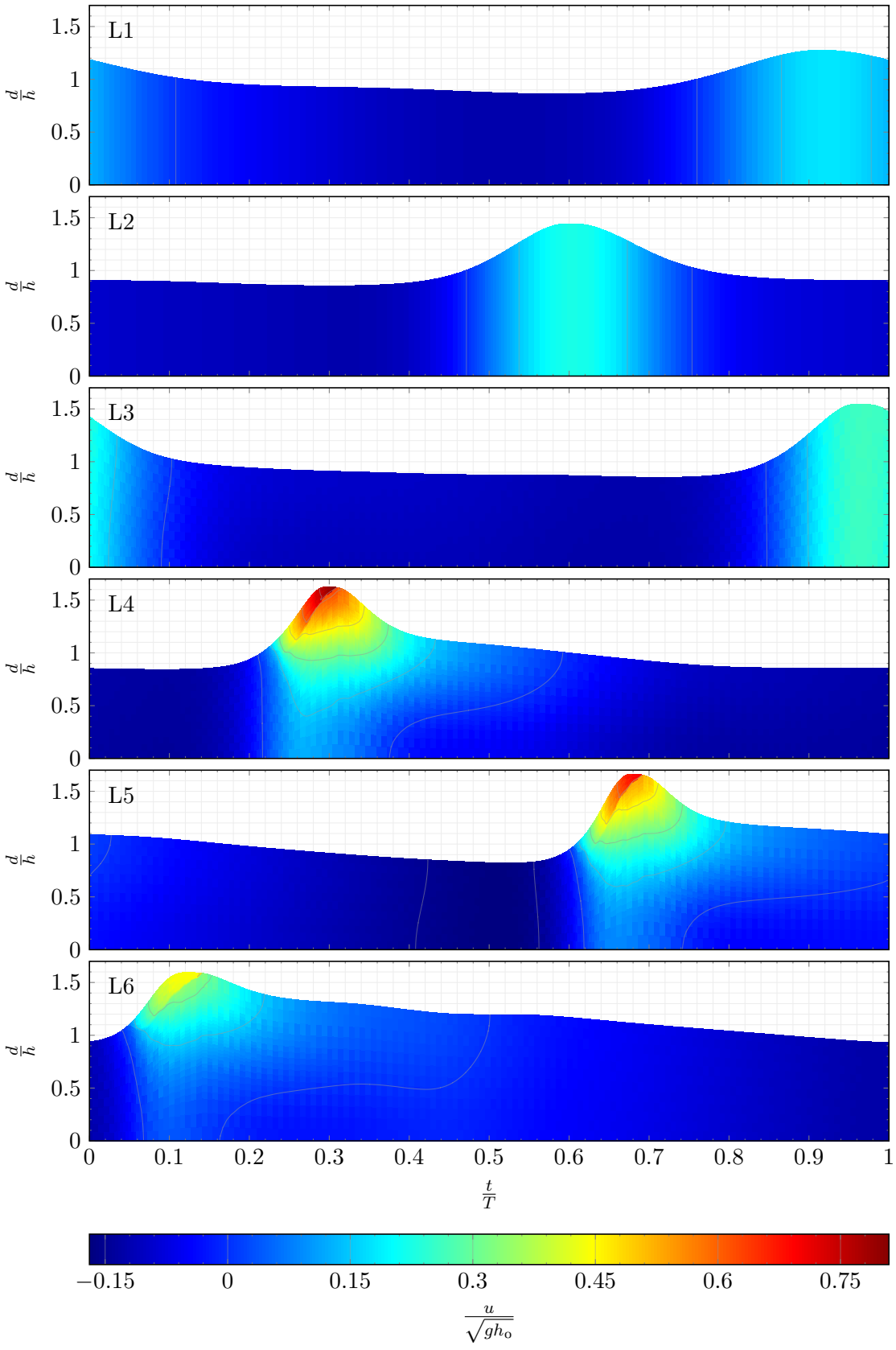

Figure 6.16: Temporal evolution of horizontal velocity calculated by model at six locations.

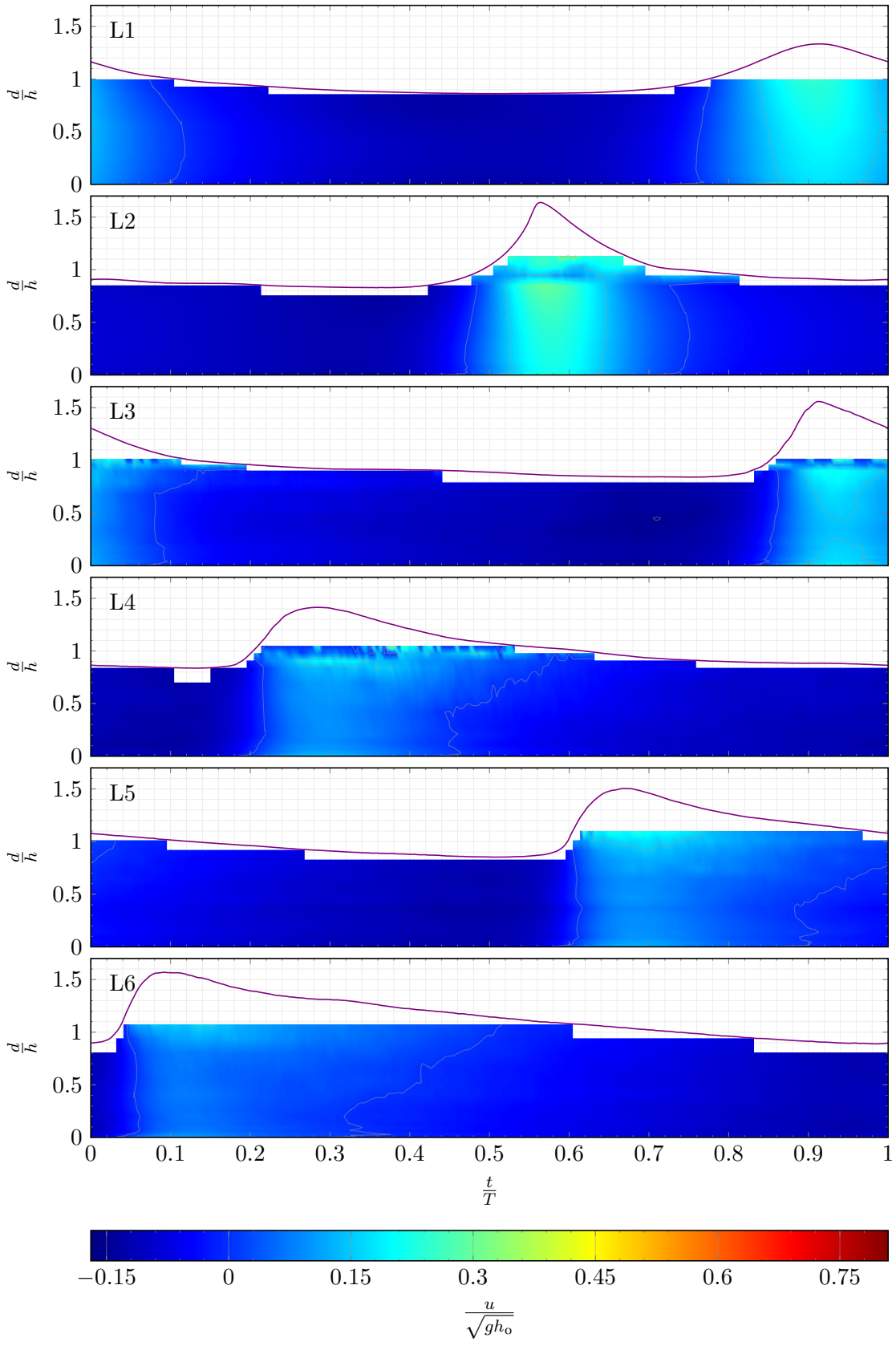

Figure 6.17: Temporal evolution of surface profile (——) and horizontal velocity from experimental LDV measurements (Cox et al., 1995) at six locations.

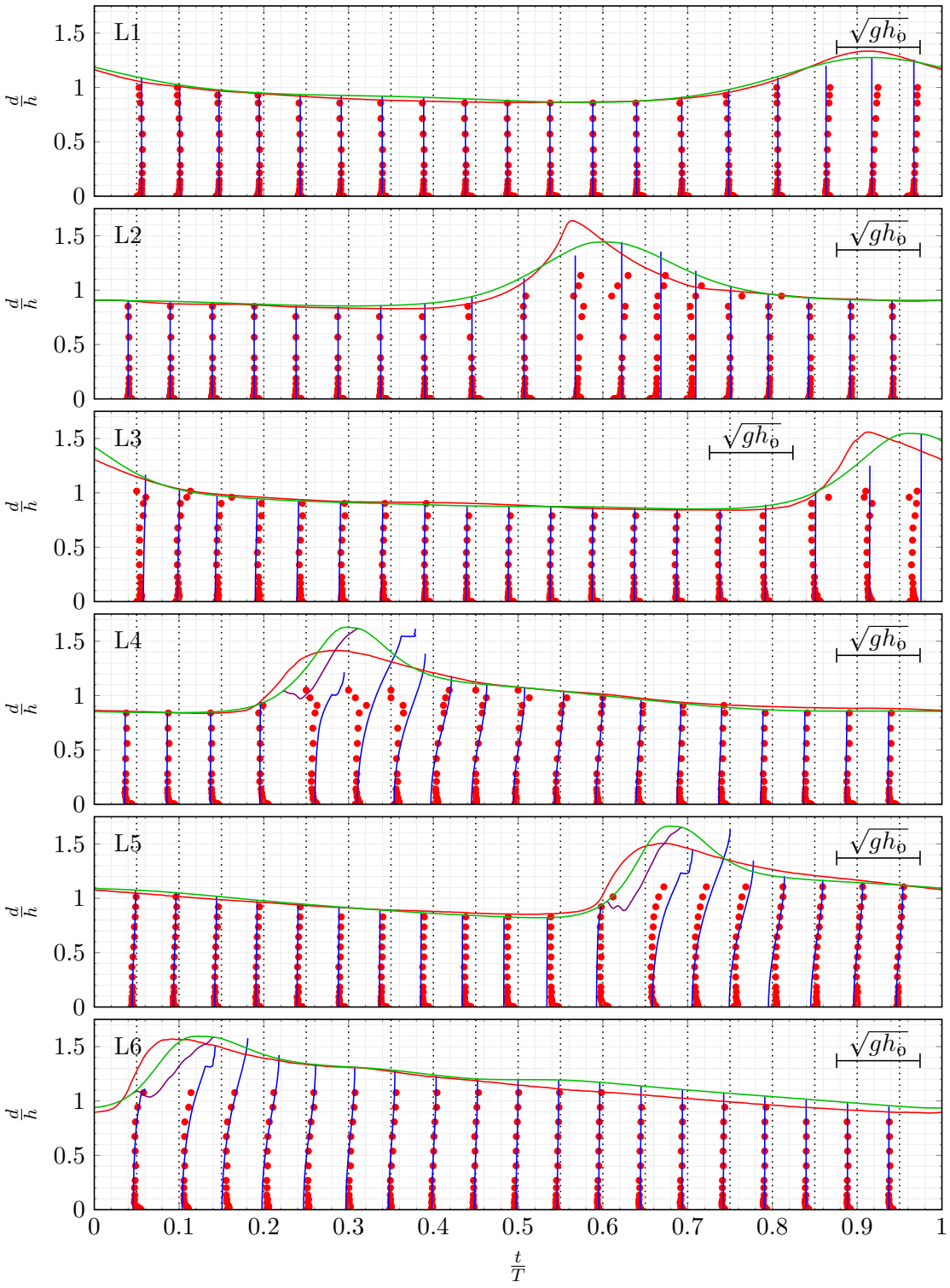

Figure 6.18: Model surface profile (——) with lower roller edge (——) and total horizontal velocity (——) compared with surface profile (——) and LDV horizontal velocity measurements (•) of Cox et al. (1995). Velocities are nondimensionalised and scaled according to the celerity, with a zero velocity indicated for each sampled time (·····).

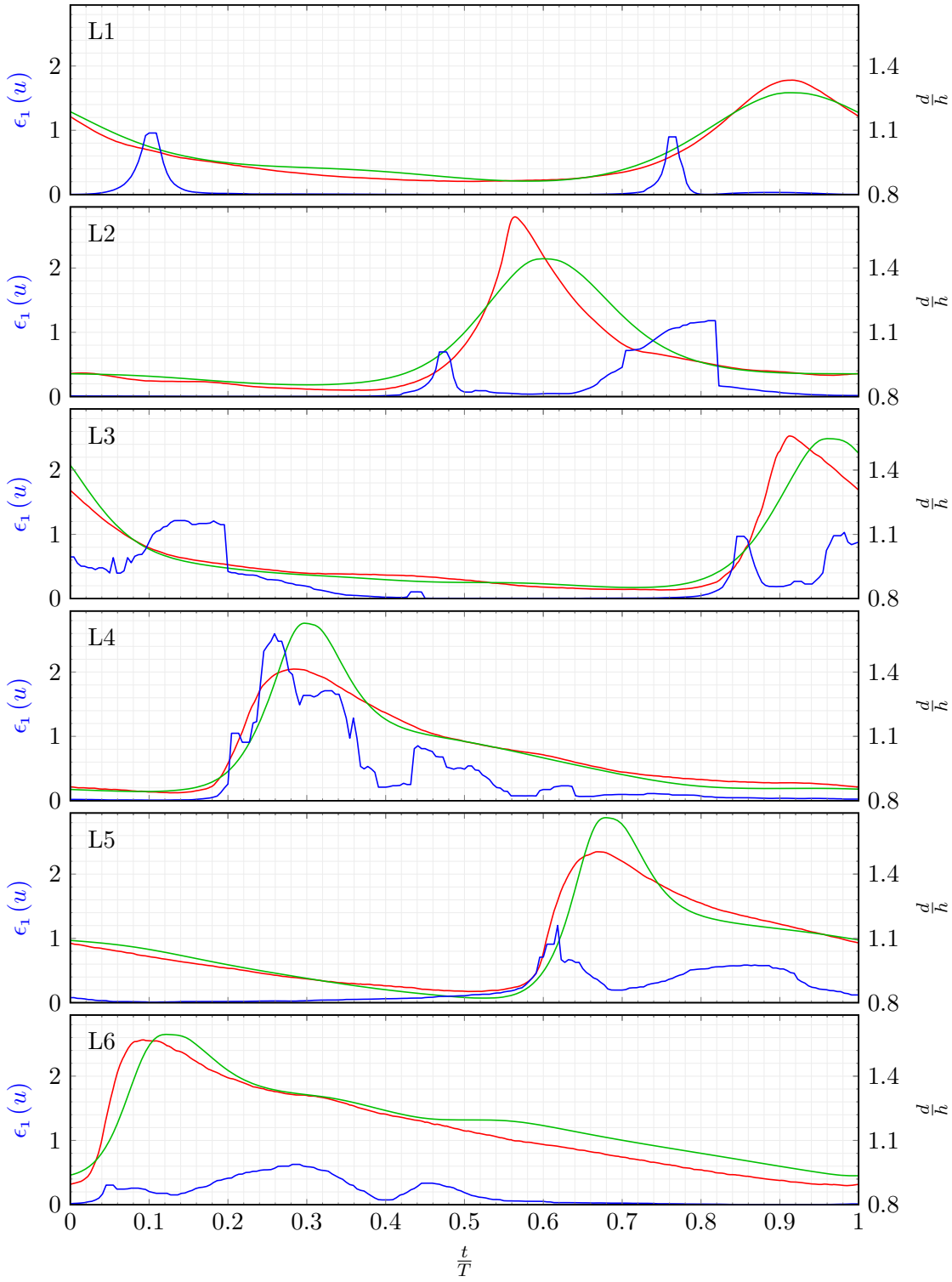

Figure 6.19: Quadratic error between total horizontal velocity of model and experimental data of Cox et al. (1995) (——) and free surface profile of model (——) and experimental data (——).

to occur where the shoaling predicted by the model differs most from that observed experimentally. The variation in the wave height means the model predicts the initiation of breaking to be further onshore. This results in some small disagreements in the shape of the wave, which means particular features will inevitably become misaligned. The strong introduction of vorticity at the toe of the roller then produces larger velocities than are found experimentally. Outside of this region, the peaks in quadratic error are much smaller, and again correspond to locations where small variations in the wave shape exist. It is also important to note that some error can be attributed to noise in the experimental data.

It should be stressed that the contrasts between the predicted and measured free surface elevation and horizontal velocity are relatively slight. The feedback of the breaking process into other hydrodynamic features means the system is highly dynamic, and as such, small differences in particular aspects of the scheme are amplified. In particular, slight discrepancies between the experimental and numerical breaking points can lead to more significant variations in the behaviour in this region. The profiles show the quality of the predictions during breaking, in spite of the assumptions made in the derivation of the governing equations. The description of the physics encompassed by the model is more accurate due to the retention of the BTEs throughout the breaking process. In general, the results show a good overall agreement between the numerical and experimental data.

Breaking terms

In addition to predicting the horizontal velocity, the model also calculates breaking terms, which are used to dissipate energy from the system. Having established the accuracy of the horizontal velocity, the structure of these terms can be studied in order to assess the physics and numerics of the model in further detail. In Figure 6.20, the profile of each breaking term can be seen over one wave period at the gauges shown previously.

The shapes of the breaking terms calculated using the RBM with an FVFD scheme are broadly the same as that found with an FD scheme, as in Musumeci et al. (2005). This is to be expected, as the similarities in the adopted breaking scheme should be reflected in the distribution of these terms, although some variation should be anticipated due to a number of factors. It is reasonable to expect some changes when a different numerical scheme is used, but further distinctions are introduced by changes permitted by the shock-capturing scheme. The sudden injection of vorticity produced by the RBM created instabilities when used in an FD scheme, and therefore had to be gradually introduced over the initial period following the inception of breaking. The greater stability attained with the FVFD scheme allows this abrupt introduction to be included in an unhindered manner, thereby producing a more realistic representation of the physics. This also means the total quantity of injected vorticity is greater when using equivalent values for the breaking calibration parameters. The lower value of ω_s reflects this difference and is

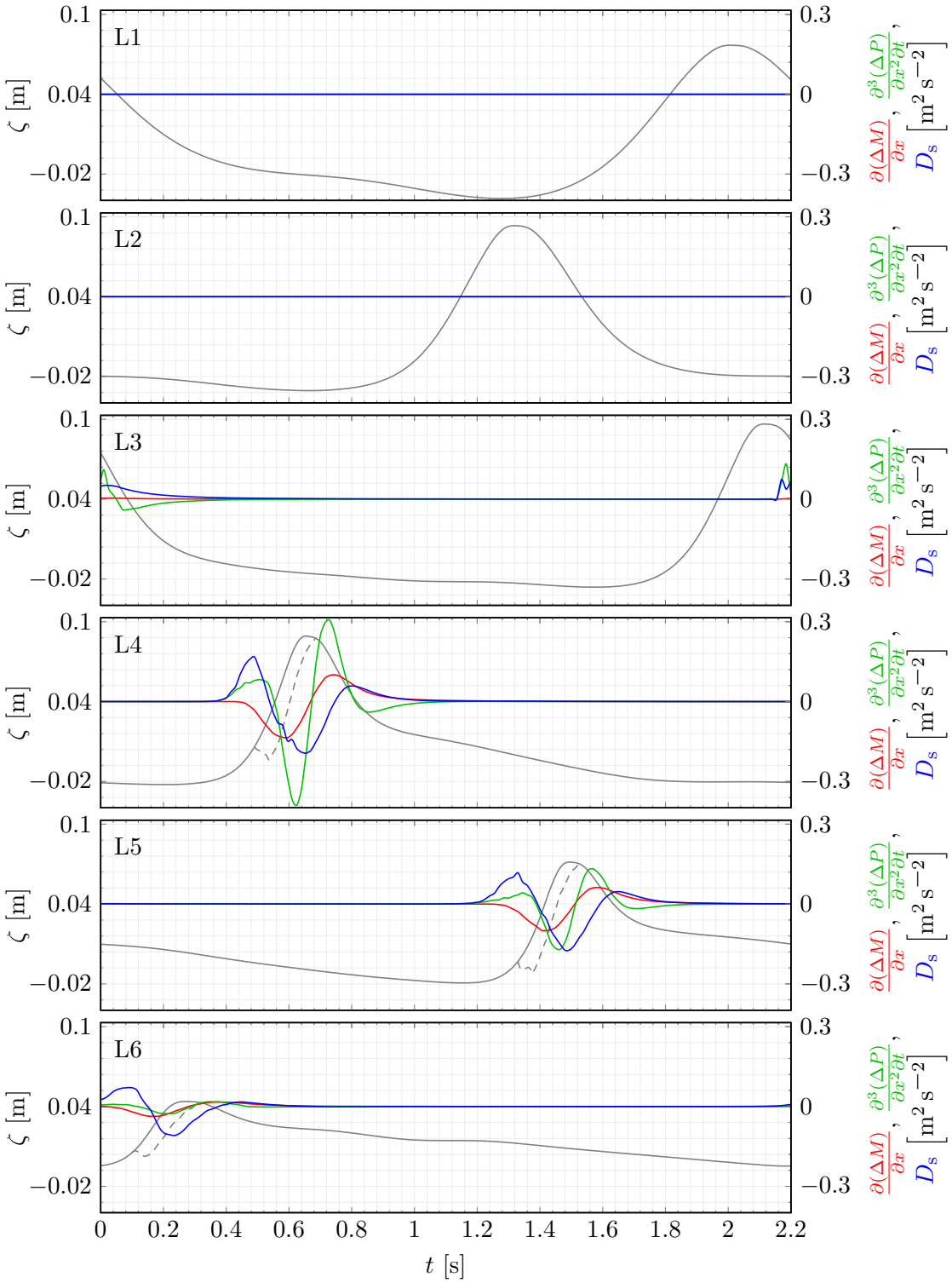

Figure 6.20: Model breaking terms $\frac{\partial(\Delta M)}{\partial x}$ (——), $\frac{\partial^3(\Delta P)}{\partial x^2 \partial t}$ (——) and D_s (——), with free surface profile (——) and lower roller edge (- - - -) for Cox et al. (1995) test.

a major cause of the more significant differences in the values adopted for calibrating FD and FVFD RBMs. A larger value of t^* is also found to produce better predictions of the horizontal velocity, meaning the development of the roller is slowed slightly. While the magnitude of the terms is generally of the same order as those calculated in Musumeci et al. (2005), there is a noticeable difference in D_s. This is again symptomatic of the different calibration required when the RBM is implemented using an FVFD scheme rather than an FD scheme.

It should also be noted that the advection of vorticity in the wake of the roller means the effects of breaking are felt further offshore. Consequently, despite being located prior to breaking initiation point and therefore where no roller is present, the breaking terms at L3 are noteworthy as their magnitude is not insignificant.

Flow rotation

As estimates for both the horizontal velocity and breaking terms are constructed from the rotationality introduced into the flow, it is sensible to also scrutinise the vorticity and rotational velocity obtained by the model. The vorticity is visualised in Figure 6.21, and presented on an alternative scale in Figure 6.22 in order to expose variations of smaller magnitude. The highest levels of vorticity are found near the point of injection, along the lower edge of the roller, where the distribution of ω_s defined by Equation (4.97) is seen to produce larger values towards the toe. The subsequent transport of vorticity is also clearly evident, and very small quantities can be found far from the roller. The observed decay in the wake of the roller shows that the vorticity has no appreciable effect across consecutive waves. This is further reinforced by the strength of the vorticity found at the front of the breaker, which outweighs any residual vorticity remaining from preceding waves. As such, there is no evidence of any meaningful interaction between adjacent breaking events.

The vorticity distribution predicted by the FVFD RBM is found to closely resemble that obtained with the FD scheme of Musumeci et al. (2005), with similarities in both the magnitude and dissemination of the procured values. Although the aforementioned work adopts a subgrid to help concentrate vorticity towards the spatial toe of the roller, the increased number of cells and finer temporal detail gained when using the FVFD scheme results in maximum values closer to the toe. While the vorticity predicted by the present model reaches as far as the bed, the wake sees the bulk quantities towards the centre of the water column, mirroring the FD RBM of Musumeci et al. (2005). The RBM of Dimas and Dimakopoulos (2009) produces vorticity that remains close to the surface of the wave, implying that less vorticity is diffused into the deeper regions of the flow. The increased permeation found with the present RBM can be attributed to the diffusion of turbulent vorticity which is not considered by the model of Dimas and Dimakopoulos (2009).

Figure 6.23 provides a view of the rotational velocity, which increases from the toe

of the roller onwards, and is greatest in the crest of the wave. The vast majority of the rotational velocity behind the peak of the wave remains towards the surface of the flow, but is quickly dissipated in accordance with the decay in vorticity discussed previously. The largest values are found within the roller and along the lower edge of this region.

Spatial properties

While the experimental results allow matching wave gauge results to be compared, the numerical model also offers views of the spatial distribution of each variable, allowing values to be scrutinised in further detail. Accordingly, the horizontal and rotational velocities and the vorticity are presented in Figure 6.24 at a single point in time. The section of the domain presented here shows the distribution of each quantity from before the onset of breaking over a distance greater than one wavelength, in order to yield a more complete picture of the stages of the breaking process.

Figure 6.24 shows the inception of breaking is located shortly beyond L3. This reaffirms the previous conclusion that, despite the absence of a roller, ω is very low at this gauge due to the small amount of offshore transportation of vorticity. Similarly, the breaking terms at this gauge are shown to be small but noteworthy in the wake of the propagating wave. While the VTE continues to act in a similar manner throughout the domain, the vorticity found at L1 and L2 can be considered purely numerical in nature and does not hold any notable physical meaning. The numerical representation means very small numbers persist as the vorticity decays, but these are insignificant and remain practically imperceptible at the scales presented here, even with the magnification afforded by Figure 6.22.

At the early stages of breaking, the vertical profile of the horizontal velocity outside the roller region is relatively uniform. Towards the latter stages of breaking, the continued injection of vorticity has caused more mixing of the fluid, and leads to greater variation across the water column. The accumulative effects of vorticity injection are also made apparent by the tail in the vorticity and rotational velocity that emerges as the wave propagates further onshore.

Undertow

Having established a prediction of the horizontal velocity, it is also possible to estimate the undertow, which is key in driving sediment transport processes. This is calculated according to

$$u_{\mathrm{u}} = \frac{1}{T}\int_0^T u \, \mathrm{d}t - \mathcal{S}, \tag{6.24}$$

where

$$\mathcal{S} = \frac{1}{T\left(h_{\mathrm{o}} + \zeta_{\mathrm{m}}\right)}\int_0^T \int_{-h}^{\zeta_{\mathrm{t}}} u \, \mathrm{d}z \, \mathrm{d}t \tag{6.25}$$

denotes the slosh, and ζ_{t} indicates the trough of the free surface elevation. The term defined in Equation (6.25) accounts for the net volume flux over each wave period. A

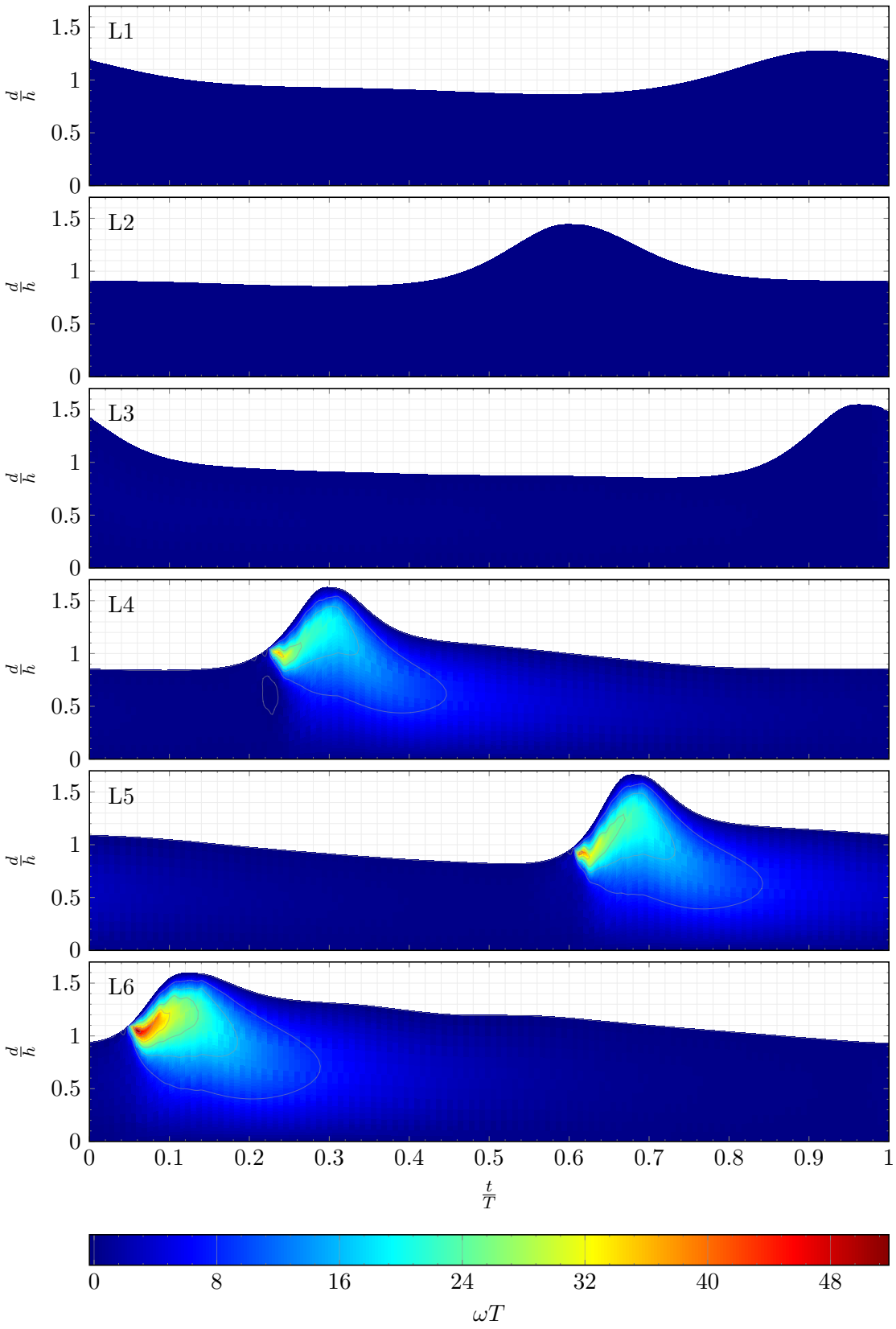

Figure 6.21: Temporal evolution of vorticity calculated by model at six locations using a linear scale.

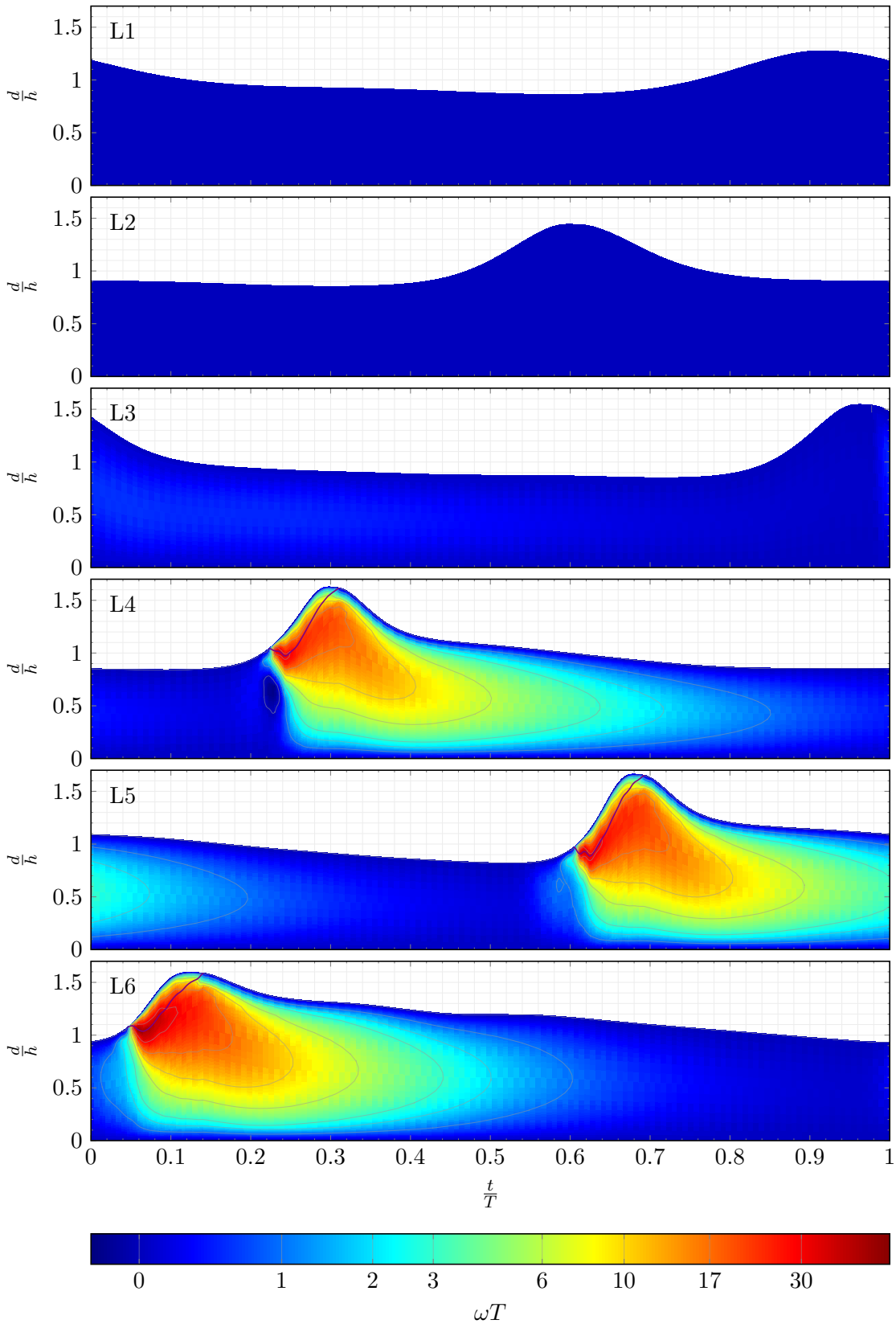

Figure 6.22: Temporal evolution of lower edge of roller (——) and vorticity calculated by model at six locations using an inverse hyperbolic sine scale.

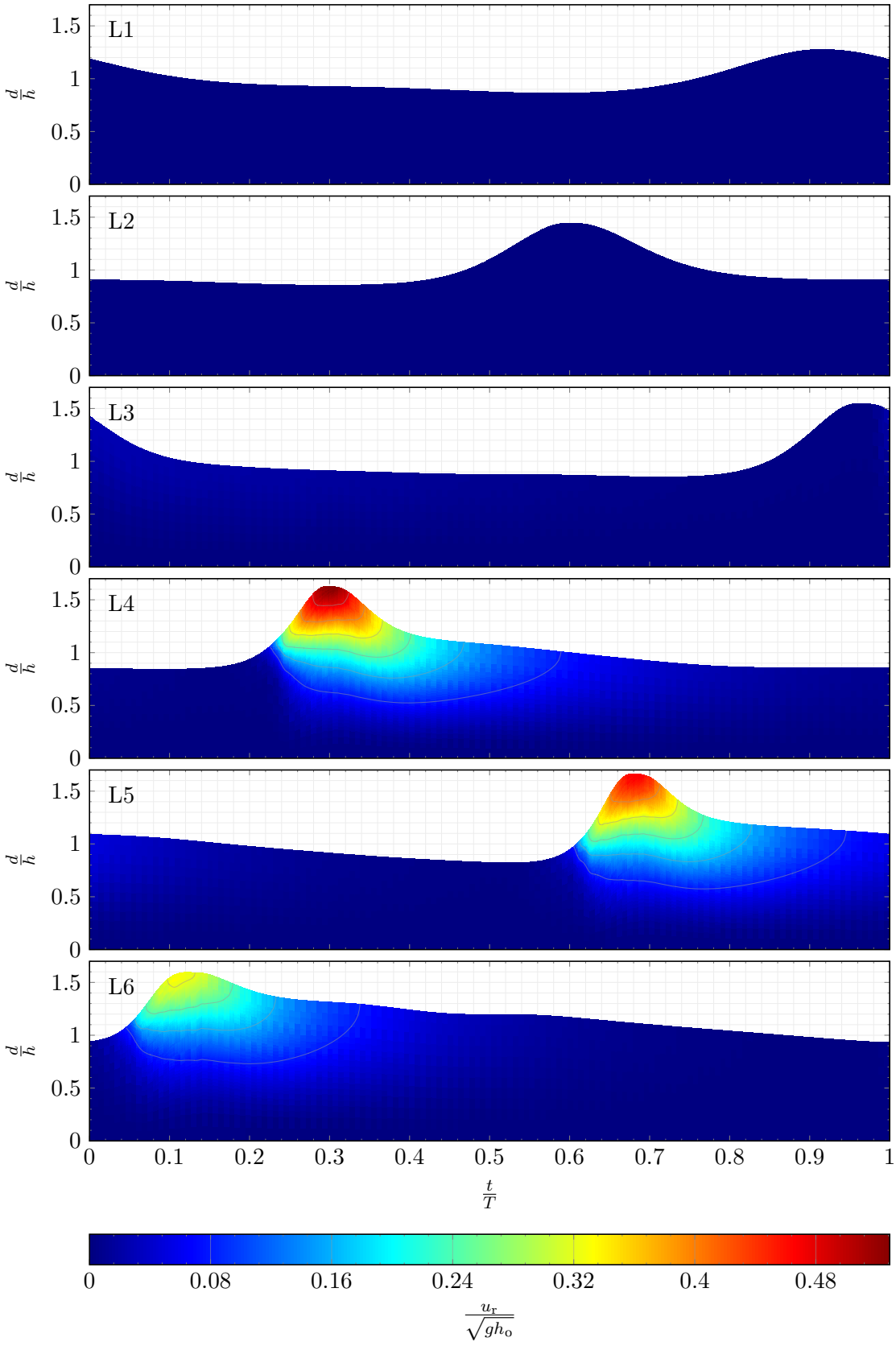

Figure 6.23: Temporal evolution of rotational velocity calculated by model at six locations.

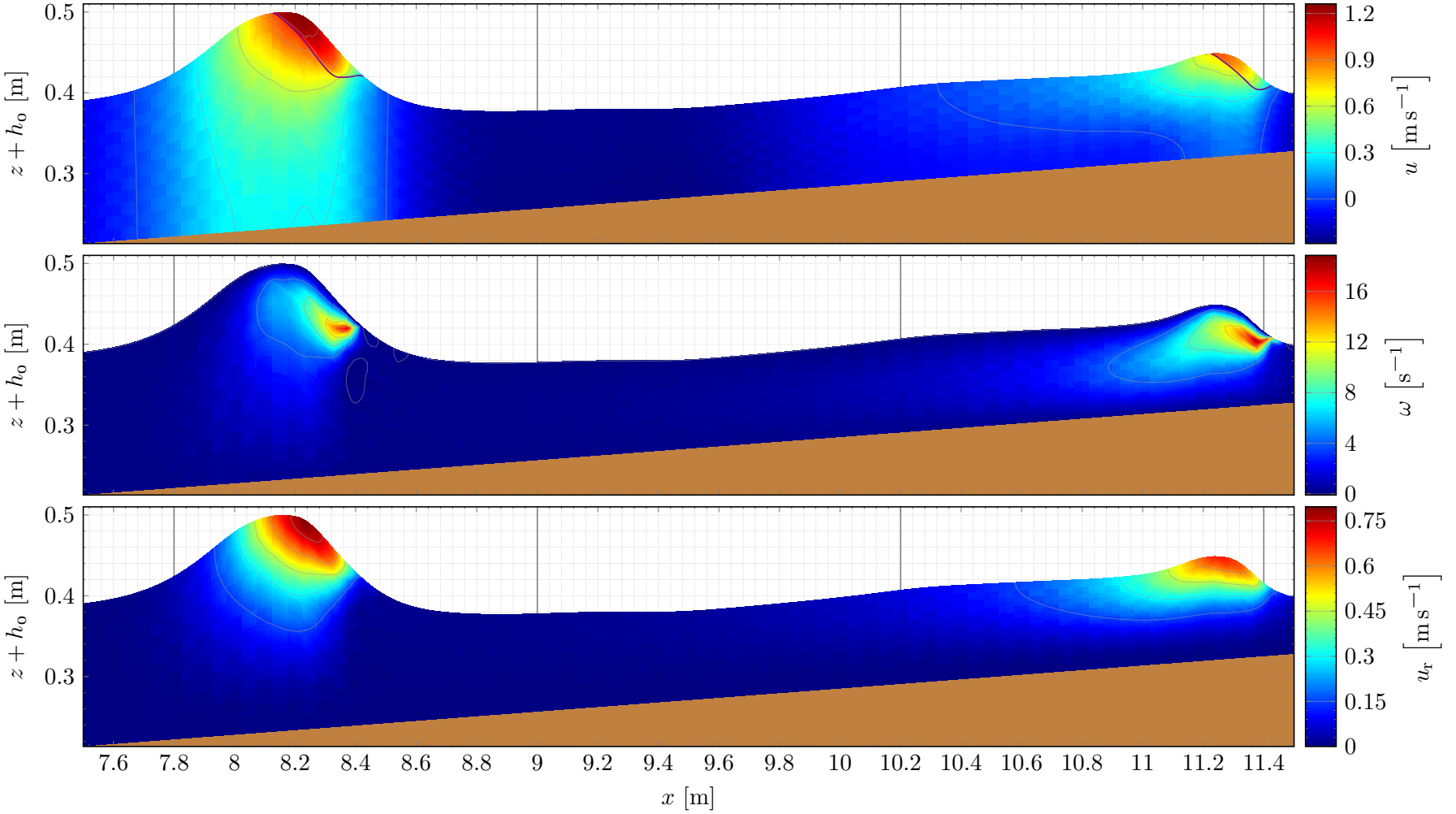

Figure 6.24: Wave propagation onshore, with distribution of horizontal velocity, vorticity and rotational velocity calculated by model. The location of gauges L3, L4, L5 and L6 are shown (——), and the lower edge of the roller region is visualised (——, top).

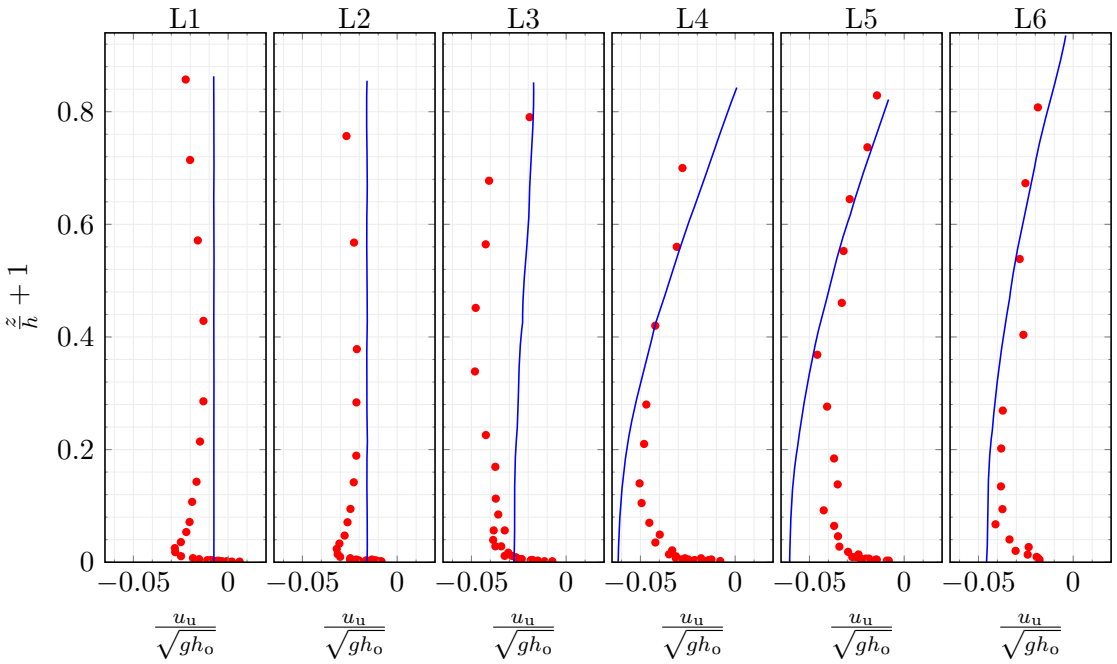

Figure 6.25: Model undertow (——) compared with undertow from measurements (•) of Cox et al. (1995).

major benefit of SRMs is their ability to predict the undertow within BTMs which, due to the absence of roller effects within the model, is not otherwise possible. The undertow distributions corresponding to the horizontal velocities shown previously are given in Figure 6.25. The assumptions of inviscid flow and absence of a bottom boundary layer in the present model are clearly evident in the undertow predictions. The magnitude of the undertow prior to breaking is also found to be slightly less than that given by the experimental results, although the values are still of similar order, and demonstrate the ability of the BTM to reasonably replicate this quantity where no roller is present. Following the onset of breaking, the roller is shown to act appropriately. Away from the bottom boundary layer, a very good agreement is found between the undertow calculated from the experimental and numerical results. With further work, the model could be extended to incorporate the effects of bed friction.

Table 6.4 provides indicative values of the error in the horizontal velocity and undertow at each gauge location, indicating the similarity between the experimental and numerical data as the wave propagates onshore. This once more shows the undertow error to be largest before breaking, although the most substantial overall error in horizontal velocity is found at L4. This is again explained by the shortcomings of the WNBs in fully replicating the shoaling, with the subsequent difference in wave heights and velocities greatest at L4.

The undertow error can be partly attributed to the different progression of the breaking process required by the model in each case. The smaller wave height at the onset of breaking means a different amount of energy should be dissipated at each stage.

Table 6.4: Quadratic error in horizontal velocity field and undertow.

Gauge	x [m]	$\epsilon_2(u)$	$\epsilon_1(u_\mathrm{u})$
L1	4.2	0.016	0.355
L2	6.6	0.068	0.11
L3	7.8	0.229	0.167
L4	9	0.384	0.049
L5	10.2	0.19	0.156
L6	11.4	0.085	0.033

This leads to a small variation in the role of the roller, which becomes most evident at L5. Briganti et al. (2004) provide a comparison of the error in undertow using an FD RBM BTM with both a semi-analytical integration along the water column, as used in the present study, and a number of numerical approaches. Compared to any of the aforementioned methods, the model proposed in the present work obtains a smaller error at gauges L4 and L6. Although the numerical approaches show improvement at gauge L5, the corresponding semi-analytical approach again produces a much larger quadratic error.

6.5 Wave groups

The behaviour of the RBM is particularly sensitive to the location of the breaking point, as this significantly influences the resulting dissipative terms. The breaking location exhibited in the monochromatic wave tests presented previously remains relatively static due to the regular nature of the incoming waves. More advanced processes can be investigated by varying the properties of the wave over time. The increase in complexity is especially noteworthy due to the dynamic nature of the system. Changes in the breaking process influence the subsequent system state, which in turn alters the characteristics of breaking events that follow.

The group wave tests performed here provide an effective means to analyse the robustness of a model and assess its ability to adapt dynamically to ongoing changes. It is important that the model is capable of accurately replicating the breaking process for a range of scenarios without requiring external intervention or independent calibration for individual waves. Aside from the still water depth of $h_\mathrm{o} = 0.4\,\mathrm{m}$ and still water slope length of $l_\mathrm{s} = 14\,\mathrm{m}$, the experimental setup described in Section 6.4.1 is duplicated. A cyclic series of five waves is generated according to

$$H_n = H_\mathrm{g}\left[1 + \frac{\mathcal{G}}{2}\sin\left(\frac{2n\pi}{5}\right)\right] \quad n \in \mathbb{N}_1, \tag{6.26}$$

where H_g is the wave height of the group, and the groupiness, $\mathcal{G}$, allows control of the variability of the height of the wave train. This produces a repeating sequence of five

Table 6.5: Wave parameters for Svendsen and Veeramony (2001) tests.

Test	$f_{\mathrm{w}}\left[\mathrm{s}^{-1}\right]$	H_{g} [m]	$\mathcal{G}$
W01	0.667	0.0668	0.1
W03	0.4	0.0948	0.2
W06	0.625	0.1	0.5

waves, where the height of the nth wave is given by H_n. The parameters for each test are given in Table 6.5.

The remaining model parameters are inherited from Section 6.3, with $\Delta x = 0.04\,\mathrm{m}$ and $\Delta t = 0.012\,\mathrm{s}$. When generating incoming waves, it is again ensured that the resulting wave height at the toe of the slope matches that observed experimentally. In order to obtain a suitably representative value for the range of different waves, some discretion is required where, within the numerical and experimental groups, there is deviation between the variability of the wave height and frequency.

In order to separate any variance between the experimental and numerical set-up and allow a more direct comparison between the wave shapes in each case, the results presented here are modified according to the mean water level at each gauge. This is achieved by presenting adjusted free surface profiles in terms of

$$\zeta_{\mathrm{s}} = \zeta - \zeta_{\mathrm{m}}. \tag{6.27}$$

Figure 6.26 provides the results for the first of the group tests, which comprises the smallest mean wave height and groupiness. Here, the eddy viscosity is taken as $\nu_{\mathrm{t}} = 0.02\,\mathrm{m}^2\,\mathrm{s}^{-1}$. The wave height observed experimentally is shown to be very well reproduced by the model throughout the region of interest. Some minor variation in the phase of the waves can be seen across the group, and a slight difference in the surface profile is again observed in the shoaling region. These two discrepancies are related, and show the influence of the total water depth on the speed at which waves propagate.

For the second group wave test, the RBM is calibrated with $\nu_{\mathrm{t}} = 0.03\,\mathrm{m}^2\,\mathrm{s}^{-1}$. The findings of the first group wave case are reiterated by the comparison given in Figure 6.27, although the increase in groupiness and incoming wave height means the features become more conspicuous. A delay in the effects of wave breaking is evident for some parts of the group, with the numerical and experimental surface profiles diverging in the surf-zone, and then converging towards the inner surf-zone. This again highlights the sensitivity of the breaking location and the difficulties presented when trying to replicate complicated dissipation mechanisms with a BTM. The qualitative evolution in the wave shape is reproduced, nonetheless, and the total decay in the wave height is comparable across the recorded region.

The final test validating the FVFD RBM uses $\nu_{\mathrm{t}} = 0.04\,\mathrm{m}^2\,\mathrm{s}^{-1}$. The results for this case are provided in Figure 6.28, which again allows the capabilities of the model to be

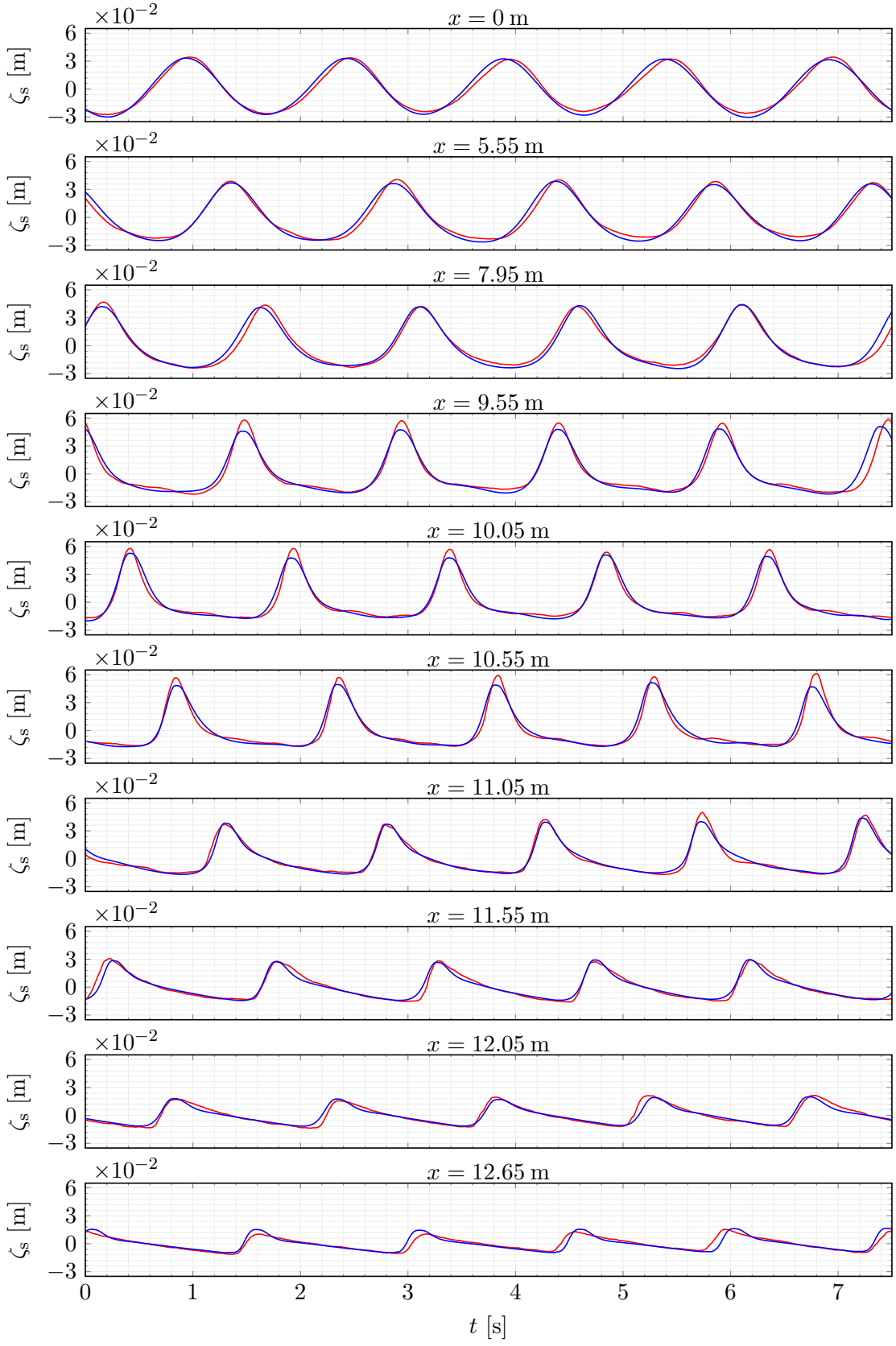

Figure 6.26: Experimental (——) and numerical (——) results for group wave test W01.

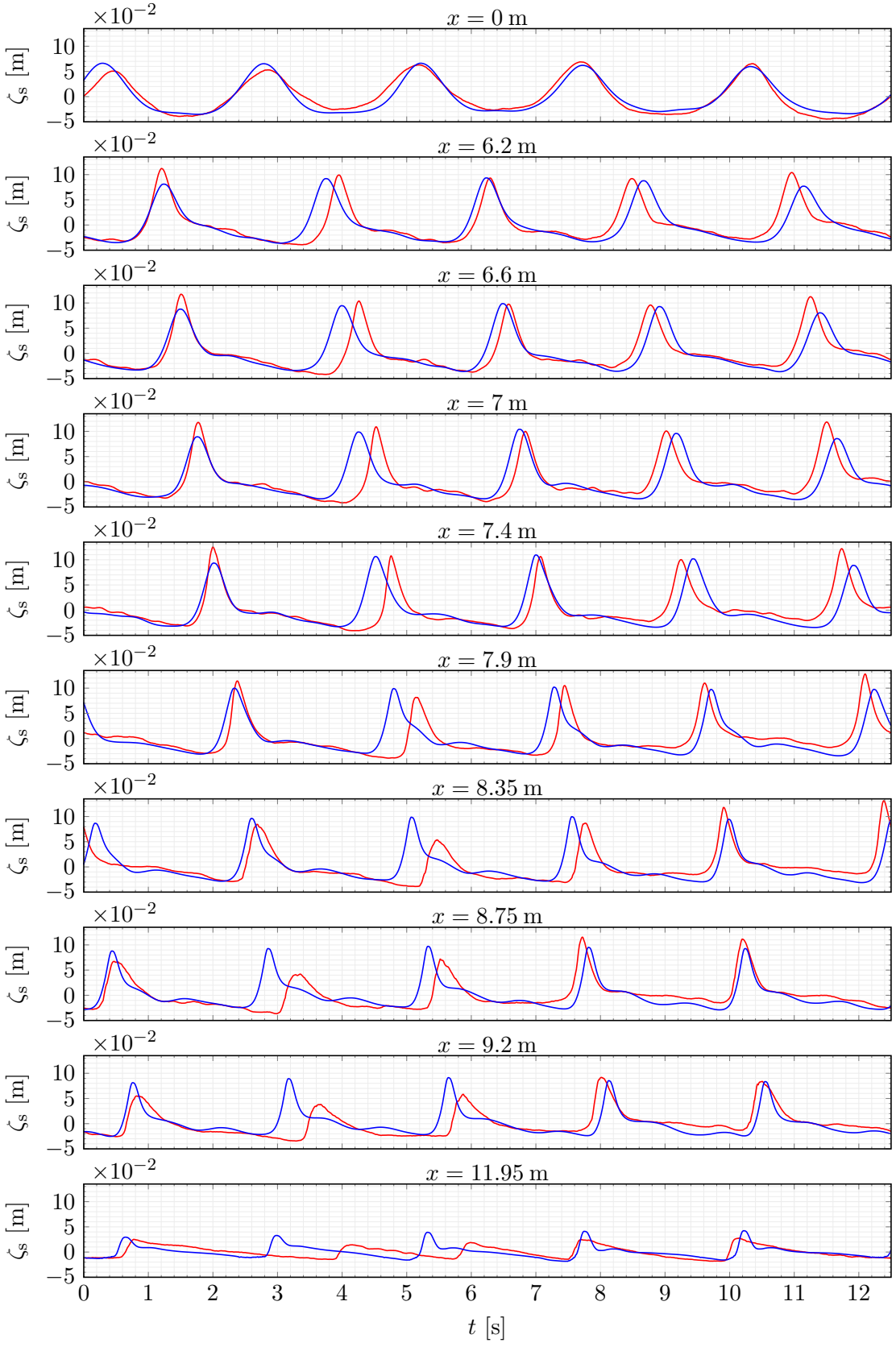

Figure 6.27: Experimental (——) and numerical (——) results for group wave test W03.

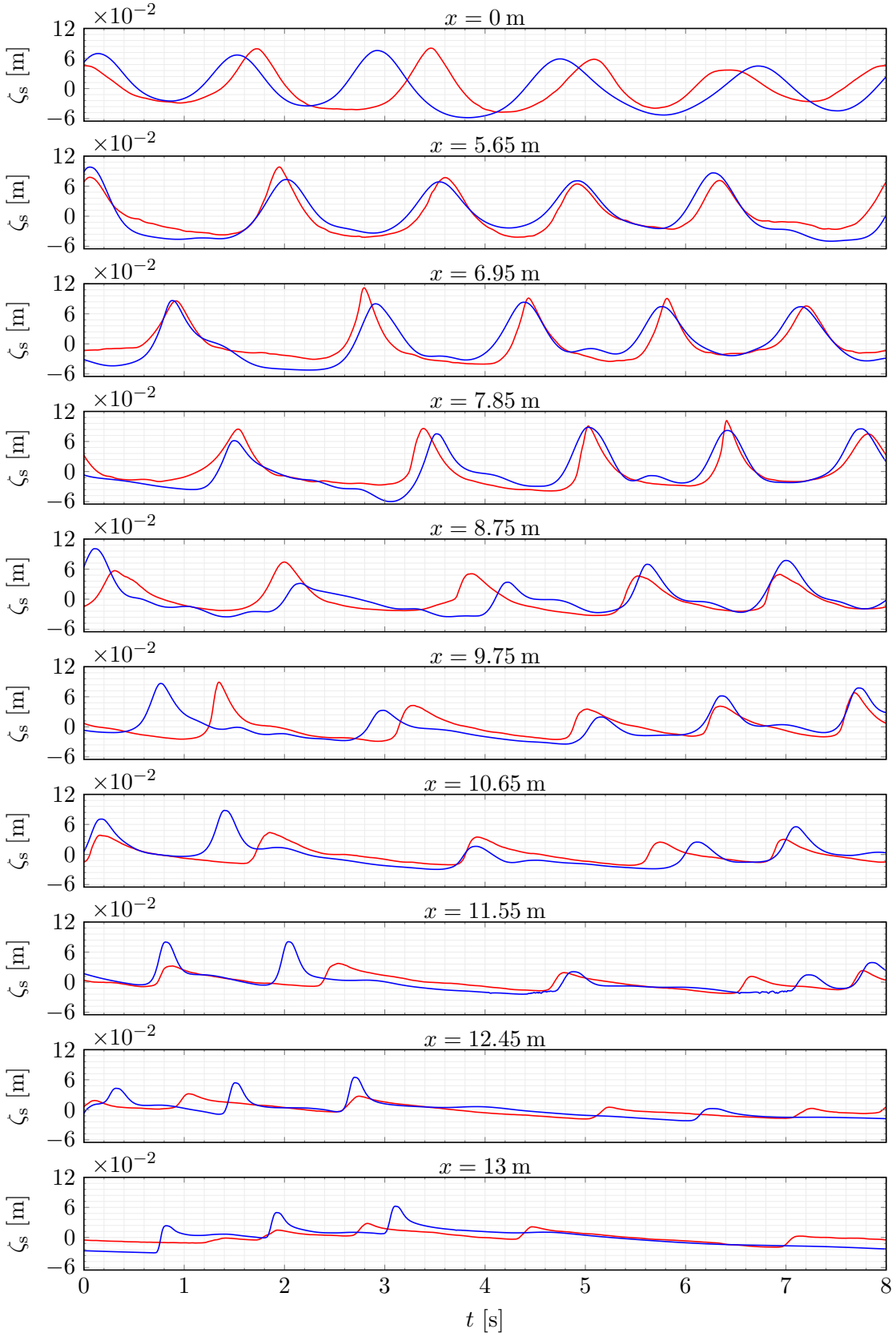

Figure 6.28: Experimental (——) and numerical (——) results for group wave test W06.

assessed against experimental data. The challenges presented by the variation across the wave train are clear, and the differences observed with the previous two group tests intensified. Even so, similarities in the qualitative transformation of the surface profile remain apparent, and the reduction in wave height is reasonable for much of the group. In particular, the grouping between sequential waves due to the variation in the rate of change of the phase speed is visible.

6.6 Summary of results

The tests presented in this chapter have demonstrated the capabilities of the proposed model used in this study and identified the limitations of the adopted approach. Good agreement with analytical solutions to dam break and steady flow tests show the competency of the numerical scheme for solving the components of the governing equations treated using the FV method. The shock-capturing capabilities of this technique are evidenced, and the effect of the limiters used by the FOCMT scheme is shown to be sufficiently small when applied to these problems.

The solitary wave tests extend the validation to assess the inclusion of higher-order Boussinesq terms, thereby allowing the model to be evaluated with the WNBs used for subsequent cases involving wave breaking. The numerical dissipation visible is consistent with that observed in previous studies of models using similar schemes.

The addition of an RBM is shown to provide appropriate energy dissipation for the model during the breaking process. The resulting reduction in wave height closely matches experimental observations and is similar to that achieved with an HBM, although the WNBs are found to understate the shoaling in the nearshore region. By incorporating additional terms describing the rotational components of the flow, the RBM provides velocity profiles and undertow predictions across the water column. Comparisons with experimental data show these results to be realistic and support the selected calibration parameters used for the breaking model.

Finally, the group wave tests included in this chapter illustrate the behaviour of the model for a series of waves with differing height. The sequence of waves produces a variation in the location at which breaking initiates, and therefore demonstrates the model to be capable of adjusting in response to changes in local conditions. Although differences in the wave height due to the weakly-nonlinear nature of the model further increase some discrepancies between experimental and numerical results, a good overall agreement is obtained.

Chapter 7

Dissipation mechanisms

7.1 Rationale for analyses

When solving complex processes such as those studied here, physical phenomena may be reproduced incorrectly. The highly turbulent flow present during wave breaking results in a significant amount of energy dissipation. Since this is not replicated by irrotational BTEs, it is necessary to add an external mechanism to represent this aspect of the hydrodynamics. By considering the physical nature of the dissipative process, a realistic method can be developed which removes the correct amount of energy from the system. In order to assess the impact of proposed dissipation mechanisms, it is important to quantify their effects. A number of alternative techniques are compared here. Any properties of the numerical scheme resulting in similar behaviour beyond the point of breaking initiation should also be identified, as these can artificially dissipate energy and give the illusion of breaking, without replicating the turbulence within the flow.

As the dissipation of energy introduced by the RBM constitutes a large part of the study presented here, it is important to investigate the behaviour of the numerics in detail. In particular, in order to correctly represent the physics, it is important to mitigate against the impact of any significant actions resulting from numerical effects. The nature of the mathematics describing the breaking process in RBMs demands the use of higher-order derivatives, which can introduce a need for more aggressive numerical filtering to limit unwanted oscillations in the FD solution. As noted by Brocchini (2013), the influence of this within the numerical scheme requires careful reflection.

Three courses of investigation are pursued here, the first of which investigates the effect of the injected vorticity distribution on the reduction in wave height in the surf-zone. The second compares the reduction in wave height obtained with different breaking approaches, while the final tests examine the energy dissipation achieved with various combinations of limiters and resolutions. While it is not possible to explicitly separate the external dissipation techniques from the numerical effects, the comparison performed

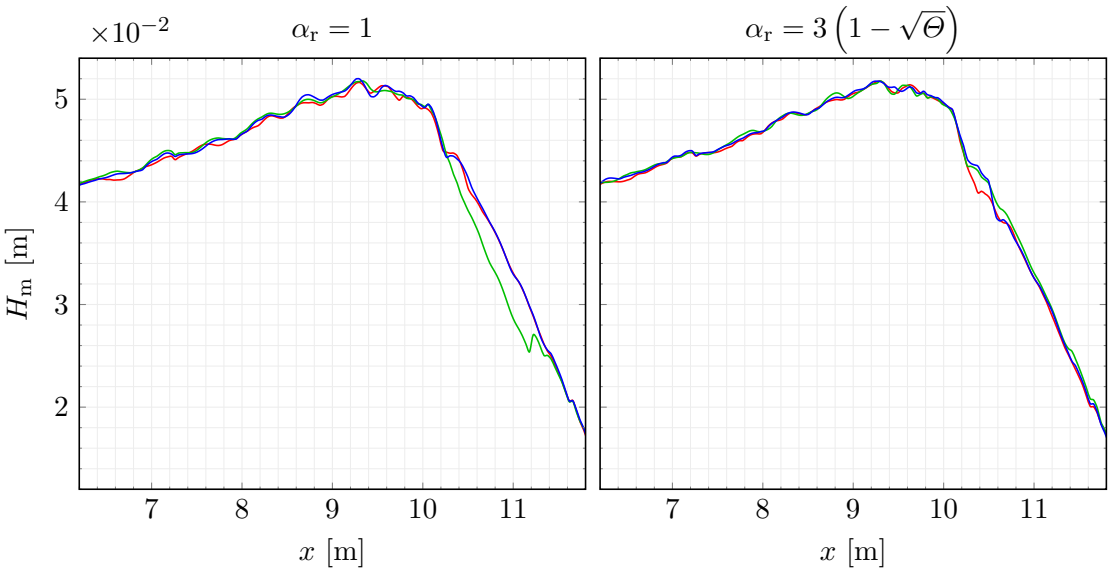

Figure 7.1: Wave height for Test O for a range of vorticity injection profiles using $\alpha_v = 20$ (——), $\alpha_v = 40$ (——), and $\alpha_v = 80$ (——) with different distribution functions given by α_r.

here provides an effective indication of the role of the breaking mechanism in each case.

7.2 Vorticity injection

As explained in Section 4.9, the RBM looks to replicate the physics of the rotational processes when injecting vorticity into the flow. In order to ease the demand placed on the model by the high gradient in ω_s, Equation (4.98) includes a modification to the empirically derived formula of Veeramony and Svendsen (2000) used to define the distribution of injected vorticity. In order to more thoroughly investigate the numerical properties of this technique, the dissipation achieved using different functions to describe v is explored. The RBM is employed with different functions for α_r, along with a range of values for α_v, thereby testing the different profiles illustrated in Figure 4.2.

While the resilience of the FVFD scheme allows steep gradients to be included in the definition of v, the FD scheme employed in the solution of the breaking terms means the choice of function must still be carefully considered. With lower values of α_v, the strain on the numerical scheme is reduced as the gradient in the profile at the toe is less severe. As this also results in a smaller quantity of injected vorticity in this region, a balance must be reached. The spatial discretisation performed for the tests studied here means the different values of α_v typically affect only one cell significantly. The more distinctive change in v seen with the different functions for α_r results in considerably different numerical values throughout the roller region.

The tests described in Section 6.4.1 are repeated using numerous combinations of α_r and α_v, and the resulting wave height envelopes given in Figures 7.1 to 7.3. Although

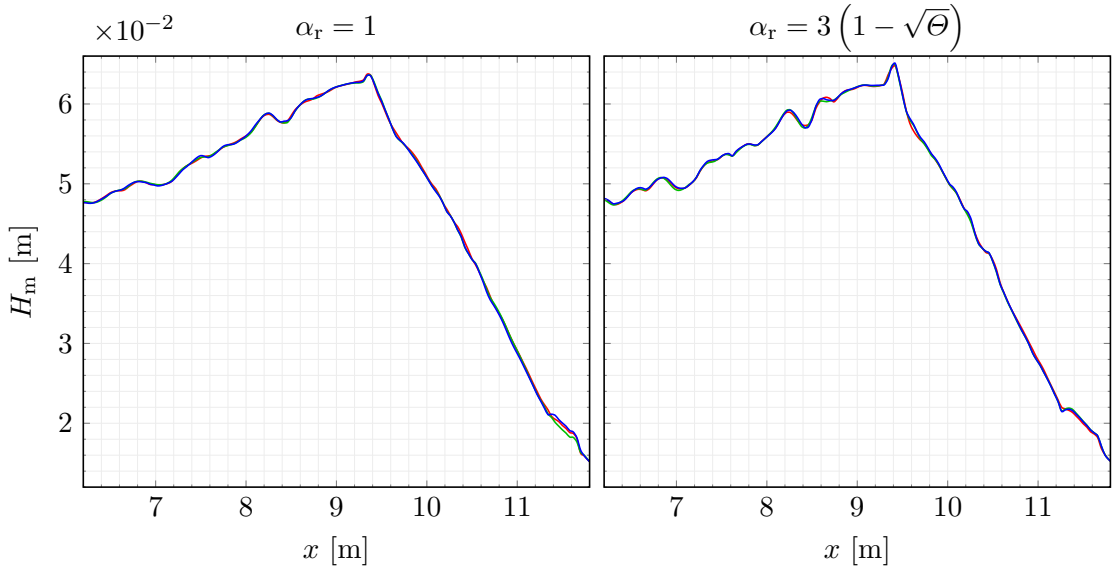

Figure 7.2: Wave height for Test Q for a range of vorticity injection profiles using $\alpha_v = 20$ (——), $\alpha_v = 40$ (——), and $\alpha_v = 80$ (——) with different distribution functions given by α_r.

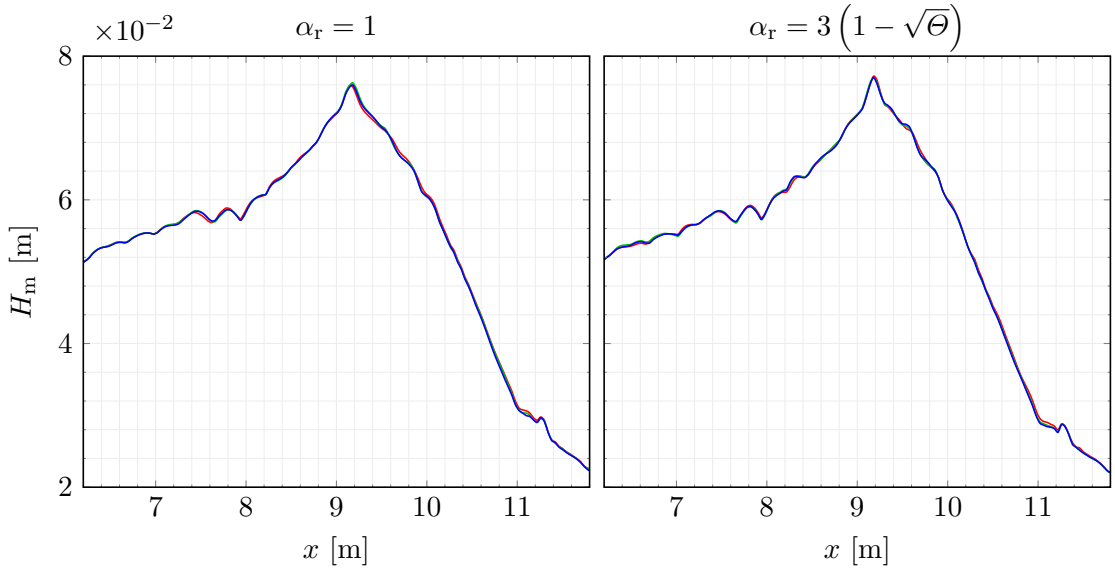

Figure 7.3: Wave height for Test R for a range of vorticity injection profiles using $\alpha_v = 20$ (——), $\alpha_v = 40$ (——), and $\alpha_v = 80$ (——) with different distribution functions given by α_r.

some variation is observed, the effect of α_{v} is not found to be significant. The results for Test O show little difference in wave height decay with different values of α_{r}, except in the case with $\alpha_{\mathrm{v}} = 40$ and $\alpha_{\mathrm{r}} = 1$, where an obvious variation exists. This can be attributed to the calibration of the other breaking parameters, which have been kept constant throughout. As such, the adjusted distribution of vorticity acts slightly differently during the breaking process, resulting in more obvious differences in H_{m}. With Test Q and Test R, a larger peak wave height is achieved with $\alpha_{\mathrm{r}} = 3\left(1 - \sqrt{\Theta}\right)$, beyond which the wave height is then below that observed with $\alpha_{\mathrm{r}} = 1$. Although the difference is very small, this trend is consistent for all values of α_{v} with Test Q and Test R.

The analysis performed here only considers the calibration outlined previously. The results in each case could be improved with individual tuning of each breaking parameter which, for the purposes of clarity and consistency, remain unchanged here. As only α_{v} and α_{r} have been altered between tests, the total injected vorticity varies in each case, according to the values provided in Table 4.1. Although further investigation into the effect of combining different parameters could incorporate more acute management of the RBM for each case, the limited variation seen here suggests the difference between the specified profiles for v to be minimal, thereby confirming the values selected for this study to be appropriate.

7.3 Numerical effects

Considering both the HBM and RBM allows the behaviour of each approach to be compared. By also executing the same tests with no breaking model (NBM), the performance of the scheme without any external dissipation mechanism can be quantified. This gives a sense of how much energy is dissipated by the HBM and RBM, and allows the inherent numerical properties of the FOCMT scheme to be estimated. Additionally, the eddy viscosity approach used by Cienfuegos et al. (2010) is employed to allow the performance of the model to be further compared using another existing dissipative technique.

7.3.1 Eddy viscosity method

The eddy viscosity breaking model (EVBM) used here adopts the SRM employed by the RBM for the present study, thereby allowing a direct comparison of the two dissipation techniques with the same roller. The calibrations made by Cienfuegos et al. (2010) for a spilling breaker are applied here. Based on the assumption that the distribution of the maximum shear stress and the local roller thickness are similar, the EVBM defines a diffusivity function reminiscent of that given in Equation (4.94):

$$\nu_{\mathrm{h}} = 2\sqrt{gh^3}\Theta\left(1 - \Theta\right)\exp\left(-\Theta\right) \tag{7.1}$$

This term forms the basis of two new dissipative terms,

$$D_{\mathrm{h}} = \frac{\partial}{\partial x}\left(\nu_{\mathrm{h}}\frac{\partial d}{\partial x}\right) \tag{7.2}$$

Table 7.1: Offshore Iribarren number, ξ_o, for the considered range of numerical tests.

Wave frequency, f_w $\left[s^{-1}\right]$	Offshore wave height, H_0 [m]				
	0.035	0.037	0.039	0.041	0.043
0.6	0.264	0.257	0.25	0.244	0.238
0.55	0.278	0.27	0.263	0.256	0.25
0.5	0.293	0.285	0.278	0.271	0.264
0.45	0.311	0.302	0.295	0.287	0.281
0.4	0.332	0.322	0.314	0.306	0.299
0.35	0.356	0.346	0.337	0.329	0.321
0.3	0.386	0.376	0.366	0.357	0.348

and

$$D_u = 10\frac{\partial}{\partial x}\left(\nu_h \frac{\partial q}{\partial x}\right), \tag{7.3}$$

which are then introduced into the continuity and momentum equations, respectively. These replace the breaking terms included previously with the RBM, and a modified form of Equation (3.63) used to define the source term:

$$\boldsymbol{S} = \begin{bmatrix} D_h \\ gd\dfrac{\partial h}{\partial x} - Bgh^2\left(2\dfrac{\partial h}{\partial x}\dfrac{\partial^2 \zeta}{\partial x^2} + h\dfrac{\partial^3 \zeta}{\partial x^3}\right) + D_u \end{bmatrix} \tag{7.4}$$

It should be noted that the EVBM used here does not consider the roller thickness in the calculation of the viscous terms, the impact of which is investigated by Klonaris et al. (2013). As with the RBM, a first-order Shapiro filter is used to manage any oscillations in the FD breaking terms. The calibration parameters used to define the geometry of the roller mirror those used for the RBM for all tests presented here.

7.3.2 Wave height decay

Assessing the model for a range of wave frequencies and amplitudes provides an overview of the characteristics of the different configurations of the numerical model. The setup described in Section 6.4.1 is employed again, along with the wave characteristics outlined in Table 7.1 which details the range of test cases presented here and provides the corresponding Iribarren number in each case. All of the tests performed here use spatial and temporal resolutions of $\Delta x = 0.04\,\text{m}$ and $\Delta t = 0.012\,\text{s}$, respectively. In each case, the internal wave generation is calibrated to ensure the appropriate wave height is obtained at $x = -2\,\text{m}$. In order to allow a direct comparison of the behaviour of the RBM with differing physical parameters, the calibration variables remain constant, with $\nu_t = 0.01\,\text{m}^2\,\text{s}^{-1}$ and the values listed in Section 6.3 used throughout.

Figures 7.4 and 7.5 present the wave height decay for a number of different combinations of wave frequency and amplitude using both van-Leer and minmod third-order limiters. In each case, the location of the breaking point found furthest from the shore during the final four wave periods with the RBM is indicated. With the parameters selected here, the RBM does not result in any breaking when the van-Leer limiter is used with $f_w = 0.6\,s^{-1}$ and $H_o = 0.035\,m$ or $H_o = 0.037\,m$. The vertical lines marked in Figure 7.4 indicate the earliest breaking locations in the remaining cases. The stronger dissipation found with the minmod limiter results in reduced shoaling, preventing the waves from becoming steep enough for breaking to initiate. As a consequence of this, several of the results in Figure 7.5 are identical for tests with and without external dissipation mechanisms.

The model is shown to be consistent across a range of scenarios, with the relative reduction in wave height largest with smaller wave frequencies and incoming wave heights. In the context of the present study, the variation between different breaking approaches is also of interest. Where breaking occurs, the RBM and HBM both reliably dissipate more energy from the selected part of the domain than with NBM. This illustrates the need for an external dissipation mechanism in order to improve the accuracy with which the breaking process is described. In most cases, the EVBM also results in smaller wave heights than with NBM, but some tests show convergence at later stages of breaking, suggesting the dissipation is not sustained throughout the breaking process when this method is used. The HBM is repeatedly shown to result in a larger reduction in wave height than the RBM, although the two profiles converge as the rate of decay of the wave height achieved with the HBM declines.

The difference between the simulations with NBM, an RBM, an EVBM and an HBM becomes more prominent with larger wave heights and smaller frequencies. The EVBM exhibits less stability than the RBM, but often creates a steeper reduction in wave height immediately after the initiation of breaking. It should be emphasised that in many cases, with individually tailored breaking calibration parameters, the RBM is capable of dissipating more energy than for the tests performed here. The EVBM used here inherits several simplifications from that studied by Cienfuegos et al. (2010), which would allow similar adjustments to the calibration parameters in order to improve the reduction in wave height achieved. The dissipative nature of the minmod limiter restricts the shoaling and therefore causes wave breaking to initiate closer to the shore. The trends between breaking approaches otherwise remains generally the same as with the van-Leer limiter.

7.3.3 Energy dissipation

By considering the change in energy observed during breaking for the tests of Hansen and Svendsen (1979), it is possible to quantify the energy dissipated by the model. The variance of the surface profile, E, is proportional to the wave energy, and can be calculated by integrating ζ in time. The analysis performed here determines the variance

over the final four wave periods using the following relation (Goda, 2010; Weisse, 2010):

$$E = \frac{1}{M_\mathrm{t}} \sum_{n=1}^{M_\mathrm{t}} \left(\zeta^{(n)}\right)^2 - \left(\frac{1}{M_\mathrm{t}} \sum_{n=1}^{M_\mathrm{t}} \zeta^{(n)}\right)^2 \tag{7.5}$$

Here, the number of timesteps within four wave periods is taken to be

$$M_\mathrm{t} = \left\lfloor \frac{4T}{\Delta t} \right\rfloor. \tag{7.6}$$

The peak wave height recorded from the experimental tests is then used as an estimate of the location of breaking initiation, at which point the variance of the wave surface profile is given by E_b. The change in variance relative to this point is then calculated as

$$\Delta E = E_\mathrm{b} - E. \tag{7.7}$$

While the solitary wave tests performed in Section 6.2.3 illustrate the FOCMT scheme is capable of simulating wave propagation over a flat bathymetry without excessive levels of numerical dissipation, the subsequent tests involve cases where the Boussinesq terms become more significant. With larger higher-order terms, the influence of the limiters becomes greater, as they must counteract more significant oscillations that may result from the discretisation used for the calculation of the derivatives. This signals two aspects of the scheme that require further study with regards to energy dissipation, specifically the selected model resolution and the slope limiters used. In order to retain a comparable Courant number coefficient in each case, the spatial and temporal resolutions are adjusted simultaneously, with $\Delta t = 0.012\,\mathrm{s}$ used when $\Delta x = 0.04\,\mathrm{m}$, and $\Delta t = 0.009375\,\mathrm{s}$ when $\Delta x = 0.03125\,\mathrm{m}$.

The change in energy from the breaking point found with Test O is presented in Figure 7.6 for a range of spatial and temporal resolutions and using both van-Leer and minmod limiters. The equivalent analyses for Test Q and Test R are provided in Figures 7.7 and 7.8, respectively. The same trends between the dissipation approaches observed in the previous section are again visible, with the reduction in energy achieved by the RBM typically lying between that found with NBM and the HBM.

The EVBM consistently dissipates less energy than the RBM, but is also typically placed between the results with NBM and the HBM. Closer to the shoreline, the rate of dissipation is noticeably reduced. In the most extreme instances, less energy is dissipated with the EVBM than with NBM, although this does not imply a smaller wave height in the inner surf-zone. Instead, this occurs when the external dissipation mechanism provided by the EVBM results in a lower peak, since breaking initiates prior to the decay in wave height caused by the numerical scheme.

The interaction between numerous facets of the model can complicate efforts to distinguish between the causes of different characteristics that are observed. Any dissimilarities between each case should therefore be carefully considered in order to reasonably separate the effects of each aspect of the model. This is exemplified when the

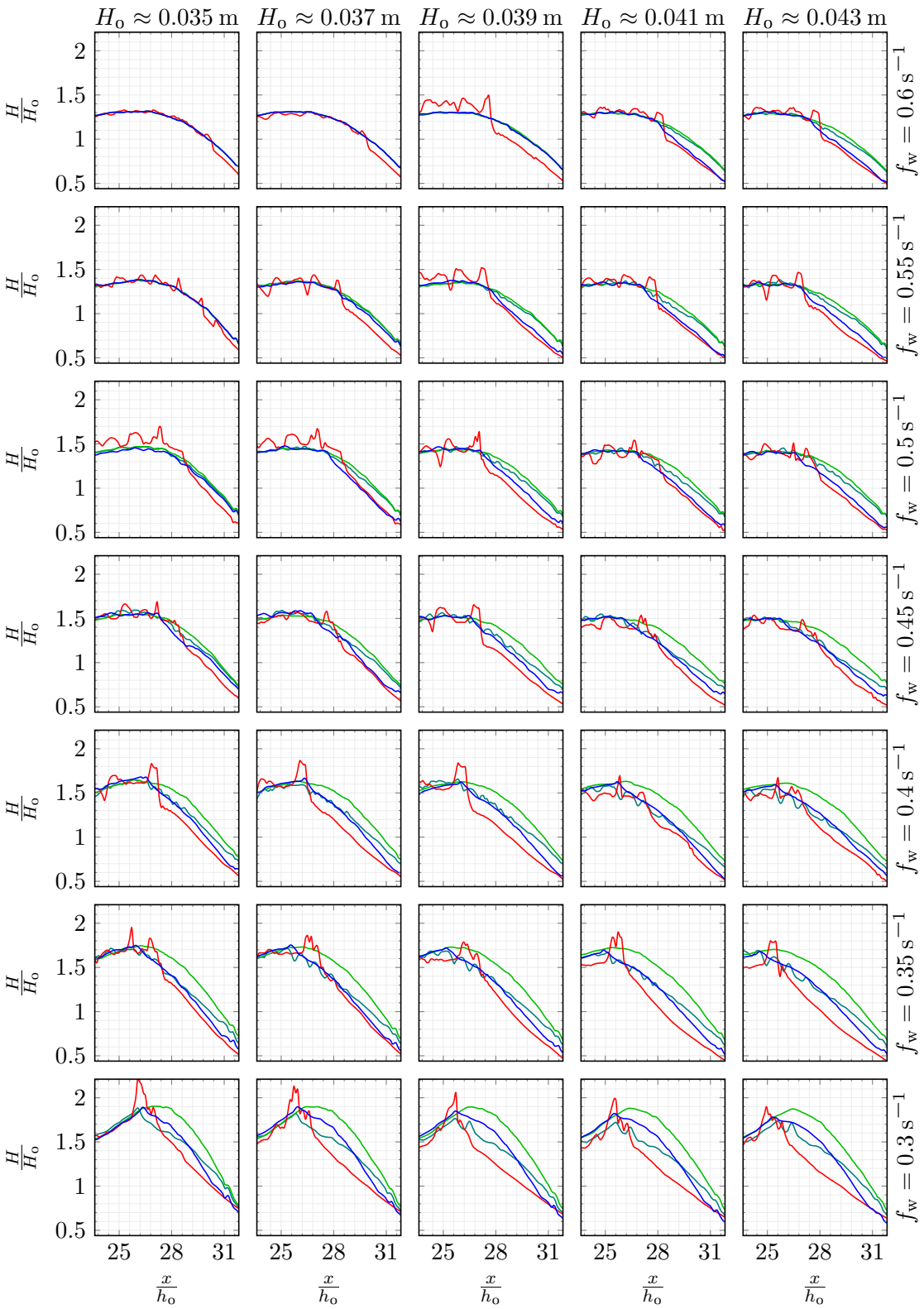

Figure 7.4: Wave height for a range of wave frequencies and amplitudes using $\phi_3 = \phi_v$ with NBM (——), and with an EVBM (——), an HBM (——) and an RBM (——), along with the minimum breaking location established by the RBM (——).

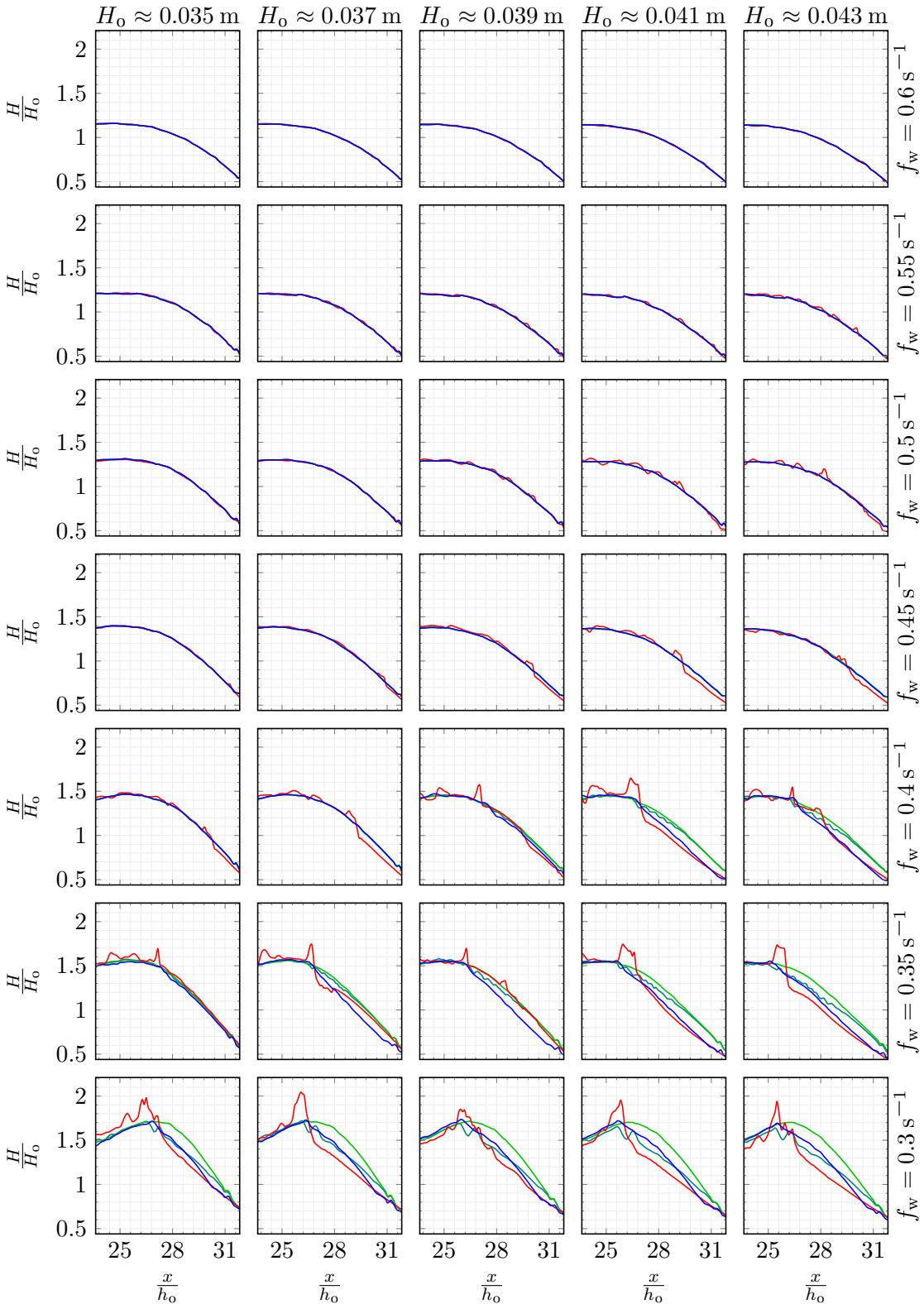

Figure 7.5: Wave height for a range of wave frequencies and amplitudes using $\phi_3 = \phi_m$ with NBM (——), and with an EVBM (——), an HBM (——) and an RBM (——), along with the minimum breaking location established by the RBM (——).

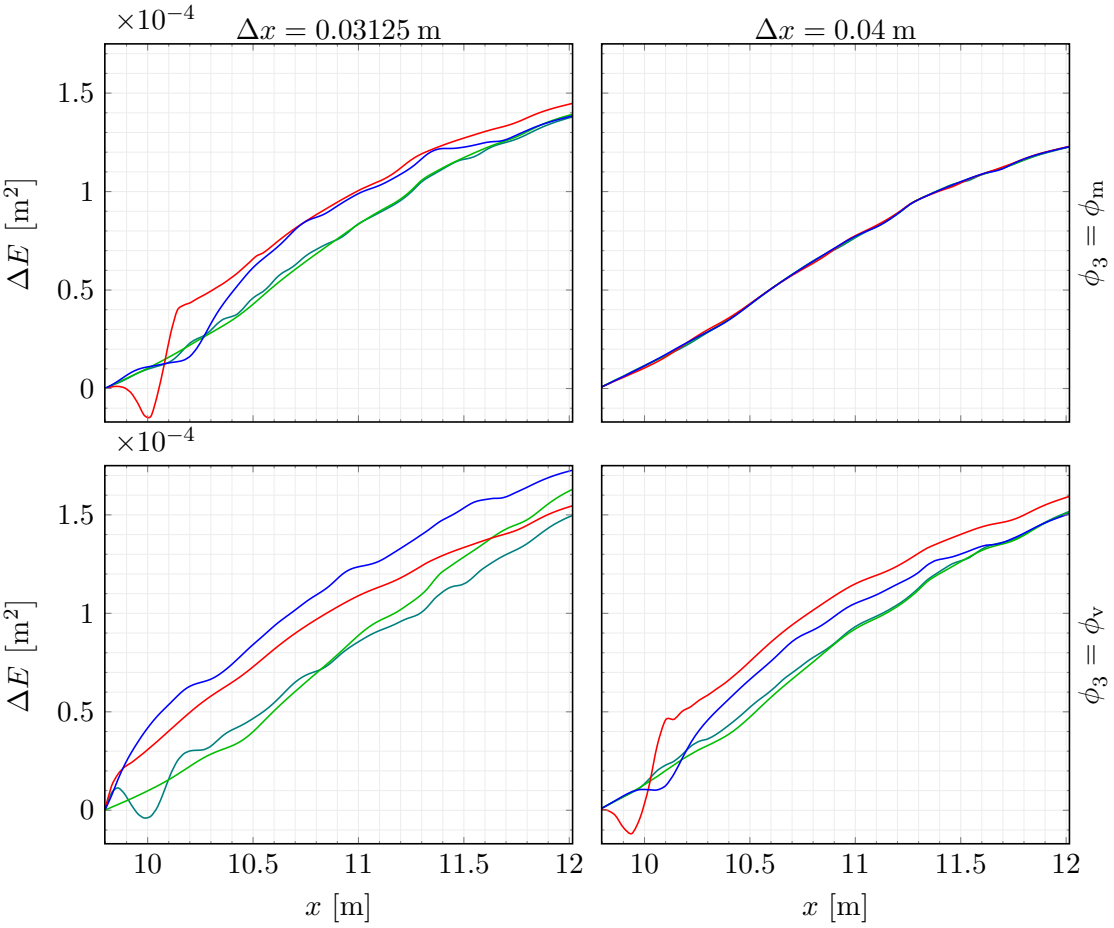

Figure 7.6: Change in variance from experimental breaking point for Test O using NBM (——), and using an EVBM (——), an HBM (——) and an RBM (——) with van-Leer and minmod limiters and differing resolutions.

numerical influence of the breaking terms is considered. While these terms are inserted to restore rotationality into the description of the flow, the accompanying introduction of higher-order derivatives places an increased reliance on the limiters used by the FOCMT scheme when coupled with an RBM. Consequently, in tandem with the physical dissipation portrayed with the breaking terms, an increase in the numerical dissipation produced by the scheme can be expected.

The more dissipative nature of the minmod limiter can also be seen throughout, and in particular with Test O, where the inherent numerical properties of the FOCMT scheme then dominate the energy dissipation, thereby nullifying the effects of the RBM and HBM. Elsewhere, the external breaking mechanisms are still able to introduce dissipation into the system with the minmod limiter, but the effects are less significant than with the van-Leer limiter. The resolution also has a slight impact on the amount of energy dissipation, with finer spatial and temporal grids largely resulting in higher levels of energy dissipation. Crucially, the universal increase in dissipation observed with smaller grid sizes when using the RBM suggests a better resolved roller could offer an improved

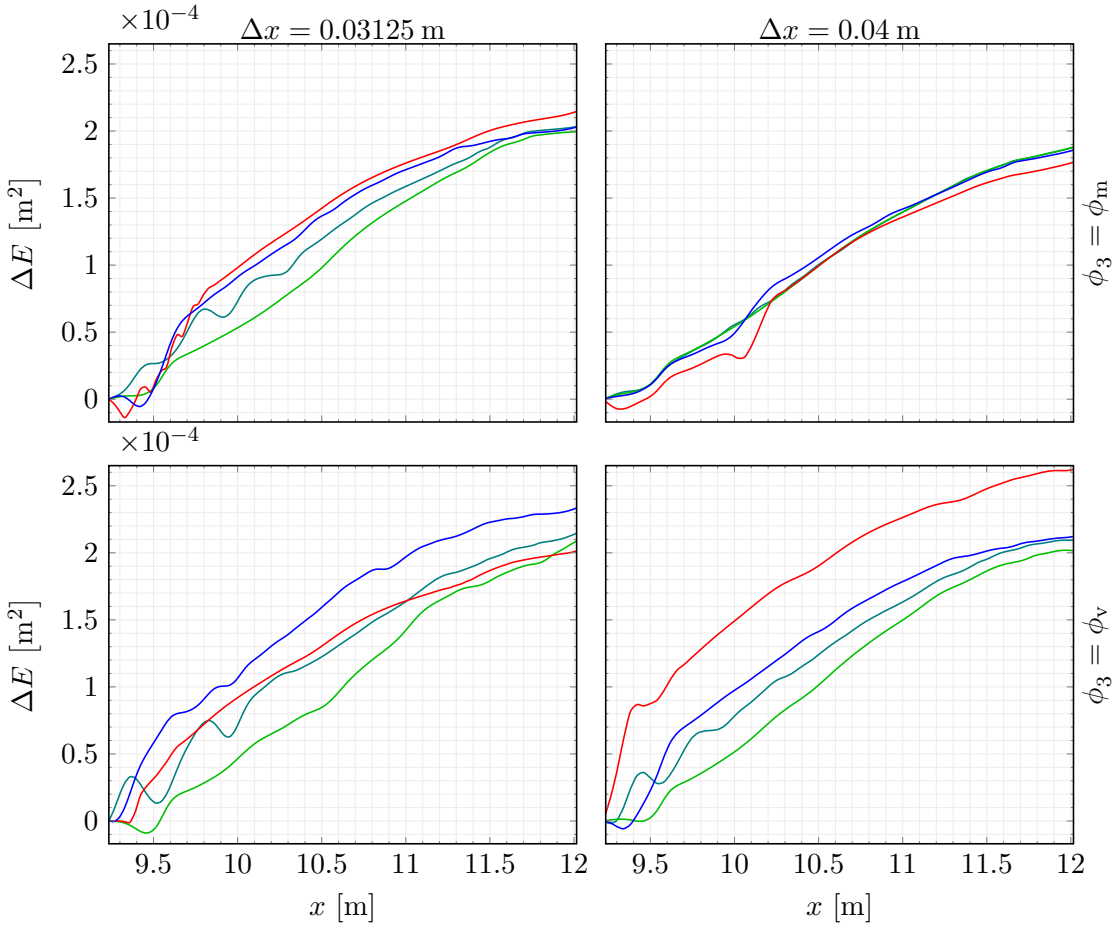

Figure 7.7: Change in variance from experimental breaking point for Test Q using NBM (——), and using an EVBM (——), an HBM (——) and an RBM (——) with van-Leer and minmod limiters and differing resolutions.

description of the physics. The main drawback of reducing Δx and Δt with the RBM is the resulting instabilities produced by the FD scheme, which outweigh the relatively small gains in dissipation introduced by the breaking process.

While individually tuning each variable for separate tests offers some benefits, it is important that a flexible approach that can be applied to a range of cases is preserved. With further development, the breaking model could be automatically calibrated based on wave parameters. The Reynolds number, R_e, is one such dimensionless variable that could be adopted for this purpose and is widely used to predict turbulence in fluid flows. By estimating this quantity for breaking waves according to

$$R_e = \frac{u\lambda}{\nu}, \tag{7.8}$$

the nature of the turbulence generated in the roller region can be parameterised according to known properties (Thorpe, 2007; Zhao and Armfield, 2014).

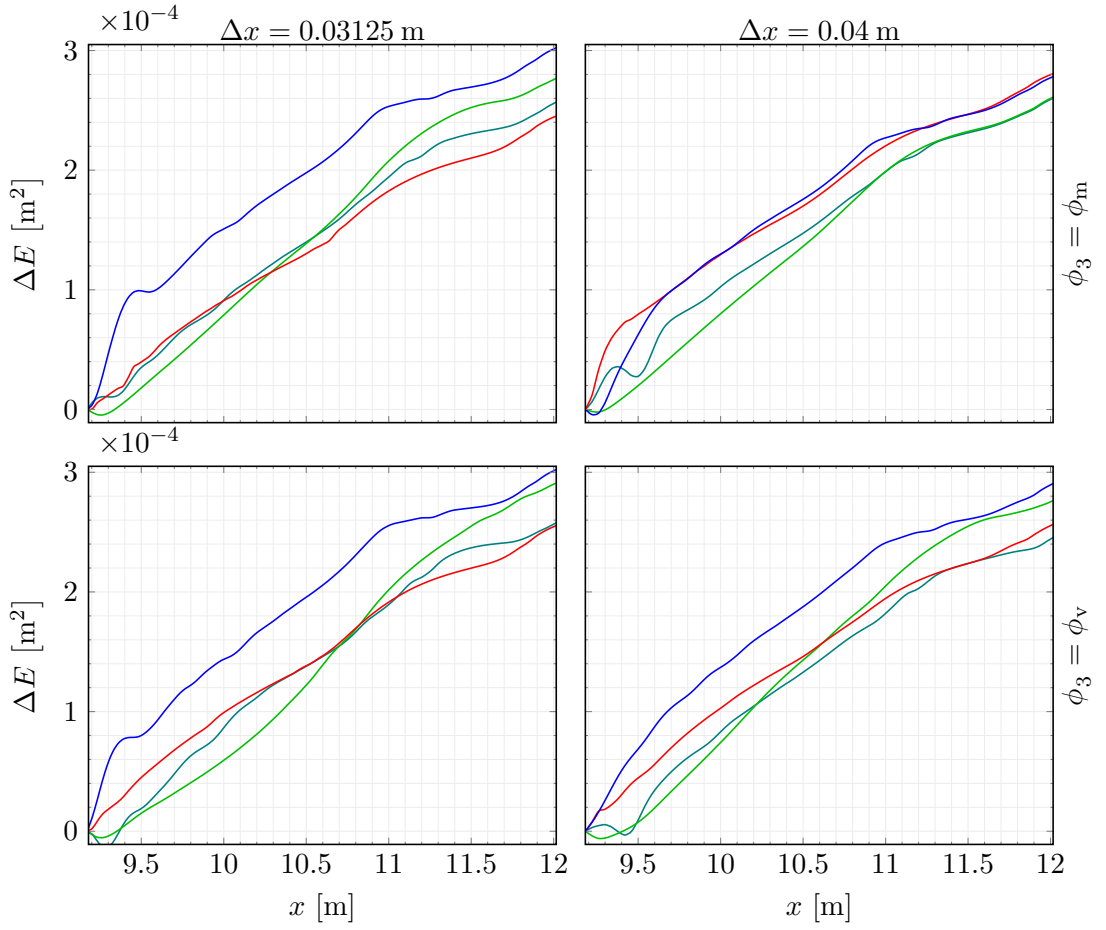

Figure 7.8: Change in variance from experimental breaking point for Test R using NBM (——), and using an EVBM (——), an HBM (——) and an RBM (——) with van-Leer and minmod limiters and differing resolutions.

Chapter 8

Conclusion

This thesis has examined the behaviour of a new numerical model simulating wave propagation in the nearshore region using an FVFD RBM. Solving the BTEs in such a way provides a method for predicting coastal hydrodynamics which includes a description of the turbulent motion encountered during wave breaking, while maintaining a level of computational efficiency rivalling other depth averaged solvers. The mathematical formulation of the proposed approach has been provided and the technical aspects of the implementation described. The derivation results in WNBs, and considers the rotationality expected in the surf-zone by injecting vorticity along the roller region. This builds on the work of Veeramony and Svendsen (2000), adopting a more modern hybrid FVFD scheme that provides improved model stability and offers better shock-capturing capabilities that are key to correctly replicating the breaking process. The adopted FOCMT scheme provides a more sophisticated numerical technique, which also assists in incorporating a shoreline in a relatively straightforward manner. The use of BTEs allows a more accurate description of the hydrodynamics throughout the domain which, following the improvements to the dispersive characteristics included in the present model, can be extended to greater depths.

The results provided in Chapter 6 show analytical and laboratory data to be reproduced well, with a good agreement achieved between numerical and experimental free surface profiles and horizontal velocity predictions. The inability of the model to accurately reproduce features anticipated in the shoaling region can be attributed to the weakly-nonlinear nature of the governing equations. This means some limitations are encountered as fully-nonlinear characteristics become more significant. The numerical scheme adopted for the present study prohibits the extension of the governing equations to FNBs. This is due to the tridiagonal algorithm, which is unable to treat the higher-order terms introduced when considering the fully-nonlinear formulation.

A relatively high number of previous methods have used FD schemes to solve the FNBs, including that presented by Gobbi et al. (2000). Cienfuegos et al. (2006, 2007) present

an FV approach to solve the FNBs, reflecting the more recent adoption of such schemes. Although Gallerano et al. (2014) showed that the undertow can be predicted with FNBs by using the method proposed by Lynett (2006), this additional aspect of the model operates independently. Conversely, undertow predictions obtained using the RBM are inherently associated with the dissipation mechanism, and therefore offer a more unified approach where the governing physical processes are better connected. This allows a more realistic description of the hydrodynamics to be obtained where nonlinearity is less prevalent.

Proper consideration of the relevant physics and numerics ensures suitable caution is exercised when analysing the data collected during this study. By acknowledging the caveats of the model, a number of details can be gleaned from the results and new insight gained into RBMs considering the transport of vorticity. The changes in the tuning parameters of the breaking model over comparable implementations raise questions about the suitability of using hydraulic jump measurements to calibrate RBMs in a way that ensures the physical description of the flow is correct.

The selected value of ω_{m} used for the present study differs from that deduced from the experimental observations of Veeramony and Svendsen (2000), but more faithfully reproduces the horizontal velocity profiles under a breaking wave measured by Cox et al. (1995). While the limited availability of velocity data under breaking waves and vorticity measurements in the roller means it is difficult to identify the cause with certainty, the most obvious difference is the static nature of the hydraulic jump. Consequently, the hydraulic jump analogy fails to capture the dynamic process occurring during wave breaking and does not consider the $\frac{\partial^3(\Delta P)}{\partial x^2 \partial t}$ component of χ included in the RBM. In the early stages of the breaking process, this was found to make the largest contribution of the breaking terms. As such, it is reasonable to expect a smaller momentum balance across the hydraulic jump, as non-hydrostatic processes dominate the energy dissipation instead.

Further investigation into the calibration variables and nondimensional parameterisation may allow the process of tuning the breaking model to be automated, and better tailored to each case. As the variables introduced by the RBM are based on physical quantities, the characteristics of each test could be used to specify suitable values. This could be further extended to dynamically update each parameter locally according to the current state of each wave. The research discussed in the present work has shown some correlation between the physical properties of the system and the appropriate calibration constants.

As demonstrated by Briganti et al. (2004), an improvement in the vertical structure of the vorticity within an RBM can be accomplished by removing the assumption that the eddy viscosity profile is uniform across the water column. This suggests some inaccuracies in the vertical profile of rotational quantities may emerge from the semi-analytical solution of the VTE used in the current study. Improvements in the predicted horizontal velocity

and undertow profiles of the FVFD RBM further support the proposed changes to the calibration parameters. By altering the decay in vorticity, the magnitude of the injected quantity introduced over the lifespan of the roller can be reduced, and the conflict between the experimental measurements and breaking parameters further justified. This is supported by the fact that the magnitude and distribution of the vorticity resembles that found with previous RBMs.

It is possible that the calibration of the model relies on some non-physical changes to the breaking parameters in order to compensate for the numerical properties of the FOCMT scheme. From the findings outlined in Chapter 7, it is evident that the FOCMT scheme inherently dissipates energy within the model. The inclusion of an RBM ensures the breaking process initiates further offshore and better reflects the physical behaviour noted by laboratory investigations, enabling the model to capture more of the true nature of the hydrodynamics. While it is clear that numerical dissipation is more prevalent in the curtailment of energy when using a minmod limiter, the successful introduction of vorticity as a dissipation mechanism has been demonstrated with the use of a van-Leer limiter, which forms the focus of the present work. The spatial and temporal resolutions selected for this study are also shown to be appropriate for the FVFD RBM, where their impact on the numerics is minimal.

This thesis has presented research into an efficient numerical model of surf-zone hydrodynamics using WNBs. The turbulent processes occurring in this region are represented using an RBM, which solves the VTE to determine the vorticity in the fluid and introduce physically derived dissipative terms. This work has shown that an FOCMT scheme can be used as part of a hybrid FVFD model to implement such an approach, and has demonstrated the advantages of this technique. While it is evident that adopting FNBs as the governing equations would provide compelling improvements in the accuracy of predictions, the mathematical formulation required for the FVFD scheme used here has been found to be unsuitable. The feasibility of both the RBM and FVFD components of this study have previously been proven in two-dimensions, suggesting such an expansion would form a natural extension to the model outlined here. The present evaluation makes clear that continued development is required to further alleviate numerical effects when implementing a more physical description of the breaking process such as this. The need for further experimental investigation of the hydrodynamics occurring within the roller region during breaking is also emphasised. The model constructed here advances the potential of nearshore simulations by combining the improved stability and shock-capturing capabilities of the FVFD scheme with the rotational description of the flow provided by the RBM.

Appendix A

Derivation of standard Boussinesq equations

A.1 Continuity equation

The continuity equation can be obtained by inspecting the mass within a control volume, $\mathcal{V}$. By observing that the rate at which this mass changes is equal to the rate at which mass exits the considered volume, the following statement can be made (Graebel, 2007; Hirsch, 2007):

$$\frac{\partial}{\partial t}\iiint_{\mathcal{V}} \rho \, \mathrm{d}\mathcal{V} + \iiint_{\mathcal{V}} \boldsymbol{\nabla} \cdot (\rho \boldsymbol{u}) \, \mathrm{d}\mathcal{V} = 0 \tag{A.1}$$

It then follows that, for a fixed control volume,

$$\frac{\mathrm{d}\rho}{\mathrm{d}t} + \boldsymbol{\nabla} \cdot (\rho \boldsymbol{u}) = 0. \tag{A.2}$$

For the purposes of modelling nearshore flows, it is realistic to assume that the fluid is incompressible and the density remains constant and uniform throughout the domain. On this basis, Equation (A.2) then reduces to the continuity equation used hereinafter:

$$\boldsymbol{\nabla} \cdot \boldsymbol{u} = 0 \tag{A.3}$$

A.2 Navier-Stokes equations

The derivation outlined here begins by considering the forces acting on the element of fluid shown in Figure A.1. These forces represent the effects of the surrounding fluid, and can be written in terms of stresses acting over an area as follows:

$$\begin{bmatrix} F_{xx}^{\pm} \\ F_{xy}^{\pm} \\ F_{xz}^{\pm} \end{bmatrix} = \left(\begin{bmatrix} \sigma_{xx} \\ \breve{\tau}_{xy} \\ \breve{\tau}_{xz} \end{bmatrix} \pm \frac{\Delta x}{2} \frac{\partial}{\partial x} \begin{bmatrix} \sigma_{xx} \\ \breve{\tau}_{xy} \\ \breve{\tau}_{xz} \end{bmatrix} \right) \Delta y \Delta z \tag{A.4}$$

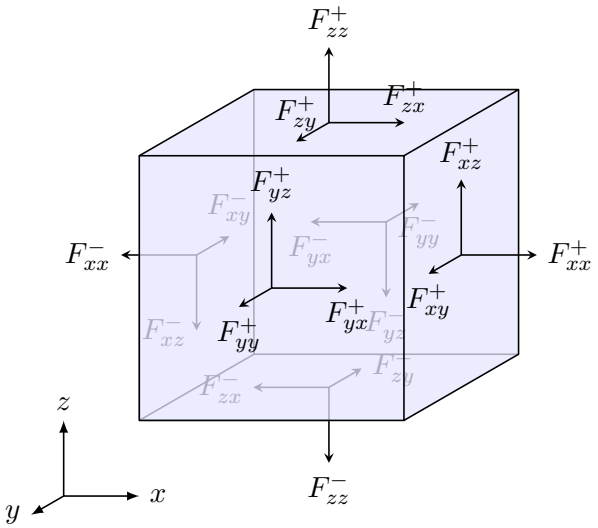

Figure A.1: Forces acting on the surface of a fluid element.

$$\begin{bmatrix} F_{yx}^{\pm} \\ F_{yy}^{\pm} \\ F_{yz}^{\pm} \end{bmatrix} = \left(\begin{bmatrix} \check{\tau}_{yx} \\ \sigma_{yy} \\ \check{\tau}_{yz} \end{bmatrix} \pm \frac{\Delta y}{2} \frac{\partial}{\partial y} \begin{bmatrix} \check{\tau}_{yx} \\ \sigma_{yy} \\ \check{\tau}_{yz} \end{bmatrix} \right) \Delta x \Delta z \tag{A.5}$$

$$\begin{bmatrix} F_{zx}^{\pm} \\ F_{zy}^{\pm} \\ F_{zz}^{\pm} \end{bmatrix} = \left(\begin{bmatrix} \check{\tau}_{zx} \\ \check{\tau}_{zy} \\ \sigma_{zz} \end{bmatrix} \pm \frac{\Delta z}{2} \frac{\partial}{\partial z} \begin{bmatrix} \check{\tau}_{zx} \\ \check{\tau}_{zy} \\ \sigma_{zz} \end{bmatrix} \right) \Delta x \Delta y \tag{A.6}$$

By defining the location of a fluid particle in three-dimensional space with the vector $\boldsymbol{r}$, the velocity can be written as

$$\boldsymbol{u} = \frac{\mathrm{d}\boldsymbol{r}}{\mathrm{d}t}. \tag{A.7}$$

Using the chain rule, the total derivative of a function, $f(\boldsymbol{r}, t)$, can then be defined as

$$\frac{\mathrm{d}f}{\mathrm{d}t} = \frac{\partial f}{\partial t} + \boldsymbol{u} \cdot \boldsymbol{\nabla} f. \tag{A.8}$$

These definitions will be used during the procedures that follows.

It is assumed that the only body force acting on the fluid element is that due to gravitational effects. The total force exerted on the fluid element is equal to the sum of the surface forces indicated in Figure A.1 and the force due to gravity. Newton's second law of motion states that the rate of change of momentum is equal to the force exerted on a body. By equating the forces acting on the fluid element, the following relation is then obtained:

$$\Delta m \frac{\mathrm{d}\boldsymbol{u}}{\mathrm{d}t} = \Delta m \boldsymbol{g} + \Delta x \Delta y \Delta z \left(\boldsymbol{\nabla} \cdot \boldsymbol{\sigma} \right) \tag{A.9}$$

Here, m is the mass of the fluid,

$$\boldsymbol{\sigma} = \begin{bmatrix} \sigma_{xx} & \check{\tau}_{xy} & \check{\tau}_{xz} \\ \check{\tau}_{yx} & \sigma_{yy} & \check{\tau}_{yz} \\ \check{\tau}_{zx} & \check{\tau}_{zy} & \sigma_{zz} \end{bmatrix}, \tag{A.10}$$

$$\boldsymbol{u} = \begin{bmatrix} \check{u} & \check{v} & \check{w} \end{bmatrix}^{\intercal} \tag{A.11}$$

and

$$\boldsymbol{\nabla} = \begin{bmatrix} \dfrac{\partial}{\partial x} & \dfrac{\partial}{\partial y} & \dfrac{\partial}{\partial z} \end{bmatrix}^{\intercal} \tag{A.12}$$

is the gradient operator, where $\boldsymbol{X}^{\intercal}$ denotes the transpose of $\boldsymbol{X}$. The coordinate system is aligned such that gravitational effects are only present in the z-axis, thereby giving

$$\boldsymbol{g} = \begin{bmatrix} 0 & 0 & -g \end{bmatrix}^{\intercal} \tag{A.13}$$

as the vector describing acceleration due to gravity. Applying the relation provided in Equation (A.8) to $\boldsymbol{u}$ in Equation (A.9) and then dividing by $\Delta m = \rho \Delta x \Delta y \Delta z$ gives

$$\frac{\partial \boldsymbol{u}}{\partial t} + (\boldsymbol{u} \cdot \boldsymbol{\nabla})\, \boldsymbol{u} = \boldsymbol{g} + \frac{\boldsymbol{\nabla} \cdot \boldsymbol{\sigma}}{\rho}. \tag{A.14}$$

For an incompressible Newtonian fluid, viscous stresses are linearly proportional to the rate of deformation of the fluid. The normal stresses can then be expressed as

$$\sigma_{xx} = 2\rho\nu \frac{\partial \check{u}}{\partial x} - \check{p}, \tag{A.15}$$

$$\sigma_{yy} = 2\rho\nu \frac{\partial \check{v}}{\partial y} - \check{p} \tag{A.16}$$

and

$$\sigma_{zz} = 2\rho\nu \frac{\partial \check{w}}{\partial z} - \check{p}, \tag{A.17}$$

and the shear stresses as

$$\check{\tau}_{xy} = \check{\tau}_{yx} = \rho\nu \left(\frac{\partial \check{u}}{\partial y} + \frac{\partial \check{v}}{\partial x} \right), \tag{A.18}$$

$$\check{\tau}_{yz} = \check{\tau}_{zy} = \rho\nu \left(\frac{\partial \check{v}}{\partial z} + \frac{\partial \check{w}}{\partial y} \right) \tag{A.19}$$

and

$$\check{\tau}_{zx} = \check{\tau}_{xz} = \rho\nu \left(\frac{\partial \check{w}}{\partial x} + \frac{\partial \check{u}}{\partial z} \right). \tag{A.20}$$

The kinematic viscosity is assumed to be constant throughout. Here, the pressure is given by the average of the normal stresses, such that

$$\check{p} = -\frac{1}{3} \left(\sigma_{xx} + \sigma_{yy} + \sigma_{zz} \right). \tag{A.21}$$

With Equations (A.3) and (A.15) to (A.20), Equation (A.14) can be rewritten to provide the NSE:

$$\frac{\partial \boldsymbol{u}}{\partial t} + (\boldsymbol{u} \cdot \boldsymbol{\nabla})\, \boldsymbol{u} = \boldsymbol{g} - \frac{\boldsymbol{\nabla} \check{p}}{\rho} + \nu \boldsymbol{\nabla}^2 \boldsymbol{u} \tag{A.22}$$

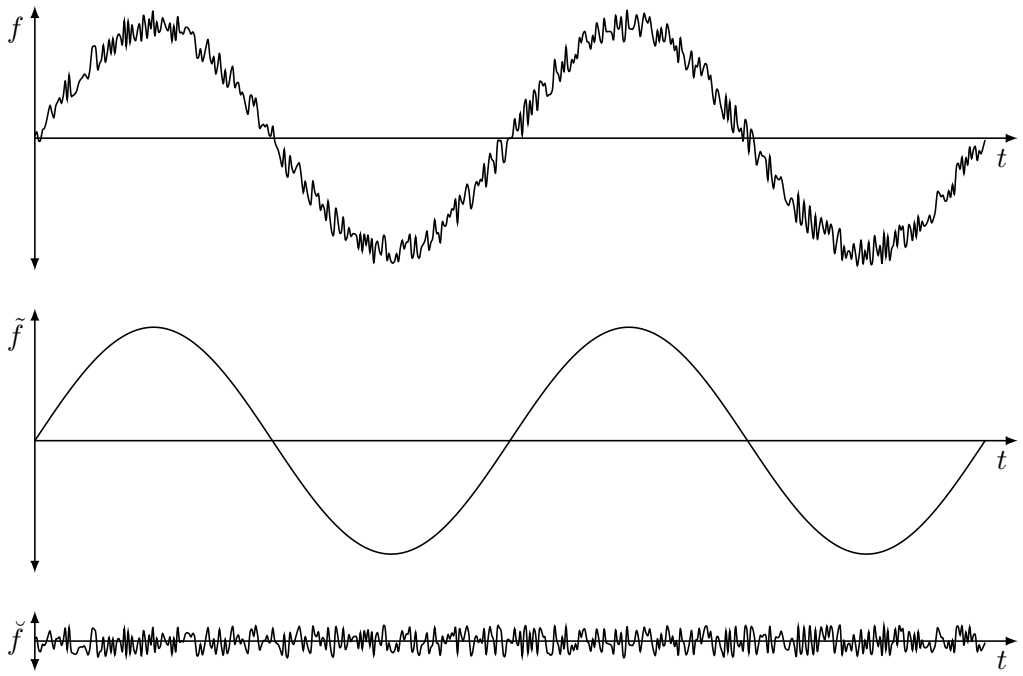

Figure A.2: Decomposition of turbulent flow into mean and turbulent components.

A.3 Reynolds averaged Navier-Stokes equations

In many practical cases, the computational demands of solving the NSEs are prohibitively expensive. The formulation of the RANS equations simplifies turbulent flow occurring over small timescales using a Reynold's decomposition:

$$f = \tilde{f} + \breve{f} \tag{A.23}$$

As illustrated in Figure A.2, this divides the flow into two components, $\tilde{f}$ and $\breve{f}$, representing the mean value and the fluctuation respectively. The timescale, Δt, over which this averaging is performed is defined so that

$$\widetilde{\breve{f}} = 0. \tag{A.24}$$

Ensemble averaging provides an average value of a quantity from many repetitions of an identical event. This can be achieved by defining the timescale, Δt, in Equation (A.23) such that it is equal to the length of the event. The time averaged value of a given variable, f, is taken as

$$\tilde{f} = \frac{1}{\Delta t} \int_{t_0}^{t_0+\Delta t} f \, \mathrm{d}t. \tag{A.25}$$

As the manipulation of equations involving turbulence is conventionally done using tensor notation, Equations (A.3) and (A.22) are each rewritten accordingly:

$$\frac{\partial u_i}{\partial x_i} = 0 \quad i \in \{1, 2, 3\} \tag{A.26}$$

$$\frac{\partial u_j}{\partial t} + u_i \frac{\partial u_j}{\partial x_i} = g\delta_{3,j} + \frac{\partial}{\partial x_i}\left[\nu\left(\frac{\partial u_i}{\partial x_j} + \frac{\partial u_j}{\partial x_i}\right) - \frac{\breve{p}}{\rho}\delta_{i,j}\right] \quad i,j \in \{1,2,3\} \tag{A.27}$$

Here, the notation is defined such that the spatial coordinates are defined by

$$\begin{bmatrix} x_1 & x_2 & x_3 \end{bmatrix}^\intercal \equiv \begin{bmatrix} x & y & z \end{bmatrix}^\intercal, \tag{A.28}$$

the velocities by

$$\begin{bmatrix} u_1 & u_2 & u_3 \end{bmatrix}^\intercal \equiv \boldsymbol{u} \tag{A.29}$$

and the Kronecker delta function as

$$\begin{bmatrix} \delta_{1,1} & \delta_{1,2} & \delta_{1,3} \\ \delta_{2,1} & \delta_{2,2} & \delta_{2,3} \\ \delta_{3,1} & \delta_{3,2} & \delta_{3,3} \end{bmatrix} \equiv \begin{bmatrix} 1 & 0 & 0 \\ 0 & 1 & 0 \\ 0 & 0 & 1 \end{bmatrix}. \tag{A.30}$$

Adding Equation (A.26) to Equation (A.27) allows the momentum equation to be written in an alternate form. The Reynolds decomposition described by Equation (A.23) is applied to $\boldsymbol{u}$ and $\breve{p}$ as follows:

$$\boldsymbol{u} = \begin{bmatrix} \tilde{u}_1 + \breve{u}_1 & \tilde{u}_2 + \breve{u}_2 & \tilde{u}_3 + \breve{u}_3 \end{bmatrix}^\intercal \tag{A.31}$$

$$\breve{p} = \tilde{p} + \breve{p} \tag{A.32}$$

This allows Equations (A.26) and (A.27) to then be written as

$$\frac{\partial \tilde{u}_i}{\partial x_i} + \frac{\partial \breve{u}_i}{\partial x_i} = 0 \quad i \in \{1,2,3\} \tag{A.33}$$

and

$$\frac{\partial \tilde{u}_j}{\partial t} + \frac{\partial \breve{u}_j}{\partial t} + \frac{\partial}{\partial x_i}\left[\left(\tilde{u}_i + \breve{u}_i\right)\left(\tilde{u}_j + \breve{u}_j\right)\right] = g\delta_{3,j} + \frac{\partial}{\partial x_i}\left\{\nu\left[\frac{\partial}{\partial x_j}\left(\tilde{u}_i + \breve{u}_i\right) + \frac{\partial}{\partial x_i}\left(\tilde{u}_j + \breve{u}_j\right)\right] - \frac{\tilde{p} + \breve{p}}{\rho}\delta_{i,j}\right\} \quad i,j \in \{1,2,3\}, \tag{A.34}$$

respectively. Noting that Equations (A.33) and (A.34) can be ensemble averaged, and that

$$\widetilde{\frac{\partial \tilde{f}}{\partial X}} \equiv \widetilde{\frac{\partial f}{\partial X}} \equiv \frac{\partial \tilde{f}}{\partial X} \tag{A.35}$$

and

$$\widetilde{\tilde{X}Y} \equiv \tilde{X}\tilde{Y}, \tag{A.36}$$

the turbulent component can be removed according to Equation (A.24) to give

$$\frac{\partial \tilde{u}_i}{\partial x_i} = 0 \quad i \in \{1,2,3\} \tag{A.37}$$

and

$$\frac{\partial \tilde{u}_j}{\partial t}+\frac{\partial}{\partial x_i}\left(\tilde{u}_i\tilde{u}_j+\widetilde{\breve{u}_i\breve{u}_j}\right)=g\delta_{3,j}+\frac{\partial}{\partial x_i}\left[\nu\left(\frac{\partial \tilde{u}_i}{\partial x_j}+\frac{\partial \tilde{u}_j}{\partial x_i}\right)-\frac{\tilde{p}}{\rho}\delta_{i,j}\right] \quad i,j\in\{1,2,3\}. \tag{A.38}$$

The stresses described by Equation (A.38) can be written as a Reynolds stress,

$$\breve{\tau}_{i,j}=-\rho\widetilde{\breve{u}_i\breve{u}_j} \quad i,j\in\{1,2,3\}, \tag{A.39}$$

and viscous stress,

$$\tau^v_{i,j}=\rho\nu\left(\frac{\partial \tilde{u}_i}{\partial x_j}+\frac{\partial \tilde{u}_j}{\partial x_i}\right) \quad i,j\in\{1,2,3\}, \tag{A.40}$$

to give

$$\frac{\partial \tilde{u}_j}{\partial t}+\frac{\partial}{\partial x_i}\left(\tilde{u}_i\tilde{u}_j\right)=g\delta_{3,j}-\frac{1}{\rho}\frac{\partial \tilde{p}}{\partial x_i}+\frac{1}{\rho}\frac{\partial}{\partial x_i}\left(\tau^v_{i,j}+\breve{\tau}_{i,j}\right) \quad i,j\in\{1,2,3\}. \tag{A.41}$$

A.3.1 Turbulence closure

The imbalance between the number of unknown variables and equations provided in Equation (A.41) forms the basis of the turbulence closure problem. Several models have been proposed to meet this requirement, including the method suggested by Boussinesq that is used here. This introduces the concept of eddy viscosity,

$$\nu_\mathrm{t}=l_\mathrm{t}\sqrt{\frac{1}{2}\left(\widetilde{\breve{u}_1^2}+\widetilde{\breve{u}_2^2}+\widetilde{\breve{u}_3^2}\right)}, \tag{A.42}$$

with l_t characterising the length scale of the turbulence. As $\tau^v_{i,j}\ll\breve{\tau}_{i,j}$ in turbulent flows, the viscous stresses can be assumed to be negligible. With this in mind, the total shear stress within the flow is modelled by

$$\tau_{i,j}=\rho\nu_\mathrm{t}\left(\frac{\partial \tilde{u}_i}{\partial x_j}+\frac{\partial \tilde{u}_j}{\partial x_i}\right) \quad i,j\in\{1,2,3\}, \tag{A.43}$$

and Equation (A.41) written as

$$\frac{\partial \tilde{u}_j}{\partial t}+\frac{\partial}{\partial x_i}\left(\tilde{u}_i\tilde{u}_j\right)=g\delta_{3,j}-\frac{1}{\rho}\frac{\partial \tilde{p}}{\partial x_i}+\frac{1}{\rho}\frac{\partial \tau_{i,j}}{\partial x_i} \quad i,j\in\{1,2,3\}. \tag{A.44}$$

Here, the following tensor notation is used:

$$\begin{bmatrix}\tau_{1,1} & \tau_{1,2} & \tau_{1,3}\\ \tau_{2,1} & \tau_{2,2} & \tau_{2,3}\\ \tau_{3,1} & \tau_{3,2} & \tau_{3,3}\end{bmatrix}\equiv\begin{bmatrix}\tau_{xx} & \tau_{xy} & \tau_{xz}\\ \tau_{yx} & \tau_{yy} & \tau_{yz}\\ \tau_{zx} & \tau_{zy} & \tau_{zz}\end{bmatrix} \tag{A.45}$$

$$\begin{bmatrix}\tilde{u}_1 & \tilde{u}_2 & \tilde{u}_3\end{bmatrix}^\mathsf{T}\equiv\begin{bmatrix}u & v & w\end{bmatrix}^\mathsf{T} \tag{A.46}$$

Here, v denotes the velocity in the y-direction. Additionally,

$$\tilde{p}\equiv p. \tag{A.47}$$

A.4 Depth integrated Reynolds averaged Navier-Stokes equations

In order to obtain a one-dimensional set of equations, the two-dimensional form of the RANS equations provided by Equations (A.37) and (A.44) are averaged over the depth of the fluid. This neglects processes occurring along the y-direction, and then assumes a uniform flow across the water column by integrating with respect to z. First, the two-dimensional Reynolds continuity equation is written as

$$\frac{\partial u}{\partial x} + \frac{\partial w}{\partial z} = 0, \tag{A.48}$$

and the horizontal and vertical Reynolds momentum equations as

$$\frac{\partial u}{\partial t} + \frac{\partial u^2}{\partial x} + \frac{\partial}{\partial z}(uw) = \frac{1}{\rho}\left(\frac{\partial \tau_{xx}}{\partial x} + \frac{\partial \tau_{xz}}{\partial z}\right) - \frac{1}{\rho}\frac{\partial p}{\partial x} \tag{3.1}$$

and

$$\frac{\partial w}{\partial t} + \frac{\partial}{\partial x}(uw) + \frac{\partial w^2}{\partial z} = \frac{1}{\rho}\left(\frac{\partial \tau_{xz}}{\partial x} + \frac{\partial \tau_{zz}}{\partial z}\right) - \frac{1}{\rho}\frac{\partial p}{\partial z} - g, \tag{3.2}$$

respectively.

A.4.1 Continuity

Depth averaging of Equation (A.48) is then performed by integrating from $z = -h$ to $z = \zeta$, which gives

$$\int_{-h}^{\zeta} \frac{\partial u}{\partial x}\,\mathrm{d}z + w|_{z=\zeta} - w|_{z=-h} = 0. \tag{A.49}$$

Noting that a fluid particle cannot move beyond the free surface, Equations (A.7) and (A.8) can be used to obtain the kinematic free surface boundary condition:

$$w|_{z=\zeta} = \frac{\partial \zeta}{\partial t} + u|_{z=\zeta}\frac{\partial \zeta}{\partial x} \tag{A.50}$$

Similarly, for an impermeable bed, the bottom boundary condition is obtained:

$$w|_{z=-h} = -\frac{\partial h}{\partial t} - u|_{z=-h}\frac{\partial h}{\partial x} \tag{A.51}$$

Substituting Equations (A.50) and (A.51) into Equation (A.49) provides

$$\int_{-h}^{\zeta} \frac{\partial u}{\partial x}\,\mathrm{d}z + \frac{\partial \zeta}{\partial t} + \frac{\partial h}{\partial t} + u|_{z=\zeta}\frac{\partial \zeta}{\partial x} + u|_{z=-h}\frac{\partial h}{\partial x} = 0, \tag{A.52}$$

which, with Equations (3.8), (3.9) and (3.39), becomes

$$\frac{\partial d}{\partial t} + \frac{\partial q}{\partial x} = 0. \tag{3.6}$$

A.4.2 Momentum

Integrating Equation (3.1) from the bed to the free surface and applying Equations (3.4), (3.5) and (3.39) provides

$$\frac{\partial}{\partial t}\int_{-h}^{\zeta} u \,\mathrm{d}z - u|_{z=\zeta}\frac{\partial \zeta}{\partial t} + \frac{\partial}{\partial x}\int_{-h}^{\zeta} u^2 \,\mathrm{d}z - u^2\Big|_{z=\zeta}\frac{\partial \zeta}{\partial x} - u^2\Big|_{z=-h}\frac{\partial h}{\partial x} + (uw)|_{z=\zeta} - (uw)|_{z=-h} = \frac{1}{\rho}\left(\frac{\partial}{\partial x}\int_{-h}^{\zeta}\tau_{xx}\,\mathrm{d}z - \tau_{xx}|_{z=\zeta}\frac{\partial \zeta}{\partial x} - \tau_{xx}|_{z=-h}\frac{\partial h}{\partial x} + \tau_{xz}|_{z=\zeta} - \tau_{xz}|_{z=-h} - \frac{\partial}{\partial x}\int_{-h}^{\zeta} p \,\mathrm{d}z + p|_{z=-h}\frac{\partial h}{\partial x}\right). \quad \text{(A.53)}$$

Integrating Equation (3.2) from an arbitrary depth, which is independent of x and t, to $z = \zeta$, and again using Equation (3.39) gives

$$\frac{\partial}{\partial t}\int_{z}^{\zeta} w \,\mathrm{d}z' - w|_{z=\zeta}\frac{\partial \zeta}{\partial t} + \frac{\partial}{\partial x}\int_{z}^{\zeta} uw \,\mathrm{d}z' - (uw)|_{z=\zeta}\frac{\partial \zeta}{\partial x} + w^2\Big|_{z=\zeta} - w^2 = \frac{1}{\rho}\left(\frac{\partial}{\partial x}\int_{z}^{\zeta}\tau_{xz}\,\mathrm{d}z' - \tau_{xz}|_{z=\zeta}\frac{\partial \zeta}{\partial x} + \tau_{zz}|_{z=\zeta} - \tau_{zz} - p|_{z=\zeta} + p\right) - g\left(\zeta - z\right). \quad \text{(A.54)}$$

With Equations (A.50), (A.51) and (3.4), Equation (A.53) becomes

$$\frac{\partial}{\partial t}\int_{-h}^{\zeta} u \,\mathrm{d}z + \frac{\partial}{\partial x}\int_{-h}^{\zeta} u^2 \,\mathrm{d}z = \frac{1}{\rho}\left[\frac{\partial}{\partial x}\int_{-h}^{\zeta}\tau_{xx} - p \,\mathrm{d}z + \left(\tau_{xz} - \tau_{xx}\frac{\partial \zeta}{\partial x}\right)\Big|_{z=\zeta} - \left(\tau_{xx}\frac{\partial h}{\partial x} + \tau_{xz} - p\frac{\partial h}{\partial x}\right)\Big|_{z=-h}\right]. \quad \text{(A.55)}$$

Applying the boundary conditions in Equations (A.50) and (3.5), Equation (A.54) becomes

$$\frac{\partial}{\partial t}\int_{z}^{\zeta} w \,\mathrm{d}z' + \frac{\partial}{\partial x}\int_{z}^{\zeta} uw \,\mathrm{d}z' - w^2 = \frac{1}{\rho}\left[\frac{\partial}{\partial x}\int_{z}^{\zeta}\tau_{xz}\,\mathrm{d}z' + \left(\tau_{zz} - \tau_{xz}\frac{\partial \zeta}{\partial x}\right)\Big|_{z=\zeta} - \tau_{zz} + p\right] - g\left(\zeta - z\right). \quad \text{(A.56)}$$

An expression for the pressure can then be obtained by multiplying by ρ and rearranging:

$$p = \overbrace{\rho g\left(\zeta - z\right)}^{\text{(I)}} + \overbrace{\rho\frac{\partial}{\partial t}\int_{z}^{\zeta} w \,\mathrm{d}z'}^{\text{(II)}} + \overbrace{\frac{\partial}{\partial x}\left(\int_{z}^{\zeta}\rho uw - \tau_{xz}\,\mathrm{d}z'\right)}^{\text{(III)}} + \overbrace{\left(\tau_{xz}\frac{\partial \zeta}{\partial x} - \tau_{zz}\right)\Big|_{z=\zeta}}^{\text{(IV)}} + \overbrace{\tau_{zz} - \rho w^2}^{\text{(V)}} \quad \text{(A.57)}$$

The total pressure described in Equation (A.57) is due to the hydrostatic pressure (I), the integrated vertical accelerations of the water column above z (II), the net vertical

force due to the Reynolds shear stresses acting along the sides of the column (III), and the stresses acting at the surface (IV). This pressure is reduced by the vertical momentum of the fluid due to the action of the velocity, which helps to carry the weight of the water (V).

As a common term in both vertical and horizontal momentum equations, the pressure can be eliminated from Equation (A.55). First, Equation (A.57) must be differentiated with respect to x and then integrated across the water column, which with Equations (3.5) and (3.39), provides the following:

$$\begin{aligned}\frac{\partial}{\partial x}\int_{-h}^{\zeta} p \,\mathrm{d}z = \rho g\left(\zeta+h\right)\frac{\partial \zeta}{\partial x} + p|_{z=-h}\frac{\partial h}{\partial x} + \rho\int_{-h}^{\zeta}\frac{\partial^2}{\partial x \partial t}\int_{z}^{\zeta} w \,\mathrm{d}z' \,\mathrm{d}z \\ + \int_{-h}^{\zeta}\frac{\partial^2}{\partial x^2}\left(\int_{z}^{\zeta}\rho u w - \tau_{xz}\,\mathrm{d}z'\right)\,\mathrm{d}z \\ + \left(\zeta+h\right)\frac{\partial}{\partial x}\left[\left(\tau_{xz}\frac{\partial \zeta}{\partial x} - \tau_{zz}\right)\Big|_{z=\zeta}\right] + \int_{-h}^{\zeta}\frac{\partial \tau_{zz}}{\partial x}\,\mathrm{d}z - \rho\int_{-h}^{\zeta}\frac{\partial w^2}{\partial x}\,\mathrm{d}z\end{aligned} \tag{A.58}$$

The continuity equation is then used to eliminate w from Equation (A.58), although it should be noted that this term is still present in τ_{xz} and τ_{zz} and must therefore be treated accordingly. Integrating Equation (A.48) from the bed to an arbitrary depth and applying Equation (3.39) provides

$$w - w|_{z=-h} = u\frac{\partial z}{\partial x} + u|_{z=-h}\frac{\partial h}{\partial x} - \frac{\partial}{\partial x}\int_{-h}^{z} u \,\mathrm{d}z', \tag{A.59}$$

which, with Equation (A.51), gives the following relation:

$$w = -\frac{\partial}{\partial x}\int_{-h}^{z} u \,\mathrm{d}z' \tag{4.54}$$

Substituting Equation (4.54) into Equation (A.58) gives

$$\begin{aligned}\frac{\partial}{\partial x}\int_{-h}^{\zeta} p \,\mathrm{d}z = \rho g\left(\zeta+h\right)\frac{\partial \zeta}{\partial x} + p|_{z=-h}\frac{\partial h}{\partial x} - \rho\int_{-h}^{\zeta}\frac{\partial^2}{\partial x \partial t}\int_{z}^{\zeta}\frac{\partial}{\partial x}\int_{-h}^{z'} u \,\mathrm{d}z'' \,\mathrm{d}z' \,\mathrm{d}z \\ - \int_{-h}^{\zeta}\frac{\partial^2}{\partial x^2}\left(\int_{z}^{\zeta}\rho u\frac{\partial}{\partial x}\int_{-h}^{z'} u \,\mathrm{d}z'' + \tau_{xz}\,\mathrm{d}z'\right)\,\mathrm{d}z \\ + \left(\zeta+h\right)\frac{\partial}{\partial x}\left[\left(\tau_{xz}\frac{\partial \zeta}{\partial x} - \tau_{zz}\right)\Big|_{z=\zeta}\right] + \int_{-h}^{\zeta}\frac{\partial}{\partial x}\left[\tau_{zz} - \rho\left(\frac{\partial}{\partial x}\int_{-h}^{z} u \,\mathrm{d}z'\right)^2\right]\,\mathrm{d}z.\end{aligned} \tag{A.60}$$

The combined momentum equation is then obtained by substituting Equations (A.60), (3.8) and (3.9) into Equation (A.55) (Massey and Ward-Smith, 2006; Svendsen, 2006;

Young et al., 2010):

$$\begin{aligned}
&\frac{\partial q}{\partial t} + \frac{\partial}{\partial x}\int_{-h}^{\zeta} u^2 - \frac{\tau_{xx}}{\rho}\,\mathrm{d}z + gd\frac{\partial \zeta}{\partial x} - \int_{-h}^{\zeta}\frac{\partial^2}{\partial x \partial t}\int_{z}^{\zeta}\frac{\partial}{\partial x}\int_{-h}^{z'} u\,\mathrm{d}z''\,\mathrm{d}z'\,\mathrm{d}z \\
&\quad - \int_{-h}^{\zeta}\frac{\partial^2}{\partial x^2}\left(\int_{z}^{\zeta} u\frac{\partial}{\partial x}\int_{-h}^{z'} u\,\mathrm{d}z'' + \frac{\tau_{xz}}{\rho}\,\mathrm{d}z'\right)\mathrm{d}z \\
&\quad + \int_{-h}^{\zeta}\frac{\partial}{\partial x}\left[\frac{\tau_{zz}}{\rho} - \left(\frac{\partial}{\partial x}\int_{-h}^{z} u\,\mathrm{d}z'\right)^2\right]\mathrm{d}z - d\frac{\partial}{\partial x}\left[\left(\frac{\tau_{zz}}{\rho} - \frac{\tau_{xz}}{\rho}\frac{\partial \zeta}{\partial x}\right)\Big|_{z=\zeta}\right] \\
&\quad - \left(\frac{\tau_{xz}}{\rho} - \frac{\tau_{xx}}{\rho}\frac{\partial \zeta}{\partial x}\right)\Big|_{z=\zeta} + \left(\frac{\tau_{xz}}{\rho} + \frac{\tau_{xx}}{\rho}\frac{\partial h}{\partial x}\right)\Big|_{z=-h} = 0
\end{aligned} \tag{3.7}$$

A.5 Reformulation of momentum equation

Having neglected the shear forces at the free surface and the bed, the nondimensional form of Equation (3.7) is given by

$$\begin{aligned}
&\frac{\partial \hat{q}}{\partial \hat{t}} + \delta\frac{\partial}{\partial \hat{x}}\int_{-\hat{h}}^{\delta\hat{\zeta}}\hat{u}^2\,\mathrm{d}\hat{z} + \hat{d}\frac{\partial \hat{\zeta}}{\partial \hat{x}} - \mu^2\int_{-\hat{h}}^{\delta\hat{\zeta}}\frac{\partial^2}{\partial \hat{x}\partial \hat{t}}\int_{\hat{z}}^{\delta\hat{\zeta}}\frac{\partial}{\partial \hat{x}}\int_{-\hat{h}}^{\hat{z}'}\hat{u}\,\mathrm{d}\hat{z}''\,\mathrm{d}\hat{z}'\,\mathrm{d}\hat{z} \\
&\quad - \mu^2\int_{-\hat{h}}^{\delta\hat{\zeta}}\frac{\partial^2}{\partial \hat{x}^2}\int_{\hat{z}}^{\delta\hat{\zeta}}\hat{\nu}_{\mathrm{t}}\frac{\partial \hat{u}}{\partial \hat{z}}\,\mathrm{d}\hat{z}'\,\mathrm{d}\hat{z} - \delta\mu^2\int_{-\hat{h}}^{\delta\hat{\zeta}}\frac{\partial^2}{\partial \hat{x}^2}\int_{\hat{z}}^{\delta\hat{\zeta}}\hat{u}\frac{\partial}{\partial \hat{x}}\int_{-\hat{h}}^{\hat{z}'}\hat{u}\,\mathrm{d}\hat{z}''\,\mathrm{d}\hat{z}'\,\mathrm{d}\hat{z} \\
&\quad - \delta\mu^2\int_{-\hat{h}}^{\delta\hat{\zeta}}\frac{\partial}{\partial \hat{x}}\left[\left(\frac{\partial}{\partial \hat{x}}\int_{-\hat{h}}^{\hat{z}}\hat{u}\,\mathrm{d}\hat{z}'\right)^2\right]\mathrm{d}\hat{z} - \mu^4\int_{-\hat{h}}^{\delta\hat{\zeta}}\frac{\partial^2}{\partial \hat{x}^2}\int_{\hat{z}}^{\delta\hat{\zeta}}\hat{\nu}_{\mathrm{t}}\frac{\partial \hat{w}}{\partial \hat{x}}\,\mathrm{d}\hat{z}'\,\mathrm{d}\hat{z} = 0.
\end{aligned} \tag{3.30}$$

In order to express the horizontal velocity in terms of potential and rotational velocities, it is necessary to reformulate Equation (3.30). This process is simplified by first obtaining several intermediate relations and then neglecting terms considered sufficiently small.

Using Equations (3.3), (3.21) to (3.23) and (3.43), the nondimensional depth averaged potential velocity is found to be

$$\begin{aligned}
\hat{\bar{u}}_{\mathrm{p}} &= \frac{1}{\delta\hat{\zeta} + \hat{h}}\int_{-\hat{h}}^{\delta\hat{\zeta}}\hat{u}_{\mathrm{p}}\,\mathrm{d}\hat{z} = \hat{u}|_{\hat{z}=-\hat{h}} - \mu^2\left(\delta\hat{\zeta} + \hat{h}\right)\left[\frac{\partial \hat{h}}{\partial \hat{x}}\frac{\partial}{\partial \hat{x}}\left(\hat{u}|_{\hat{z}=-\hat{h}}\right) + \frac{\hat{u}|_{\hat{z}=-\hat{h}}}{2}\frac{\partial^2 \hat{h}}{\partial \hat{x}^2}\right] \\
&\quad - \frac{\mu^2}{6}\left(\delta\hat{\zeta} + \hat{h}\right)^2\frac{\partial^2}{\partial \hat{x}^2}\left(\hat{u}|_{\hat{z}=-\hat{h}}\right) + \mathcal{O}\left(\mu^4\right) \\
&= \hat{u}|_{\hat{z}=-\hat{h}} - \frac{\mu^2}{2}\left(\delta\hat{\zeta} + \hat{h}\right)\left[\frac{\partial^2}{\partial \hat{x}^2}\left(\hat{h}\,\hat{u}|_{z=-\hat{h}}\right) + \frac{\delta\hat{\zeta} - 2\hat{h}}{3}\frac{\partial^2}{\partial \hat{x}^2}\left(\hat{u}|_{\hat{z}=-\hat{h}}\right)\right] + \mathcal{O}\left(\mu^4\right).
\end{aligned} \tag{A.61}$$

The nondimensional horizontal velocity at the bed can then be written as

$$\hat{u}|_{\hat{z}=-\hat{h}} = \hat{\bar{u}}_{\mathrm{p}} + \frac{\mu^2}{2}\left(\delta\hat{\zeta} + \hat{h}\right)\left[\frac{\partial^2}{\partial \hat{x}^2}\left(\hat{h}\,\hat{u}|_{z=-\hat{h}}\right) + \frac{\delta\hat{\zeta} - 2\hat{h}}{3}\frac{\partial^2}{\partial \hat{x}^2}\left(\hat{u}|_{\hat{z}=-\hat{h}}\right)\right] + \mathcal{O}\left(\mu^4\right), \tag{A.62}$$

and substituted back into Equation (3.43) to eliminate the nondimensional velocity at the bed from the expression for the nondimensional potential velocity:

$$\begin{aligned}\hat{u}_{\mathrm{p}} &= \hat{\bar{u}}_{\mathrm{p}} + \frac{\mu^2}{2}\left(\delta\hat{\zeta}+\hat{h}\right)\left[\frac{\partial^2}{\partial\hat{x}^2}\left(\hat{h}\hat{\bar{u}}_{\mathrm{p}}\right)+\frac{\delta\hat{\zeta}-2\hat{h}}{3}\frac{\partial^2\hat{\bar{u}}_{\mathrm{p}}}{\partial\hat{x}^2}\right] \\ &\quad -\mu^2\left(\hat{z}+\hat{h}\right)\left[\frac{\partial^2}{\partial\hat{x}^2}\left(\hat{h}\hat{\bar{u}}_{\mathrm{p}}\right)+\frac{\hat{z}-\hat{h}}{2}\frac{\partial^2\hat{\bar{u}}_{\mathrm{p}}}{\partial\hat{x}^2}\right]+\mathcal{O}\left(\mu^4\right) \\ &= \hat{\bar{u}}_{\mathrm{p}} + \mu^2\left(\frac{\delta\hat{\zeta}-\hat{h}}{2}-\hat{z}\right)\frac{\partial^2}{\partial\hat{x}^2}\left(\hat{h}\hat{\bar{u}}_{\mathrm{p}}\right)+\frac{\mu^2}{2}\left(\frac{\delta^2\hat{\zeta}^2-\delta\hat{\zeta}\hat{h}+\hat{h}^2}{3}-\hat{z}^2\right)\frac{\partial^2\hat{\bar{u}}_{\mathrm{p}}}{\partial\hat{x}^2}+\mathcal{O}\left(\mu^4\right)\end{aligned} \tag{A.63}$$

In order to express Equation (3.30) as a function of $\hat{\bar{u}}_{\mathrm{p}}$ and $\hat{u}_{\mathrm{r}}$, it is convenient to determine some additional terms separately using Equations (A.63) and (3.42). First, $\hat{u}^2$ is calculated as

$$\begin{aligned}\hat{u}^2 &= \left[\hat{\bar{u}}_{\mathrm{p}}+\mu^2\left(\frac{\delta\hat{\zeta}-\hat{h}}{2}-\hat{z}\right)\frac{\partial^2}{\partial\hat{x}^2}\left(\hat{h}\hat{\bar{u}}_{\mathrm{p}}\right)+\frac{\mu^2}{2}\left(\frac{\delta^2\hat{\zeta}^2-\delta\hat{\zeta}\hat{h}+\hat{h}^2}{3}-\hat{z}^2\right)\frac{\partial^2\hat{\bar{u}}_{\mathrm{p}}}{\partial\hat{x}^2}+\hat{u}_{\mathrm{r}}\right]^2 \\ &\quad +\mathcal{O}\left(\mu^4\right) \\ &= \left(\hat{\bar{u}}_{\mathrm{p}}+\hat{u}_{\mathrm{r}}\right)^2 \\ &\quad +\mu^2\left(\hat{\bar{u}}_{\mathrm{p}}+\hat{u}_{\mathrm{r}}\right)\left[\left(\delta\hat{\zeta}-\hat{h}-2\hat{z}\right)\frac{\partial^2}{\partial\hat{x}^2}\left(\hat{h}\hat{\bar{u}}_{\mathrm{p}}\right)+\left(\frac{\delta^2\hat{\zeta}^2-\delta\hat{\zeta}\hat{h}+\hat{h}^2}{3}-\hat{z}^2\right)\frac{\partial^2\hat{\bar{u}}_{\mathrm{p}}}{\partial\hat{x}^2}\right]+\mathcal{O}\left(\mu^4\right).\end{aligned} \tag{A.64}$$

The depth averaged form of Equation (3.42) provides

$$\hat{\bar{u}} = \hat{\bar{u}}_{\mathrm{p}} + \hat{\bar{u}}_{\mathrm{r}}, \tag{A.65}$$

from which the following expression is obtained:

$$\begin{aligned}\left(\hat{\bar{u}}_{\mathrm{p}}+\hat{u}_{\mathrm{r}}\right)^2 &= \left(\hat{\bar{u}}+\hat{u}_{\mathrm{r}}-\hat{\bar{u}}_{\mathrm{r}}\right)^2 = \hat{\bar{u}}^2+\left(2\hat{\bar{u}}+\hat{u}_{\mathrm{r}}-\hat{\bar{u}}_{\mathrm{r}}\right)\left(\hat{u}_{\mathrm{r}}-\hat{\bar{u}}_{\mathrm{r}}\right) \\ &= \hat{\bar{u}}^2+\left[2\left(\hat{\bar{u}}_{\mathrm{p}}+\hat{\bar{u}}_{\mathrm{r}}\right)+\hat{u}_{\mathrm{r}}-\hat{\bar{u}}_{\mathrm{r}}\right]\left(\hat{u}_{\mathrm{r}}-\hat{\bar{u}}_{\mathrm{r}}\right) \\ &= \hat{\bar{u}}^2+2\hat{\bar{u}}_{\mathrm{p}}\left(\hat{u}_{\mathrm{r}}-\hat{\bar{u}}_{\mathrm{r}}\right)-\hat{\bar{u}}_{\mathrm{r}}^2+\hat{u}_{\mathrm{r}}^2\end{aligned} \tag{A.66}$$

Additionally, Equation (3.28) allows the following relation to be used:

$$\hat{d}\frac{\partial\hat{\zeta}}{\partial\hat{x}} = \frac{\hat{d}}{\delta}\frac{\partial}{\partial\hat{x}}\left(\hat{d}-\hat{h}\right) = \frac{1}{\delta}\left[\frac{\partial}{\partial\hat{x}}\left(\frac{\hat{d}^2}{2}\right)-\hat{d}\frac{\partial\hat{h}}{\partial\hat{x}}\right] \tag{A.67}$$

Integrating Equation (A.64) across the water column, differentiating with respect to $\hat{x}$, and then substituting Equations (A.65), (A.66), (3.3), (3.28), (3.29) and (3.46)

provides

$$\begin{aligned}\frac{\partial}{\partial\hat{x}}\int_{-\hat{h}}^{\delta\hat{\zeta}}\hat{u}^2\,\mathrm{d}\hat{z} &= \frac{\partial}{\partial\hat{x}}\int_{-\hat{h}}^{\delta\hat{\zeta}}\hat{\bar{u}}^2+2\hat{\bar{u}}_\mathrm{p}\left(\hat{u}_\mathrm{r}-\hat{\bar{u}}_\mathrm{r}\right)-\hat{\bar{u}}_\mathrm{r}^2+\hat{u}_\mathrm{r}^2\,\mathrm{d}\hat{z}\\ &\quad+\mu^2\frac{\partial}{\partial\hat{x}}\int_{-\hat{h}}^{\delta\hat{\zeta}}\left\{\left(\hat{\bar{u}}+\hat{u}_\mathrm{r}-\hat{\bar{u}}_\mathrm{r}\right)\left[\left(\delta\hat{\zeta}-\hat{h}-2\hat{z}\right)\frac{\partial^2}{\partial\hat{x}^2}\left(\hat{h}\hat{\bar{u}}_\mathrm{p}\right)\right.\right.\\ &\qquad\left.\left.+\left(\frac{\delta^2\hat{\zeta}^2-\delta\hat{\zeta}\hat{h}+\hat{h}^2}{3}-\hat{z}^2\right)\frac{\partial^2\hat{\bar{u}}_\mathrm{p}}{\partial\hat{x}^2}\right]\right\}\,\mathrm{d}\hat{z}+\mathcal{O}\left(\mu^4\right)\\ &=\frac{\partial}{\partial\hat{x}}\left(\frac{\hat{q}^2}{\hat{d}}\right)+\frac{\partial}{\partial\hat{x}}\left(\widehat{\Delta M}\right)+\mu^2\frac{\partial}{\partial\hat{x}}\int_{-\hat{h}}^{\delta\hat{\zeta}}\left\{\left(\hat{u}_\mathrm{r}-\hat{\bar{u}}_\mathrm{r}\right)\left[\left(\delta\hat{\zeta}-\hat{h}-2\hat{z}\right)\frac{\partial^2}{\partial\hat{x}^2}\left(\hat{h}\hat{\bar{u}}_\mathrm{p}\right)\right.\right.\\ &\qquad\left.\left.+\left(\frac{\delta^2\hat{\zeta}^2-\delta\hat{\zeta}\hat{h}+\hat{h}^2}{3}-\hat{z}^2\right)\frac{\partial^2\hat{\bar{u}}_\mathrm{p}}{\partial\hat{x}^2}\right]\right\}\,\mathrm{d}\hat{z}+\mathcal{O}\left(\mu^4\right).\end{aligned} \tag{A.68}$$

As the z-dependent terms in Equation (3.43) are $\mathcal{O}\left(\mu^2\right)$ or less, it follows that

$$\hat{\bar{u}}_\mathrm{p}=\hat{u}_\mathrm{p}+\mathcal{O}\left(\mu^2\right), \tag{A.69}$$

which, with Equations (A.65) and (3.42), allows the nondimensional horizontal velocity to be written as

$$\hat{u}=\hat{\bar{u}}+\hat{u}_\mathrm{r}-\hat{\bar{u}}_\mathrm{r}+\mathcal{O}\left(\mu^2\right). \tag{A.70}$$

With Equation (3.26), the dimensional form of Equation (A.70) can be obtained accurate to $\mathcal{O}\left(\mu^2\right)$, giving

$$u=\bar{u}+u_\mathrm{r}-\bar{u}_\mathrm{r}. \tag{4.53}$$

Equations (A.70), (3.39) and (3.47) provide the following relation:

$$\begin{aligned}\int_{-\hat{h}}^{\delta\hat{\zeta}}\frac{\partial^2}{\partial\hat{x}\partial\hat{t}}\int_{\hat{z}}^{\delta\hat{\zeta}}\frac{\partial}{\partial\hat{x}}\int_{-\hat{h}}^{\hat{z}'}\hat{u}\,\mathrm{d}\hat{z}''\,\mathrm{d}\hat{z}'\,\mathrm{d}\hat{z} &= \int_{-\hat{h}}^{\delta\hat{\zeta}}\frac{\partial^2}{\partial\hat{x}\partial\hat{t}}\int_{\hat{z}}^{\delta\hat{\zeta}}\frac{\partial}{\partial\hat{x}}\int_{-\hat{h}}^{\hat{z}'}\hat{\bar{u}}\,\mathrm{d}\hat{z}''\,\mathrm{d}\hat{z}'\,\mathrm{d}\hat{z}-\frac{\partial^3}{\partial\hat{x}^2\partial\hat{t}}\left(\widehat{\Delta P}\right)\\ &\quad-\frac{\partial^2}{\partial\hat{x}\partial\hat{t}}\left(\frac{\partial\hat{h}}{\partial\hat{x}}\int_{-\hat{h}}^{\delta\hat{\zeta}}\int_{-\hat{h}}^{\hat{z}}\hat{u}_\mathrm{r}-\hat{\bar{u}}_\mathrm{r}\,\mathrm{d}\hat{z}'\,\mathrm{d}\hat{z}\right)\\ &\quad-\delta\frac{\partial^2}{\partial\hat{x}\partial\hat{t}}\int_{-\hat{h}}^{\delta\hat{\zeta}}\frac{\partial\hat{\zeta}}{\partial\hat{x}}\int_{-\hat{h}}^{\delta\hat{\zeta}}\hat{u}_\mathrm{r}-\hat{\bar{u}}_\mathrm{r}\,\mathrm{d}\hat{z}'\,\mathrm{d}\hat{z}\\ &\quad-\frac{\partial\hat{h}}{\partial\hat{x}}\frac{\partial}{\partial\hat{t}}\int_{-\hat{h}}^{\delta\hat{\zeta}}\frac{\partial}{\partial\hat{x}}\int_{-\hat{h}}^{\hat{z}}\hat{u}_\mathrm{r}-\hat{\bar{u}}_\mathrm{r}\,\mathrm{d}\hat{z}'\,\mathrm{d}\hat{z}+\mathcal{O}\left(\mu^2\right)\end{aligned} \tag{A.71}$$

Expanding the first term in Equation (A.71) gives

$$\begin{aligned}\int_{-\hat{h}}^{\delta\hat{\zeta}}\frac{\partial^2}{\partial\hat{x}\partial\hat{t}}\int_{\hat{z}}^{\delta\hat{\zeta}}\frac{\partial}{\partial\hat{x}}\int_{-\hat{h}}^{\hat{z}'}\hat{\tilde{u}}\,\mathrm{d}\hat{z}''\,\mathrm{d}\hat{z}'\,\mathrm{d}\hat{z} &= \frac{1}{3}\left(\delta\hat{\zeta}+\hat{h}\right)^3\frac{\partial^3\hat{\tilde{u}}}{\partial\hat{x}^2\partial\hat{t}}+\left(\delta\hat{\zeta}+\hat{h}\right)^2\left(\frac{1}{2}\frac{\partial^2\hat{h}}{\partial\hat{x}^2}\frac{\partial\hat{\tilde{u}}}{\partial\hat{t}}\right.\\ &\quad\left.+\frac{\partial\hat{h}}{\partial\hat{x}}\frac{\partial^2\hat{\tilde{u}}}{\partial\hat{x}\partial\hat{t}}+\delta\frac{\partial^2\hat{\tilde{u}}}{\partial\hat{x}^2}\frac{\partial\hat{\zeta}}{\partial\hat{t}}+\delta\frac{\partial\hat{\tilde{u}}}{\partial\hat{x}}\frac{\partial^2\hat{\zeta}}{\partial\hat{x}\partial\hat{t}}+\delta\frac{\partial^2\hat{\tilde{u}}}{\partial\hat{x}\partial\hat{t}}\frac{\partial\hat{\zeta}}{\partial\hat{x}}\right)\\ &\quad+\left(\delta\hat{\zeta}+\hat{h}\right)\left[\delta\frac{\partial^2\hat{\zeta}}{\partial\hat{x}\partial\hat{t}}\frac{\partial\hat{h}}{\partial\hat{x}}\hat{\tilde{u}}+\delta\frac{\partial\hat{\zeta}}{\partial\hat{x}}\frac{\partial\hat{h}}{\partial\hat{x}}\frac{\partial\hat{\tilde{u}}}{\partial\hat{t}}+\delta\frac{\partial\hat{\zeta}}{\partial\hat{t}}\frac{\partial^2\hat{h}}{\partial\hat{x}^2}\hat{\tilde{u}}\right.\\ &\quad\left.+\delta\frac{\partial\hat{\tilde{u}}}{\partial\hat{x}}\left(\delta\frac{\partial\hat{\zeta}}{\partial\hat{x}}\frac{\partial\hat{\zeta}}{\partial\hat{t}}+\frac{\partial\hat{\zeta}}{\partial\hat{t}}\frac{\partial\hat{h}}{\partial\hat{x}}+\delta\frac{\partial\hat{\zeta}}{\partial\hat{t}}\frac{\partial\hat{h}}{\partial\hat{x}}\right)\right].\end{aligned} \tag{A.72}$$

Equation (A.70) also allows the following relation to be obtained:

$$\begin{aligned}&\int_{-\hat{h}}^{\delta\hat{\zeta}}\frac{\partial^2}{\partial\hat{x}^2}\int_{\hat{z}}^{\delta\hat{\zeta}}\hat{u}\frac{\partial}{\partial\hat{x}}\int_{-\hat{h}}^{\hat{z}'}\hat{u}\,\mathrm{d}\hat{z}''\,\mathrm{d}\hat{z}'\,\mathrm{d}\hat{z}\\ &=\left(\delta\hat{\zeta}+\hat{h}\right)\left[\delta\frac{\partial^2\hat{\zeta}}{\partial\hat{x}^2}\frac{\partial\hat{h}}{\partial\hat{x}}\hat{\tilde{u}}^2+2\delta\frac{\partial\hat{\zeta}}{\partial\hat{x}}\frac{\partial^2\hat{h}}{\partial\hat{x}^2}\hat{\tilde{u}}^2+6\delta\frac{\partial\hat{\zeta}}{\partial\hat{x}}\frac{\partial\hat{h}}{\partial\hat{x}}\frac{\partial\hat{\tilde{u}}}{\partial\hat{x}}\hat{\tilde{u}}+\left(\delta\frac{\partial\hat{\zeta}}{\partial\hat{x}}\right)^2\frac{\partial\hat{\tilde{u}}}{\partial\hat{x}}\hat{\tilde{u}}\right]\\ &\quad+\left(\delta\hat{\zeta}+\hat{h}\right)^2\left[\frac{\partial\hat{\tilde{u}}}{\partial\hat{x}}\hat{\tilde{u}}\frac{\partial^2}{\partial\hat{x}^2}\left(\delta\hat{\zeta}+\hat{h}\right)+2\frac{\partial}{\partial\hat{x}}\left(\delta\hat{\zeta}+\hat{h}\right)\frac{\partial}{\partial\hat{x}}\left(\frac{\partial\hat{\tilde{u}}}{\partial\hat{x}}\hat{\tilde{u}}\right)+\frac{1}{2}\frac{\partial^3\hat{h}}{\partial\hat{x}^3}\hat{\tilde{u}}^2+\frac{3}{2}\frac{\partial^2\hat{h}}{\partial\hat{x}^2}\frac{\partial\hat{\tilde{u}}}{\partial\hat{x}}\hat{\tilde{u}}\right]\\ &\quad+\left(\delta\hat{\zeta}+\hat{h}\right)^3\left(\frac{1}{3}\frac{\partial^3\hat{\tilde{u}}}{\partial\hat{x}^3}\hat{\tilde{u}}+\frac{\partial^2\hat{\tilde{u}}}{\partial\hat{x}^2}\frac{\partial\hat{\tilde{u}}}{\partial\hat{x}}\right)\\ &\quad+\int_{-\hat{h}}^{\delta\hat{\zeta}}\frac{\partial^2}{\partial\hat{x}^2}\int_{\hat{z}}^{\delta\hat{\zeta}}\left(\hat{u}_\mathrm{r}-\hat{\tilde{u}}_\mathrm{r}\right)\frac{\partial}{\partial\hat{x}}\int_{-\hat{h}}^{\hat{z}'}\hat{\tilde{u}}\,\mathrm{d}\hat{z}''+\left(\hat{\tilde{u}}+\hat{u}_\mathrm{r}-\hat{\tilde{u}}_\mathrm{r}\right)\frac{\partial}{\partial\hat{x}}\int_{-\hat{h}}^{\hat{z}'}\hat{u}_\mathrm{r}-\hat{\tilde{u}}_\mathrm{r}\,\mathrm{d}\hat{z}''\,\mathrm{d}\hat{z}'\,\mathrm{d}\hat{z}\end{aligned} \tag{A.73}$$

A final expansion is performed using Equation (A.70):

$$\begin{aligned}&\int_{-\hat{h}}^{\delta\hat{\zeta}}\frac{\partial}{\partial\hat{x}}\left[\left(\frac{\partial}{\partial\hat{x}}\int_{-\hat{h}}^{\hat{z}}\hat{u}\,\mathrm{d}\hat{z}'\right)^2\right]\,\mathrm{d}\hat{z}\\ &=\int_{-\hat{h}}^{\delta\hat{\zeta}}\frac{\partial}{\partial\hat{x}}\left[\left(\frac{\partial}{\partial\hat{x}}\int_{-\hat{h}}^{\hat{z}}\hat{\tilde{u}}\,\mathrm{d}\hat{z}'\right)^2+\left(\frac{\partial}{\partial\hat{x}}\int_{-\hat{h}}^{\hat{z}}\hat{u}_\mathrm{r}-\hat{\tilde{u}}_\mathrm{r}\,\mathrm{d}\hat{z}'\right)\left(\frac{\partial}{\partial\hat{x}}\int_{-\hat{h}}^{\hat{z}}2\hat{\tilde{u}}+\hat{u}_\mathrm{r}-\hat{\tilde{u}}_\mathrm{r}\,\mathrm{d}\hat{z}'\right)\right]\,\mathrm{d}\hat{z}\\ &=\frac{2}{3}\left(\delta\hat{\zeta}+\hat{h}\right)^3\frac{\partial\hat{\tilde{u}}}{\partial\hat{x}}\frac{\partial^2\hat{\tilde{u}}}{\partial\hat{x}^2}+\left(\delta\hat{\zeta}+\hat{h}\right)^2\frac{\partial}{\partial\hat{x}}\left(\hat{\tilde{u}}\frac{\partial\hat{\tilde{u}}}{\partial\hat{x}}\frac{\partial\hat{h}}{\partial\hat{x}}\right)+2\left(\delta\hat{\zeta}+\hat{h}\right)\hat{\tilde{u}}\frac{\partial\hat{h}}{\partial\hat{x}}\left(\hat{\tilde{u}}\frac{\partial^2\hat{h}}{\partial\hat{x}^2}+2\frac{\partial\hat{\tilde{u}}}{\partial\hat{x}}\frac{\partial\hat{h}}{\partial\hat{x}}\right)\\ &\quad+\int_{-\hat{h}}^{\delta\hat{\zeta}}\frac{\partial}{\partial\hat{x}}\left[\left(\frac{\partial}{\partial\hat{x}}\int_{-\hat{h}}^{\hat{z}}\hat{u}_\mathrm{r}-\hat{\tilde{u}}_\mathrm{r}\,\mathrm{d}\hat{z}'\right)\left(\frac{\partial}{\partial\hat{x}}\int_{-\hat{h}}^{\hat{z}}2\hat{\tilde{u}}+\hat{u}_\mathrm{r}-\hat{\tilde{u}}_\mathrm{r}\,\mathrm{d}\hat{z}'\right)\right]\,\mathrm{d}\hat{z}\end{aligned} \tag{A.74}$$

Substituting Equations (A.67), (A.68), (A.71) to (A.74), (3.28) and (3.46) to (3.48) into Equation (3.30) provides a nondimensionalised form of the momentum equation

with depth averaged, potential and rotational flow components:

$$
\begin{aligned}
&\frac{\partial \hat{q}}{\partial \hat{t}} + \frac{1}{\delta}\left[\frac{\partial}{\partial \hat{x}}\left(\frac{\hat{d}^2}{2}\right) - \hat{d}\frac{\partial \hat{h}}{\partial \hat{x}}\right] + \delta\left[\frac{\partial}{\partial \hat{x}}\left(\frac{\hat{q}^2}{\hat{d}}\right) + \frac{\partial}{\partial \hat{x}}\left(\widehat{\Delta M}\right)\right] \\
&- \mu^2\left[\frac{\hat{d}^3}{3}\frac{\partial^3 \hat{\bar{u}}}{\partial \hat{x}^2 \partial \hat{t}} + \hat{d}^2\left(\frac{1}{2}\frac{\partial^2 \hat{h}}{\partial \hat{x}^2}\frac{\partial \hat{\bar{u}}}{\partial \hat{t}} + \frac{\partial \hat{h}}{\partial \hat{x}}\frac{\partial^2 \hat{\bar{u}}}{\partial \hat{x}\partial \hat{t}}\right) - \frac{\partial^3}{\partial \hat{x}^2 \partial \hat{t}}\left(\widehat{\Delta P}\right)\right. \\
&\left. - \frac{\partial^2}{\partial \hat{x}\partial \hat{t}}\left(\frac{\partial \hat{h}}{\partial \hat{x}}\int_{-\hat{h}}^{\delta\hat{\zeta}}\int_{-\hat{h}}^{\hat{z}} \hat{u}_\mathrm{r} - \hat{\bar{u}}_\mathrm{r}\,\mathrm{d}\hat{z}'\,\mathrm{d}\hat{z}\right) - \frac{\partial \hat{h}}{\partial \hat{x}}\frac{\partial}{\partial \hat{t}}\int_{-\hat{h}}^{\delta\hat{\zeta}}\frac{\partial}{\partial \hat{x}}\int_{-\hat{h}}^{\hat{z}} \hat{u}_\mathrm{r} - \hat{\bar{u}}_\mathrm{r}\,\mathrm{d}\hat{z}'\,\mathrm{d}\hat{z} + \widehat{D}_\mathrm{s}\right] \\
&- \delta\mu^2\left\{\hat{d}^3\left(\frac{1}{3}\frac{\partial^3 \hat{\bar{u}}}{\partial \hat{x}^3}\hat{\bar{u}} + \frac{\partial^2 \hat{\bar{u}}}{\partial \hat{x}^2}\frac{\partial \hat{\bar{u}}}{\partial \hat{x}} + \frac{2}{3}\frac{\partial \hat{\bar{u}}}{\partial \hat{x}}\frac{\partial^2 \hat{\bar{u}}}{\partial \hat{x}^2}\right) - \hat{d}^2\left[\frac{\partial^2 \hat{\bar{u}}}{\partial \hat{x}^2}\frac{\partial \hat{\zeta}}{\partial \hat{t}} + \frac{\partial \hat{\bar{u}}}{\partial \hat{x}}\frac{\partial^2 \hat{\zeta}}{\partial \hat{x}\partial \hat{t}} + \frac{\partial^2 \hat{\bar{u}}}{\partial \hat{x}\partial \hat{t}}\frac{\partial \hat{\zeta}}{\partial \hat{x}}\right.\right. \\
&\left. - \frac{\partial \hat{\bar{u}}}{\partial \hat{x}}\hat{\bar{u}}\frac{\partial^2 \hat{d}}{\partial \hat{x}^2} - 2\frac{\partial \hat{d}}{\partial \hat{x}}\frac{\partial}{\partial \hat{x}}\left(\frac{\partial \hat{\bar{u}}}{\partial \hat{x}}\hat{\bar{u}}\right) - \frac{1}{2}\frac{\partial^3 \hat{h}}{\partial \hat{x}^3}\hat{\bar{u}}^2 - \frac{3}{2}\frac{\partial^2 \hat{h}}{\partial \hat{x}^2}\frac{\partial \hat{\bar{u}}}{\partial \hat{x}}\hat{\bar{u}} + \frac{\partial}{\partial \hat{x}}\left(\hat{\bar{u}}\frac{\partial \hat{\bar{u}}}{\partial \hat{x}}\frac{\partial \hat{h}}{\partial \hat{x}}\right)\right] \\
&- \hat{d}\left[\frac{\partial^2 \hat{\zeta}}{\partial \hat{x}\partial \hat{t}}\frac{\partial \hat{h}}{\partial \hat{x}}\hat{\bar{u}} + \frac{\partial \hat{\zeta}}{\partial \hat{x}}\frac{\partial \hat{h}}{\partial \hat{x}}\frac{\partial \hat{\bar{u}}}{\partial \hat{t}} + \frac{\partial \hat{\zeta}}{\partial \hat{t}}\frac{\partial^2 \hat{h}}{\partial \hat{x}^2}\hat{\bar{u}} + \frac{\partial \hat{\bar{u}}}{\partial \hat{x}}\frac{\partial \hat{\zeta}}{\partial \hat{t}}\frac{\partial \hat{h}}{\partial \hat{x}} - 2\hat{\bar{u}}\frac{\partial \hat{h}}{\partial \hat{x}}\left(\hat{\bar{u}}\frac{\partial^2 \hat{h}}{\partial \hat{x}^2} + 2\frac{\partial \hat{\bar{u}}}{\partial \hat{x}}\frac{\partial \hat{h}}{\partial \hat{x}}\right)\right] \\
&+ \frac{\partial^2}{\partial \hat{x}\partial \hat{t}}\int_{-\hat{h}}^{\delta\hat{\zeta}}\frac{\partial \hat{\zeta}}{\partial \hat{x}}\int_{-\hat{h}}^{\delta\hat{\zeta}} \hat{u}_\mathrm{r} - \hat{\bar{u}}_\mathrm{r}\,\mathrm{d}\hat{z}'\,\mathrm{d}\hat{z} \\
&- \frac{\partial}{\partial \hat{x}}\int_{-\hat{h}}^{\delta\hat{\zeta}}\left(\hat{u}_\mathrm{r} - \hat{\bar{u}}_\mathrm{r}\right)\left[\left(\hat{d} - 2\hat{h} - 2\hat{z}\right)\frac{\partial^2}{\partial \hat{x}^2}\left(\hat{h}\hat{\bar{u}}_\mathrm{p}\right) + \left(\frac{\hat{d}^2}{3} + \hat{h}^2 - \hat{d}\hat{h} - \hat{z}^2\right)\frac{\partial^2 \hat{\bar{u}}_\mathrm{p}}{\partial \hat{x}^2}\right]\,\mathrm{d}\hat{z} \\
&+ \int_{-\hat{h}}^{\delta\hat{\zeta}}\frac{\partial^2}{\partial \hat{x}^2}\int_{\hat{z}}^{\delta\hat{\zeta}}\left(\hat{u}_\mathrm{r} - \hat{\bar{u}}_\mathrm{r}\right)\frac{\partial}{\partial \hat{x}}\int_{-\hat{h}}^{\hat{z}'}\hat{\bar{u}}\,\mathrm{d}\hat{z}'' + \left(\hat{\bar{u}} + \hat{u}_\mathrm{r} - \hat{\bar{u}}_\mathrm{r}\right)\frac{\partial}{\partial \hat{x}}\int_{-\hat{h}}^{\hat{z}'} \hat{u}_\mathrm{r} - \hat{\bar{u}}_\mathrm{r}\,\mathrm{d}\hat{z}''\,\mathrm{d}\hat{z}'\,\mathrm{d}\hat{z} \\
&\left. + \int_{-\hat{h}}^{\delta\hat{\zeta}}\frac{\partial}{\partial \hat{x}}\left[\left(\frac{\partial}{\partial \hat{x}}\int_{-\hat{h}}^{\hat{z}} \hat{u}_\mathrm{r} - \hat{\bar{u}}_\mathrm{r}\,\mathrm{d}\hat{z}'\right)\left(\frac{\partial}{\partial \hat{x}}\int_{-\hat{h}}^{\hat{z}} 2\hat{\bar{u}} + \hat{u}_\mathrm{r} - \hat{\bar{u}}_\mathrm{r}\,\mathrm{d}\hat{z}'\right)\right]\,\mathrm{d}\hat{z}\right\} \\
&- \delta^2\mu^2\hat{d}\left[\left(\frac{\partial^2 \hat{\zeta}}{\partial \hat{x}^2}\frac{\partial \hat{h}}{\partial \hat{x}} + 2\frac{\partial \hat{\zeta}}{\partial \hat{x}}\frac{\partial^2 \hat{h}}{\partial \hat{x}^2}\right)\hat{\bar{u}}^2 - \frac{\partial \hat{\bar{u}}}{\partial \hat{x}}\left(\frac{\partial \hat{\zeta}}{\partial \hat{x}}\frac{\partial \hat{\zeta}}{\partial \hat{t}} + \frac{\partial \hat{\zeta}}{\partial \hat{t}}\frac{\partial \hat{h}}{\partial \hat{x}} - 6\frac{\partial \hat{\zeta}}{\partial \hat{x}}\frac{\partial \hat{h}}{\partial \hat{x}}\hat{\bar{u}}\right)\right] \\
&- \delta^3\mu^2\hat{d}\left(\frac{\partial \hat{\zeta}}{\partial \hat{x}}\right)^2\frac{\partial \hat{\bar{u}}}{\partial \hat{x}}\hat{\bar{u}} = \mathcal{O}\left(\mu^4\right)
\end{aligned}
\tag{A.75}
$$

By assuming the gradient and the change in the gradient of the bed to be relatively small, terms $\mathcal{O}\left(\mu^2\frac{\partial \hat{h}}{\partial \hat{x}}\right)$ can be neglected from the rotational terms within Equation (A.75). This then provides the momentum equation for the FNBs. In the work presented here, the complexity of the equations is further reduced by also removing terms $\mathcal{O}\left(\delta\mu^2\right)$ in order to obtain WNBs. Noting that, from Equation (3.28),

$$
\hat{d} = \hat{h} + \mathcal{O}\left(\delta\right), \tag{A.76}
$$

Equation (A.75) can then be written as

$$
\begin{aligned}
&\frac{\partial \hat{q}}{\partial \hat{t}} + \frac{1}{\delta}\left[\frac{\partial}{\partial \hat{x}}\left(\frac{\hat{d}^2}{2}\right) - \hat{d}\frac{\partial \hat{h}}{\partial \hat{x}}\right] + \delta\left[\frac{\partial}{\partial \hat{x}}\left(\frac{\hat{q}^2}{\hat{d}}\right) + \frac{\partial}{\partial \hat{x}}\left(\widehat{\Delta M}\right)\right] - \mu^2\left[\frac{\hat{d}^3}{3}\frac{\partial^3 \hat{\bar{u}}}{\partial \hat{x}^2 \partial \hat{t}}\right. \\
&\left. + \hat{d}^2\left(\frac{1}{2}\frac{\partial^2 \hat{h}}{\partial \hat{x}^2}\frac{\partial \hat{\bar{u}}}{\partial \hat{t}} + \frac{\partial \hat{h}}{\partial \hat{x}}\frac{\partial^2 \hat{\bar{u}}}{\partial \hat{x}\partial \hat{t}}\right) - \frac{\partial^3}{\partial \hat{x}^2 \partial \hat{t}}\left(\widehat{\Delta P}\right) + \widehat{D}_\mathrm{s}\right] = \mathcal{O}\left(\delta\mu^2, \mu^2\frac{\partial \hat{h}}{\partial \hat{x}}, \mu^4\right).
\end{aligned}
\tag{A.77}
$$

In order to express the depth averaged velocity in Equation (A.77) in terms of a flow rate, Equations (3.28) and (3.29) are used to derive the following expressions:

$$\frac{\partial^2 \hat{\bar{u}}}{\partial \hat{x}\partial \hat{t}} = \frac{\partial^2}{\partial \hat{x}\partial \hat{t}}\left(\frac{\hat{q}}{\hat{d}}\right) = \frac{1}{\hat{d}}\frac{\partial^2 \hat{q}}{\partial \hat{x}\partial \hat{t}} - \frac{1}{\hat{d}^2}\frac{\partial \hat{q}}{\partial \hat{x}}\frac{\partial \hat{d}}{\partial \hat{t}} - \frac{1}{\hat{d}^2}\frac{\partial \hat{q}}{\partial \hat{t}}\frac{\partial \hat{d}}{\partial \hat{x}} - \frac{\hat{q}}{\hat{d}^2}\frac{\partial^2 \hat{d}}{\partial \hat{x}\partial \hat{t}} + 2\frac{\hat{q}}{\hat{d}^3}\frac{\partial \hat{d}}{\partial \hat{x}}\frac{\partial \hat{d}}{\partial \hat{t}} \tag{A.78}$$

$$\begin{aligned}\frac{\partial^3 \hat{\bar{u}}}{\partial \hat{x}^2\partial \hat{t}} = {} & \frac{1}{\hat{d}}\frac{\partial^3 \hat{q}}{\partial \hat{x}^2\partial \hat{t}} - 2\frac{1}{\hat{d}^2}\frac{\partial^2 \hat{q}}{\partial \hat{x}\partial \hat{t}}\frac{\partial \hat{d}}{\partial \hat{x}} - \frac{1}{\hat{d}^2}\frac{\partial^2 \hat{q}}{\partial \hat{x}^2}\frac{\partial \hat{d}}{\partial \hat{t}} - 2\frac{1}{\hat{d}^2}\frac{\partial \hat{q}}{\partial \hat{x}}\frac{\partial^2 \hat{d}}{\partial \hat{x}\partial \hat{t}} + \frac{4}{\hat{d}^3}\frac{\partial \hat{q}}{\partial \hat{x}}\frac{\partial \hat{d}}{\partial \hat{x}}\frac{\partial \hat{d}}{\partial \hat{t}} - \frac{1}{\hat{d}^2}\frac{\partial \hat{q}}{\partial \hat{t}}\frac{\partial^2 \hat{d}}{\partial \hat{x}^2} \\ & + \frac{2}{\hat{d}^3}\frac{\partial \hat{q}}{\partial \hat{t}}\left(\frac{\partial \hat{d}}{\partial \hat{x}}\right)^2 - \frac{\hat{q}}{\hat{d}^2}\frac{\partial^3 \hat{d}}{\partial \hat{x}^2\partial \hat{t}} + \frac{4\hat{q}}{\hat{d}^3}\frac{\partial \hat{d}}{\partial \hat{x}}\frac{\partial^2 \hat{d}}{\partial \hat{x}\partial \hat{t}} + \frac{2\hat{q}}{\hat{d}^3}\frac{\partial^2 \hat{d}}{\partial \hat{x}^2}\frac{\partial \hat{d}}{\partial \hat{t}} - \frac{6\hat{q}}{\hat{d}^4}\left(\frac{\partial \hat{d}}{\partial \hat{x}}\right)^2\frac{\partial \hat{d}}{\partial \hat{t}}\end{aligned} \tag{A.79}$$

Together, Equations (A.78), (A.79) and (3.28) give

$$\begin{aligned}\frac{\hat{d}^3}{3}\frac{\partial^3 \hat{\bar{u}}}{\partial \hat{x}^2\partial \hat{t}} + \hat{d}^2\left(\frac{1}{2}\frac{\partial^2 \hat{h}}{\partial \hat{x}^2}\frac{\partial \hat{\bar{u}}}{\partial \hat{t}} + \frac{\partial \hat{h}}{\partial \hat{x}}\frac{\partial^2 \hat{\bar{u}}}{\partial \hat{x}\partial \hat{t}}\right) = {} & \frac{\hat{h}}{3}\left[\hat{d}\frac{\partial^3 \hat{q}}{\partial \hat{x}^2\partial \hat{t}} - 2\frac{\partial^2 \hat{q}}{\partial \hat{x}\partial \hat{t}}\frac{\partial \hat{d}}{\partial \hat{x}} - \frac{\partial^2 \hat{q}}{\partial \hat{x}^2}\frac{\partial \hat{d}}{\partial \hat{t}} - 2\frac{\partial \hat{q}}{\partial \hat{x}}\frac{\partial^2 \hat{d}}{\partial \hat{x}\partial \hat{t}}\right. \\ & + \frac{4}{\hat{d}}\frac{\partial \hat{q}}{\partial \hat{x}}\frac{\partial \hat{d}}{\partial \hat{x}}\frac{\partial \hat{d}}{\partial \hat{t}} - \frac{\partial \hat{q}}{\partial \hat{t}}\frac{\partial^2 \hat{d}}{\partial \hat{x}^2} + \frac{2}{\hat{d}}\frac{\partial \hat{q}}{\partial \hat{t}}\left(\frac{\partial \hat{d}}{\partial \hat{x}}\right)^2 \\ & - \hat{q}\frac{\partial^3 \hat{d}}{\partial \hat{x}^2\partial \hat{t}} + \frac{4\hat{q}}{\hat{d}}\frac{\partial \hat{d}}{\partial \hat{x}}\frac{\partial^2 \hat{d}}{\partial \hat{x}\partial \hat{t}} + \frac{2\hat{q}}{\hat{d}}\frac{\partial^2 \hat{d}}{\partial \hat{x}^2}\frac{\partial \hat{d}}{\partial \hat{t}} \\ & \left. - \frac{6\hat{q}}{\hat{d}^2}\left(\frac{\partial \hat{d}}{\partial \hat{x}}\right)^2\frac{\partial \hat{d}}{\partial \hat{t}}\right] \\ & + \frac{\partial \hat{h}}{\partial \hat{x}}\left(\hat{d}\frac{\partial^2 \hat{q}}{\partial \hat{x}\partial \hat{t}} - \frac{\partial \hat{q}}{\partial \hat{x}}\frac{\partial \hat{d}}{\partial \hat{t}} - \frac{\partial \hat{q}}{\partial \hat{t}}\frac{\partial \hat{d}}{\partial \hat{x}} - \hat{q}\frac{\partial^2 \hat{d}}{\partial \hat{x}\partial \hat{t}}\right. \\ & \left. + 2\frac{\hat{q}}{\hat{d}}\frac{\partial \hat{d}}{\partial \hat{x}}\frac{\partial \hat{d}}{\partial \hat{t}}\right) + \frac{\hat{d}^2}{2}\frac{\partial^2 \hat{h}}{\partial \hat{x}^2}\frac{\partial \hat{\bar{u}}}{\partial \hat{t}} + \frac{\delta}{3}\hat{d}^2\hat{\zeta}\frac{\partial^3 \hat{\bar{u}}}{\partial \hat{x}^2\partial \hat{t}} \\ = {} & \frac{\hat{h}}{3}\frac{\partial}{\partial \hat{t}}\left(\hat{h}\frac{\partial^2 \hat{q}}{\partial \hat{x}^2} + \frac{\partial \hat{h}}{\partial \hat{x}}\frac{\partial \hat{q}}{\partial \hat{x}}\right) + \mathcal{O}\left[\delta, \left(\frac{\partial \hat{h}}{\partial \hat{x}}\right)^2, \frac{\partial^2 \hat{h}}{\partial \hat{x}^2}\right].\end{aligned} \tag{A.80}$$

With Equation (A.80), Equation (A.77) can be written as

$$\begin{aligned}& \frac{\partial \hat{q}}{\partial \hat{t}} + \frac{1}{\delta}\left[\frac{\partial}{\partial \hat{x}}\left(\frac{\hat{d}^2}{2}\right) - \hat{d}\frac{\partial \hat{h}}{\partial \hat{x}}\right] + \delta\left[\frac{\partial}{\partial \hat{x}}\left(\frac{\hat{q}^2}{\hat{d}}\right) + \frac{\partial}{\partial \hat{x}}\left(\widehat{\Delta M}\right)\right] \\ & - \mu^2\left[\frac{\hat{h}}{3}\frac{\partial}{\partial \hat{t}}\left(\hat{h}\frac{\partial^2 \hat{q}}{\partial \hat{x}^2} + \frac{\partial \hat{h}}{\partial \hat{x}}\frac{\partial \hat{q}}{\partial \hat{x}}\right) - \frac{\partial^3}{\partial \hat{x}^2\partial \hat{t}}\left(\widehat{\Delta P}\right) + \widehat{D_{\mathrm{s}}}\right] = \mathcal{O}\left(\delta\mu^2, \mu^2\frac{\partial \hat{h}}{\partial \hat{x}}, \mu^4\right).\end{aligned} \tag{3.45}$$

A.6 Lagrangian stream function

The Lagrangian stream function, ψ, defines the path of a streamline, across which there is no flow. The continuity equation can be used to express the horizontal and vertical velocities as derivatives of the stream function. The resulting expressions are subsequently used several times in Section 3.2.

Integrating Equation (A.48) along a closed streamline gives

$$\int u \, \mathrm{d}z + \int w \, \mathrm{d}x = 0. \tag{A.81}$$

Equation (A.81) can then be used to express the stream function as

$$\psi = \int u \, \mathrm{d}z = - \int w \, \mathrm{d}x, \tag{A.82}$$

allowing the horizontal and vertical velocities to be written as

$$u = \frac{\partial \psi}{\partial z} \tag{3.15}$$

and

$$w = -\frac{\partial \psi}{\partial x}, \tag{3.16}$$

respectively (Apel, 1988; White, 2003).

Appendix B

Numerical calculation of rotational and breaking terms

B.1 Computational efficiency

The method outlined in Section 4.8.1 is used in the calculation of the breaking terms, vorticity, and rotational and horizontal velocities. This chapter explicitly details the application of this technique for determining each specific quantity. The formulation presented here provides a method of calculating each term using matrix multiplication. Such an approach is well suited to numerical computation, and allows established and well optimised numerical techniques and algorithms to be employed. Although computational performance is not a major focus of the present study, it is important to consider the economy of such schemes, as numerical efficiency is an important motivation in the development of BTMs.

B.2 Rotational velocity

A vertical discretisation is achieved by sampling σ at L points according to

$$s_l = \frac{l-1}{L-1} \quad o \in \{1, 2, \ldots, L\}. \tag{B.1}$$

The rotational velocity given by Equation (4.51) can then be approximated at L points from the bed to the lower edge of the roller according to the relation

$$R_l \simeq (h + \zeta_e) \sum_{n=1}^{M} \frac{G_n}{n\pi} \left[1 - \cos\left(n\pi s_l\right)\right] \quad l \in \{1, 2, \ldots, L\}, \tag{B.2}$$

where

$$R_l \equiv u_r|_{\sigma=s_l} \quad l \in \{1, 2, \ldots, L\}. \tag{B.3}$$

The solution to Equation (B.2) is then obtained using a method similar to that described previously in Equations (4.89) to (4.92):

$$\boldsymbol{R}_{N,L} = \operatorname{diag}\left(\boldsymbol{h}_N + \boldsymbol{\eta}_N\right)\left(\mathfrak{G}_{N,M}\mathfrak{R}_{M,L}\right) \tag{B.4}$$

Here, $\boldsymbol{R}$ provides a two-dimensional matrix of rotational velocities across the x-z plane, and $\mathfrak{G}$ denotes a matrix of the M components of G for each of the N cells in the domain along the x-axis. The precomputed elements of $\mathfrak{R}$ are given by

$$\mathfrak{R}_{n,l} = \frac{1-\cos\left(n\pi s_l\right)}{n\pi} \quad n \in \{1,2,\ldots,M\}\,,\; o \in \{1,2,\ldots,L\}. \tag{B.5}$$

The diagonalisation of a vector is performed according to

$$\operatorname{diag}\left(f_n\right) = \begin{bmatrix} f_1 & 0 & \ldots & 0 \\ 0 & f_2 & \ldots & 0 \\ \vdots & \vdots & \ddots & \vdots \\ 0 & 0 & \ldots & f_n \end{bmatrix}, \tag{B.6}$$

while the following vectors provide values of h and ζ_e for each cell in the domain:

$$\boldsymbol{h}_N = \begin{bmatrix} h_1 & h_2 & \ldots & h_N \end{bmatrix}^\mathsf{T} \tag{B.7}$$

$$\boldsymbol{\eta}_N = \begin{bmatrix} (\zeta_\mathrm{e})_1 & (\zeta_\mathrm{e})_2 & \ldots & (\zeta_\mathrm{e})_N \end{bmatrix}^\mathsf{T} \tag{B.8}$$

In reality, the numerical calculation does not require the diagonalisation of $\boldsymbol{h}$ and $\boldsymbol{\eta}$. Instead, each row of the matrix obtained from the product of $\mathfrak{G}$ and $\mathfrak{R}$ is subsequently multiplied element-wise by the original vector.

B.3 Horizontal velocity and vorticity

The same approach is adopted for the two-dimensional matrices of horizontal velocity and vorticity outside the roller region, which are calculated from Equations (4.43) and (4.56) as

$$\mathbf{u}_{N,L} = \bar{\mathbf{u}}_{N,L} - \operatorname{diag}\left(\boldsymbol{h}_N\right)\mathfrak{G}^{(1)}_{N,M}\mathfrak{C}_{M,L} \tag{B.9}$$

and

$$\boldsymbol{\omega}_{N,L} = \boldsymbol{\Omega}_{N,L} + \left(\mathfrak{G}^{(1)}_{N,M} + \mathfrak{G}^{(2)}_{N,M}\right)\mathfrak{V}_{M,L}, \tag{B.10}$$

respectively. Here

$$\bar{\mathbf{u}}_{N,L} = \begin{bmatrix} \bar{u}_1 & \bar{u}_1 & \ldots & \bar{u}_1 \\ \bar{u}_2 & \bar{u}_2 & \ldots & \bar{u}_2 \\ \vdots & \vdots & \ddots & \vdots \\ \bar{u}_N & \bar{u}_N & \ldots & \bar{u}_N \end{bmatrix}, \tag{B.11}$$

$$\boldsymbol{\Omega}_{N,L} = \begin{bmatrix} s_1\left(\omega_\mathrm{s}\right)_1 & s_2\left(\omega_\mathrm{s}\right)_1 & \dots & s_L\left(\omega_\mathrm{s}\right)_1 \\ s_1\left(\omega_\mathrm{s}\right)_2 & s_2\left(\omega_\mathrm{s}\right)_2 & \dots & s_L\left(\omega_\mathrm{s}\right)_2 \\ \vdots & \vdots & \ddots & \vdots \\ s_1\left(\omega_\mathrm{s}\right)_N & s_2\left(\omega_\mathrm{s}\right)_N & \dots & s_L\left(\omega_\mathrm{s}\right)_N \end{bmatrix} \tag{B.12}$$

and the elements of $\mathfrak{C}$ and $\mathfrak{V}$ are calculated according to the following relations, respectively:

$$\mathfrak{C}_{n,l} = \frac{\cos\left(n\pi s_l\right)}{n\pi} \quad n \in \{1,2,\dots,M\},\ o \in \{1,2,\dots,L\} \tag{B.13}$$

$$\mathfrak{V}_{n,l} = \sin\left(n\pi s_l\right) \quad n \in \{1,2,\dots,M\},\ o \in \{1,2,\dots,L\} \tag{B.14}$$

Due to the fact that the numerical approximation given by Equation (4.46) results in zero vorticity at the lower edge of the roller, the model presented here uses Equation (4.43) for the calculation of ω.

B.4 Breaking terms

In a similar manner, the breaking terms given in Equations (4.62) and (4.66) can be calculated as

$$\begin{aligned} \boldsymbol{M}_N = {} & (\boldsymbol{h}_N + \boldsymbol{\eta}_N) \odot (\boldsymbol{h}_N + \boldsymbol{\eta}_N) \odot (\boldsymbol{h}_N + \boldsymbol{\eta}_N) \\ & \odot \left[(\mathfrak{G}_{N,M}\boldsymbol{\Pi}_M) \odot (\mathfrak{G}_{N,M}\boldsymbol{\Pi}_M) + \frac{1}{2}\left(\mathfrak{G}_{N,M} \odot \mathfrak{G}_{N,M}\right)\left(\boldsymbol{\Pi}_M \odot \boldsymbol{\Pi}_M\right) \right] \\ & + (\boldsymbol{\zeta}_N - \boldsymbol{\eta}_N) \odot \left\{ \mathfrak{r} \odot \mathfrak{r}_N + \mathfrak{v}_N \odot (\boldsymbol{\zeta}_N - \boldsymbol{\eta}_N) \odot \left[\frac{2}{3}\mathfrak{r}_N + \frac{2}{15}(\boldsymbol{\zeta}_N - \boldsymbol{\eta}_N) \right] \right\} - \mathfrak{d}_N \\ & \odot \left[(\boldsymbol{h}_N + \boldsymbol{\eta}_N) \odot (\boldsymbol{h}_N + \boldsymbol{\eta}_N) \odot (\mathfrak{G}_{N,M}\boldsymbol{\Pi}_M) + (\boldsymbol{\zeta}_N - \boldsymbol{\eta}_N) \odot \left(\mathfrak{r}_N + \frac{\boldsymbol{\zeta}_N - \boldsymbol{\eta}_N}{3} \right) \right] \\ & \odot \left[(\boldsymbol{h}_N + \boldsymbol{\eta}_N) \odot (\boldsymbol{h}_N + \boldsymbol{\eta}_N) \odot (\mathfrak{G}_{N,M}\boldsymbol{\Pi}_M) + (\boldsymbol{\zeta}_N - \boldsymbol{\eta}_N) \odot \left(\mathfrak{r}_N + \frac{\boldsymbol{\zeta}_N - \boldsymbol{\eta}_N}{3} \right) \right] \end{aligned} \tag{B.15}$$

and

$$\begin{aligned} \boldsymbol{P}_N = {} & (\boldsymbol{h}_N + \boldsymbol{\eta}_N) \odot (\boldsymbol{h}_N + \boldsymbol{\eta}_N) \odot (\boldsymbol{h}_N + \boldsymbol{\eta}_N) \\ & \odot \left[4\boldsymbol{h}_N \odot \mathfrak{U}_N \odot (\mathfrak{G}_{N,M}\mathfrak{p}_M) - (\boldsymbol{h}_N + \boldsymbol{\eta}_N) \odot (\mathfrak{G}_{N,M}\mathfrak{p}_M) \right], \end{aligned} \tag{B.16}$$

respectively, where

$$\boldsymbol{\Pi}_M = \begin{bmatrix} \frac{1}{\pi} & \frac{1}{2\pi} & \dots & \frac{1}{M\pi} \end{bmatrix}^\intercal, \tag{B.17}$$

$$\boldsymbol{\zeta}_N = \begin{bmatrix} \zeta_1 & \zeta_2 & \dots & \zeta_N \end{bmatrix}^\intercal, \tag{B.18}$$

$$\mathfrak{r}_N = \begin{bmatrix} \left(u_\mathrm{r}|_{z=\zeta_\mathrm{e}}\right)_1 & \left(u_\mathrm{r}|_{z=\zeta_\mathrm{e}}\right)_2 & \dots & \left(u_\mathrm{r}|_{z=\zeta_\mathrm{e}}\right)_N \end{bmatrix}^\intercal, \tag{B.19}$$

$$\mathfrak{v}_N = \begin{bmatrix} (\omega_\mathrm{s})_1 & (\omega_\mathrm{s})_2 & \dots & (\omega_\mathrm{s})_N \end{bmatrix}^\intercal, \tag{B.20}$$

$$\mathfrak{d}_N = \begin{bmatrix} \dfrac{1}{h_1+\zeta_1} & \dfrac{1}{h_2+\zeta_2} & \cdots & \dfrac{1}{h_N+\zeta_N} \end{bmatrix}^\intercal, \tag{B.21}$$

$$\mathfrak{p}_M = \begin{bmatrix} \dfrac{-1}{\pi^3} & \dfrac{1}{8\pi^3} & \cdots & \dfrac{(-1)^M}{M^3\pi^3} \end{bmatrix}^\intercal \tag{B.22}$$

and

$$\mathfrak{U}_N = \begin{bmatrix} \left(\dfrac{\partial \bar{u}}{\partial x}\right)_1 & \left(\dfrac{\partial \bar{u}}{\partial x}\right)_2 & \cdots & \left(\dfrac{\partial \bar{u}}{\partial x}\right)_N \end{bmatrix}^\intercal. \tag{B.23}$$

Appendix C

Mathematical theorems and numerical approximations

C.1 The Leibniz rule

First, a function describing a partial derivative is defined:

$$f(X,Y) = \frac{\partial Z(X,Y)}{\partial Y} \tag{C.1}$$

Integrating both sides from $Y = V(X)$ to $Y = W(X)$ provides

$$\int_V^W f \, \mathrm{d}Y = Z|_{Y=W} - Z|_{Y=V}\,, \tag{C.2}$$

which, using the chain rule, can be differentiated with respect to X as follows:

$$\frac{\mathrm{d}}{\mathrm{d}X}\int_V^W f \, \mathrm{d}Y = \left.\frac{\partial Z}{\partial X}\right|_{Y=W} - \left.\frac{\partial Z}{\partial X}\right|_{Y=V} + \left.\frac{\partial Z}{\partial Y}\right|_{Y=W}\frac{\mathrm{d}W}{\mathrm{d}X} - \left.\frac{\partial Z}{\partial Y}\right|_{Y=V}\frac{\mathrm{d}V}{\mathrm{d}X} \tag{C.3}$$

Differentiating Equation (C.1) with respect to X and then integrating from $Y = V$ to $Y = W$ gives

$$\int_V^W \frac{\partial f}{\partial X}\,\mathrm{d}Y = \int_V^W \frac{\partial^2 Z}{\partial X \partial Y}\,\mathrm{d}Y = \left.\frac{\partial Z}{\partial X}\right|_{Y=W} - \left.\frac{\partial Z}{\partial X}\right|_{Y=V}. \tag{C.4}$$

Substituting Equations (C.1) and (C.4) into Equation (C.3) then provides the Leibniz rule (Flanders, 1973; Thomas et al., 2005):

$$\frac{\mathrm{d}}{\mathrm{d}X}\left[\int_{V(X)}^{W(X)} f(X,Y)\;\mathrm{d}Y\right] = \int_V^W \frac{\partial f}{\partial X}\,\mathrm{d}Y + f|_{Y=W}\frac{\mathrm{d}W}{\mathrm{d}X} - f|_{Y=V}\frac{\mathrm{d}V}{\mathrm{d}X} \tag{3.39}$$

C.2 Integration by parts

Differentiating the product of V and W with respect to X gives

$$\frac{\partial}{\partial X}(VW) = V\frac{\partial W}{\partial X} + W\frac{\partial V}{\partial X}, \tag{C.5}$$

which can then be rearranged and integrated to give the following formula (Bird, 2014):

$$\int V(X)\frac{\partial W}{\partial X}\,\mathrm{d}X = VW - \int W\frac{\partial V}{\partial X}\,\mathrm{d}X \tag{4.69}$$

C.3 Taylor series expansion

The Taylor series expansion is obtained by first considering the integral of a derivative between two points:

$$\int_Y^{X'}\frac{\partial f}{\partial X}\,\mathrm{d}X = f|_{X=X'} - f|_{X=Y} \tag{C.6}$$

By rearranging and integrating by parts with Equation (4.69), the following statement can be written:

$$f|_{X=X'} = f|_{X=Y} - \frac{Y-X'}{1!}\left.\frac{\partial f}{\partial X}\right|_{X=Y} - \int_Y^{X'}\frac{X-X'}{1!}\frac{\partial^2 f}{\partial X^2}\,\mathrm{d}X \tag{C.7}$$

The expansion provided by Equation (4.69) can then be indefinitely repeated recursively. This then provides the Taylor series expansion theorem, which allows an analytic function, $f(X)$, centred at Y, to be written as an ascending power series about Y (Mei, 1997; Krantz, 2004):

$$f(X) = \sum_{n=0}^{\infty}\frac{(X-Y)^n}{n!}\left.\frac{\partial^n f}{\partial X^n}\right|_{X=Y} \tag{C.8}$$

C.4 Fourier series

By expressing a function, $f(X)$, that is periodic such that

$$f|_{X=0} = f|_{X=n} \quad n \in \mathbb{N}_1, \tag{C.9}$$

as an infinite summation of terms with increasing frequency, the function can be approximated as (Mei, 1997; Rahman, 2011)

$$f(X) = \frac{Y_0}{2} + \sum_{n=1}^{\infty}\left[Y_n\cos(n\pi X) + Z_n\sin(n\pi X)\right], \tag{C.10}$$

where

$$Y_n = \int_{-1}^{1} f(X)\cos(n\pi X)\;\mathrm{d}X \quad n \in \mathbb{N}_0 \tag{C.11}$$

and

$$Z_n = \int_{-1}^{1} f(X)\sin(n\pi X)\;\mathrm{d}X \quad n \in \mathbb{N}_1. \tag{C.12}$$

Since it is known that, for an odd function,

$$f(-X) = -f(X), \tag{C.13}$$

it then follows that

$$Y_n = 0 \quad n \in \mathbb{N}_0 \tag{C.14}$$

and

$$Z_n = 2\int_0^1 f(X)\sin(n\pi X)\ \mathrm{d}X \quad n \in \mathbb{N}_1. \tag{C.15}$$

C.5 Trigonometric identities

The following identities are useful for reformulating equations involving trigonometric functions (Cheney and Kincaid, 2008; Zill, 2009):

$$\sin(VX)\sin(WX) = \frac{1}{2}\cos[(V-W)X] - \frac{1}{2}\cos[(V+W)X] \tag{C.16}$$

$$\sin(VX)\cos(WX) = \frac{1}{2}\sin[(V-W)X] + \frac{1}{2}\sin[(V+W)X] \tag{C.17}$$

C.6 Polynomial interpolation

An interpolated form of a function, f, can be obtained from the value of that function at a number of discrete points in X according to the following polynomial (Press et al., 1992):

$$\mathcal{L}_{\mathcal{N}} = \sum_{n=0}^{\mathcal{N}} \ell_{\mathcal{N},n}\, f|_{X=X_n} \quad \mathcal{N} \in \mathbb{N}_1 \tag{C.18}$$

Here, $\mathcal{N}$ denotes the degree of the polynomial used to interpolate the original function, and

$$\ell_{\mathcal{N},n} = \prod_{\substack{l=0 \\ l\neq n}}^{\mathcal{N}} \frac{X - X_l}{X_n - X_l} \quad n \in \mathbb{N}_0. \tag{C.19}$$

If the function is evaluated at regular intervals, Equations (C.18) and (C.19) can be written as

$$\mathcal{L}_{\mathcal{N}} = \sum_{n=0}^{\mathcal{N}} \left[\prod_{\substack{l=0 \\ l\neq n}}^{\mathcal{N}} \frac{X - X_l}{(n-l)\,\Delta X} \right] f|_{X=X_n} \quad \mathcal{N} \in \mathbb{N}_1, \tag{C.20}$$

where

$$\Delta X = X_{n+1} - X_n \quad n \in \mathbb{N}_0. \tag{C.21}$$

Equation (C.20) then gives the following quadratic and cubic polynomial interpolations, respectively:

$$\begin{aligned}\mathcal{L}_2 &= \sum_{n=0}^{2}\left[\prod_{\substack{l=0\\l\neq n}}^{2}\frac{X-X_l}{(n-l)\,\Delta X}\right] f|_{X=X_n}\\ &= \frac{X^2-(X_1+X_2)\,X+X_1X_2}{2\Delta X^2}\, f|_{X=X_0}\\ &\quad -\frac{X^2-(X_0+X_2)\,X+X_0X_2}{\Delta X^2}\, f|_{X=X_1}+\frac{X^2-(X_0+X_1)\,X+X_0X_1}{2\Delta X^2}\, f|_{X=X_2}\end{aligned} \tag{C.22}$$

$$\begin{aligned}\mathcal{L}_3 &= \sum_{n=0}^{3}\left[\prod_{\substack{l=0\\l\neq n}}^{3}\frac{X-X_l}{(n-l)\,\Delta X}\right] f|_{X=X_n}\\ &= -\frac{X^3-(X_1+X_2+X_3)\,X^2+[X_1X_2+(X_1+X_2)\,X_3]\,X-X_1X_2X_3}{6\Delta X^3}\, f|_{X=X_0}\\ &\quad +\frac{X^3-(X_0+X_2+X_3)\,X^2+[X_0X_2+(X_0+X_2)\,X_3]\,X-X_0X_2X_3}{2\Delta X^3}\, f|_{X=X_1}\\ &\quad -\frac{X^3-(X_0+X_1+X_3)\,X^2+[X_0X_1+(X_0+X_1)\,X_3]\,X-X_0X_1X_3}{2\Delta X^3}\, f|_{X=X_2}\\ &\quad +\frac{X^3-(X_0+X_1+X_2)\,X^2+[X_0X_1+(X_0+X_1)\,X_2]\,X-X_0X_1X_2}{6\Delta X^3}\, f|_{X=X_3}\end{aligned} \tag{C.23}$$

C.7 Finite difference scheme

By differentiating Equation (C.20), the gradient of a function can be evaluated at a point, X_i, on the fixed grid:

$$\begin{aligned}\left.\frac{\partial\mathcal{L}_{\mathcal{N}}}{\partial X}\right|_{X=X_i} &= \left(\sum_{n=0}^{\mathcal{N}}\left\{\sum_{\substack{r=0\\r\neq n}}^{\mathcal{N}}\left[\frac{1}{(n-r)\,\Delta X}\prod_{\substack{l=0\\n\neq l\neq r}}^{\mathcal{N}}\frac{X-X_l}{(n-l)\,\Delta X}\right]\right\} f|_{X=X_n}\right)\Bigg|_{X=X_i}\\ &= \sum_{n=0}^{\mathcal{N}}\left[\sum_{\substack{r=0\\r\neq n}}^{\mathcal{N}}\left(\frac{1}{n-r}\prod_{\substack{l=0\\n\neq l\neq r}}^{\mathcal{N}}\frac{i-l}{n-l}\right)\right]\frac{f|_{X=X_n}}{\Delta X}\quad \mathcal{N}\in\mathbb{N}_1\end{aligned} \tag{C.24}$$

With $X_i = X_{\frac{N}{2}}$, Equation (C.24) provides a central FD scheme. Accordingly, the first derivative of f can be written with second-order accuracy as

$$\left(\frac{\partial f}{\partial X}\right)_1 \simeq \left.\frac{\partial\mathcal{L}_2}{\partial X}\right|_{X=X_1} = \sum_{n=0}^{2}\left[\sum_{\substack{r=0\\r\neq n}}^{2}\left(\frac{1}{n-r}\prod_{\substack{l=0\\n\neq l\neq r}}^{2}\frac{1-l}{n-l}\right)\right]\frac{f|_{X=X_n}}{\Delta X} = \frac{f_2-f_0}{2\Delta X}. \tag{C.25}$$

With Equation (C.25), the second derivatives of f can also be written with second-order accuracy:

$$\left(\frac{\partial^2 f}{\partial X^2}\right)_1 = \frac{\frac{f_2 - f_1}{\Delta X} - \frac{f_1 - f_0}{\Delta X}}{\Delta X} = \frac{f_2 - 2f_1 + f_0}{\Delta X^2} \tag{C.26}$$

References

Apel, J. R. (1988). *Principles of Ocean Physics*. Volume 38. International Geophysics. Academic Press.

Bashforth, F. and Adams, J. C. (1883). *An Attempt to Test the Theories of Capillary Action by Comparing the Theoretical and Measured Forms of Drops of Fluid. With an explanation of integration employed in construction of integrating the tables which give the theoretical forms of such drops*. Cambridge University Press.

Battjes, J. A. (1974). 'Surf similarity'. *Proceedings of the 14th International Conference on Coastal Engineering*. American Society of Civil Engineers. Copenhagen, Denmark.

Bellotti, G. and Brocchini, M. (2002). 'On using Boussinesq-type equations near the shoreline: a note of caution'. *Ocean Engineering* 29.12, 1569–1575.

Bird, J. (2014). *Engineering Mathematics*. 7th edition. Routledge.

Boussinesq, J. (1872). 'Théorie des ondes et des remous qui se propagent le long d'un canal rectangulaire horizontal, en communiquant au liquide contenu dans ce canal des vitesses sensiblement pareilles de la surface au fond'. *Journal de mathématiques pures et appliquées*. 2nd series 17, 55–108.

Briganti, R. and Dodd, N. (2009). 'Shoreline motion in nonlinear shallow water coastal models'. *Coastal Engineering* 56.5-6, 495–505.

Briganti, R., Musumeci, R. E., Bellotti, G., Brocchini, M. and Foti, E. (2004). 'Boussinesq modeling of breaking waves: description of turbulence'. *Journal of Geophysical Research* 109.C07015, 1–17.

Brocchini, M. (2013). 'A reasoned overview on Boussinesq-type models: the interplay between physics, mathematics and numerics'. *Proceedings of the Royal Society A: Mathematical, Physical and Engineering Science* 469.2160.

Butcher, J. C. (2008). *Numerical Methods for Ordinary Differential Equations*. 2nd edition. John Wiley & Sons.

Cheney, E. W. and Kincaid, D. R. (2008). *Numerical Mathematics and Computing*. 6th edition. Thomson Brooks/Cole.

Chivers, I. and Sleightholme, J. (2012). *Introduction to Programming with Fortran. With Coverage of Fortran 90, 95, 2003, 2008 and 77*. 2nd edition. Springer.

Christensen, E. D. and Deigaard, R. (2001). 'Large eddy simulation of breaking waves'. *Coastal Engineering* 42.1, 53–86.

Cienfuegos, R., Barthélemy, E. and Bonneton, P. (2006). 'A fourth-order compact finite volume scheme for fully nonlinear and weakly dispersive Boussinesq-type equations. Part I: model development and analysis'. *International Journal for Numerical Methods in Fluids* 51.11, 1217–1253.

Cienfuegos, R., Barthélemy, E. and Bonneton, P. (2007). 'A fourth-order compact finite volume scheme for fully nonlinear and weakly dispersive Boussinesq-type equations. Part II: boundary conditions and validation'. *International Journal for Numerical Methods in Fluids* 53.9, 1423–1455.

Cienfuegos, R., Barthélemy, E. and Bonneton, P. (2010). 'Wave-breaking model for Boussinesq-type equations including roller effects in the mass conservation equation'. *Journal of Waterway, Port, Coastal and Ocean Engineering* 136.1, 10–26.

Courant, R., Friedrichs, K. and Lewy, H. (1928). 'Über die partiellen differenzengleichungen der mathematischen physik'. *Mathematische Annalen* 100.1, 32–74.

Cox, D. T., Kobayashi, N. and Okayasu, A. (1995). *Experimental and numerical modeling of surf zone hydrodynamics*. Technical report CACR-95-97. University of Delaware: Center for Applied Coastal Research.

Cox, D. T., Kobayashi, N. and Okayasu, A. (1996). 'Bottom shear stress in the surf zone'. *Journal of Geophysical Research: Oceans* 101.C6, 14337–14348.

Dabiri, D. and Gharib, M. (1997). 'Experimental investigation of the vorticity generation within a spilling water wave'. *Journal of Fluid Mechanics* 330, 113–139.

Davis, R. A. (1994). *The Evolving Coast*. 48. Scientific American Library.

Davis, R. A. and Fitzgerald, D. M. (2009). *Beaches and Coasts*. Wiley.

Dean, R. G. and Dalrymple, R. A. (1991). *Water Wave Mechanics for Engineers and Scientists*. Advanced Series in Ocean Engineering. World Scientific.

Deigaard, R. and Fredsøe, J. (1989). 'Shear stress distribution in dissipative water waves'. *Coastal Engineering* 13.4, 357–378.

Delestre, O., Lucas, C., Ksinant, P., Darboux, F., Laguerre, C., Tuoi Vo, T. N., James, F. and Cordier, S. (2012). 'SWASHES: a compilation of shallow water analytic solutions for hydraulic and environmental studies'. *International Journal for Numerical Methods in Fluids*.

Dimakopoulos, A. S. and Dimas, A. A. (2011). 'Large-wave simulation of three-dimensional, cross-shore and oblique, spilling breaking on constant slope beach'. *Coastal Engineering* 58.8, 790–801.

Dimas, A. A. and Dimakopoulos, A. S. (2009). 'Surface roller model for the numerical simulation of spilling wave breaking over constant slope beach'. *Journal of Waterway, Port, Coastal, and Ocean Engineering* 135.5, 235–244.

Donahue, A. S., Zhang, Y., Kennedy, A. B., Westerink, J. J., Panda, N. and Dawson, C. (2015). 'A Boussinesq-scaled, pressure-Poisson water wave model'. *Ocean Modelling* 86, 36–57.

Duncan, J. H. (2001). 'Spilling breakers'. *Annual Review of Fluid Mechanics* 33.1, 519–547.

Erduran, K. S., Ilic, S. and Kutija, V. (2005). 'Hybrid finite-volume finite-difference scheme for the solution of Boussinesq equations'. *International Journal for Numerical Methods in Fluids* 49.11, 1213–1232.

Flanders, H. (1973). 'Differentiation under the integral sign'. *The American Mathematical Monthly* 80.6, 615–627.

Foiaş, C. I., Manley, O., Rosa, R. M. S. and Temam, R. (2001). *Navier-Stokes equations and turbulence*. Encyclopedia of Mathematics and its Applications 83. Cambridge University Press.

Fredsøe, J. and Deigaard, R. (1992). *Mechanics of Coastal Sediment Transport*. Volume 3. Advanced Series on Ocean Engineering. World Scientific.

Gallerano, F., Cannata, G. and Villani, M. (2014). 'An integral contravariant formulation of the fully non-linear Boussinesq equations'. *Coastal Engineering* 83, 119–136.

Galvin, C. J. (1968). 'Breaker type classification on three laboratory beaches'. *Journal of Geophysical Research* 73.12, 3651–3659.

Gobbi, M. F., Kirby, J. T. and Wei, G. (2000). 'A fully nonlinear Boussinesq model for surface waves. Part 2. Extension to $O(kh)^4$'. *Journal of Fluid Mechanics* 405, 181–210.

Goda, Y. (2010). *Random Seas and Design of Maritime Structures*. 3rd edition. Volume 33. Advanced Series on Ocean Engineering. World Scientific.

Graebel, W. P. (2007). *Advanced Fluid Mechanics*. Elsevier Science & Tech.

Hansen, J. B. (1980). 'Experimental investigations of periodic waves near breaking'. *Proceedings of the 17th International Conference on Coastal Engineering*. Sydney, Australia, 260–277.

Hansen, J. B. and Svendsen, I. A. (1979). *Regular waves in shoaling water: experimental data*. Technical report Series paper No. 21. Technical University of Denmark: Institute of Hydrodynamics and Hydraulic Engineering.

Harten, A., Lax, P. D. and Leer, B. van (1983). 'On upstream differencing and Godunov-type schemes for hyperbolic conservation laws'. *SIAM Review* 25.1, 35–61.

Hervouet, J.-M. (2007). *Hydrodynamics of Free Surface Flows. Modelling with the Finite Element Method*. John Wiley & Sons.

Hirsch, C. (2007). *Numerical Computation of Internal and External Flows. Fundamentals of Computational Fluid Dynamics*. 2nd edition. Volume 1. Elsevier.

Holthuijsen, L. H. (2007). *Waves in Oceanic and Coastal Waters*. Cambridge University Press.

Karambas, Th. V. and Koutitas, C. (1992). 'A breaking wave propagation model based on the Boussinesq equations'. *Coastal Engineering* 18.1-2, 1–19.

Kazolea, M. and Delis, A. I. (2013). 'A well-balanced shock-capturing hybrid finite volume-finite difference numerical scheme for extended 1D Boussinesq models'. *Applied Numerical Mathematics* 67, 167–186.

Kennedy, A. B., Chen, Q., Kirby, J. T. and Dalrymple, R. A. (2000). 'Boussinesq modeling of wave transformation, breaking and runup. I: one dimension'. *Journal of Waterway, Port, Coastal and Ocean Engineering* 126, 39–47.

Kinsman, B. (1984). *Wind Waves. Their Generation and Propagation on the Ocean Surface*. Dover Publications.

Klonaris, G. Th., Memos, C. and Karambas, Th. V. (2013). 'A Boussinesq-type model including wave-breaking terms in both continuity and momentum equations'. *Ocean Engineering* 57, 128–140.

Krantz, S. G. (2004). *Real Analysis and Foundations*. 2nd edition. Chapman and Hall/CRC.

Leer, B. van (1977). 'Towards the ultimate conservative difference scheme III. Upstream-centered finite-difference schemes for ideal compressible flow'. *Journal of Computational Physics* 23.3, 263–275.

Leer, B. van (1984). 'On the relation between the upwind-differencing schemes of Godunov, Engquist-Osher and Roe'. *SIAM Journal on Scientific and Statistical Computing* 5.1, 1–20.

LeVeque, R. J. (2002). *Finite Volume Methods for Hyperbolic Problems*. Cambridge Texts in Applied Mathematics 31. Cambridge University Press.

Lin, P. (2008). *Numerical Modeling of Water Waves*. Taylor & Francis.

Lo Re, C., Musumeci, R. E. and Foti, E. (2012). 'A shoreline boundary condition for a highly nonlinear Boussinesq model for breaking waves'. *Coastal Engineering* 60, 41–52.

Longo, S., Petti, M. and Losada, I. J. (2002). 'Turbulence in the swash and surf zones: a review'. *Coastal Engineering* 45.3-4: *Surface and Swash Zone Mechanics*, 129–147.

Longuet-Higgins, M. S. and Stewart, R. W. (1964). 'Radiation stresses in water waves; a physical discussion, with applications'. *Deep-Sea Research* 11.4, 529–562.

Losada, I. J., Lara, J. L., Christensen, E. D. and Garcia, N. (2005). 'Modelling of velocity and turbulence fields around and within low-crested rubble-mound breakwaters'. *Coastal Engineering* 52.10-11, 887–913.

Lubin, P., Vincent, S., Abadie, S. and Caltagirone, J.-P. (2006). 'Three-dimensional large eddy simulation of air entrainment under plunging breaking waves'. *Coastal Engineering* 53.8, 631–655.

Lynett, P. J. (2006). 'Wave breaking velocity effects in depth-integrated models'. *Coastal Engineering* 53.4, 325–333.

Madsen, P. A., Murray, R. and Sørensen, O. R. (1991). 'A new form of the Boussinesq equations with improved linear dispersion characteristics'. *Coastal Engineering* 15.4, 371–388.

Madsen, P. A. and Schäffer, H. A. (1998). 'Higher-order Boussinesq-type equations for surface gravity waves: derivation and analysis'. *Philosophical Transactions of the Royal Society of London. Series A: Mathematical, Physical and Engineering Sciences* 356.1749, 3123–3181.

Madsen, P. A. and Sørensen, O. R. (1992). 'A new form of the Boussinesq equations with improved linear dispersion characteristics. Part 2. A slowly-varying bathymetry'. *Coastal Engineering* 18.3-4, 183–204.

Madsen, P. A., Sørensen, O. R. and Schäffer, H. A. (1997). 'Surf zone dynamics simulated by a Boussinesq type model. Part I: model description and cross-shore motion of regular waves'. *Coastal Engineering* 32.4, 255–287.

Madsen, P. A. and Svendsen, I. A. (1983). 'Turbulent bores and hydraulic jumps'. *Journal of Fluid Mechanics* 129, 1–25.

Massey, B. S. and Ward-Smith, A. J. (2006). *Mechanics of Fluids*. 8th edition. Mechanics of Series. Taylor & Francis.

McCabe, M. V., Stansby, P. K. and Apsley, D. D. (2013). 'Random wave runup and overtopping a steep sea wall: shallow-water and Boussinesq modelling with generalised breaking and wall impact algorithms validated against laboratory and field measurements'. *Coastal Engineering* 74, 33–49.

Mei, C. C. (1989). *The Applied Dynamics of Ocean Surface Waves*. Volume 1. Advanced Series on Ocean Engineering. World Scientific.

Mei, C. C. (1997). *Mathematical Analysis in Engineering. How to Use the Basic Tools*. Cambridge University Press.

Muller, J.-M., Brisebarre, N., Dinechin, F. de, Jeannerod, C.-P., Lefèvre, V., Melquiond, G., Revol, N., Stehlé, D. and Torres, S. (2010). *Handbook of Floating-Point Arithmetic*. Birkhäuser.

Munk, W. H. (1950). 'Origin and generation of waves'. *Proceedings of the 1st International Conference on Coastal Engineering*. Long Beach, California.

Musumeci, R. E., Svendsen, I. A. and Veeramony, J. (2005). 'The flow in the surf zone: a fully nonlinear Boussinesq-type of approach'. *Coastal Engineering* 52.7, 565–598.

Nwogu, O. (1993). 'Alternative form of Boussinesq equations for nearshore wave propagation'. *Journal of Waterway, Port, Coastal and Ocean Engineering* 119.6, 618–638.

Orszaghova, J., Borthwick, A. G. L. and Taylor, P. H. (2012). 'From the paddle to the beach - a Boussinesq shallow water numerical wave tank based on Madsen and Sørensen's equations'. *Journal of Computational Physics* 231.2, 328–344.

Pagliara, S. and Chiavaccini, P. (2005). 'Shallow water waves'. *Water Encyclopedia*. Edited by J. Lehr, J. Keeley and J. Lehr. Volume 4. John Wiley & Sons.

Panda, N., Dawson, C., Zhang, Y., Kennedy, A. B., Westerink, J. J. and Donahue, A. S. (2014). 'Discontinuous Galerkin methods for solving Boussinesq-Green-Naghdi equations in resolving non-linear and dispersive surface water waves'. *Journal of Computational Physics* 273, 572–588.

Peregrine, D. H. (1967). 'Long waves on a beach'. *Journal of Fluid Mechanics* 27.4, 815–827.

Powers, D. L. (2006). *Boundary Value Problems. And Partial Differential Equations*. 5th edition. Elsevier Academic Press.

Press, W. H., Teukolsky, S. A., Vetterling, W. T. and Flannery, B. P. (1992). *Numerical Recipes in Fortran 77. The Art of Scientific Computing*. 2nd edition. Volume 1. Fortran Numerical Recipes. Cambridge University Press.

Puleo, J. A., Beach, R. A., Holman, R. A. and Allen, J. S. (2000). 'Swash zone sediment suspension and transport and the importance of bore-generated turbulence'. *Journal of Geophysical Research: Oceans* 105.C7, 17021–17044.

Rahman, M. (2011). *Applications of Fourier Transforms to Generalized Functions*. WIT Press.

Roeber, V. and Cheung, K. F. (2012). 'Boussinesq-type model for energetic breaking waves in fringing reef environments'. *Coastal Engineering* 70, 1–20.

Roeber, V., Cheung, K. F. and Kobayashi, M. H. (2010). 'Shock-capturing Boussinesq-type model for nearshore wave processes'. *Coastal Engineering* 57.4, 407–423.

Sagaut, P. (2006). *Large Eddy Simulation for Incompressible Flows. An Introduction*. 3rd edition. Scientific Computation. Springer.

Schäffer, H. A., Madsen, P. A. and Deigaard, R. (1993). 'A Boussinesq model for waves breaking in shallow water'. *Coastal Engineering* 20.3-4, 185–202.

Schäffer, H. A. and Sørensen, O. R. (2006). 'On the internal wave generation in Boussinesq and mild-slope equations'. *Coastal Engineering* 53.4, 319–323.

Shapiro, R. (1970). 'Smoothing, filtering, and boundary effects'. *Reviews of Geophysics* 8.2, 359–387.

Shi, F., Kirby, J. T., Harris, J. C., Geiman, J. D. and Grilli, S. T. (2012). 'A high-order adaptive time-stepping TVD solver for Boussinesq modeling of breaking waves and coastal inundation'. *Ocean Modelling* 43-44, 36–51.

Shirkavand, A. and Badiei, P. (2014). 'The application of a Godunov-type shock capturing scheme for the simulation of waves from deep water up to the swash zone'. *Coastal Engineering* 94, 1–9.

Smit, P., Zijlema, M. and Stelling, G. (2013). 'Depth-induced wave breaking in a non-hydrostatic, near-shore wave model'. *Coastal Engineering* 76, 1–16.

Smith, J. M. (2003). 'Surf zone hydrodynamics'. *Coastal Engineering Manual*. Volume 2. Engineer Manual 1110-2-1100 4. U.S. Army Corps of Engineers.

Son, S. and Lynett, P. J. (2014). 'Interaction of dispersive water waves with weakly sheared currents of arbitrary profile'. *Coastal Engineering* 90, 64–84.

Svendsen, I. A. (1984a). 'Mass flux and undertow in a surf zone'. *Coastal Engineering* 8.4, 347–365.

Svendsen, I. A. (1984b). 'Wave heights and set-up in a surf zone'. *Coastal Engineering* 8.4, 303–329.

Svendsen, I. A. (2006). *Introduction to Nearshore Hydrodynamics*. Volume 24. Advanced Series on Ocean Engineering. World Scientific.

Svendsen, I. A. and Madsen, P. A. (1984). 'A turbulent bore on a beach'. *Journal of Fluid Mechanics* 148, 73–96.

Svendsen, I. A. and Veeramony, J. (2001). 'Wave breaking in wave groups'. *Journal of Waterway, Port, Coastal, and Ocean Engineering* 127.4, 200–212.

Svendsen, I. A., Veeramony, J., Bakunin, J. and Kirby, J. T. (2000). 'The flow in weak turbulent hydraulic jumps'. *Journal of Fluid Mechanics* 418, 25–57.

Svendsen, I. A., Yu, K. and Veeramony, J. (1996). 'A Boussinesq breaking wave model with vorticity'. *Proceedings of the 25th International Conference on Coastal Engineering*. Amercian Society of Civil Engineers. Orlando, Florida, 1192–1204.

Tatlock, B., Briganti, R. and Musumeci, R. E. (2014). 'Wave breaking using a roller approach in a hybrid finite-volume finite-difference Boussinesq-type model'. *Proceedings of the 34th International Conference on Coastal Engineering*. Amercian Society of Civil Engineers. Seoul, Korea.

Thomas, G. B., Weir, M. D., Hass, J. R. and Giordano, F. R. (2005). *Thomas' Calculus*. 11th edition. Pearson Addison Wesley.

Thorpe, S. A. (2007). *An Introduction to Ocean Turbulence*. Cambridge University Press.

Tissier, M., Bonneton, P., Marche, F., Chazel, F. and Lannes, D. (2012). 'A new approach to handle wave breaking in fully non-linear Boussinesq models'. *Coastal Engineering* 67, 54–66.

Tonelli, M. and Petti, M. (2009). 'Hybrid finite volume - finite difference scheme for 2DH improved Boussinesq equations'. *Coastal Engineering* 56.5-6, 609–620.

Tonelli, M. and Petti, M. (2010). 'Finite volume scheme for the solution of 2D extended Boussinesq equations in the surf zone'. *Ocean Engineering* 37.7, 567–582.

Toro, E. F. (2001). *Shock-Capturing Methods for Free-Surface Shallow Flows*. John Wiley.

Toro, E. F. (2009). *Riemann Solvers and Numerical Methods for Fluid Dynamics. A Practical Introduction*. 3rd edition. Springer-Verlag.

Vázquez-Cendón, M. E. (1999). 'Improved treatment of source terms in upwind schemes for the shallow water equations in channels with irregular geometry'. *Journal of Computational Physics* 148.2, 497–526.

Veeramony, J. and Svendsen, I. A. (2000). 'The flow in surf-zone waves'. *Coastal Engineering* 39.2-4, 93–122.

Wei, G., Kirby, J. T. and Sinha, A. (1999). 'Generation of waves in Boussinesq models using a source function method'. *Coastal Engineering* 36.4, 271–299.

Weisse, R. (2010). *Marine Climate and Climate Change*. 1st edition. Springer-Verlag Berlin Heidelberg.

White, R. E. (2003). *Computational Mathematics. Models, Methods, and Analysis with MATLAB and MPI*. Chapman and Hall/CRC.

Xing, Y. and Shu, C.-W. (2005). 'High order finite difference WENO schemes with the exact conservation property for the shallow water equations'. *Journal of Computational Physics* 208.1, 206–227.

Yamamoto, S. and Daiguji, H. (1993). 'Higher-order-accurate upwind schemes for solving the compressible Euler and Navier-Stokes equations'. *Computers & Fluids* 22.2-3, 259–270.

Yamamoto, S., Kano, S. and Daiguji, H. (1998). 'An efficient CFD approach for simulating unsteady hypersonic shock-shock interference flows'. *Computers & Fluids* 27.5-6, 571–580.

Young, D. F., Munson, B. R., Okiishi, T. H. and Huebsch, W. W. (2010). *A Brief Introduction To Fluid Mechanics*. John Wiley & Sons.

Zelt, J. A. (1991). 'The run-up of nonbreaking and breaking solitary waves'. *Coastal Engineering* 15.3, 205–246.

Zhang, Y., Kennedy, A. B., Donahue, A. S., Westerink, J. J., Panda, N. and Dawson, C. (2014). 'Rotational surf zone modeling for $O(\mu^4)$ Boussinesq-Green-Naghdi systems'. *Ocean Modelling* 79, 43–53.

Zhang, Y., Kennedy, A. B., Panda, N., Dawson, C. and Westerink, J. J. (2013). 'Boussinesq-Green-Naghdi rotational water wave theory'. *Coastal Engineering* 73, 13–27.

Zhao, Q. and Armfield, S. W. (2014). 'Recent advances in turbulence modeling for unsteady breaking waves'. *Advances in Numerical Simulation of Nonlinear Water Waves*. Edited by Q. Ma. Volume 11. Advances in Coastal and Ocean Engineering. World Scientific.

Zhou, J. G., Causon, D. M., Mingham, C. G. and Ingram, D. M. (2001). 'The surface gradient method for the treatment of source terms in the shallow-water equations'. *Journal of Computational Physics* 168.1, 1–25.

Zijlema, M., Stelling, G. and Smit, P. (2011). 'SWASH: an operational public domain code for simulating wave fields and rapidly varied flows in coastal waters'. *Coastal Engineering* 58.10, 992–1012.

Zill, D. G. (2009). *A First Course in Differential Equations with Modeling Applications*. 9th edition. Brooks/Cole.

Index